UNIVERSITY OF CALIFORNIA
RIVERSIDE

Well-Defined Heterogeneous Catalysts for Selective Transformations

A Dissertation submitted in partial satisfaction
of the requirements for the degree of

Doctor of Philosophy

in

Chemistry

by

Jessica E. Rodriguez

June 2022

Dissertation Committee:
Dr. Matthew P. Conley, Chairperson
Dr. W. Hill Harman
Dr. Timothy A. Su

The Dissertation of Jessica E. Rodriguez is approved:

Committee Chairperson

University of California, Riverside

Acknowledgments

I am not a big believer in chance, but I do think that some outside forces pushed me to Riverside for whatever reason, and it was honestly one of the best things to happen.

I would like to give my deepest thanks to Matt Conley. Throughout my time at UCR, Matt has hung in there with me as I figured out the ropes of all things chemistry, and even as I over described the color of anything that I made. This entire work would not have been possible without his patience, guidance, and one liners. The opportunity to do chemistry in the Conley Lab is something that I will forever be thankful for.

I would like to thank Dr. Lingchao Zhou for his never-ending patience when it comes to anything NMR related. A very special thank you to Prisciliano Saavedra for being the go to person for anything and everything. Chapters 5 and 6 would not have been possible without Dr. Maxime Boudjelel and Professor Richard Schrock.

I was fortunate to have some incredible labmates throughout my time in the Conley Lab. I would like to thank Dr. Hosein Tafazolian, Damien Culver, and Winn Hyunh for their friendship and guidance. You three made adjusting to graduate school infinitely easier. A very special thanks to Kavya Samudrala and Jiaxin Gao, I will deeply miss the antics, the laughs, and both of you.

To my grandparents, Karen and Richard, words will always fail me to say thank you. I am so glad that I have both of you in my corner no matter what or where I go in life. To my parents, Kim and Clyde, I love you deeply and am so thankful for all that you have done and all that you continue to do. To my siblings, Christian, Parker, Taylor, and Olivia, thank

you for being with me through everything in life and for being my sounding board. To my sister Olivia, thank you for everything and anything in between (mainly the free coffee). To my soul sister Hayley, this entire journey would have been a million times more difficult without you. There is no other person I could imagine going through this.

Throughout my time at UCR, I was beyond lucky to meet some of the most incredible people. I am still not sure how I lucked out with you all, but I'm so glad that you all stuck around. You kept me sane, and reminded me that there is always a light at the end of the tunnel (or a great drink after a several hours long hike on an island that we vastly over packed for).

Finally, to MPB thank you for always having a surprise desk snack for me, reminding me to enjoy every second of it all, and for eating our way through almost every taco place in Riverside.

The text figures, and schemes for the following chapters have been reproduced in part, from the following manuscripts.

Chapter 2:
J. Rodriguez, D. B. Culver, and M.P. Conley Generation of Phosphonium Sites on Sulfated Zirconium Oxide: Relationship to Brønsted Acid Strength of –OH Sites. *J. Am. Chem. Soc.* **2019**, *141*, 1484-1488.

Chapter 3:
J. Rodriguez and M.P. Conley Ethylene Polymerization Activity of $(R_3P)Ni(codH)^+$ (cod = 1,5-cylcooctadiene) Sites Supported on Sulfated Zirconium Oxide. *Inorg. Chem.* 2021, *60*, 6946-6949.

The co-author (Matthew P. Conley) listed in the above publications directed and supervised the research which forms the basis for this dissertation.

ABSTRACT OF THE DISSERTATION

Well-Defined Heterogeneous Catalysts for Selective Transformations

by

Jessica E. Rodriguez

Doctor of Philosophy, Graduate Program in Chemistry
University of California, Riverside, June 2022
Dr. Matthew P. Conley, Chairperson

Heterogeneous catalysts are widely used in industry. Common methods of synthesizing heterogeneous catalysts can lead to distributions of metal coordination environments making it challenging to apply structure–property relationships common in homogeneous chemistry. Surface organometallic chemistry (SOMC) combines the advantages of homogeneous and heterogeneous catalysis fields to develop well-defined heterogeneous catalysts that allow for structure-property optimization. The most common method to generate catalytic active sites in SOMC is to react an organometallic with a high surface area oxide. The speciation of $M–O_x$ sites on high surface area metal oxides depends on the Brønsted acidity of surface –OH sites. For example, supporting an organometallic on SiO_2 results in the formation of $M–O_x$ sites while supporting an organometallic on

sulfated zirconium oxide (**SZO**) results in the formation of [M][Ox] electrostatic ion-pairs. The first part of this thesis examines the acidity of **SZO** dehydroxylated at 300°C (**SZO_{300}**) through the generation of [R_3PH][**SZO**] ion pairs. [R_3PH][**SZO**] can further react with bis(cyclooctadiene)nickel ([$Ni(cod)_2$]) to form [$Ni(PAr_3)(codH)$][**SZO_{300}**] which are active for the polymerization of ethylene. A part of this thesis presents the synthesis of [Ir(cod)py][**SZO_{300}**] via two complementary synthetic methods. [Ir(cod)py][**SZO_{300}**] is active for the dearomative borylation of pyridines. The characterization and reactivity of these ion pairs will be discussed. The next part of this thesis focuses on developing a well-defined Schrock alkylidene on **SZO**. W=O(Adene)(2,5-Me_2pyr)$_2$ reacts with **SZO** to form [W=O(Adene)(2,5-Me_2pyr)][**SZO_{300}**], and has activity for the metathesis of terminal olefins with high E selectivity. This is the first example of a supported W-oxo alkylidene on a sulfated oxide. The final part of this thesis studies at the reaction of $W(C_4H_8)(NAr)(OSiPh_3)_2$ (NAr = 2,6-$iPr_2C_6H_3$) with partially dehydroxylated silica to form (≡SiO)(W(NAr)(C_4H_8)($OSiPh_3$). This supported metallacyclopentane undergoes thermal ring contraction to form (≡SiO)(W(NAr)(C_3H_8Me)($OSiPh_3$). This reaction also occurs in the presence of blue LEDs (λ = 450nm). This reaction establishes a route to access active olefin metathesis intermediates without generating an alkylidene. (≡SiO)(W(NAr)(C_4H_8)($OSiPh_3$) is active for the direct conversion of ethylene to propylene.

Table of Contents

List of Figures

List of Schemes

List of Tables

Table 3.5.1. Poisoning of **1Ni** with pyridine 113

Table 3.5.2. Optimization conditions using **[3-Ni(codH)][SZO$_{300}$]** 115

Chapter 1 Introduction to the Dissertation

Roughly 80% of industrial chemical synthesis uses a heterogeneous catalyst in at least one reaction step. The common methods of synthesizing heterogeneous catalysts are 1) incipient wetness impregnation, 2) co-precipitation, and 3) thermal deposition.[1–4] Incipient wetness impregnation fills the pore volume of a support with a solution containing a metal precursor. The paste is then dried and treated in air and/or hydrogen to remove organics and to reduce the metal to its active form. Co-precipitation involves mixing onto an existing support where the precipitating agent is slowly and uniformly introduced to avoid nucleation in solution. Thermal deposition uses metal complexes and thermolytically converts (<473K) the molecular species to three-dimensional networks. These methods often result in distributions of metal coordination environments as a mixture of both active and dormant sites. Due to this uncertainty, applying structure–property relationships is challenging with heterogeneous catalysis.

WO_3/SiO_2, an olefin metathesis catalyst, illustrates some of these challenges in studying classical heterogeneous catalysis. WO_3/SiO_2 catalyzes the ethenolysis of 2-butenes to give propene, Scheme 1.1.[5] WO_3/SiO_2 is prepared by incipient wetness impregnation of ammonium metatungstate onto silica followed by calcination under air at 550°C. WO_3/SiO_2 is active in the ethenolysis of 2-butene, an enthalpically favorable reaction at 298K, only at elevated temperatures (>300°C). Raman studies show that a distribution of W-oxo species are present on the silica surface, but clear identification of a $W{=}CH_2$ group that must be present for olefin metathesis has been elusive.[6] This has posed

a question: are the forcing conditions in WO_3/SiO_2 related to formation of the active site or poor reactivity of W-alkylidenes on silica surfaces?

a)

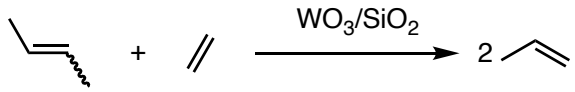

b)

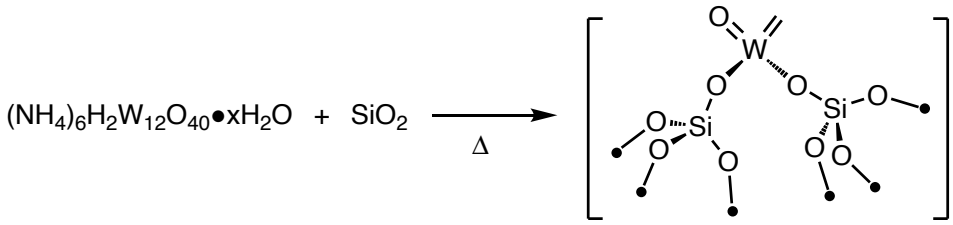

Scheme 1.1.1. Industrially used process to generate propylene from 2-butenes and ethylene (a) Reaction of ammonium metatungstate with silica to generate WO_3/SiO_2 (b); shown is the proposed active site as the active site has not yet been isolated

Well-defined heterogeneous catalysts for olefin metathesis species are accessible through the introduction of molecular alkylidene complexes onto partially dehydroxylated silica.[7] For example the reaction of W(=O)(=CH^{t}Bu)(OR)$_2$ (OR = 2,6-dimesitylphenoxide) with partially dehydroxylated silica at 700°C ($SiO_{2\text{-}700}$) forms (≡SiO)W(=CH^{t}Bu)(OR) as the metathesis active W-alkylidene, Scheme 1.1.2.[8] This material is orders of magnitude more active than WO_3/SiO_2 and 100 times more active than W(=O)(=CH^{t}Bu)(OR)$_2$ in solution. Related examples containing organometallic tungsten supported on SiO_2 show similar increases in activity in propene metathesis, [9–12] suggesting that the sluggish reactivity of WO_3/SiO_2 is related to the formation of the active site. This also shows that incorporating well-defined organometallics onto oxides is a viable strategy to achieve more efficient and selective heterogeneous catalysts.

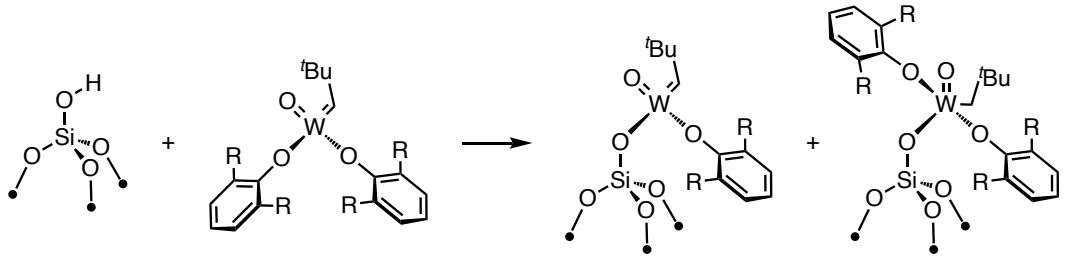

Scheme 1.1.2. Grafting reaction of $W(=O)(=CH^tBu)(OR)_2$ with SiO_2 to form $[(\equiv SiO)W(=CH^tBu)(OR)]$ and $[(\equiv SiO)W(=CH_2{}^tBu)(OR)]$

Formation of well-defined organometallics on heterogeneous supports through direct reaction of an organometallic with a high surface area oxide (or through functionalization of hybrid organic-inorganic oxides) is surface organometallic chemistry (SOMC).[13–18] SOMC combines the advantages of homogenous and heterogenous catalysis fields to develop well-defined heterogenous catalysts.[4,15–21] This allows for the generation of well-defined catalysts with known coordination spheres that allow for preparation and characterization similar to homogenous chemistry. Supported organometallic species tend to not undergo bi- or multimolecular degradation which is a deactivation pathway in homogenous catalysis.[22]

Organometallics react with oxides by one of the pathways shown in Scheme 1.1.3. The most common method is to react a partially dehydroxylated oxide, terminated with –OH groups, with a generic $L_nM–CH_3$ to form $[ML_n][OE\equiv]$ ion-pairs or $\equiv EO–ML_n$, Figure 1.1.3.

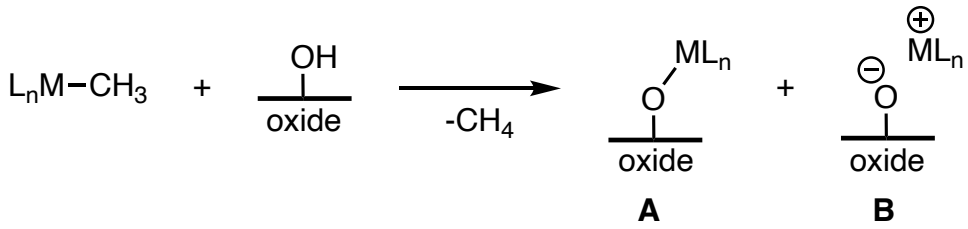

Scheme 1.1.3. Reaction of $L_nM–CH_3$ with a high surface area metal oxide utilizing the protonolysis pathway.

Most studies focus on reactions of organometallics with partially dehydroxylated silica.[23–26] Silica contains Si–O–Si bridges, physisorbed water, and hydroxyls (Si–OH). Heating this material to 140°C releases physisorbed water which results in the surface containing isolated, vicinal, and geminal surface sites, Scheme 1.1.4a.[27] Treatment under vacuum at high temperatures (>500°C) results in dehydroxylation of the vicinal silanols to form water and Si–O–Si bridges, Scheme 1.1.4b. Silica contains –OH groups that are weak acids which react with organometallics to form ≡SiO–M groups as described above in Scheme 1.1.3A.

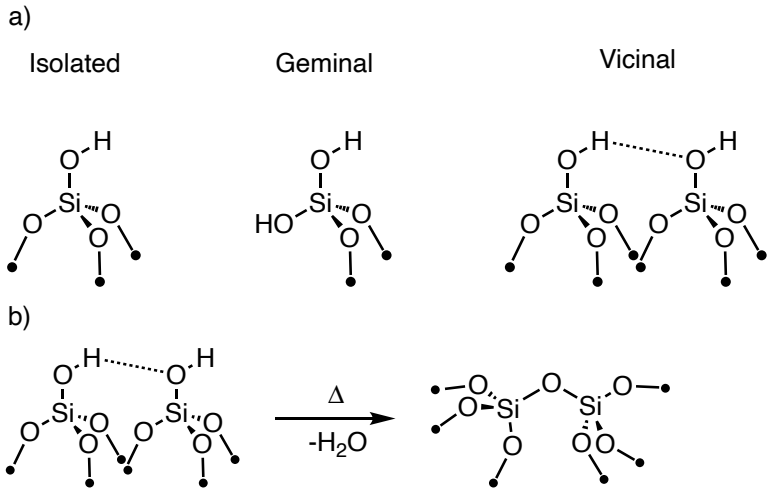

Scheme 1.1.4. Silanols present on the surface of silica (a) and condensation of vicinal silanols to release water to form ≡Si–O–Si≡ (b)

Sulfated metal oxides (SMOs) are prepared by contacting a native oxide with dilute sulfuric acid followed by high temperature calcination. The surface of SMOs is complex, but –OH groups present on SMOs are more acidic than the isolated silanols on silica. The reaction of $Cp^*_2ZrMe_2$ with oxides illustrates the difference in reaction chemistry with the–OH sites present on silica or SMOs. [28–30] The reaction of $Cp^*_2ZrMe_2$ with **SAO** generates [Cp^*_2ZrMe][**SAO**], Scheme 1.1.5, and methane. The ^{13}C NMR displays a signal for the Zr–Me^+ at 46 ppm which is similar to the chemical shift for [Cp^*_2ZrMe][$MeB(C_6F_5)_3$] (50.4 ppm).[31] [Cp^*_2ZrMe][**SAO**] is active in ethylene polymerization reactions. Additionally, DFT studies showed that [Cp^*_2ZrMe]$^+$ does not interact with Al–O–Al bridges on **SAO** due to unfavorable steric interactions between the sulfated alumina surface and the organozirconium fragment.[32] This is in contrast to the reaction of SiO_2 with $Cp^*_2ZrMe_2$ to form ≡SiO-ZrMe(Cp^*)$_2$, Scheme 1.1.5, which contains a signal at 31.5 ppm in the ^{13}C CPMAS NMR and is similar to values obtained for $Cp^*_2ZrMe(OR)$.[33] ≡SiO-ZrMe(Cp^*)$_2$

does not catalyze olefin polymerization due to the siloxy ligand not behaving as a weakly coordinating ligand.

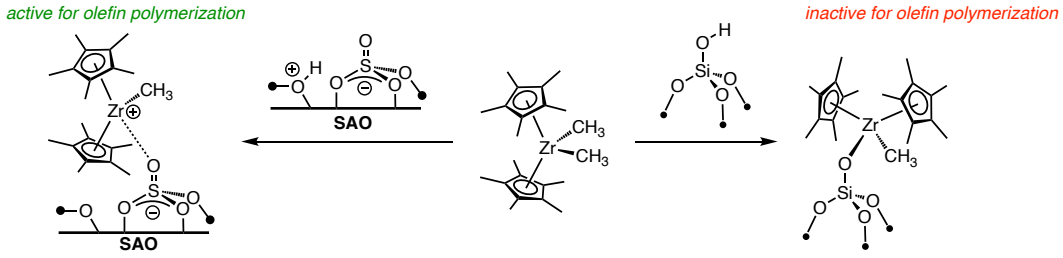

Scheme 1.1.5. The effect of the oxide support on surface speciation

SMOs have demonstrated that they can form weakly coordination ion pairs (e.g. $Cp^*_2ZrMe_2$ with **SAO**). Supported species on SMOs contain similarities with Group 4[30,45] or Group 10[46] organometallics for olefin polymerization reactions, but the application of SMOs extends past olefin polymerization reactions. $Cp^*IrMe_2(PMe)_3$ reacts with SMOs to form $[Cp^*IrMe(PMe)_3][\mathbf{SMO}]$ which is active for H/D reactions.[47] (^{dm}Phebox)Ir(OAc)$_2$ reacts with **SZO** to generate an electrophilic Ir site that is active for C–H bond activation and olefin hydrogenation reactions.[48] Allyltriisopropylsilane reacts with **SZO** to form $[^iPr_3Si][\mathbf{SZO}]$ ion pairs, which is active for hydrodefluoronation reactions in the presence of Et_3SiH. The formation of these ion pairs demonstrates the weakly coordinating ability of the sulfate site on **SZO**.[49]

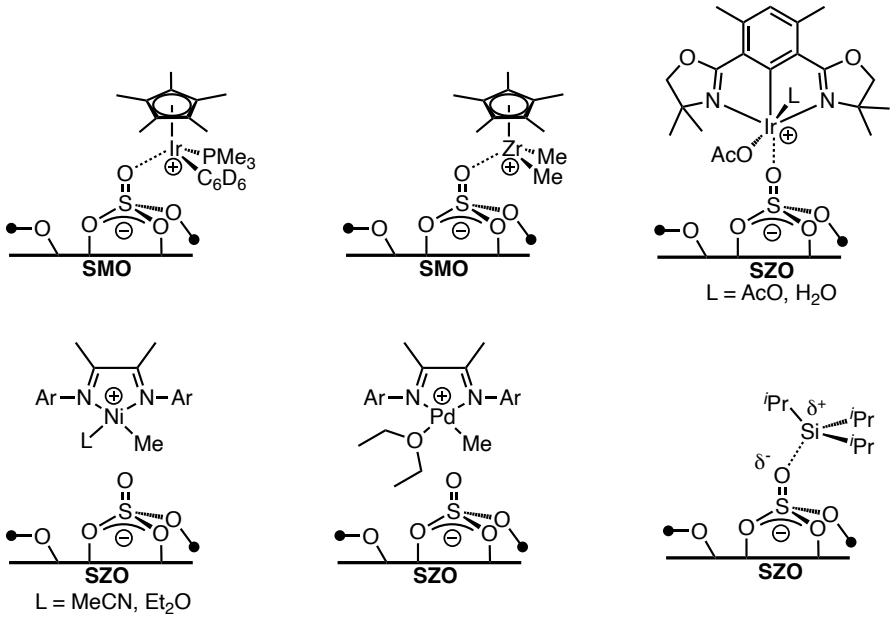

Figure 1.1.1. Well-defined species on SMOs

To generate ion-pairs in solution, homogeneous chemistry has relied on solution weakly coordinating anions (WCAs). The first generation of WCAs (e.g. SbF_6^-, PF_6^-) were discovered when studying superacidic media, however they were too reactive or too coordinating to stabilize these highly reactive cations. These anions are designed to be able to delocalize the charge throughout the structure of the weakly coordinating anion. As discussed earlier, $B(C_6F_5)_3$ and $[Ph_3C][B(C_6F_5)_4]$ can be used with Group IV metallacenes to generate olefin polymerization catalysts, [30] but there are many more solution weakly coordination anions to choose from, Figure 1.1.2. However, development of heterogeneous weakly coordination ion pairs is not as straightforward as solution (see discussion in Chapter 3).

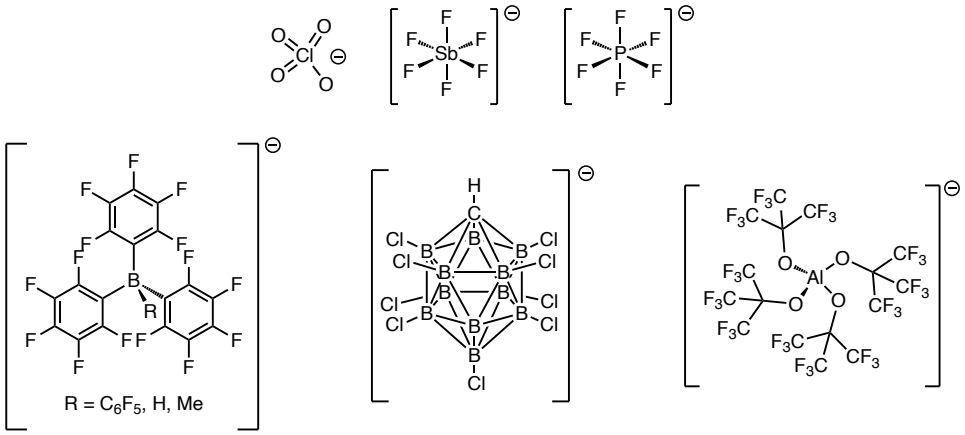

Figure 1.1.2. Examples of soluble WCAs

The ability for the oxides to form a strong or weak ion pair is directly related to the strength of the conjugate Brønsted acidity. A Brønsted acid is a species that donates a proton and can be defined by equation 1.1:

Equation 1.1.:

$$AH \rightarrow A^- + H^+$$

Quantifying surface acidity for solids is challenging and concepts used for solution acidity such as pK_a or H_0 are not applicable to solids, which complicates the understanding.[34,35] In solution, ions interact with solvent molecules which provides stabilization of charged intermediates. The acid sites present in solid acids react with bases in the gas phase, but strong ion pairing and lack of solution restricts the application of solid acidity. Brønsted acid strength of solids is usually measured by temperature programmed desorption of NH_3,[35] measurement of ν_{NH} stretches of ammonium salts by FT-IR,[36] and absorption of probe molecules.[37–39]

Sulfated zirconium oxide (**SZO**) reacts with aromatic colorimetric superacid indicators suggesting that the –OH sites on **SZO** are roughly four orders of magnitude more acidic than H_2SO_4.[40] However, colorimetric protonation studies using Hammett indicators on oxides can be misleading.[41] Reactions studies are also complicated. For example, **SZO** isomerizes *n*-butane at lower temperatures than H_2SO_4 which suggests strong Brønsted acidity. However, this is behavior is a result of trace amounts of butene in the reaction feed,[42] and pyrosulfate sites are responsible for the isomerization activity in reaction feeds that lack butene.[43] Solid-state NMR studies of **SZO** after adsorption of probe molecules showed that in addition to Brønsted sites, the surface contains Lewis acid sites.[44] This discussion highlights the complex surface of **SZO**, and the challenges encountered when determining the acidity of the –OH sites.

Chapter 2 will focus on studies of Brønsted acidity of **SZO**. Solid-state NMR show that ^{t}Bu$_2$PAr react cleanly with **SZO$_{300}$** to only form [R$_3$PH][**SZO$_{300}$**]. The clean formation of [R$_3$PH][**SZO$_{300}$**] species allows for an evaluation of how pK_a relates to surface binding. **SZO$_{300}$** is also shown to not react with known Hammett indicator *p*-nitroanilinium. These studies show that **SZO$_{300}$** is in fact not superacidic.

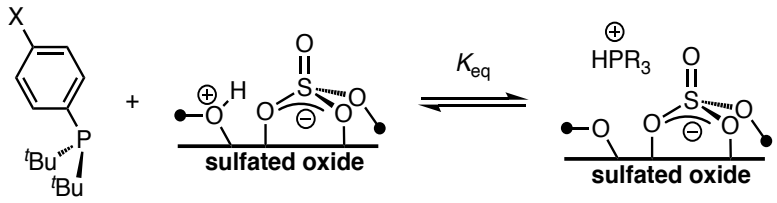

Scheme 1.1.6. Reaction of $^{t}Bu_2PAr$ with **SZO$_{300}$** to form [R_3PH][**SZO$_{300}$**]

SOMC allows for the generation of single-site catalysts with known coordination spheres. This thesis focuses on the generation of well-defined active sites on high surface area metal oxides. The reaction, characterization, and applications of these various ion pairs will be discussed.

Chapter 3 focuses on the reaction of a series of triarylphosphines with [**SZO$_{300}$**] to form [Ar_3PH][**SZO$_{300}$**]. This species further reacts with $Ni(cod)_2$ to form [$Ni(PAr_3)(codH)$][**SZO$_{300}$**] which is active in ethylene polymerization reactions. Organometallic complexes of nickel and palladium that contain *o*-phosphinoarenesulfonate ligand, {PO} are known to catalyze polymerization of ethylene to form linear polymers that possess a large functional group tolerance. [50–55] However, the application of supporting {PO}M–R (M = Ni, Pd) would form ion pairs that lack the organometallic unit required for polymer propagation.[56,57] This reaction provides a heterogenous {PO}H–type surface site to generate supported {PO}M–R species that are active for the polymerization of ethylene.

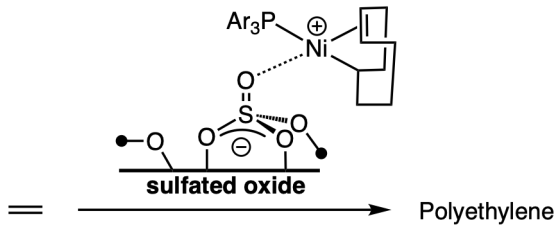

Scheme 1.1.7. Polymerization of ethylene by [Ni(PAr$_3$)(codH)][**SZO$_{300}$**]

Chapter 4 discusses the generation of a supported [Ir(py)(cod)][**SZO$_{300}$**] that is active for the hydroboration of nitrogenous heterocycles. Pyridines are one of the most prevalent heterocyclic motifs found in pharmaceuticals, agrochemicals, and material science targets. The importance of these structural motifs have encouraged the synthesis of these molecules to be further explored. We have previously studied the reaction of a series of di-*tert*-butylphenylphosphines with Brønsted sites on **SZO** to form [R$_3$PH][**SZO**].[58] Metalation of these [R$_3$PH][**SZO$_{300}$**] sites with Ir(III) organometallics results in catalysts that are active for the hydroboration of nitrogenous heterocycles.

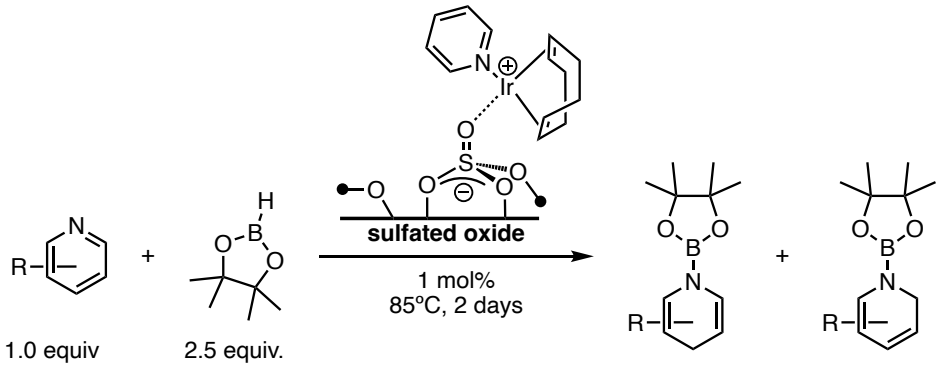

Scheme 1.1.8. General scheme reaction of pyridine and HBPin to yield hydroborated products

Chapter 5 discusses the reaction of W(=O)(=Adene)(2,5-Me$_2$pyr)$_2$ with **SZO$_{300}$** to form [W(=O)(=Adene)(2,5-Me$_2$pyr)][**SZO$_{300}$**]. The development of the sterically

demanding of W(=O)(=Adene)(2,5-Me_2pyr)$_2$ allows access to alkylidenes that were not readily accessible.[59] Insertion of ^{13}C-ethylene confirms the generation of a supported metallacyclobutane species. This catalyst is active for metathesis of both terminal and internal olefins with high selectivity for the E isomer.

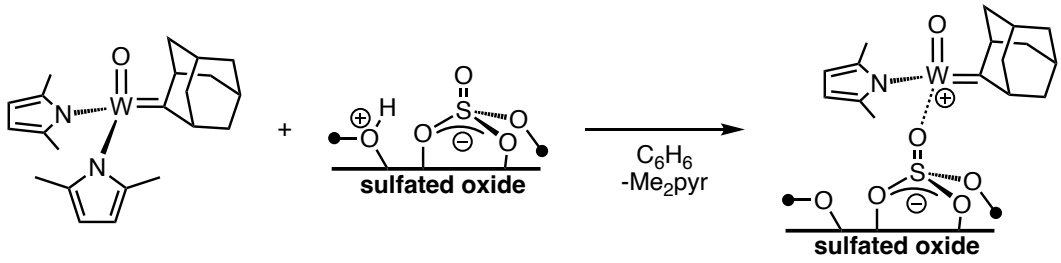

Scheme 1.1.9. Reaction W(=O)(=Adene)(2,5-Me_2pyr)$_2$ with **SZO$_{300}$** to form [W(=O)(=Adene)(2,5-Me_2pyr)][**SZO$_{300}$**]

Chapter 6 discusses the reaction of W(NAr)($OSiPh_3$)$_2$(C_4H_6) with $SiO_{2\text{-}700}$ to form [=SiO(W(NAr)($OSiPh_3$)$_2$(C_4H_6)]. Spectroscopic studies of these supported materials confirm that a supported metallacyclopentane cleanly contracts to substituted metallacyclobutane upon irradiation. This material is active for the conversion of ethylene to propylene under photocatalytic conditions.

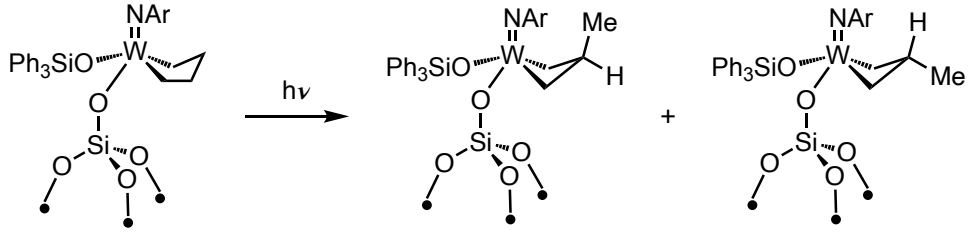

Scheme 1.1.10. Reaction of [=SiO(W(NAr)($OSiPh_3$)$_2$(C_4H_6)] with LEDs to form supported ring contracted species

1.1 References

1. Serp, P., Kalck, P. and Feurer, R. Chemical Vapor Deposition Methods for the Controlled Preparation of Supported Catalytic Materials. *Chem. Rev.* **102**, 3085–3128 (2002).

2. Eskandari, S., Tate, G., Leaphart, N. R. and Regalbuto, J. R. Nanoparticle Synthesis via Electrostatic Adsorption Using Incipient Wetness Impregnation. *ACS Catal.* **8**, 10383–10391 (2018).

3. Schwarz, J. A., Contescu, C. and Contescu, A. Methods for Preparation of Catalytic Materials. *Chem. Rev.* **95**, 477–510 (2002).

4. Munnik, P., De Jongh, P. E. and De Jong, K. P. Recent Developments in the Synthesis of Supported Catalysts. *Chem. Rev.* **115**, 6687–6718 (2015).

5. Popoff, N., Mazoyer, E., Pelletier, J., Gauvin, R. M. and Taoufik, M. Expanding the scope of metathesis: a survey of polyfunctional, single-site supported tungsten systems for hydrocarbon valorization. *Chem. Soc. Rev.* **42**, 9035–9054 (2013).

6. Lwin, S., Li, Y., Frenkel, A. I. and Wachs, I. E. Nature of WOx Sites on SiO2 and Their Molecular Structure-Reactivity/Selectivity Relationships for Propylene Metathesis. *ACS Catal.* **6**, 3061–3071 (2016).

7. Copéret, C. *et al.* Olefin metathesis: what have we learned about homogeneous and heterogeneous catalysts from surface organometallic chemistry? *Chem. Sci.* **12**, 3092–3115 (2021).

8. Conley, M. P. *et al.* A well-defined silica-supported tungsten oxo alkylidene is a highly active alkene metathesis catalyst. *J. Am. Chem. Soc.* **135**, 19068–19070 (2013).

9. Mazoyer, E. *et al.* Development of the first well-defined tungsten oxo alkyl derivatives supported on silica by SOMC: towards a model of WO3/SiO2 olefin metathesis catalyst. *Chem. Commun.* **46**, 8944–8946 (2010).

10. Merle, N. *et al.* On the track to silica-supported tungsten oxo metathesis catalysts: Input from 17O solid-state NMR. *Inorg. Chem.* **52**, 10119–10130 (2013).

11. Merle, N. *et al.* Well-Defined Molybdenum Oxo Alkyl Complex Supported on Silica by Surface Organometallic Chemistry: A Highly Active Olefin Metathesis Precatalyst. *J. Am. Chem. Soc.* **139**, 2144–2147 (2017).

12. Bouhoute, Y. *et al.* Accessing Realistic Models for the WO3-SiO2 Industrial Catalyst through the Design of Organometallic Precursors. *ACS Catal.* **6**, 1–18 (2016).

13. Marks, T. J. Surface-bound metal hydrocarbyls. Organometallic connections between heterogeneous and homogeneous catalysis. *Acc. Chem. Res.* **25**, 57–65 (1992).

14. Wegener, S. L., Marks, T. J. and Stair, P. C. Design Strategies for the Molecular Level Synthesis of Supported Catalysts. *Acc. Chem. Res.* **45**, 206–214 (2011).

15. Copéret, C., Chabanas, M., Petroff Saint-Arroman, R. and Basset, J. M. Homogeneous and heterogeneous catalysis: bridging the gap through surface organometallic chemistry. *Angew. Chem. Int. Ed. Engl.* **42**, 156–181 (2003).

16. Guzman, J. and Gates, B. C. Supported molecular catalysts: metal complexes and clusters on oxides and zeolites. *Dalt. Trans.* **3**, 3303–3318 (2003).

17. Conley, M. P., Copéret, C. and Thieuleux, C. Mesostructured hybrid organic-silica materials: Ideal supports for well-defined heterogeneous organometallic catalysts. *ACS Catal.* **4**, 1458–1469 (2014).

18. Liang, Y. and Anwander, R. Nanostructured catalysts via metal amide-promoted smart grafting. *Dalt. Trans.* **42**, 12521–12545 (2013).

19. Basset, J. M., Copéret, C., Soulivong, D., Taoufik, M. and Thivolle Cazat, J. Metathesis of alkanes and related reactions. *Acc. Chem. Res.* **43**, 323–334 (2010).

20. Stalzer, M. M., Delferro, M. and Marks, T. J. Supported Single-Site Organometallic Catalysts for the Synthesis of High-Performance Polyolefins. *Catal. Lett. 2014 1451* **145**, 3–14 (2014).

21. Wegener, S. L., Marks, T. J. and Stair, P. C. Design strategies for the molecular level synthesis of supported catalysts. *Acc. Chem. Res.* **45**, 206–214 (2012).

22. Bailey, G. A. *et al.* Bimolecular Coupling as a Vector for Decomposition of Fast-Initiating Olefin Metathesis Catalysts. *J. Am. Chem. Soc.* **140**, 6931–6944 (2018).

23. Copéret, C. *et al.* Surface Organometallic and Coordination Chemistry toward Single-Site Heterogeneous Catalysts: Strategies, Methods, Structures, and Activities. *Chem. Rev.* **116**, 323–421 (2016).

24. Copéret, C., Chabanas, M., Petroff Saint-Arroman, R. and Basset, J. M. Homogeneous and Heterogeneous Catalysis: Bridging the Gap through Surface

Organometallic Chemistry. *Angew. Chemie Int. Ed.* **42**, 156–181 (2003).

25. Pelletier, J. D. A. and Basset, J. M. Catalysis by Design: Well-Defined Single-Site Heterogeneous Catalysts. *Acc. Chem. Res.* **49**, 664–677 (2016).

26. Witzke, R. J., Chapovetsky, A., Conley, M. P., Kaphan, D. M. and Delferro, M. Nontraditional Catalyst Supports in Surface Organometallic Chemistry. *ACS Catal.* **10**, 11822–11840 (2020).

27. Zhuravlev, L. T. The surface chemistry of amorphous silica. Zhuravlev model. *Colloids Surfaces A Physicochem. Eng. Asp.* **173**, 1–38 (2000).

28. Delferro, M. and Marks, T. J. Multinuclear Olefin Polymerization Catalysts. *Chem. Rev.* **111**, 2450–2485 (2011).

29. Bochmann, M. The chemistry of catalyst activation: The case of group 4 polymerization catalysts. *Organometallics* **29**, 4711–4740 (2010).

30. Chen, E. Y. X. and Marks, T. J. Cocatalysts for Metal-Catalyzed Olefin Polymerization: Activators, Activation Processes, and Structure−Activity Relationships. *Chem. Rev.* **100**, 1391–1434 (2000).

31. Yang, X., Stern, C. L. and Marks, T. J. Cationic Zirconocene Olefin Polymerization Catalysts Based on the Organo-Lewis Acid Tris(pentafluorophenyl)borane. A Synthetic, Structural, Solution Dynamic, and Polymerization Catalytic Study. *J. Am. Chem. Soc.* **116**, 10015–10031 (1994).

32. Williams, L. A. *et al.* Surface structural-chemical characterization of a single-site d0 heterogeneous arene hydrogenation catalyst having 100% active sites. *Proc. Natl. Acad. Sci. U. S. A.* **110**, 413–418 (2013).

33. Fandos, R. *et al.* Synthesis and characterisation of Group 4 metallocene alkoxide complexes. X-ray crystal structure of Cp*2ZrCl(OCH2CH2SPh). *J. Organomet. Chem.* **606**, 156–162 (2000).

34. Boronat, M. and Corma, A. What Is Measured When Measuring Acidity in Zeolites with Probe Molecules? *ACS Catal.* **9**, 1539–1548 (2019).

35. Farneth, W. E. and Gorte, R. J. Methods for Characterizing Zeolite Acidity. *Chem. Rev.* **95**, 615–635 (1995).

36. Stoyanov, E. S., Kim, K. C. and Reed, C. A. An infrared vNH scale for weakly basic anions. Implications for single-molecule acidity and superacidity. *J. Am. Chem. Soc.* **128**, 8500–8508 (2006).

37. Osegovic, J. P. and Drago, R. S. Measurement of the Global Acidity of Solid Acids by 31P MAS NMR of Chemisorbed Triethylphosphine Oxide. *J. Phys. Chem. B* **104**, 147–154 (1999).

38. Farcasiu, D. and Ghenciu, A. Acidity functions from carbon-13 NMR. *J. Am. Chem. Soc.* **115**, 10901–10908 (1993).

39. Zheng, A., Liu, S. Bin and Deng, F. 31P NMR Chemical Shifts of Phosphorus Probes as Reliable and Practical Acidity Scales for Solid and Liquid Catalysts. *Chem. Rev.* **117**, 12475–12531 (2017).

40. Hino, M., Kobayashi, S. and Arata, K. Solid catalyst treated with anion. 2. Reactions of butane and isobutane catalyzed by zirconium oxide treated with sulfate ion. Solid superacid catalyst. *J. Am. Chem. Soc.* **101**, 6439–6441 (1979).

41. Chen, W. *et al.* Can Hammett indicators accurately measure the acidity of zeolite catalysts with confined space? Insights into the mechanism of coloration. *Catal. Sci. Technol.* **9**, 5045–5057 (2019).

42. Tabora, J. E. and Davis, R. J. On the Superacidity of Sulfated Zirconia Catalysts for Low-Temperature Isomerization of Butane. *J. Am. Chem. Soc.* **118**, 12240–12241 (1996).

43. Li, X. *et al.* Oxidative activation of n-butane on sulfated zirconia. *J. Am. Chem. Soc.* **127**, 16159–16166 (2005).

44. Haw, J. F. *et al.* NMR and theoretical study of acidity probes on sulfated zirconia catalysts. *J. Am. Chem. Soc.* **122**, 12561–12570 (2000).

45. Stalzer, M. M., Delferro, M. and Marks, T. J. Supported Single-Site Organometallic Catalysts for the Synthesis of High-Performance Polyolefins. *Catal. Letters* **145**, 3–14 (2015).

46. Ittel, S. D., Johnson, L. K. and Brookhart, M. Late-Metal Catalysts for Ethylene Homo- and Copolymerization. *Chem. Rev.* **100**, 1169–1203 (2000).

47. Kaphan, D. M. *et al.* Surface Organometallic Chemistry of Supported Iridium(III) as a Probe for Organotransition Metal-Support Interactions in C-H Activation. *ACS Catal.* **8**, 5363–5373 (2018).

48. Syed, Z. H. *et al.* Electrophilic Organoiridium(III) Pincer Complexes on Sulfated Zirconia for Hydrocarbon Activation and Functionalization. *J. Am. Chem. Soc.* **141**, 6325–6337 (2019).

49. Culver, D. B. and Conley, M. P. Activation of C−F Bonds by Electrophilic

Organosilicon Sites Supported on Sulfated Zirconia. *Angew. Chemie - Int. Ed.* **57**, 14902–14905 (2018).

50. Nakamura, A., Ito, S. and Nozaki, K. Coordination−Insertion Copolymerization of Fundamental Polar Monomers. *Chem. Rev.* **109**, 5215–5244 (2009).

51. Tan, C. and Chen, C. Emerging Palladium and Nickel Catalysts for Copolymerization of Olefins with Polar Monomers. *Angew. Chemie Int. Ed.* **58**, 7192–7200 (2019).

52. Muhammad, Q., Tan, C. and Chen, C. Concerted steric and electronic effects on α-diimine nickel- and palladium-catalyzed ethylene polymerization and copolymerization. *Sci. Bull.* **65**, 300–307 (2020).

53. Chen, C. Designing catalysts for olefin polymerization and copolymerization: beyond electronic and steric tuning. *Nat. Rev. Chem. 2018 25* **2**, 6–14 (2018).

54. Nakamura, A. *et al.* Ortho-phosphinobenzenesulfonate: A superb ligand for palladium-catalyzed coordination-insertion copolymerization of polar vinyl monomers. *Acc. Chem. Res.* **46**, 1438–1449 (2013).

55. Ittel, S. D., Johnson, L. K. and Brookhart, M. Late-Metal Catalysts for Ethylene Homo- and Copolymerization. *Chem. Rev.* **100**, 1169–1203 (2000).

56. Wucher, P., Schwaderer, J. B. and Mecking, S. Solid-supported single-component Pd(II) catalysts for polar monomer insertion copolymerization. *ACS Catal.* **4**, 2672–2679 (2014).

57. Dai, S. and Chen, C. A Self-Supporting Strategy for Gas-Phase and Slurry-Phase Ethylene Polymerization using Late-Transition-Metal Catalysts. *Angew. Chemie Int. Ed.* **59**, 14884–14890 (2020).

58. Rodriguez, J., Culver, D. B. and Conley, M. P. Generation of Phosphonium Sites on Sulfated Zirconium Oxide: Relationship to Brønsted Acid Strength of Surface -OH Sites. *J. Am. Chem. Soc.* **141**, 1484–1488 (2019).

59. Boudjelel, M., Zhai, F., Schrock, R. R., Hoveyda, A. H. and Tsay, C. Oxo 2-Adamantylidene Complexes of Mo(VI) and W(VI). *Organometallics* **40**, 838–842 (2021).

Chapter 2. Generation of Phosphonium sites on sulfated zirconium oxide: relationship to Brønsted Acid Strength of Surface –OH sites

2.1. Abstract

A series of P(^{t}Bu)$_2$Ar where the *para* position of the Ar groups contains electron-donating or electron-withdrawing groups was reacted with sulfated zirconium oxide partially dehydroxylated at 300°C to form [(^{t}Bu)$_2$ArPH][**SZO$_{300}$**]. The equilibrium binding constants of P(^{t}Bu)$_2$Ar to **SZO$_{300}$** relate to the pK_a of [(^{t}Bu)$_2$ArPH]. PR_3 species that form less acidic phosphoniums bind stronger to the **SZO$_{30}$** than PR_3 species that form more acidic phosphoniums, lower pK_a value. These studies show that the –OH groups on the surface of **SZO$_{300}$** are in not superacidic.

2.2. Introduction

An important step in synthesizing heterogeneous catalysts using a molecular strategy is understanding the reactivity of the support towards reactive inorganic species. A common method to control the structures of the active-site is to support an organometallic complex onto a partially dehydroxylated high surface area oxide to form M–O_x sites (**A** O_x = surface oxygen) or electrostatic ion pairs [M][O_x]. Understanding the factors that promote the formation between of **A**, **B**, or mixtures of these two extremes is fundamentally and practically significant. An example of the importance of the surface site

can be seen when supporting Cp_2ZrMe_2 on partially dehydroxylated sulfated oxides (**SO**) to form [Cp_2ZrMe][**SO**], a type **B** surface species, that is highly active in the polymerization of ethylene.[1–3]

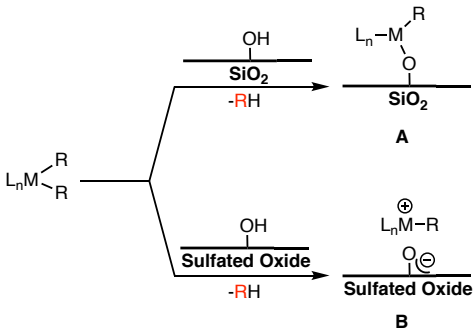

Figure 2.2.1. Chemisorption of organometallic complexes to form **A** or **B**.

The reaction of organometallic complexes with **SO** usually forms type **B** surface species that are also active in hydrogenation of arenes[4–6], and the activation of C–H bonds.[7,8] Brønsted acidity of the –OH sites on oxides is often presumed to impact the formation of **A** or **B**. The reaction of $Cp^*_2ZrMe_2$ with oxides illustrates this argument. Neutral oxides that contain weaker Brønsted –OH sites (e.g. SiO_2) tend to form **A**, and oxides that contain stronger Brønsted –OH sites (e.g. **SO**) tend to form **B**.

The Bronsted acidity of sulfated zirconium oxide (**SZO**) of the –OH sites has been a subject of a long standing debate. Initial reports showed **SZO** catalyzed the isomerization of *n*-butane to isobutane at lower temperatures than neat H_2SO_4.[9,10] This is suggestive that the Brønsted sites of **SZO** are superacidic.[11] A superacid is an acid with an acidity greater than that of 100% pure sulfuric acid, which has a Hammett acidity function (H_0) of -12.

Triflic acid (H_0 = -14.9), Fluorosulfuric acid (H_0 = -15.1), Magic Acid (H_0 = -19.2), and carborane acids ($H_0 \leq$ -18, depends on substituents) are all superacids.

The adsorption of aromatic colorimetric superacid indicators onto **SZO** further supports this,[10] and suggests that the –OH sites on **SZO** are roughly four orders of magnitude more acidic than H_2SO_4 (H_0 = - 12.0). However, isomerization of *n*-butane catalyzed by **SZO** was shown to be a result of olefin impurities in the butane feed.[12] Additionally, isothermal calorimetry showed that **SZO** binds pyridine weaker than zeolites.[13] Solid-state NMR studies of **SZO** after adsorption of probe molecules showed than in addition to Brønsted sites, the surface contains Lewis acid sites,[14] and pyrosulfates that are implicated in oxidative reaction pathways.[15] The pyrosulfate sites were suggested to be active in reactions with C – H bonds,[16,17] and are also implicated in the reaction of Ir organometallics with **SZO_{300}**.[15]

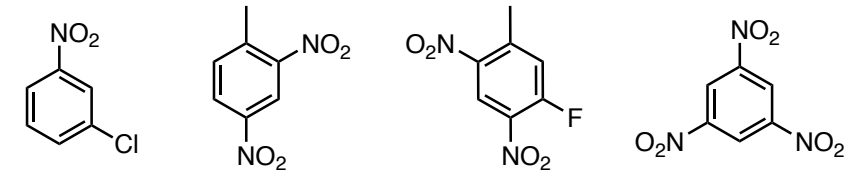

Figure 2.2.2. Hammett indicators that were reacted with **SZO**; only *m*-nitrochlorobenzene was noted to have a distinct reaction occur

There are many complexities in studying the Brønsted acidity of **SZO**, and the situation is complicated by the nature of H_0, which is a property of solution acids. There a quite a few available methods to assess the Brønsted acidity of solids: temperature-programmed desorption of NH_3,[18] measurement of ν_{NH} stretches of absorbed probe molecules by NMR spectroscopy,[19] and changes in chemical shift of adsorbed probe

molecules by NMR spectroscopy.[20,21] This chapter describes the reaction of **SZO** with a series of R_3P to form [R_3PH][**SZO**]. The $^{31}P\{^1H\}$ NMR chemical shifts of R_3P and [R_3PH] are distinguishable, and the acidity of [R_3PH] spans ~15 pK_a units in MeCN. These properties allow for the rapid assignment of [R_3PH][**SZO**] and provides an understanding of how the pK_a of [R_3PH] affects the formation of [R_3PH][**SZO**]. This chapter will show that **SZO** is certainly not superacidic.

2.3. Results and Discussion

*2.3.1. Reacting SZO_{300} with R_3P to from [R_3PH][**SZO**]*

SZO was prepared by suspending precipitated zirconium oxide in dilute aqueous H_2SO_4, followed by calcination at 600 °C. This temperature was chosen as it produces **SZO** with the strongest Brønsted acid sites based on colorimetric titrations. The reaction of gas phase PMe_3 with $\mathbf{SZO_{300}}$ forms [Me_3PH][$\mathbf{SZO_{300}}$]. The $^{31}P\{^1H\}$ magic angle spinning (MAS) NMR spectrum of [Me_3PH][$\mathbf{SZO_{300}}$] contains a major signal at – 4ppm, which is characteristic of [Me_3PH], and a minor peak at – 33 ppm which is assigned to small amounts of Me_3P bound to Lewis sites. This is important to note as previous studies have showed the **SZO** reacts with gas phase Me_3P to form mixtures of O=Me_3P, [Me_3PH], and [Me_4P]. **SZO** dehydroxylated at 500 °C results in the formation of significant amounts of [Me_4P] byproducts. The formation of [Me_3PH] as the major surface species indicates that $\mathbf{SZO_{300}}$ does not contain significant qualities of Lewis sites or pyrosulfates that are implicated in the formation of O=Me_3P or [Me_4P] byproducts.

Reacting bulkier ^{t}Bu$_3$P with **SZO$_{300}$** in a slurry of diethyl ether results in the clean formation of [^{t}Bu$_3$PH][**SZO$_{300}$**]. The FTIR spectrum contains a ν_{PH} at 2441 cm^{-1} and the ^{31}P{^{1}H} MAS NMR contains a signal at 52 ppm. There are no additional signals in the ^{31}P NMR, which is consistent with the clean and sole formation of a phosphonium species under these conditions. These results show that bulky strong donor R$_3$P are selective probes for Brønsted sites on **SZO$_{300}$.**

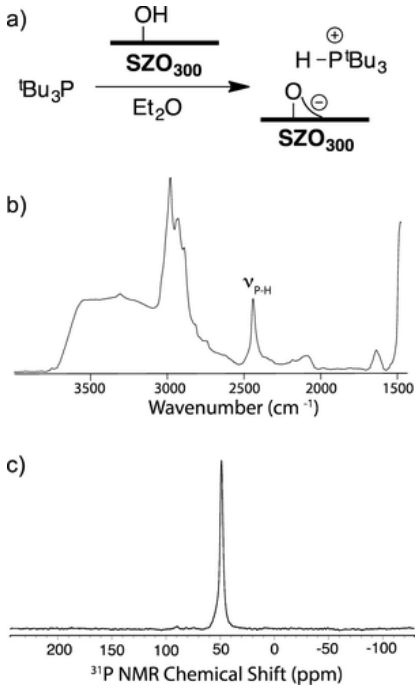

Figure 2.3.1. Reaction of ^{t}Bu$_3$P with **SZO$_{300}$** to form [^{t}Bu$_3$PH][**SZO$_{300}$**] (a); FTIR of [^{t}Bu$_3$PH][**SZO$_{300}$**] with ν_{PH} labelled for clarity (b); ^{31}P{^{1}H} MAS NMR spectrum of this material (c).

2.3.2. Synthesis and characterization of phosphoniums sites on sulfated zirconium oxide

A series of (^{t}Bu)$_2$PAr reacts with **SZO** in a slurry of MeCN, or diethyl ether, to form [R$_3$PH][**SZO**], Figure 2.3.2. The FT-IR spectrum of [R$_3$PH][**SZO**] shows the appearance of ν_{PH}, sp^3 ν_{CH}, and sp^2 ν_{CH} (table 2.3.1). The ^{31}P MAS NMR spectra are consistent with the formation of [R$_3$PH][**SZO**] (table 2.3.1).

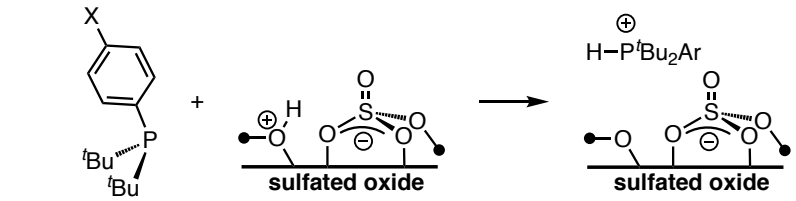

X = OMe, 1**a** H, 1**e**
^{t}Bu, 1**b** F, 1**f**
Me, 1**c** CF_3, 1**g**
TMS, 1**d** CN, 1**h**
H, 1**e**

Figure 2.3.2. Reaction of (^{t}Bu$_2$)PAr with **SZO$_{300}$** to form [(^{t}Bu$_2$)ArPH][**SZO**]

Table 2.3.1. δ^{31}P for **1a-h** and **2a-2h** and ν_{PH} for **2a –h**

(^{t}Bu)$_2$ArP	**δ^{31}P (ppm)**	**δ^{31}P 2a-h (ppm)**	**ν_{PH} (cm^{-1}) 2a-h**
1a	36.4	43	2448
1b	41.8	46	2445
1c	37.6	46	2438
1d	39.9	48	2441
1e	38.9	49	2439
1f	37.1	48	2438
1g	38.4	49	2433
1h	39.0	46	2432

2.3.3. Hammett Plot

Previous studies of phosphines showed that alkyl–aryl phosphines do not correlate well with Hammett's or Taft's parameters.[22,23] Therefore, σ values for each phosphine were calculated using equation 2.3.1

Equation 2.3.1.

$$\sigma = log\frac{K}{K_0}$$

where K is the experimental acid associate constant (K_a) for a given phosphine (Table 2.3.2) and K_0 is the reference K_a where the *para* position on the aryl is H (Table 2.3.2). The experimental σ values are reported below in Table 2.3.2. Figure 2.3.3b shows a Hammett plot using classical parameters derived from the ionization of benzoic acids. This plot is linear with a negative slope that is consistent with positive charge buildup in the reactions of ^{t}Bu$_2$PAr with **SZO$_{300}$**. However, the magnitude of ρ is lesser when using the classical Hammett values. The R^2 of this plot is also lower (R^2 = 0.87).

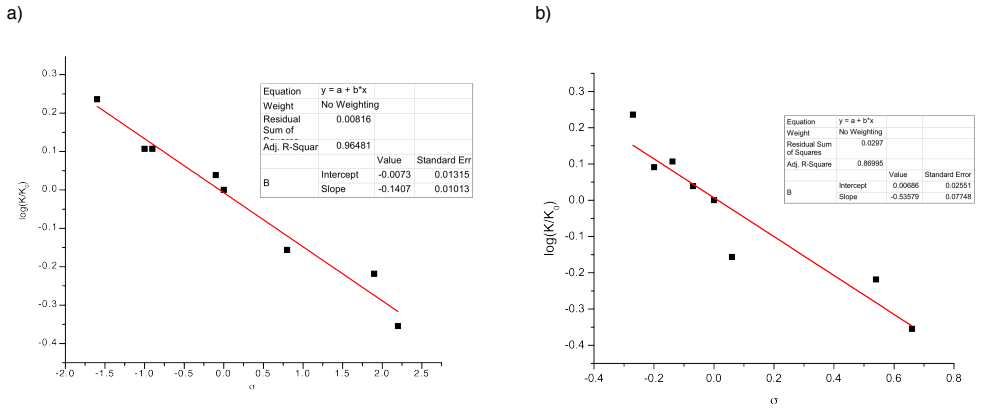

Figure 2.3.3. Hammett plot of the phosphine series **a)** Hammett plot for single-site Langmuir isotherm as described in main text **b)** Hammett plot using the classical parameters

Table 2. 3.2. Experimental σ values for 1a-1h

	pK_a	K_a	σ
1a	16.4	$3.98x10^{-17}$	-1.6
1b	15.8	$1.59X10^{-16}$	-1.0
1c	15.7	$2.00x10^{-16}$	-0.9
1d	14.9	$1.26x10^{-15}$	-0.1
1e	14.8	$1.59x10^{-15}$	0
1f	14.0	$1.00x10^{-14}$	0.8
1g	12.9	$1.26x10^{-13}$	1.9
1h	12.6	$2.51X10^{-13}$	2.2

2.3.4. Examination of Brønsted Acidity of SZO_{300}

Equilibrium binding studies were performed in anhydrous MeCN slurries at 25°C under rigorously anaerobic conditions, Table 2.3.3. A representative plot of the binding data of **1a** to SZO to form **2a** relates to the equilibrium adsorption constant K_a, equation 2.3.2, where $[HO_x]$ are Brønsted sites on **SZO** reported in mmol/g. K_a is extracted from the fits of data in Figure 2.3.4 to a single-site Langmuir isotherm, shown in Equation 2.3.2, where $[HO_x]_0$ is the initial OH loading and θ is the surface coverage of the phosphine on **SZO**.

Table 2. 3. 3. Binding Constants for Formation of **2** and pK_a of Phosphoniums

(*t*Bu)$_2$ArP	**pK_a**[a]	**K_a(x10^4 M^{-1})**[b]
1a	16.4	7.4(4)
1b	15.8	5.5(3)
1c	15.7	5.3(4)
1d	14.9	4.7(1)
1e	14.8	4.3(3)
1f	14.0	3.0(2)
1g	12.9	2.6(1)
1h	12.6	1.9(4)

[a]Determined in CD_3CN solution; [b]Average of three binding studies in MeCN slurries

The trend of this data shows that as K_a decreases as pK_a of [**1H**] decreases. A Hammett plot using data in Table 2.3.2 is linear with ρ = - 0.14, which is consistent with buildup of positive charge on phosphorous in the formation of **2a-h**.

Equation 2.3. 2.

$$K_{\mathrm{a}} = \frac{[\mathbf{2}]}{[\mathbf{1}][\mathrm{HO_x}]}$$

The data in table 2.3.3 is inconsistent with Brønsted superacid behavior. Superacids

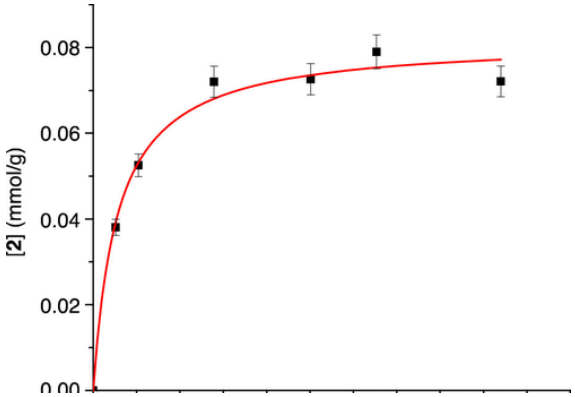

Figure 2.3.4. Langmuir isotherm of **1a** binding to **SZO$_{300}$**. This study was performed in triplicate using a phosphine stock solution of 0.3mM; the error bars are standard deviations from these binding studies.

are known to be able to protonate acetonitrile to from [(MeCN)$_x$H][X] solvates.[11] The pK_a of solvated protons in acetonitrile is 0[24], which should result in much stronger binding for bases whose conjugate acids that have pK_a values as those in Table 2.3.2.

2.3.5. Strength of – OH Sites

In order to confirm the strength of the –OH sites of **SZO**, the material was contacted with Ph_3P. The pK_a of $[Ph_3PH][BF_4]$ is 7.6 in MeCN, which implies that Ph_3P will bind to **SZO** weaker than (^{t}Bu)$_2$PAr as described in Table 2.3.2. $^{31}P\{^1H\}$ NMR studies of **SZO** suspended in acetonitrile solutions containing Ph_3P show that $K_a \sim 3\ M^{-1}$, which indicates

the Ph_3P binds significantly weaker than **1a-h**. Reacting **SZO** with $(2\text{-}FC_6H_4)Ph_2P$, pK_a of 6.11, shows no signal in the $^{31}P\{^1H\}$ MAS NMR spectrum. $^{31}P\{^1H\}$ MAS NMR spectrum shows one signal at –8 ppm, which correlates to the chemical shift of $(2\text{-}FC_6H_4)Ph_2P$ in $CDCl_3$. This establishes that the –OH sites on **SZO** cannot protonate bases whose conjugate acid has a pK_a of 6.11 or below. This is supported by the reaction of *p*-nitroaniline, a common Hammett indicator (pK_a(anilinium) = 6.22 in acetonitrile). Contacting **SZO** with a solution of *p*-nitroaniline in acetonitrile , a bright yellow solution, results in a white solid after successive washing with acetonitrile. Furthermore, the FT-IR spectrum **SZO** contacted with *p*-nitroaniline lacks the ν_{NH} stretch of a *p*-nitroanilinium, Figure 2.3.5.

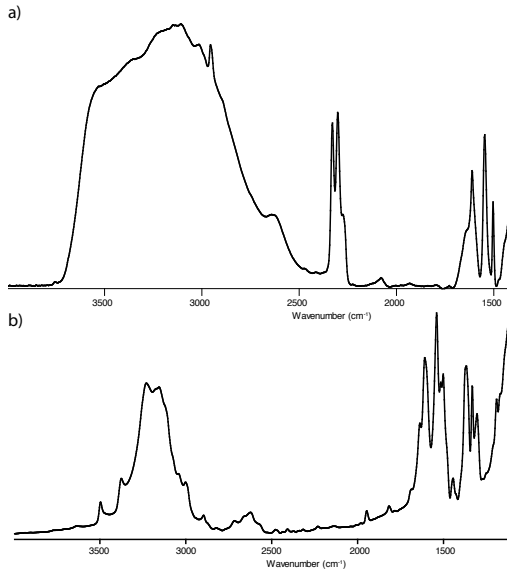

Figure 2.3.5. a) FT-IR spectrum of a solution of p-nitroaniline in MeCN contacted with **SZO$_{300}$** MeCN slurry after washing with MeCN b) FT-IR spectrum of [p-NO2-C6H4NH3]][BF4] in KBr.

2.4. Conclusions

The reaction of phosphines with **SZO** produces [R_3PH][**SZO**] without formation of byproducts that would arise from side reactions on this material. The clean formation of [R_3PH][**SZO**] allowed for an evaluation of how pK_a in [R_3PH] relates to surface binding. These studies show that **SZO** is not superacidic. If these sites were superacidic, **SZO** would be able to protonate (2-FC_6H_4)Ph_2P.

2.5. Materials and Methods

2.5.1. General Considerations

All reactions and manipulations were performed under an inert atmosphere of nitrogen or argon using standard Schlenk techniques. C_6D_6 was purchased from Cambridge

Isotope Laboratories, dried over Na/benzophenone, freeze-pump-thawed three times, and distilled under vacuum. Solvents were purchased from Fisher Scientific, dried by passing through a double-column J. C. Meyer solvent system and degassed before use. Acetonitrile was dried over CaH_2 and diethyl ether was dried over Na/benzophenone; both were distilled under vacuum before use. Other chemicals were purchased from standard suppliers. **SZO_{300}** was prepared as previously described. Solution NMR spectra were recorded on Bruker Avance 300 MHz and were referenced to C_6D_5H peak at 7.16 ppm. Solid-state NMR experiments were performed on a 600 MHz Bruker NEO. ^{1}H and ^{13}C CPMAS NMR spectra were recorded in 4 mm zirconia rotors at 10 KHz magic angle spinning. FT-IR spectra were recorded as pressed pellets using a Bruker Alpha IR spectrometer in an argon-filled glovebox.

*2.5.2. Grafting of PMe_3 onto **SZO_{300}***

In an argon filled glovebox, **SZO_{300}** (500mg, 0.065mmol OH) was loaded into a flask containing a Teflon valve and a ground glass joint for connection to a high vacuum line. A separate flask contained 1.2 equiv (6 mg, 0.078mmol) PMe_3. Each flask was evacuated and Et_2O (5mL) was transferred under vacuum. The flask containing **SZO_{300}** was cooled to 0°C and the PMe_3 solution was transferred by cannula onto **SZO_{300}**. The slurry was stirred for 1 hour at room temperature. After stirring, the solid was washed with Et_2O (3 x 5mL), which was transferred under vacuum and removed by a cannula filtration. The solid was then dried under high vacuum for 30 minutes.

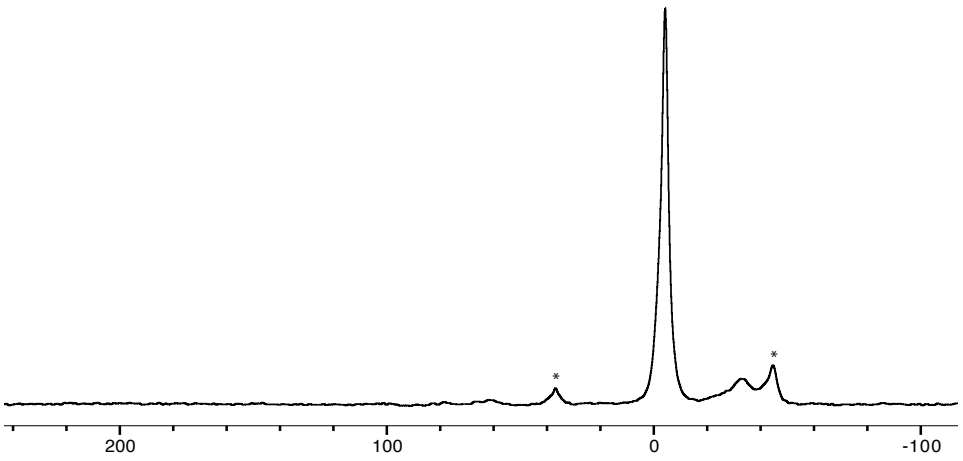

Figure 2.5.1. $^{31}P\{^{1}H\}$ MAS of $[Me_3PH]$**[SZO$_{300}$]**; the major signal is - 4 ppm from $[Me_3PH]$with the minor signal at -33ppm assigned to small amounts of PMe_3 bound to Lewis acid sites.

*2.5.3. Reaction of p-nitroaniline with **SZO$_{300}$***

In an argon filled glovebox, 1.00 g (0.13mmol OH) of **SZO$_{300}$** was loaded into a flask containing a Teflon valve and a ground glass joint for connection to a high vacuum line. A separate flask contained 21.5 mg (0.156 mmol, 1.2 equiv) of *p*-nitroaniline. Both flasks were evacuated and MeCN (5 mL) was transferred under vacuum at 77K. The flasks were warmed to room temperature and the *p*-nitroaniline solution was transferred by cannula onto the **SZO$_{300}$** slurry. After 4 hours at room temperature, the material was washed with MeCN (6 x 5mL) that was transferred under vacuum and removed by a cannula filtration. The white solid was dried for 30 minutes under high vacuum.

a) b)

Figure 2.5.2. Pictures of the reaction of p-nitroaniline with **SZO_{300}**; a) the first washing solution showing that p-nitroaniline is readily being washed off of the material b) the clear solution following six washings of material

2.5.4. Synthesis of P^{t}Bu$_2$Ar phosphines

1.0 equivalent of the bromoarene precursor was dissolved in Et_2O and cooled to -78°C, 1.2 equivalents of n-BuLi (1.6M in hexanes) was added dropwise and allowed to stir at -78°C for 10 minutes. After 30 minutes, the Et_2O was removed under vacuum and the solid was washed three times with pentane at 0°C. All Li salts were isolated and stored in an argon filled glovebox without further characterization with the exception of Li(*p*-FC_6H_4), Li(*p*-CNC_6H_4), and Li(*p*-$CF_3C_6H_4$); which were generated *in-situ*. ^{t}Bu$_2$PCl (0.83 equivalents) was dissolved in Et_2O and cooled to -78°C. The Li salt was dissolved in Et_2O and added dropwise to the tBu$_2$PCl solution. The solution was allowed to stir for 4 hours; during the reaction time a white solid precipitate out. Et_2O was again removed under reduced pressure and the solid was extracted with pentane. The pentane solution was then

filtered over a frit funnel containing celite under Ar. The clear solution was concentrated to dryness to yield pure compound. The phosphines were pure by NMR analysis and used without further purification.

1a) $P^tBu_2(p\text{-}OMeC_6H_4)$ – low melting point solid, 80% yield

1b) $P^tBu_2(p\text{-}^tBuC_6H_4)$ – clear liquid, 85%yield

1c) $P^tBu_2(p\text{-}MeC_6H_4)$ – clear liquid, 78% yield

1d) $P^tBu_2(p\text{-}TMSC_6H_4)$ – an clear viscous liquid, 90% yield

1e) P^tBu_2Ph – a clear viscous liquid, 85% yield

1f) $P^tBu_2(p\text{-}FC_6H_4)$ – an orange viscous liquid, 90% yield

1g) $P^tBu_2(p\text{-}CF_3C_6H_4)$ – a low melting point orange solid, 85% yield

1h) $P^tBu_2(p\text{-}CNC_6H_4)$ – a low melting point orange solid, 75% yield

Table 2. 5. 1.^{1}H solution NMR Data for $^{t}Bu_2PAr$

	Assignment	***δ* (ppm)**	
1a	^{t}Bu	1.22 (d), 9H	$^{3}J_{P\text{-}H}$ = 12 Hz
	MeO	3.28 (s), 3H	
	m-C_6H_2	6.76 (m), 2H	
	o-C_6H_2	7.68 (m), 2H	
1b	^{t}Bu	1.22 (d), 9H	$^{3}J_{P\text{-}H}$ = 12 Hz
	p-^{t}Bu	2.15 (s), 9H	
	m-C_6H_2	7.29 (m), 2H	
	o-C_6H_2	7.77 (m), 2H	
1c	^{t}Bu	1.22 (d), 9H	$^{3}J_{P\text{-}H}$ = 12 Hz
	Me	2.10 (s), 3H	
	m-C_6H_2	7.00 (m), 2H	
	o-C_6H_2	7.69 (m), 2H	
1d	^{t}Bu	1.21 (d), 9H	$^{3}J_{P\text{-}H}$ = 12 Hz
	TMS	0.20 (s), 9H	
	m-C_6H_2	7.45 (m), 2H	
	o-C_6H_2	7.80 (m), 2H	
1e	^{t}Bu	1.19 (d), 9H	$^{3}J_{P\text{-}H}$ = 12 Hz
	m-C_6H_2	7.14 (s), 2H	
	o-C_6H_2	7.74 (m), 2H	
1f	^{t}Bu	1.13 (d), 9H	$^{3}J_{P\text{-}H}$ = 12 Hz
	m-C_6H_2	6.89 (m), 2H	
	o-C_6H_2	7.63 (m), 2H	
1g	^{t}Bu	1.12 (d), 9H	$^{3}J_{P\text{-}H}$ = 12 Hz
	m-C_6H_2	6.90 (m), 2H	
	o-C_6H_2	7.62 (m), 2H	
1h	^{t}Bu	1.08 (d), 9H	$^{3}J_{P\text{-}H}$ = 12 Hz
	m-C_6H_2	7.30 (m), 2H	
	o-C_6H_2	7.59 (m), 2H	

Table 2. 5.2. ^{31}P solution NMR Data di-tert-butylarylphosphines in C_6D_6

	^{31}P NMR shift
1a	37.5
1b	37.3
1c	36.4
1d	38.7
1e	38.9
1f	36.9
1g	38.9
1h	38.4

2.5.5. Solution NMR

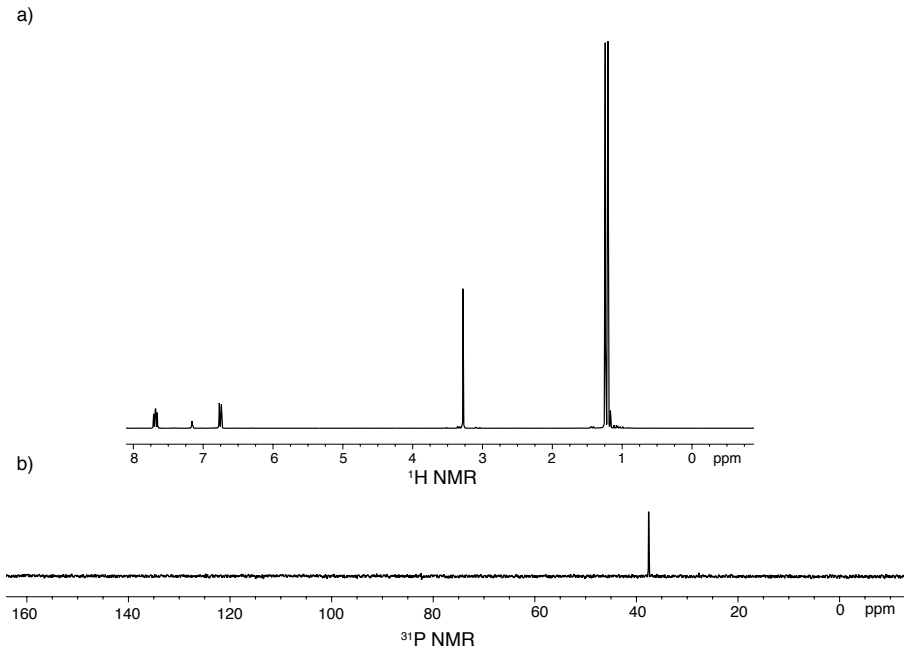

Figure 2. 5. 3. **a)**^{1}H NMR of **1a b)** ^{31}P NMR of **1a**

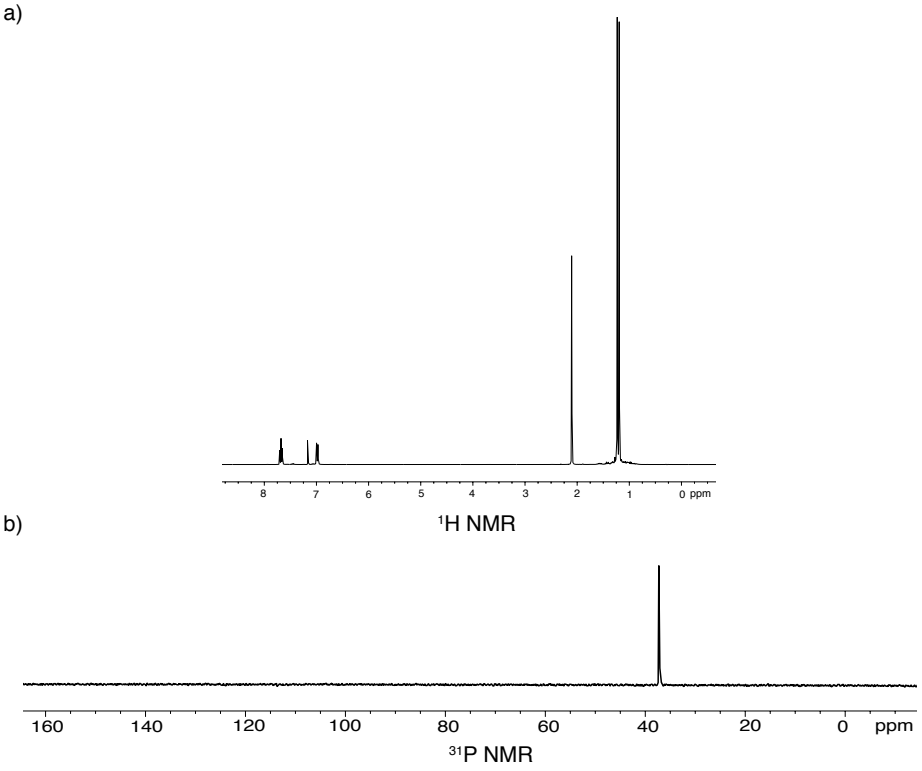

Figure 2. 5. 4. **a)**^{1}H NMR of **1b b)** ^{31}P NMR of **1b**

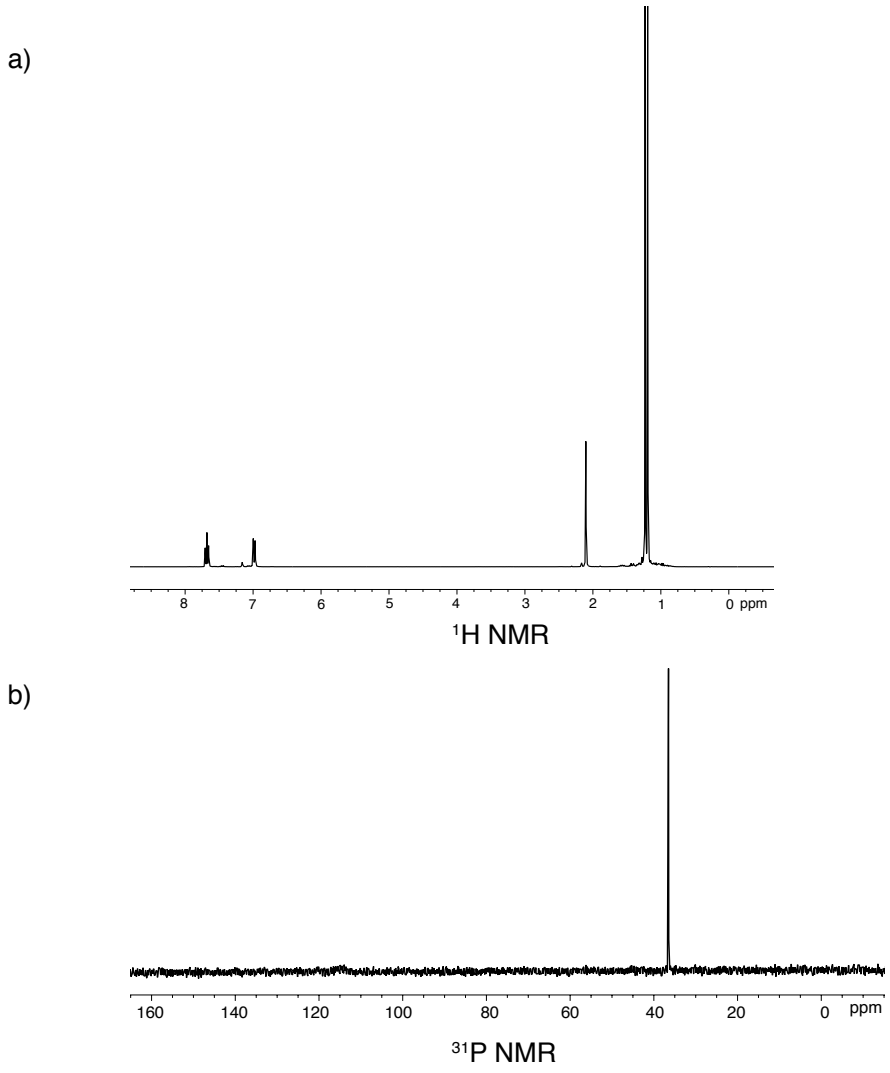

Figure 2. 5. 5. **a)** ^{1}H NMR of **1c b)** ^{31}P NMR of **1c**

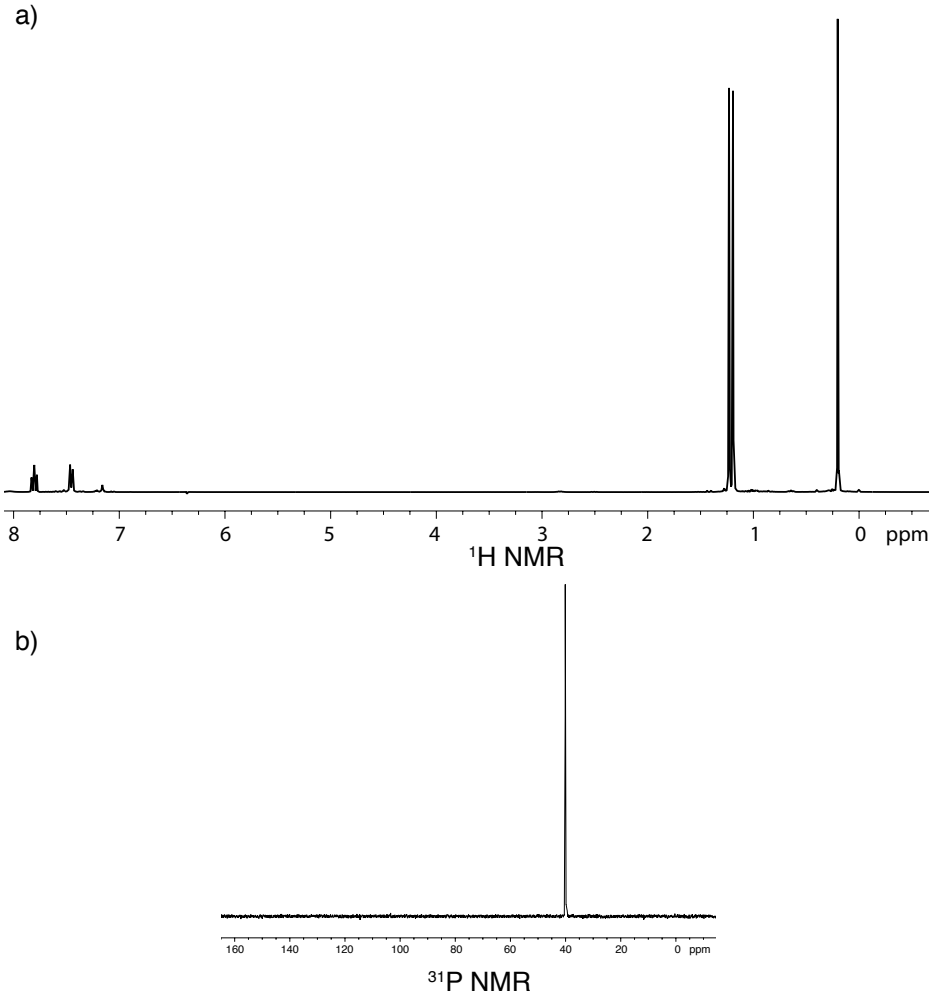

Figure 2. 5. 6. **a)** ^{1}H NMR of **1d b)** ^{31}P NMR of **1d**

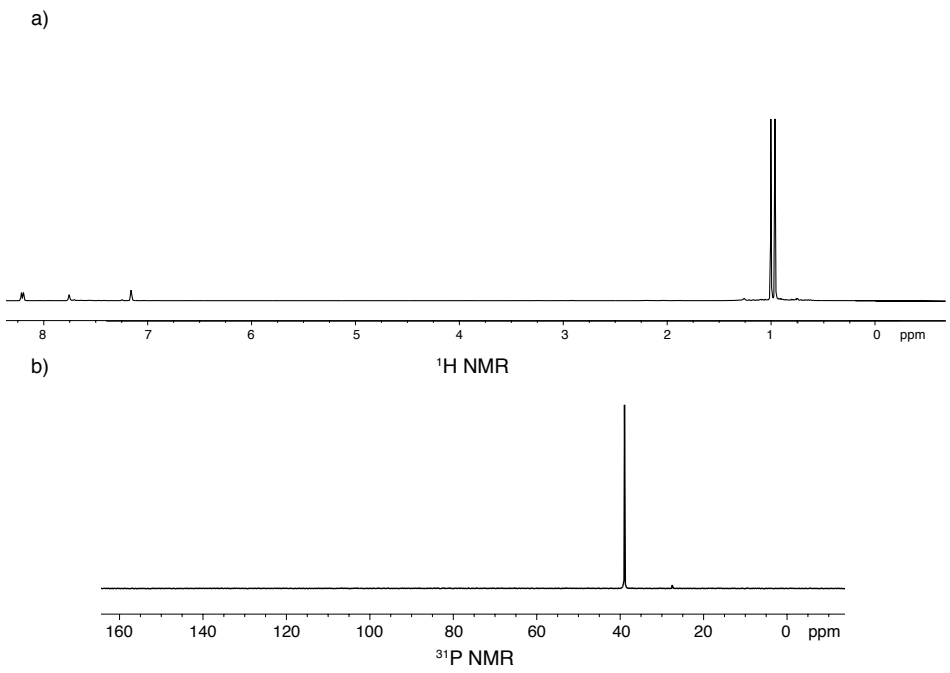

Figure 2. 5. 7. **a)** ^{1}H NMR of **1e b)** ^{31}P NMR of **1e**

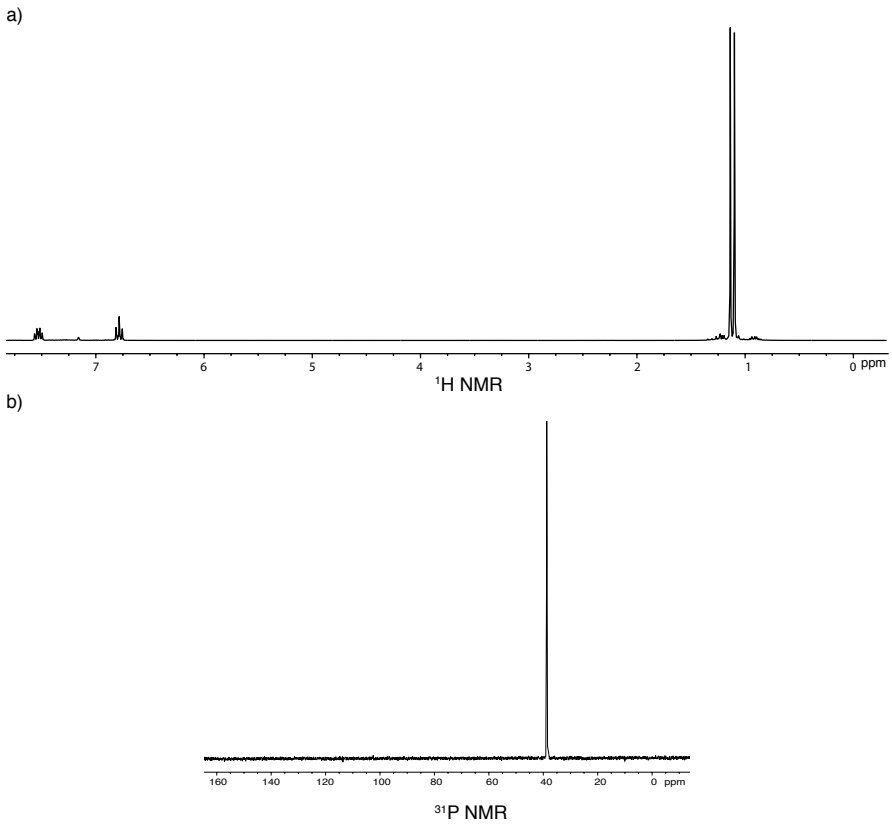

Figure 2. 5. 8. **a)** ^{1}H NMR of **1f b)** ^{31}P NMR of **1f**

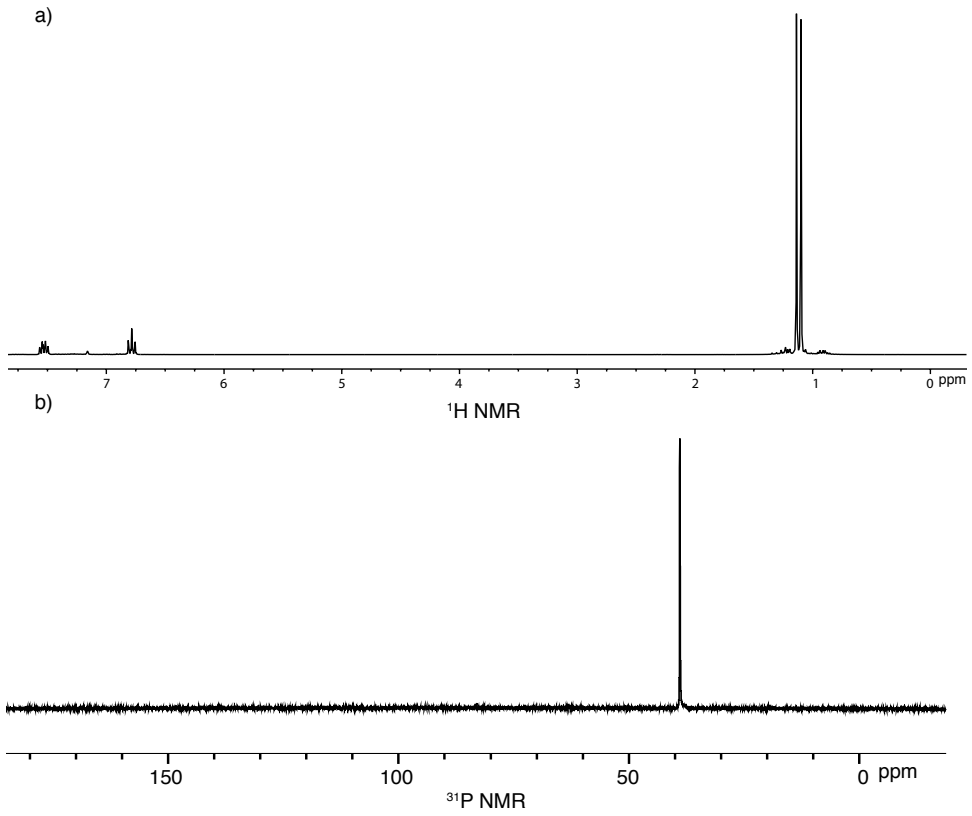

Figure 2. 5. 9. **a)** ^{1}H NMR of **1g b)** ^{31}P NMR of **1g**

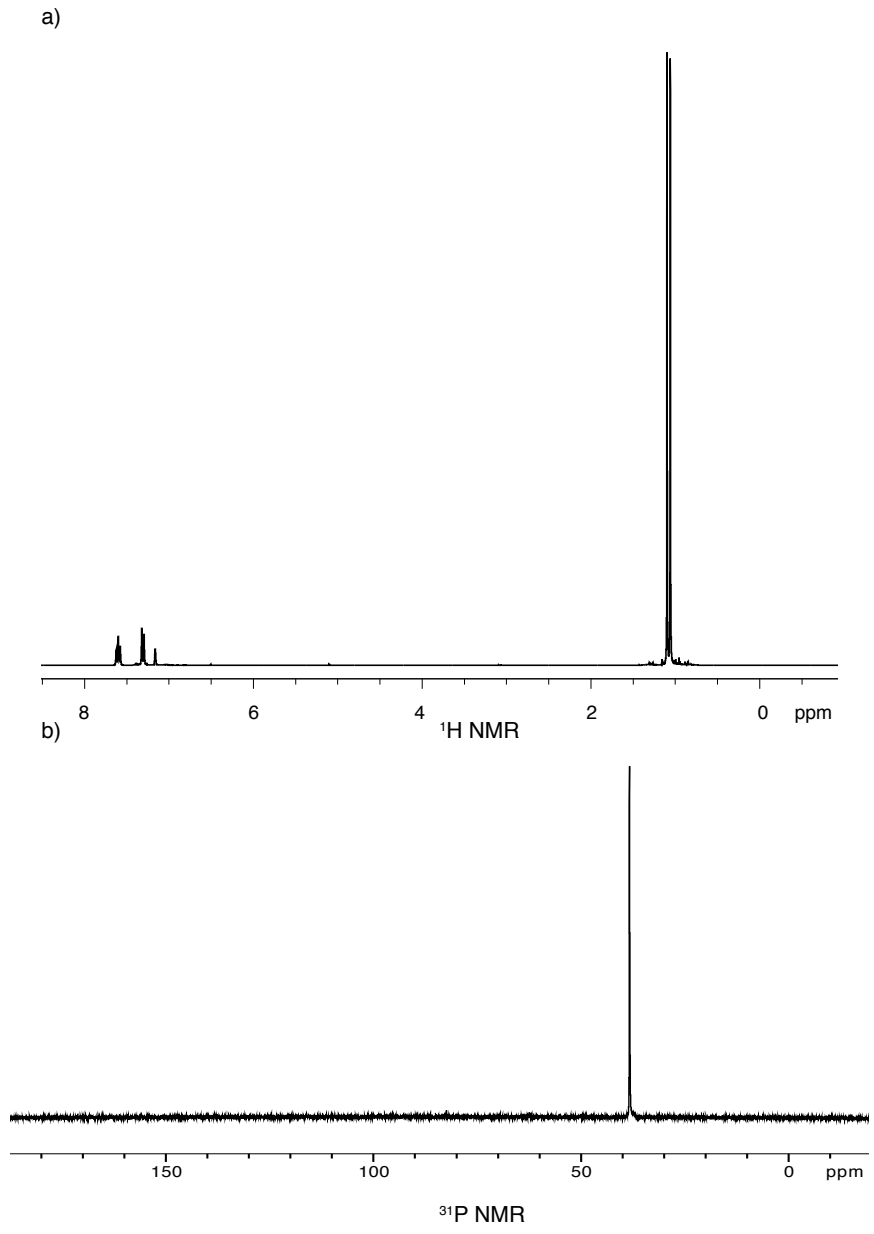

Figure 2. 5. 10. **a)** ^{1}H NMR of **1h b)** ^{31}P NMR of **1h**

2.5.6. Grafting procedure of $^tBu_2PAr$ onto ***SZO$_{300}$***

In an argon filled glovebox, **SZO$_{300}$** (500mg, 0.065mmol OH) was loaded into a flask containing a Teflon valve and a ground glass joint for connection to a high vacuum line. A separate flask contained 1.2 equiv phosphine. Each flask was evacuated and Et_2O (5mL) was transferred under vacuum. The flask containing **SZO$_{300}$** was cooled to 0°C and the phosphine solution was transferred by cannula onto **SZO$_{300}$**. The slurry was stirred for 1 hour at room temperature (4 hours for electron withdrawing phosphines). After stirring, the solid was washed with Et_2O (3 x 5mL), which was transferred under vacuum and removed by a cannula filtration. The solid was then dried under high vacuum for 30 minutes. Grafting reactions in MeCN were performed using a similar procedure.

Table 2.5.3. Summary of P-H stretches (cm^{-1}) in Et_2O; data given for MeCN graftings are in the main text

	Wavenumber (cm^{-1})
1a	2451
1b	2442
1c	2447
1d	2445
1e	2444
1f	2436
1g	2437
1h	2436

2a: Grafting in Et_2O: FTIR: 2451 cm^{-1} (ν_{P-H}); $^{31}P\{^1H\}$ MAS NMR: 46 ppm; $^{13}C\{^1H\}$ CPMAS NMR: 130 ppm (Ar), 29 ppm ($C(CH_3)_3$), 22 ppm ($C(CH_3)_3$) Grafting in MeCN:

FTIR: 2448 cm^{-1} (ν_{P-H}); $^{31}P\{^{1}H\}$ MAS NMR: 43 ppm; $^{13}C\{^{1}H\}$ CPMAS NMR: 121 ppm (Ar), 28 ppm ($C(CH_3)_3$), 21 ppm ($C(CH_3)_3$)

2b: Grafting in Et_2O: FTIR: 2442 cm^{-1} (ν_{P-H}); $^{31}P\{^{1}H\}$ MAS NMR: 47 ppm; $^{13}C\{^{1}H\}$ CPMAS NMR: 123 ppm (Ar), 29 ppm ($C(CH_3)_3$), 22 ppm ($C(CH_3)_3$) Grafting in MeCN: FTIR: 2445 cm^{-1} (ν_{P-H}); $^{31}P\{^{1}H\}$ MAS NMR: 46 ppm; $^{13}C\{^{1}H\}$ CPMAS NMR: 121 ppm (Ar), 30 ppm ($C(CH_3)_3$), 25 ppm ($C(CH_3)_3$)

2c: Grafting in Et_2O: FTIR: 2447 cm^{-1} (ν_{P-H}); $^{31}P\{^{1}H\}$ MAS NMR: 54 ppm; $^{13}C\{^{1}H\}$ CPMAS NMR: 130 ppm (Ar), 29 ppm ($C(CH_3)_3$), 21 ppm ($C(CH_3)_3$) Grafting in MeCN: FTIR: 2438 cm^{-1} (ν_{P-H}); $^{31}P\{^{1}H\}$ MAS NMR: 46 ppm; $^{13}C\{^{1}H\}$ CPMAS NMR: 122 ppm (Ar), 27 ppm ($C(CH_3)_3$), 20 ppm ($C(CH_3)_3$)

2d: Grafting in Et_2O: FTIR: 2445 cm^{-}(ν_{P-H}); $^{31}P\{^{1}H\}$ MAS NMR: 51 ppm; $^{13}C\{^{1}H\}$ CPMAS NMR: 133 ppm (Ar), 34 ppm ($C(CH_3)_3$), 26 ppm ($C(CH_3)_3$) Grafting in MeCN: FTIR: 2441 cm^{-1} (ν_{P-H}); $^{31}P\{^{1}H\}$ MAS NMR: 48 ppm; $^{13}C\{^{1}H\}$ CPMAS NMR: 127 ppm (Ar), 28 ppm ($C(CH_3)_3$), 21 ppm ($C(CH_3)_3$)

2e: Grafting in Et_2O: FTIR: 2444 cm^{-1} (ν_{P-H}); $^{31}P\{^{1}H\}$ MAS NMR: 49 ppm; $^{13}C\{^{1}H\}$ CPMAS NMR: 126 ppm (Ar), 29 ppm ($C(CH_3)_3$), 21 ppm ($C(CH_3)_3$) Grafting in MeCN: FTIR: 2439 cm^{-1} (ν_{P-H}); $^{31}P\{^{1}H\}$ MAS NMR: 49 ppm; $^{13}C\{^{1}H\}$ CPMAS NMR: 121 ppm (Ar), 30 ppm ($C(CH_3)_3$), 25 ppm ($C(CH_3)_3$)

2f: Grafting in Et_2O: FTIR: 2436 cm^{-1} (ν_{P-H}); $^{31}P\{^1H\}$ MAS NMR: 50 ppm; $^{13}C\{^1H\}$ CPMAS NMR: 113 ppm (Ar), 34 ppm ($C(CH_3)_3$), 26 ppm ($C(CH_3)_3$) Grafting in MeCN: FTIR: 2438 cm^{-1} (ν_{P-H}); $^{31}P\{^1H\}$ MAS NMR: 48 ppm; $^{13}C\{^1H\}$ CPMAS NMR: 107 ppm (Ar), 29 ppm ($C(CH_3)_3$), 21 ppm ($C(CH_3)_3$)

2g: Grafting in Et_2O: FTIR: 2437 cm^{-1} (ν_{P-H}); $^{31}P\{^1H\}$ MAS NMR: 51 ppm; $^{13}C\{^1H\}$ CPMAS NMR: 130 ppm (Ar), 29 ppm ($C(CH_3)_3$), 21 ppm ($C(CH_3)_3$) Grafting in MeCN: FTIR: 2433 cm^{-1} (ν_{P-H}); $^{31}P\{^1H\}$ MAS NMR: 49 ppm; $^{13}C\{^1H\}$ CPMAS NMR: 127 ppm (Ar), 28 ppm ($C(CH_3)_3$), 20 ppm ($C(CH_3)_3$)

2h: Grafting in Et_2O: FTIR: 2436 cm^{-1} (ν_{P-H}); $^{31}P\{^1H\}$ MAS NMR: 45 ppm; $^{13}C\{^1H\}$ CPMAS NMR: 126 ppm (Ar), 30 ppm ($C(CH_3)_3$), 20 ppm ($C(CH_3)_3$) Grafting in MeCN: FTIR: 2432 cm^{-1} (ν_{P-H}); $^{31}P\{^1H\}$ MAS NMR: 46 ppm; $^{13}C\{^1H\}$ CPMAS NMR: 128 ppm (Ar), 28 ppm ($C(CH_3)_3$), 18 ppm ($C(CH_3)_3$)

Table 2.5.4. Summary of $^{31}P\{_1H\}$ MAS NMR Chemical Shifts of [(^{t}Bu$_2$)ArPH][**SZO$_{300}$**] in Et_2O

[(^{t}Bu)$_2$ArPH][SZO$_{300}$]	**δ^{31}P (ppm)**
2a	46
2b	47
2c	54
2d	51
2e	49
2f	50
2g	51
2h	45

Table 2.5.5. Summary of $^{13}C\{^{1}H\}$ CP MAS NMR Chemical Shifts of [($^{t}Bu_2$)ArPH][**SZO$_{300}$**]

[(^{t}Bu)$_2$ArPH][SZO$_{300}$]	**Assignment**	**δ^{13}C (ppm) Et$_2$O**	**δ^{13}C (ppm) MeCN**
2a	Ar	130	121
	$C(CH_3)_3$	29	28
	$C(CH_3)_3$	22	21
2b	Ar	123	121
	$C(CH_3)_3$	29	30
	$C(CH_3)_3$	22	25
2c	Ar	130	122
	$C(CH_3)_3$	29	27
	$C(CH_3)_3$	21	20
2d	Ar	133	127
	$C(CH_3)_3$	34	28
	$C(CH_3)_3$	26	21
2e	Ar	126	121
	$C(CH_3)_3$	29	30
	$C(CH_3)_3$	21	25
2f	Ar	113	107
	$C(CH_3)_3$	34	29
	$C(CH_3)_3$	26	21
2g	Ar	130	127
		120	118
	$C(CH_3)_3$	29	28
	$C(CH_3)_3$	21	20
2h	Ar	126	128
	$C(CH_3)_3$	30	28
	$C(CH_3)_3$	20	18

*2.5.6.1. Characterization of [R_3PH][**SZO_{300}**]*

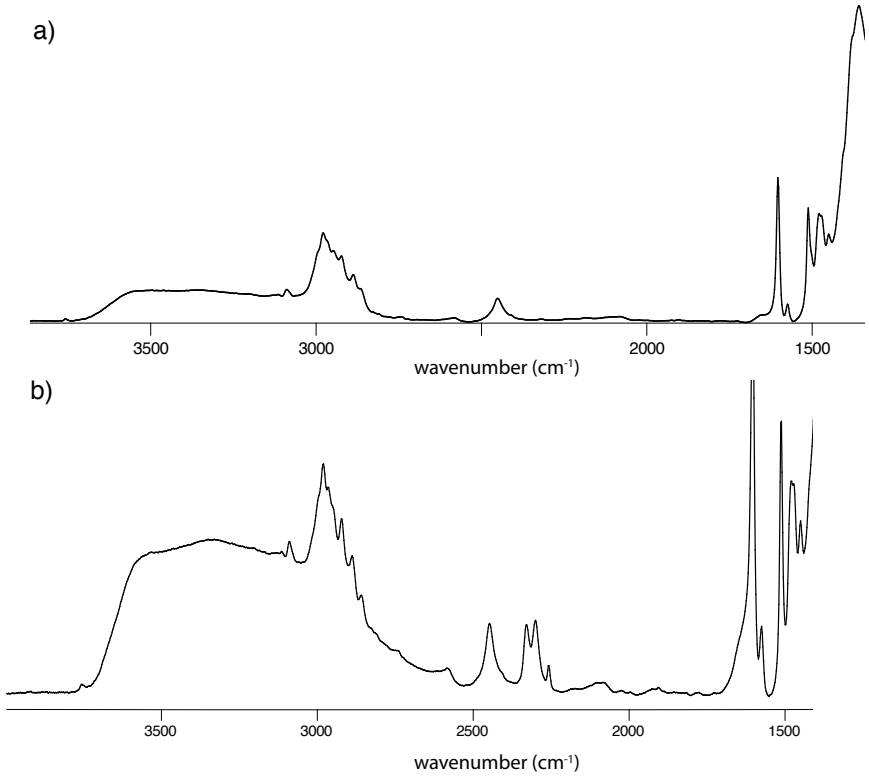

Figure 2. 5. 11. a) FT-IR spectra of **2a**; grafting was performed in Et_2O b) FT-IR spectra of **2a**; grafting performed in MeCN.

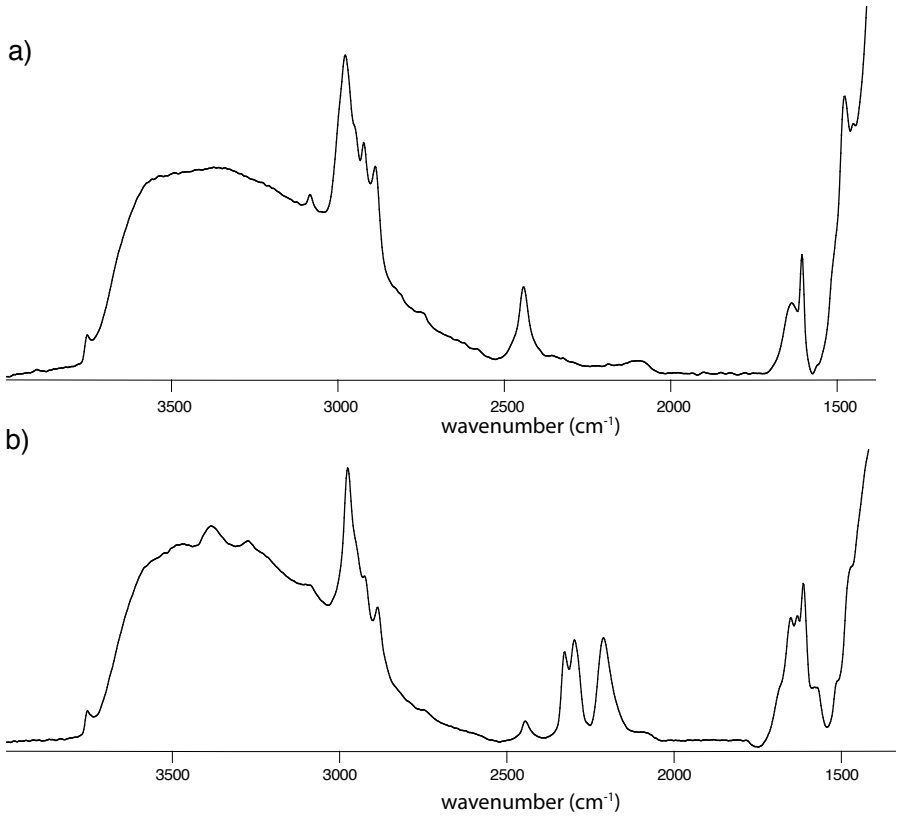

Figure 2. 5. 12. a) FT-IR spectra of **2b**; grafting performed in Et_2O b) FT-IR spectra of **2b**; grafting performed in MeCN.

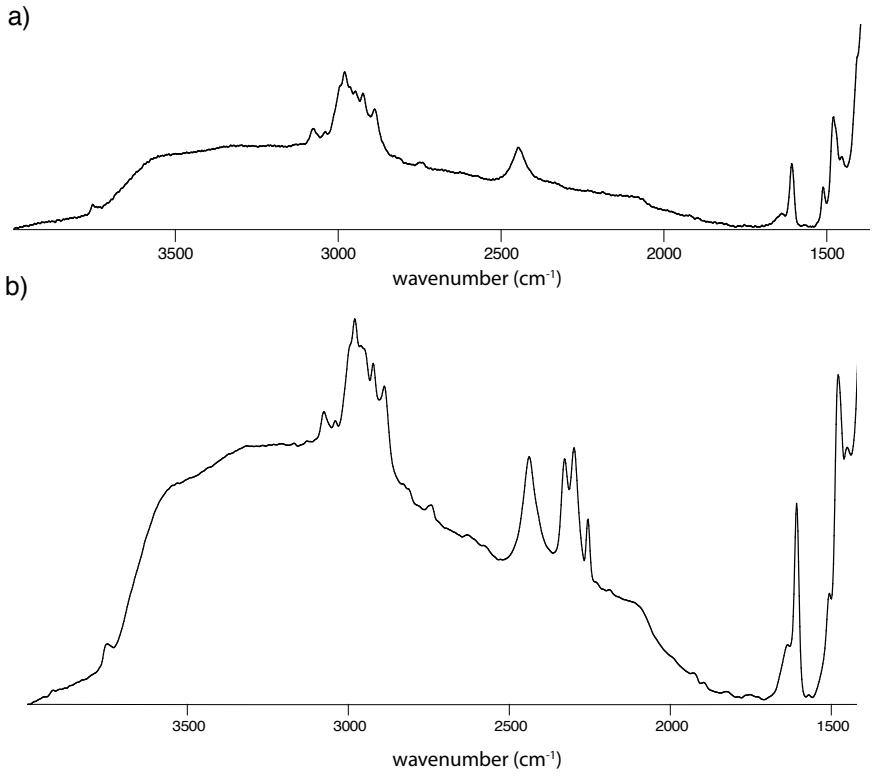

Figure 2. 5. 13. a) FT-IR spectra of **2c**; grafting performed in Et_2O b) FT-IR spectra of **2c**; grafting performed in MeCN.

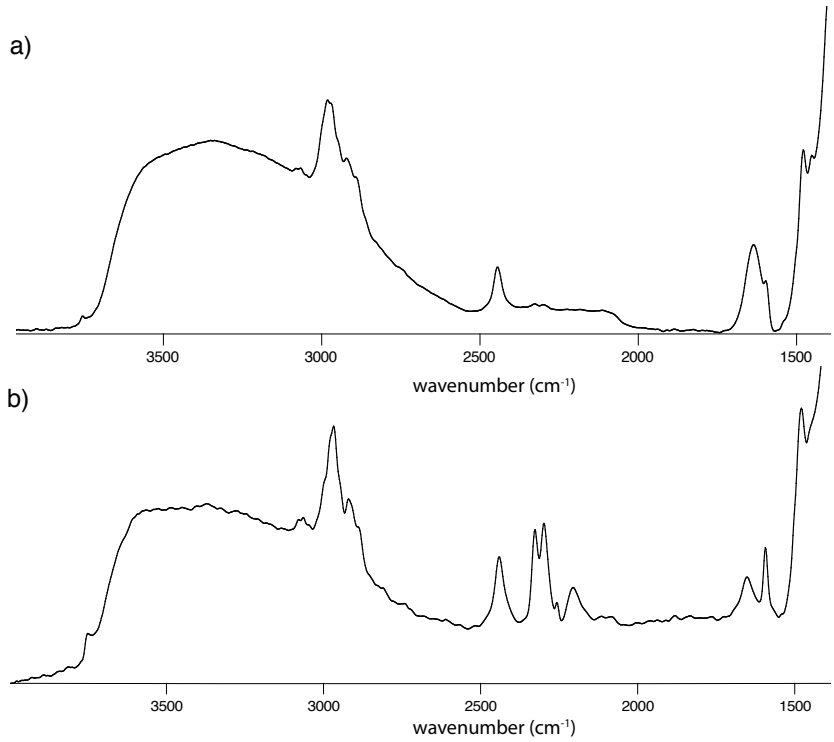

Figure 2. 5. 14. a) FT-IR spectra of **2d**; grafting performed in Et_2O b) FT-IR spectra of **2d**; grafting performed in MeCN

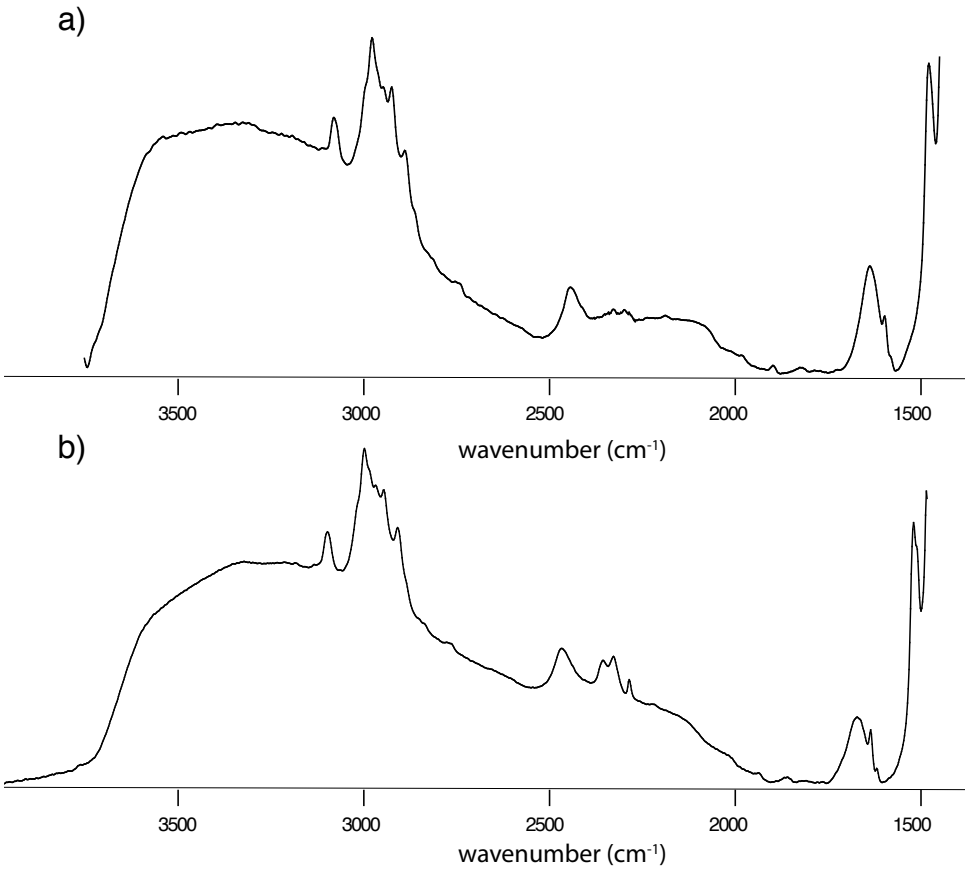

Figure 2. 5. 15. a) FT-IR spectra of **2e**; grafting performed in Et_2O b) FT-IR spectra of **2e**; grafting performed in MeCN

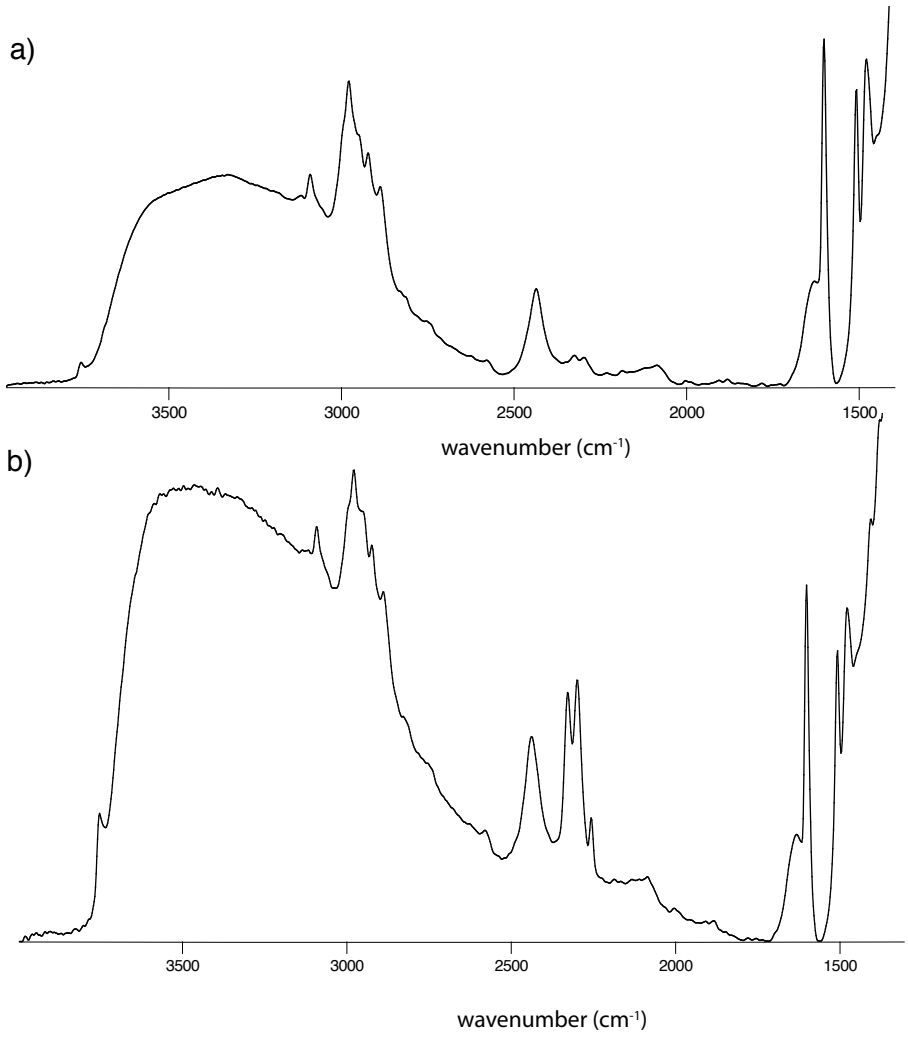

Figure 2. 5. 16. a) FT-IR spectra of **2f**; grafting performed in Et_2O b) FT-IR spectra of **2f**; grafting performed in MeCN.

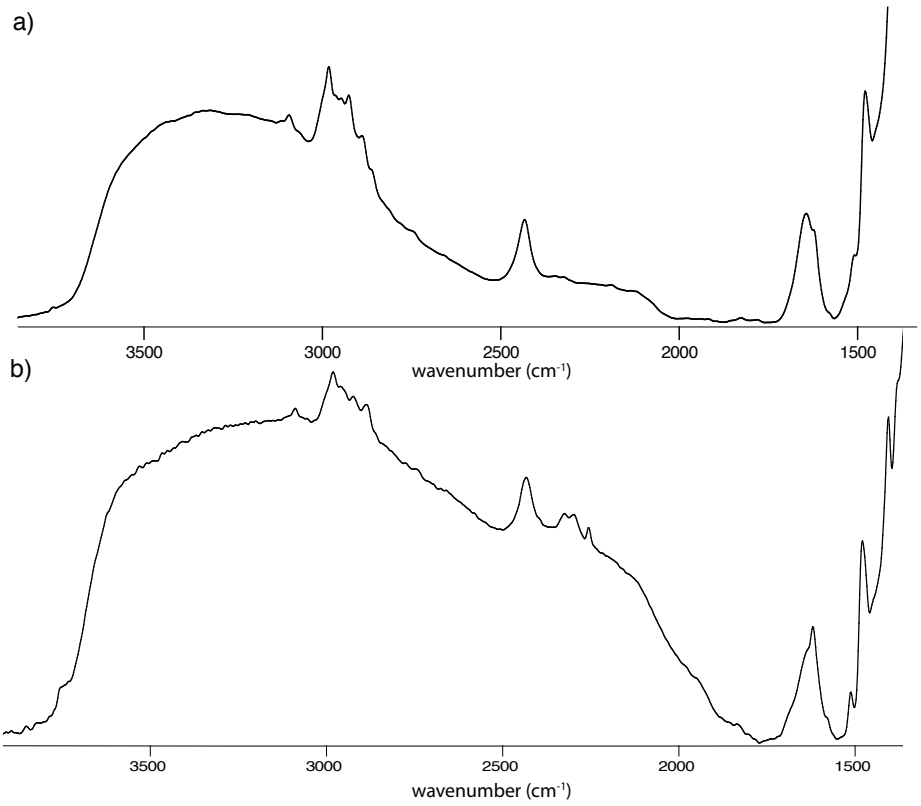

Figure 2. 5. 17. a) FT-IR spectra of **2g**; grafting performed in Et_2O b) FT-IR spectra of **2g**; grafting performed in MeCN.

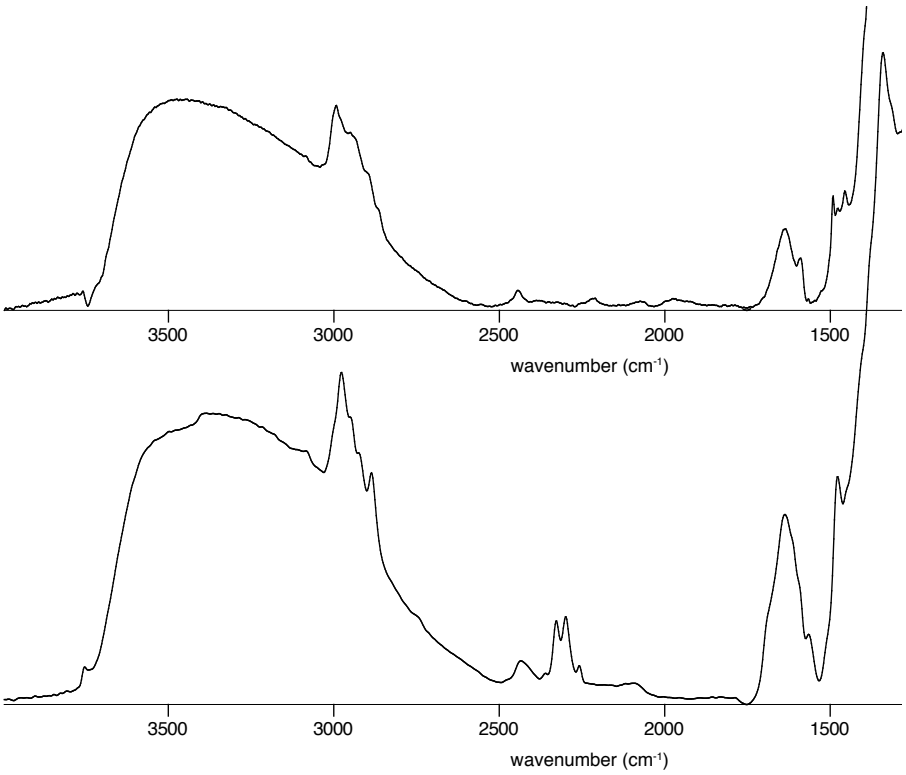

Figure 2. 5. 18. a) FT-IR spectra of **2h**; grafting performed in Et_2O b) FT-IR spectra of **2h**; reaction grafting in MeCN

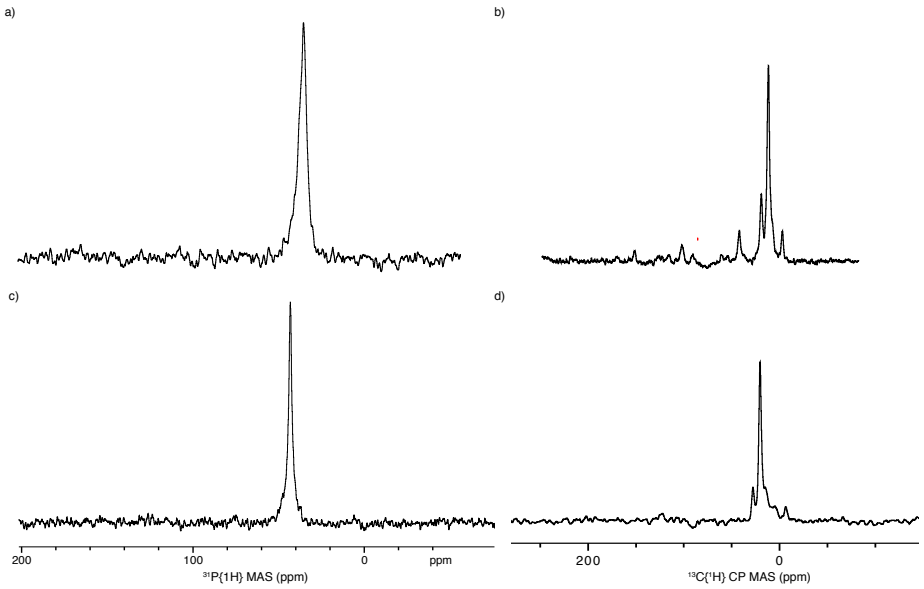

Figure 2. 5. 19. **a)** $^{31}P\{^{1}H\}$ MAS of **2a**; grafting performed in MeCN; 10 kHz; ns = 2k; d1 = 1s **b)** $^{13}C\{^{1}H\}$ CPMAS of **2a**; grafting performed in MeCN; 10 kHz; ns = 40k; d1 = 2s. **c)** $^{31}P\{^{1}H\}$ MAS of **2a**; grafting performed in Et_2O; 10 kHz; ns = 2k; d1 = 1s **d)** $^{13}C\{^{1}H\}$ CPMAS of **2a**; grafting performed in Et_2O; 10 kHz; ns = 40k; d1 = 2s.

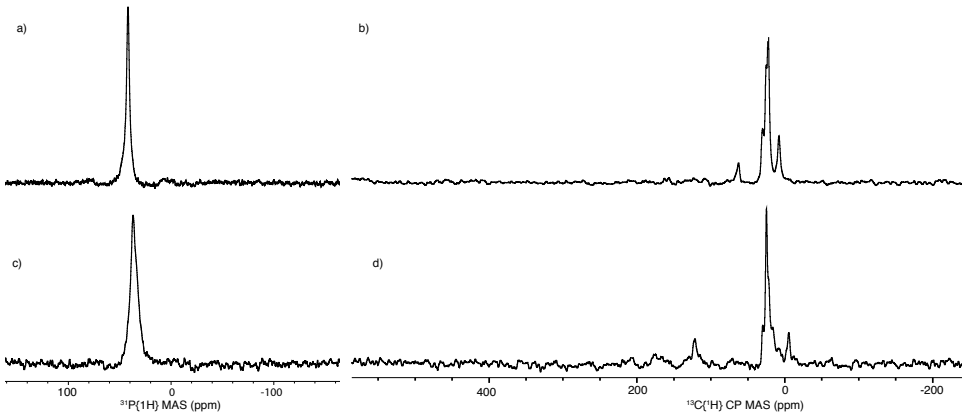

Figure 2. 5. 20. **a)** $^{31}P\{^{1}H\}$ MAS of **2b**; grafting performed in MeCN; 10 kHz; ns = 2k; d1 = 1s **b)** $^{13}C\{^{1}H\}$ CPMAS of **2b**; grafting performed in MeCN; 10 kHz; ns = 40k; d1 = 2s. **c)** $^{31}P\{^{1}H\}$ MAS of **2b**; grafting performed in Et_2O; 10 kHz; ns = 2k; d1 = 1s **d)** $^{13}C\{^{1}H\}$ CPMAS of **2b**; grafting performed in Et_2O; 10 kHz; ns = 40k; d1 = 2s.

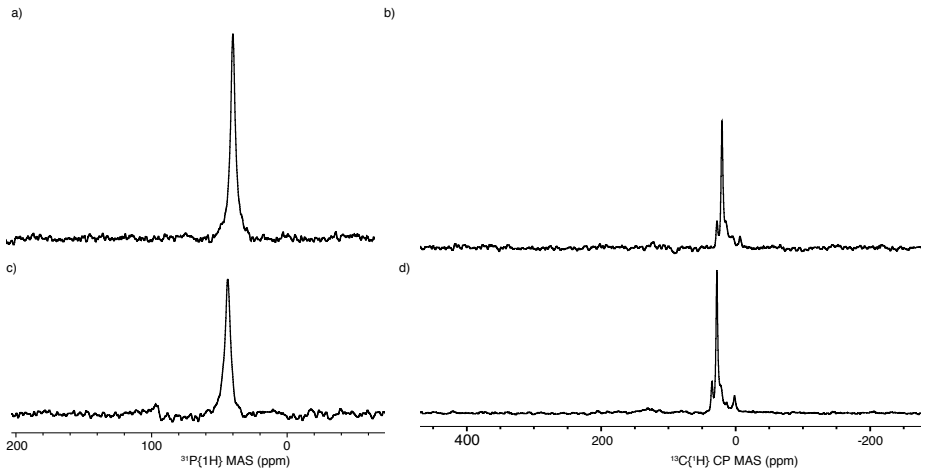

Figure 2. 5. 21. **a)** $^{31}P\{^{1}H\}$ MAS **2c**; grafting performed in MeCN; 10 kHz; ns = 2k; d1 = 1s **b)** $^{13}C\{^{1}H\}$ CPMAS of **2c**; grafting performed in MeCN; 10 kHz; ns = 40k; d1 = 2s. **c)** $^{31}P\{^{1}H\}$ MAS of **2c**; grafting performed in Et_2O; 10 kHz; ns = 2k; d1 = 1s **d)** $^{13}C\{^{1}H\}$ CPMAS of **2c**; grafting performed in Et_2O; 10 kHz; ns = 40k; d1 = 2s.

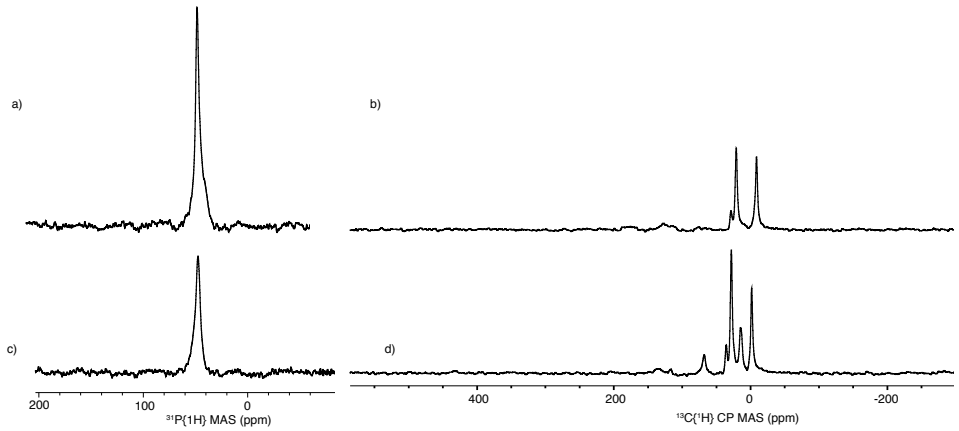

Figure 2. 5. 22. **a)** $^{31}P\{^{1}H\}$ MAS of **2d**; grafting performed in MeCN; 10 kHz; ns = 2k; d1 = 1s **b)** $^{13}C\{^{1}H\}$ CPMAS of **2d**; grafting performed in MeCN; 10 kHz; ns = 40k; d1 = 2s **c)** $^{31}P\{^{1}H\}$ MAS of **2d**; grafting performed in Et_2O; 10 kHz; ns = 2k; d1 = 1s **d)** $^{13}C\{^{1}H\}$ CPMAS of **2d**; grafting performed in Et_2O; 10 kHz; ns = 40k; d1 = 2s.

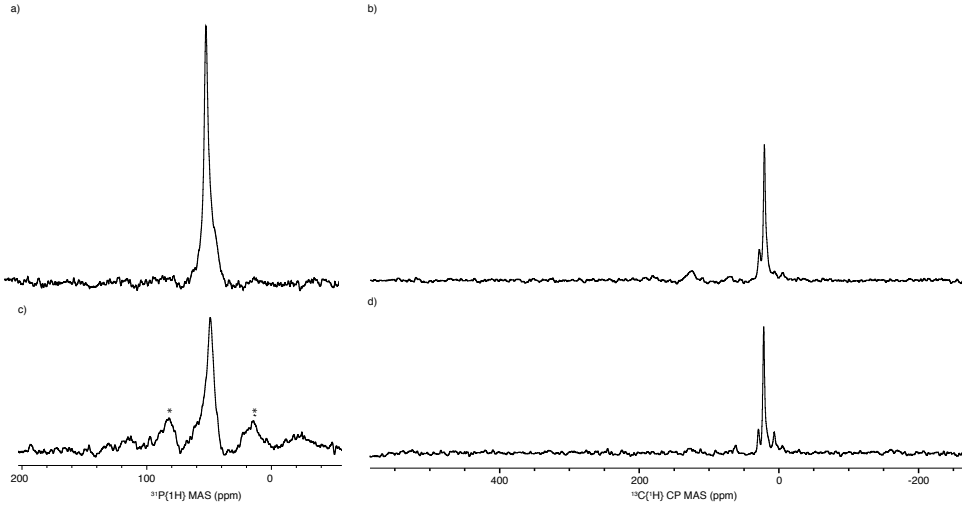

Figure 2. 5. 23. **a)** $^{31}P\{^{1}H\}$ MAS of **2e**; grafting performed in MeCN; 10 kHz; ns = 2k; d1 = 1s **b)** $^{13}C\{^{1}H\}$ CPMAS of **2e**; grafting performed in MeCN; 10 kHz; ns = 30k; d1 = 2s

c) $^{31}P\{^{1}H\}$ MAS of **2e**; grafting performed in Et_2O; 10 kHz; ns = 2k; d1 = 1s **d)** $^{13}C\{^{1}H\}$ CPMAS of **2e**; grafting performed in Et_2O; 10 kHz; ns = 30k; d1 = 2s.

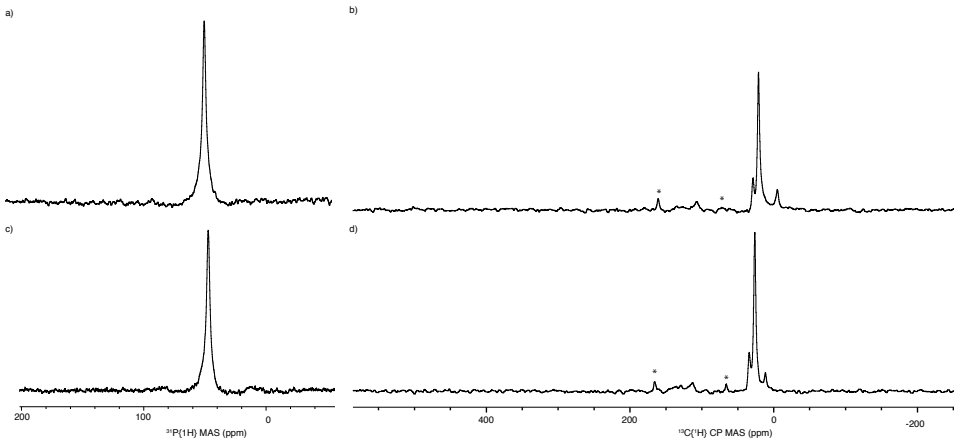

Figure 2. 5. 24. **a)** $^{31}P\{^{1}H\}$ MAS of **2f**; grafting performed in MeCN; 10 kHz; ns = 2k; d1 = 1s **b)** $^{13}C\{^{1}H\}$ CPMAS of **2f**; grafting performed in MeCN; 10 kHz; ns = 10k; d1 = 2 **c)** $^{31}P\{^{1}H\}$ MAS of **2f**; grafting performed in Et_2O; 10 kHz; ns = 2k; d1 = 1s **d)** $^{13}C\{^{1}H\}$ CPMAS of **2f**; grafting performed in Et_2O; 10 kHz; ns = 10k; d1 = 2s.

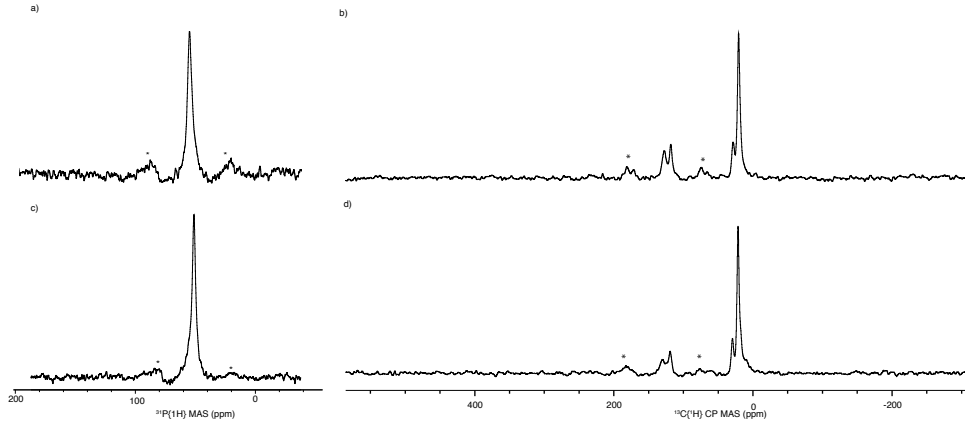

Figure 2. 5. 25. **a)** $^{31}P\{^{1}H\}$ MAS of **2g**; grafting performed in MeCN; 10 kHz; ns = 2k; d1 = 1s **b)** $^{13}C\{^{1}H\}$ CPMAS of **2g**; grafting performed in MeCN; 10 kHz; ns = 10k, d1=2s **c)** $^{31}P\{^{1}H\}$ MAS of **2g**; grafting performed in Et_2O; 10 kHz; ns = 2k; d1 = 1s **d)** $^{13}C\{^{1}H\}$ CPMAS of **2g**; grafting performed in Et_2O; 10 kHz; ns = 10k, d1=2s.

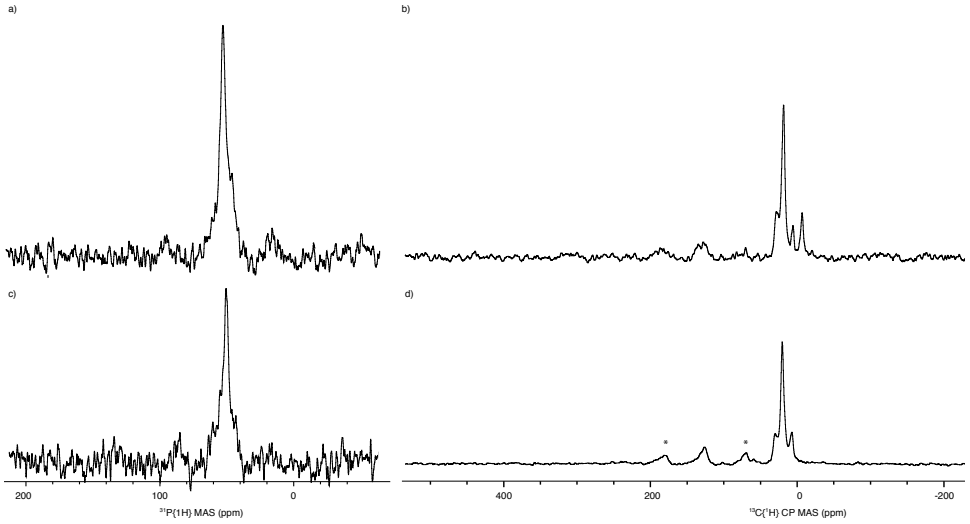

Figure 2. 5. 26. **a)** $^{31}P\{^{1}H\}$ MAS of **2h**; grafting performed in MeCN; 10 kHz; ns = 2k; d1 = 1s b) $^{13}C\{^{1}H\}$ CPMAS **2h**; grafting performed in MeCN; 10 kHz; ns = 10k; d1 = 2s c) $^{31}P\{^{1}H\}$ MAS of **2h**; grafting performed in Et_2O; 10 kHz; ns = 2k; d1 = 1s d) $^{13}C\{^{1}H\}$ CPMAS **2h**; grafting performed in Et_2O; 10 kHz; ns = 10k; d1 = 2s.

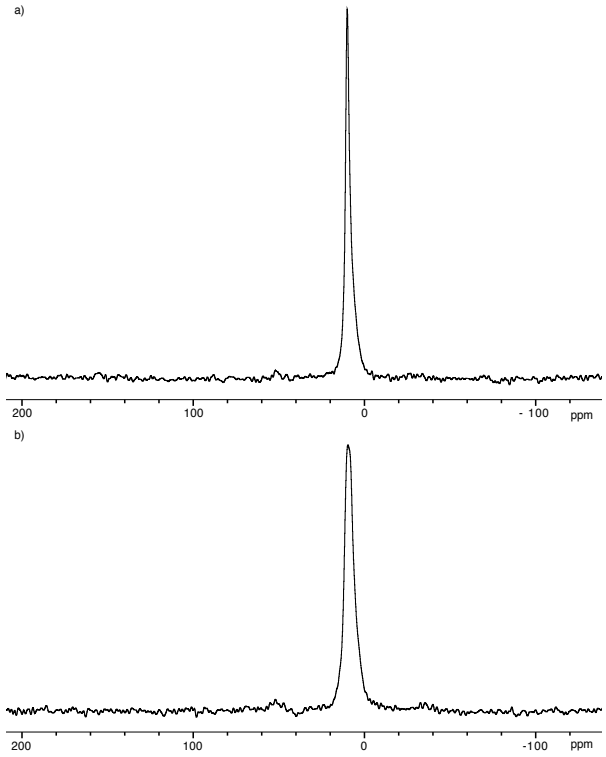

Figure 2. 5. 27. **a)** $^{31}P\{^{1}H\}$ MAS of $[HPPh_3]$**[SZO$_{300}$]**; grafting performed in MeCN; 8 kHz; ns = 2k; d1 = 1s. **b)** $^{31}P\{^{1}H\}$ MAS of $[HPPh_3]$**[SZO$_{300}$]**; grafting performed in Et_2O; 8 kHz; ns = 2k; d1 = 1s.

2.5.7. Binding Studies of [R$_3$PH][SZO$_{300}$]

Calibration curves for each phosphine were prepared to determine each molar extinction coefficients using a Cary 60 UV-Vis spectrophotometer. Molar extinction coefficients were calculated using Beer's Law:

Equation 2. 5. 1.

$$A = \varepsilon l c$$

where A is the absorbance (a.u.), l is the path length (cm), and c is the concentration of the solution (M). Emission wavelengths and molar extinction coefficients are reported below in Table 2.5.8.

Table 2. 5. 6. Molar extinction coefficients and emission wavelength for the series of phosphines

	Wavelength (nm)	**Molar extinction coefficient ($Lmol^{-1}cm^{-1}$)**
1a	272	1300
1b	250	1500
1c	250	1500
1d	250	5100
1e	250	2700
1f	250	4300
1g	250	9100
1h	250	1400

For each experiment, a vial was loaded with **SZO_{300}**. The amount of **SZO_{300}** ranged from 5mg (0.00065 mmol OH) to 250 mg (0.0325 mmol OH). The vials containing 5 to 50 mg of **SZO_{300}** were weighed out in 5 mg increments. Stock solution of each phosphine in MeCN were made and used immediately after preparation. To each vial, X mL of solution of $^{t}Bu_2PAr$ (1a = 0.30mM, 1b = 0.32 mM, 1c = 0.35 mM, 1d = 0.30 mM, 1e = 0.35 mM, 1f = 0.025 mM, 1g = 0.25 mM, 1h = 0.40 mM) was syringed onto the solid. After the addition of the phosphine, the vials were allowed to equilibrate for 36 – 48 hours. The solution was decanted, and the $^{t}Bu_2PAr$ was quantified by UV-Vis spectroscopy. The concentration of $^{t}Bu_2PAr$ adsorbed was quantified by the difference in concentration from the initial concentration of $[P]_0$ and the final concentration $[P]_f$ then multiplied by the volume of solvent as shown in equation 2.5.2.

Equation 2. 5. 2

$$\text{mmol } PR_3 = ([^tBu_2PAr]_0 - [^tBu_2PAr]_f) \times X \text{ mL}$$

The amount of $^tBu_2PAr$ adsorbed at equilibrium, q_e, was calculated using equation 2.5.3.

Equation 2. 5. 3.

$$q_e = \frac{\text{mmol absorbed phosphine}}{\text{g SZO}}$$

The isotherms were constructed by plotting free phosphine (M) versus q_e then each plot was fit to a single-site Langmuir isotherm using Origin Pro 8, equation 2.5.4.

Equation 2. 5. 4.

$$\frac{K_a[\mathbf{1}][HO_x]_0}{1 + K_a[\mathbf{1}]}$$

The error reported for each binding constant was calculated by origin whereas the error bars in the plots were calculated using the standard deviation for each of the points in the triplicate run.

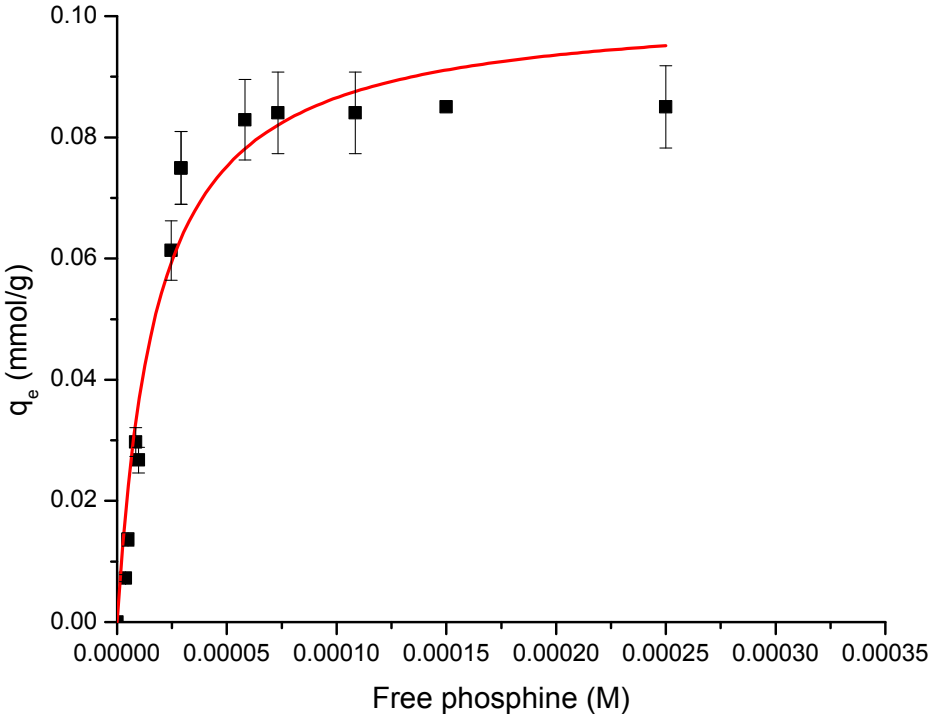

Figure 2. 5. 28. Langmuir isotherm of **1b** where K_a is calculated to be 55,00. The study was performed using a phosphine stock solution of 0.32mM.

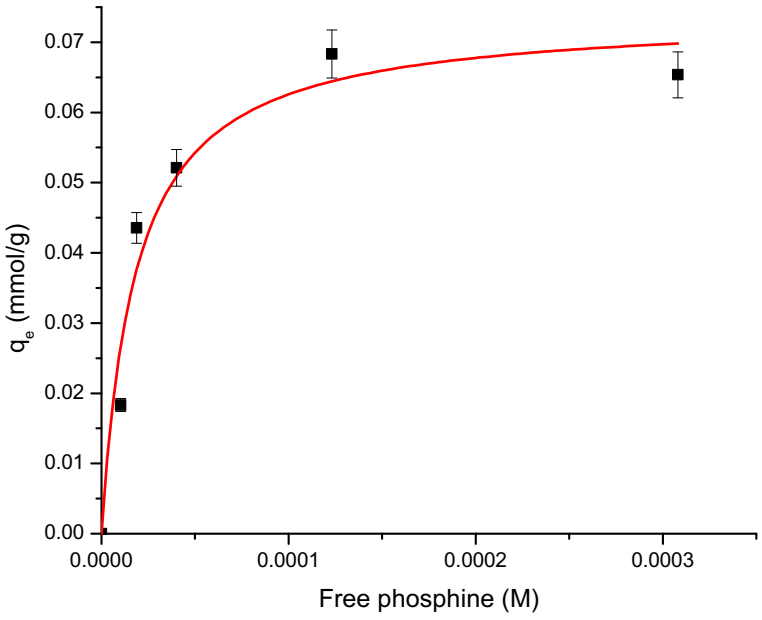

Figure 2. 5. 29. Langmuir isotherm of **1c** where K_a is calculated to be 53,000. The study was performed using a phosphine stock solution of 0.35mM.

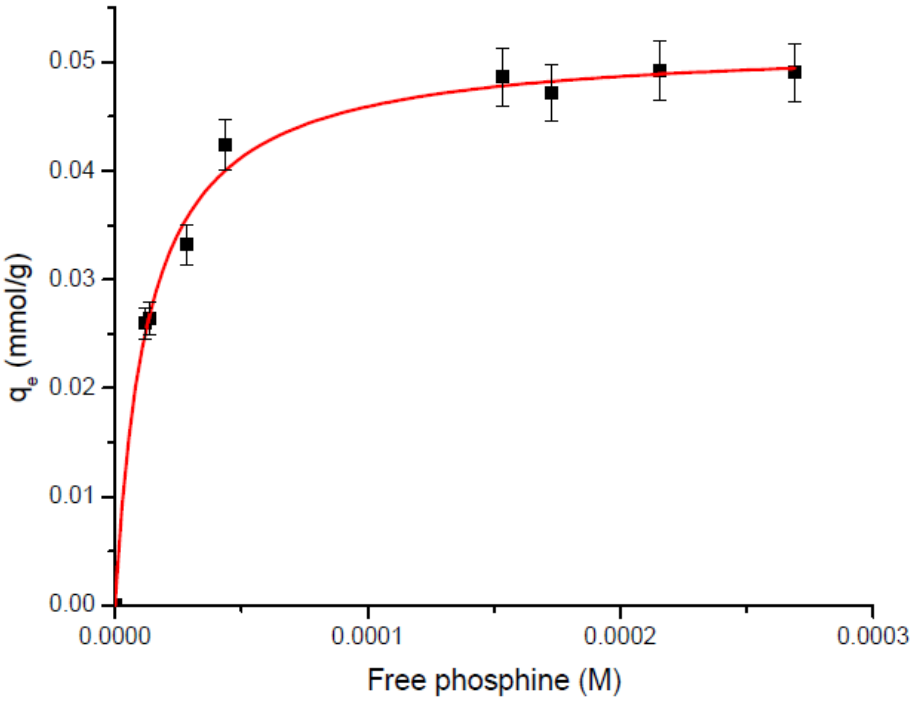

Figure 2. 5. 30. Langmuir isotherm of **1d** where K_a is calculated to be 47,000. The study was performed using a phosphine stock solution of 0.3mM.

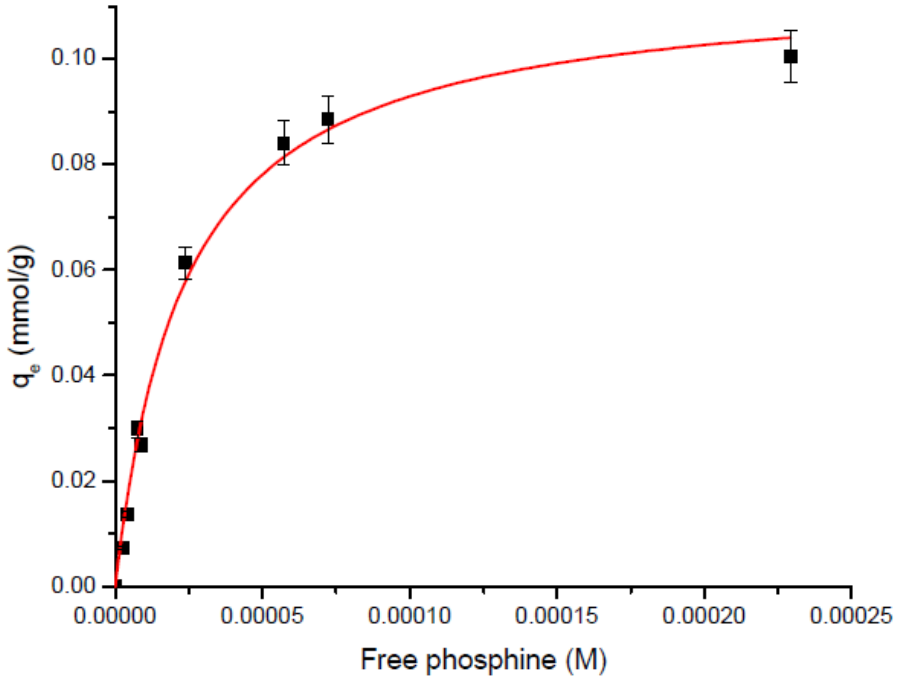

Figure 2. 5. 31. Langmuir isotherm of **1e** where K_a is calculated to be 43,000. The study was performed using a phosphine stock solution of 0.3mM.

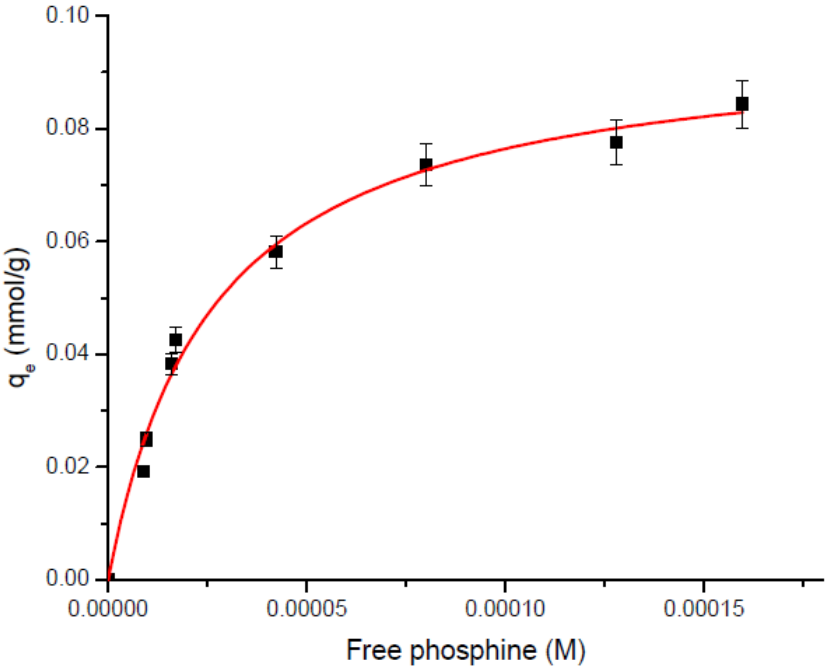

Figure 2. 5. 32. Langmuir isotherm of **1f** where K_a is calculated to be 30,000. The study was performed using a phosphine stock solution of 0.25mM.

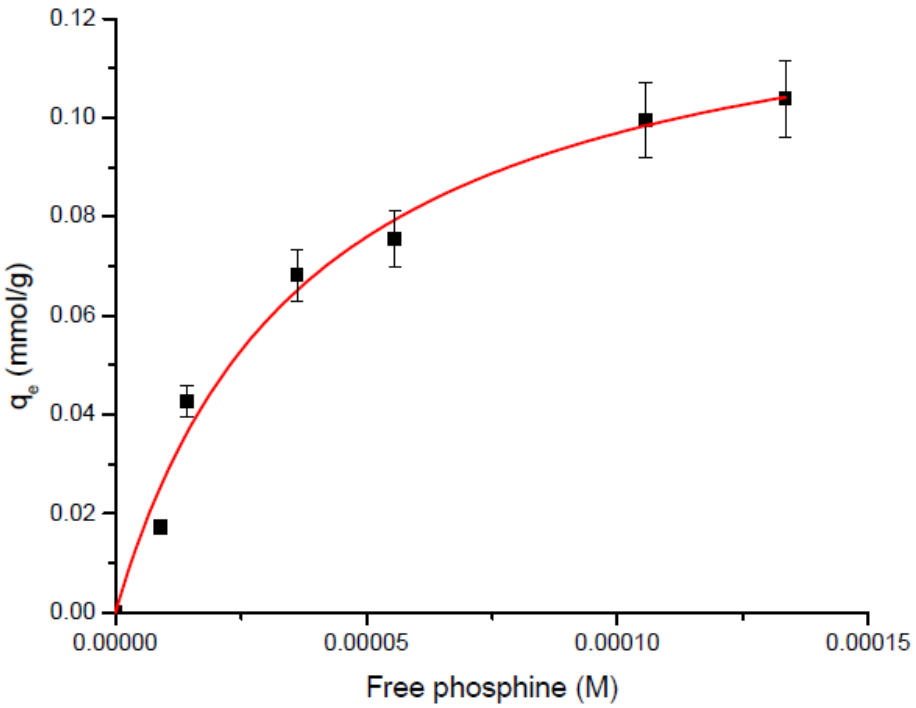

Figure 2. 5. 33. Langmuir isotherm of **1g** where K_a is calculated to be 26,000. The study was performed using a phosphine stock solution of 0.25mM.

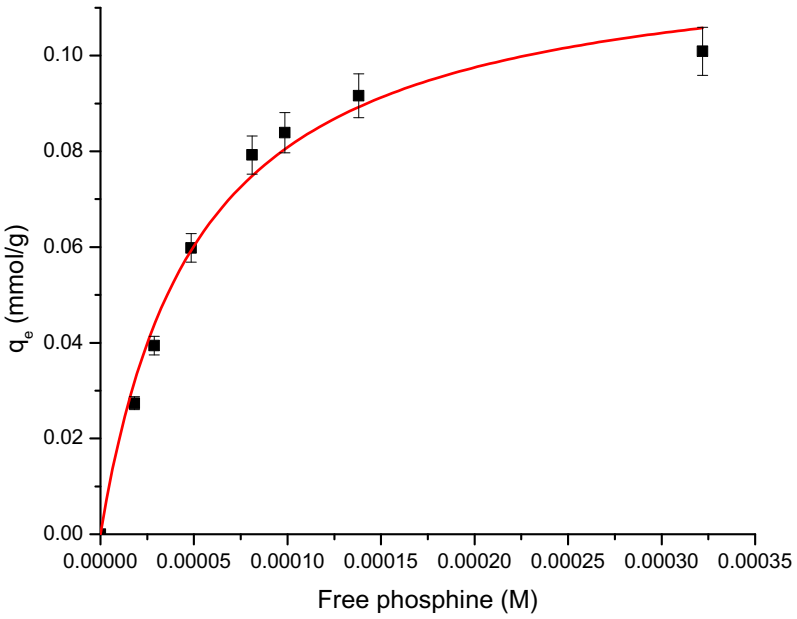

Figure 2. 5. 34. Langmuir isotherm of **1h** where K_a is calculated to be 19,000. The study was performed using a phosphine stock solution of 0.40mM.

2.5.8. Binding studies of phosphines onto ***SZO$_{300}$*** *($^{31}P\{^1H\}$ MAS Method)*

In a nitrogen filled glovebox, a 4mm rotor was loosely pack with 75mg (0.00975mmol OH) **SZO$_{300}$.** To this rotor, 31.0 µL of 0.32M PPh_3 in MeCN was added and allowed to equilibrate for 30 minutes. The sample was analyzed via $^{31}P\{^1H\}$ MAS NMR. After analysis, an additional 5.0 µL of 0.32M PPh_3 in MeCN was syringed into the original rotor in a nitrogen filled glovebox. The rotor was again allowed to equilibrate for 30 minutes and then analyzed via $^{31}P\{^1H\}$ MAS NMR. The PPh_3 in MeCN solution was systematically syringed into the rotor until the surface was completely saturated.

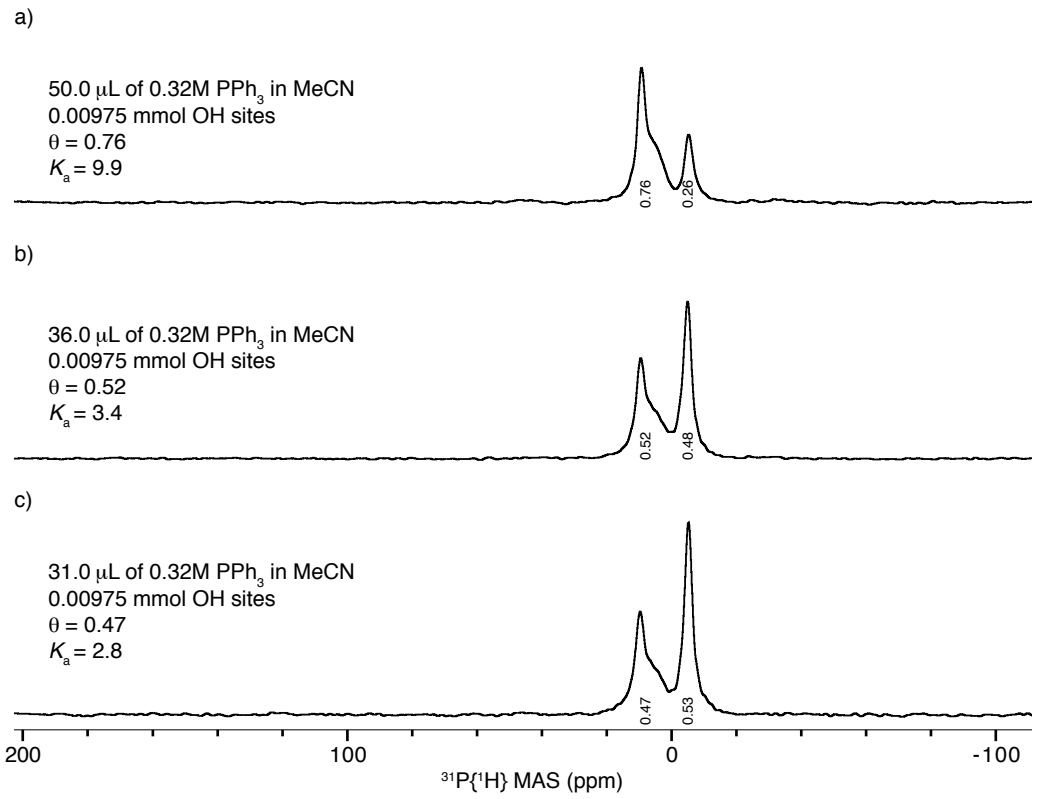

Figure 2. 5. 35.$^{31}P\{^{1}H\}$ MAS NMR of $[Ph_3PH]$**[SZO$_{300}$]** binding study; ns = 2k; d1 = 1s. The integral values for both $[Ph_3PH]$**[SZO$_{300}$]** and free Ph_3P is stated below the signal.

To determine the amount of $[Ph_3PH]$**[SZO$_{300}$]**, the ratio of $[Ph_3PH]$**[SZO$_{300}$]** to Ph_3P was determined by integrating the signal of $[Ph_3PH]$**[SZO$_{300}$]**, I_{Ph_3PH}. The I_{Ph_3PH} numerical value is equal to θ, the fractional amount of occupied sites, which can be calculated using equation 2.5.5

Equation 2. 5. 5.

$$\theta = \frac{\text{mmol of sites occupied}}{\text{mmol of OH sites present}}$$

θ can be derived by the Langmuir isotherm using K_a and C_{PR_3}, concentration of PPh_3, shown in equation 2.5.6.

Equation 2. 5. 6.

$$\theta = \frac{K_a C_{PR_3}}{\left(1 + K_a C_{PPh_3}\right)}$$

Through algebraic rearrangement of equation 2.5.5, K_a can be determined by equation 2.5.7.

Equation 2. 5. 7.

$$K_a = \frac{\theta}{(1-\theta)C_{PPh_3}}$$

2.5.9. Hammett Study

Previous studies of phosphines showed that alkyl – aryl phosphines do not correlate well with Hammett's or Taft's parameters.[22,23] Therefore, σ values for each phosphine were calculated using equation 2.5.8

Equation 2. 5. 8.

$$\sigma = log \frac{K}{K_0}$$

where K is the experimental acid associate constant (K_a) for a given phosphine (Table 2.3.2.) and K_0 is the reference K_a where the *para* position on the aryl is H (Table 2.3.2). The experimental σ values are reported in Table 2.32. The Hammett plot for the single–site Langmuir isotherms as described in above in Figure 2.5.36a. Figure 2.5.36b shows a

Hammett plot using classical parameters derived from the ionization of benzoic acids. This plot is also linear and the slope is also negative, consistent with positive charge buildup in the reactions of $^{t}Bu_2PAr$ with **SZO$_{300}$**. However, the magnitude of ρ is lesser when using the classical Hammett values. The R^2 of this plot is also lower ($R^2 = 0.87$).

a)

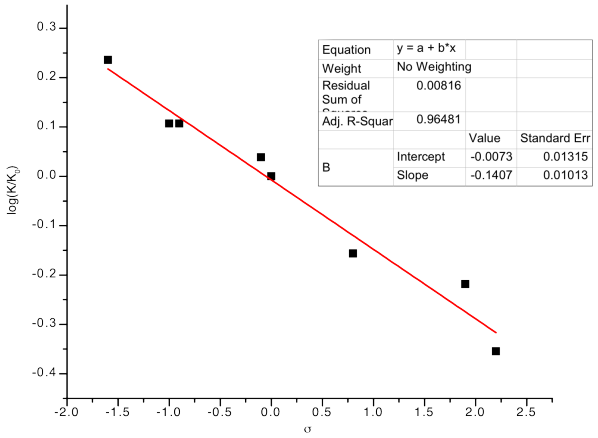

b)

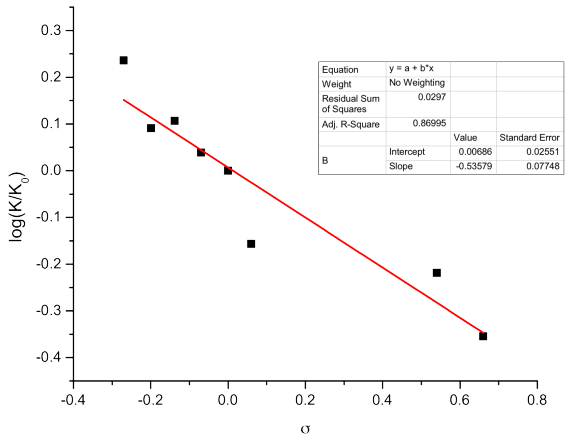

Figure 2.5.36. Hammett plot of the phosphine series **a)** Hammett plot for single-site Langmuir isotherm as described in main text **b)** Hammett plot using the classical parameters

2.5.10. Determination of pK_a

In an argon filled glovebox, a Teflon-valved NMR tube was loaded with **1** (ca. 10 mg) and either pyridinium or imidazolium tetrafluoroborate salts (ca. 1 equiv.) and dissolved in CD_3CN (0.4 – 0.5 ml). Specific acids used for individual phosphines are listed in Table S6. The samples were allowed to equilibrate for 2 hours at room temperature and were measured by $^{31}P\{^1H\}$ NMR. Due to fast exchange conditions, no free P^tBu_2Ar or $[HP^tBu_2Ar][BF_4]$ were observed when the pK_a of the acid was within 2 – 3 pK_a units. To obtain the concentration of the $[HP^tBu_2Ar]$, the weighted average of $^{31}P\{^1H\}$ chemical shift of the reaction mixture, δ_{rm}, relative to the known free $^{31}P\{^1H\}$ chemical shift of free $^tBu_2PAr$, δ_{fP}, and the known $^{31}P\{^1H\}$ chemical shift of $[^tBu_2ArPH][BF_4]$, δ_{fPH}, was determined using equations 2.5.9 – equations 2.5.11.

Equation 2. 5. 9.

$$\frac{[\mathrm{HP}]_\mathrm{f}}{[\mathrm{P}]_\mathrm{i}} = \frac{\delta_\mathrm{rm} - \delta_\mathrm{fP}}{\delta_\mathrm{fPH} - \delta_\mathrm{fP}}$$

Equation 2. 5. 10.

$$\frac{[\mathrm{HP}]_\mathrm{f}}{[\mathrm{P}]_\mathrm{i}} + \frac{[\mathrm{P}]_\mathrm{f}}{[\mathrm{P}]_\mathrm{i}} = 1$$

Equation 2. 5. 11.

$$[\mathrm{HP}]_\mathrm{f} + [\mathrm{P}]_\mathrm{f} = \mathrm{P_i}$$

$[HP]_f$ is the final concentration of fully protonated ^{t}Bu$_2$PAr, $[P]_f$ is final concentration of ^{t}Bu$_2$PAr, and $[P]_i$ is the initial concentration of ^{t}Bu$_2$PAr. Adjustments for the final concentrations of the nitrogen acid $[BH]_f$ and the nitrogen base $[B]_f$ were calculated based on equations 2.5.12 and 2.5.13.

Equation 2. 5. 12.

$$[BH]_f = [BH]_i - [P]_f$$

Equation 2. 5. 13.

$$[B]_f = [BH]_i - [HP]_f$$

Calculation of K for the reaction is a simple calculation as shown in equation 2.5.14. To determine pK, the standard transformation shown in equation 2.5.15. The pK_a of ^{t}Bu$_2$PAr is determined using equation 2.5.16.

Equation 2. 5. 14.

$$\mathrm{K} = \frac{[\mathrm{HP}]_\mathrm{f}[\mathrm{B}]_\mathrm{f}}{[\mathrm{P}]_\mathrm{f}[\mathrm{BH}]_\mathrm{f}}$$

Equation 2. 5. 15.

$$\mathrm{pK} = -\mathrm{logK} = \Delta\mathrm{pK_a}$$

Equation 2. 5. 16.

$$\mathrm{p}K_a(\mathrm{HP}) = \mathrm{p}K_a(\mathrm{BH}) + \Delta\mathrm{p}K_a$$

Determination of the sign in equation 2.5.15 can be rationalized based on the data acquired. In the case a -ΔpK_a occurs then there is more HP than BH indicating HP must be more

acidic than BH (e.g. P is more basic than B) therefore it must have a lower pK_a (vice versa for the case of a $+\Delta pK_a$. This method was reported by Morris and co-workers for the pK_a of HPR_3 in THF.[25]

Table 2. 5. 7. Summary of ^{31}P NMR shifts in C_6D_6 and CD_3CN

	^{31}P NMR shift (C_6D_6)	^{31}P NMR shift (CD_3CN)	$^{31}P\{^1H\}$ MAS (MeCN)	$^{31}P\{^1H\}$ MAS (Et_2O)
$P^tBu_2(p\text{-}MeOC_6H_4)$	37.5	36.4	43.3	46.4
$[HP^tBu_2(p\text{-}MeOC_6H_4)][BF_4]$		46.8		
$P^tBu_2(p\text{-}tBuC_6H_4)$	37.3	41.8	46.1	46.6
$[HP^tBu_2(p\text{-}^tBuC_6H_4)][BF_4]$		46.7		
$P^tBu_2(p\text{-}MeC_6H_4)$	36.4	37.6	46.3	54.4
$[HP^tBu_2(p\text{-}MeC_6H_4)][BF_4]$		47.6		
$P^tBu_2(p\text{-}TMSC_6H_4)$	38.7	39.9	47.6	51.1
$[HP^tBu_2(p\text{-}TMSC_6H_4)][BF_4]$		44.7		
P^tBu_2Ph	38.9	38.9	49.4	49.3
$[HP^tBu_2Ph][BF_4]$		48.0		
$P^tBu_2(p\text{-}FC_6H_4)$	36.9	37.1	47.5	49.50
$[HP^tBu_2(p\text{-}FC_6H_4)][BF_4]$		46.8		
$P^tBu_2(p\text{-}CNC_6H_4)$	38.4	38.4	49.6	50.8
$[HP^tBu_2(p\text{-}CNC_6H_4)][BF_4]$		47.2		
$P^tBu_2(p\text{-}CF_3C_6H_4)$	38.9	38.9	46.1	45.3
$[HP^tBu_2(p\text{-}CF_3C_6H_4)][BF_4]$		47.4		

Table 2.5.8. pK_a ladder

Entry	Base	pK_a	ΔpK_a
1	^{t}Bu$_2$P(*p*-MeOC$_6$H$_4$)	16.4	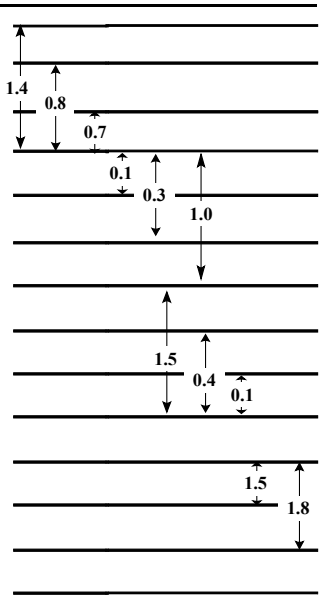
2	^{t}Bu$_2$P(*p*-^{t}BuC$_6$H$_4$)	15.8	
3	^{t}Bu$_2$P(*p*-TMSC$_6$H$_4$)	15.7	
4	Imidazole	15.0	
5	^{t}Bu$_2$P(*p*-MeC$_6$H$_4$)	14.9	
6	^{t}Bu$_2$PPh	14.7	
7	^{t}Bu$_2$P(*p*-FC$_6$H$_4$)	14.0	
8	^{t}Bu$_2$P(*p*-CNC$_6$H$_4$)	12.9	
9	^{t}Bu$_2$P(*p*-CF$_3$C$_6$I **0.3**	12.6	
10	Pyridine	12.5	
11	Benzyl amine	9.3	
12	PPh$_3$	7.8	
13	P(*p*-FC$_6$H$_4$)$_3$	7.5	
14	PPh$_2$(*o*-FC$_6$H$_4$)	6.1	

Table 2.5.9. Determination of pK_a

HP	BH	^{31}P (MeCN)	p*K*a (BH)	*K*	pK_a (ΔpK_a)	p*K*a (HP)
[HP^{t}Bu$_2$(*p*-MeOC$_6$H$_4$)][BF$_4$]	[C$_3$H$_4$N$_2$H][BF$_4$]	44.4(1.1)	15.0	0.14(±0.05)	1.4(±0.05)	16.4(±0.1)
[HP^{t}Bu$_2$(*p*-^{t}BuC$_6$H$_4$)][BF$_4$]	[C$_3$H$_4$N$_2$H][BF$_4$]	44.1(0.2)	15.0	5.37(±1.0)	-0.73(±0.14)	15.8(±0.1)
[HP^{t}Bu$_2$(*p*-MeC$_6$H$_4$)][BF$_4$]	[C$_3$H$_4$N$_2$H][BF$_4$]	45.4(1.2)	15.0	5.30(±1.3)	-0.72(±0.15)	15.7(±0.2)
[HP^{t}Bu$_2$(*p*-TMSC$_6$H$_4$)][BF$_4$]	[C$_3$H$_4$N$_2$H][BF$_4$]	42.9(0.7)	15.0	0.77(±0.3)	-0.11(±0.10)	14.9(±0.1)
[HP^{t}Bu$_2$Ph][BF$_4$]	[C$_3$H$_4$N$_2$H][BF$_4$]	42.6(0.1)	15.0	0.528(±0.015)	-0.277(±0.013)	14.7(±0.1)
[HP^{t}Bu$_2$(*p*-FC$_6$H$_4$)][BF$_4$]	[C$_3$H$_4$N$_2$H][BF$_4$]	39.8(0.2)	15.0	10(±1.16)	-1.0(±0.03)	14.0(±0.1)
[HP^{t}Bu$_2$(*p*-CNC$_6$H$_4$)][BF$_4$]	[C$_5$H$_4$NH][BF$_4$]	39.5(0.05)	12.5	1.58(±0.8)	0.23(±0.02)	12.9(±0.2)
[HP^{t}Bu$_2$(*p*-CF$_3$C$_6$H$_4$)][BF$_4$]	[C$_5$H$_4$NH][BF$_4$]	44.3(0.5)	12.5	1.62(±0.9)	0.22(±0.14)	12.6(±0.1)
[HP^{t}Bu$_2$(*3,5*-CF$_3$C$_6$H$_2$)][BF$_4$]	[C$_5$H$_4$NH][BF$_4$]	40.0(0.02)	12.5	2.51(±0.03)	0.44(±0.2)	12.1(0.2)

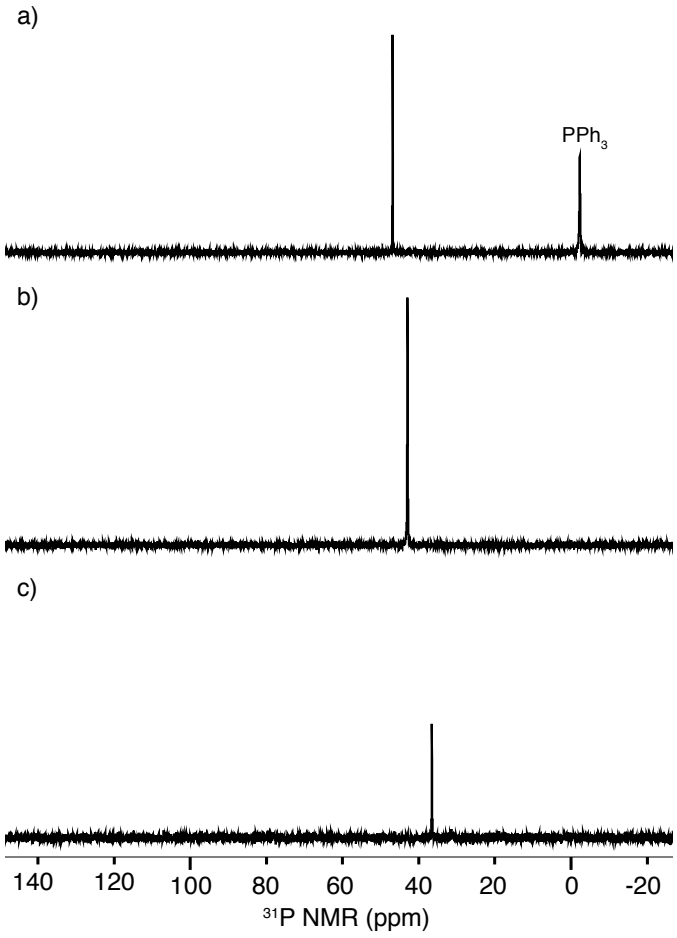

Figure 2.5.37. **1a** pK_a study **a)** fully protonated **1a** using [$HPPh_3$] **b)** pK_a experiment using [$N_2C_3H_5$][BAr_F] **c)** free **1a**

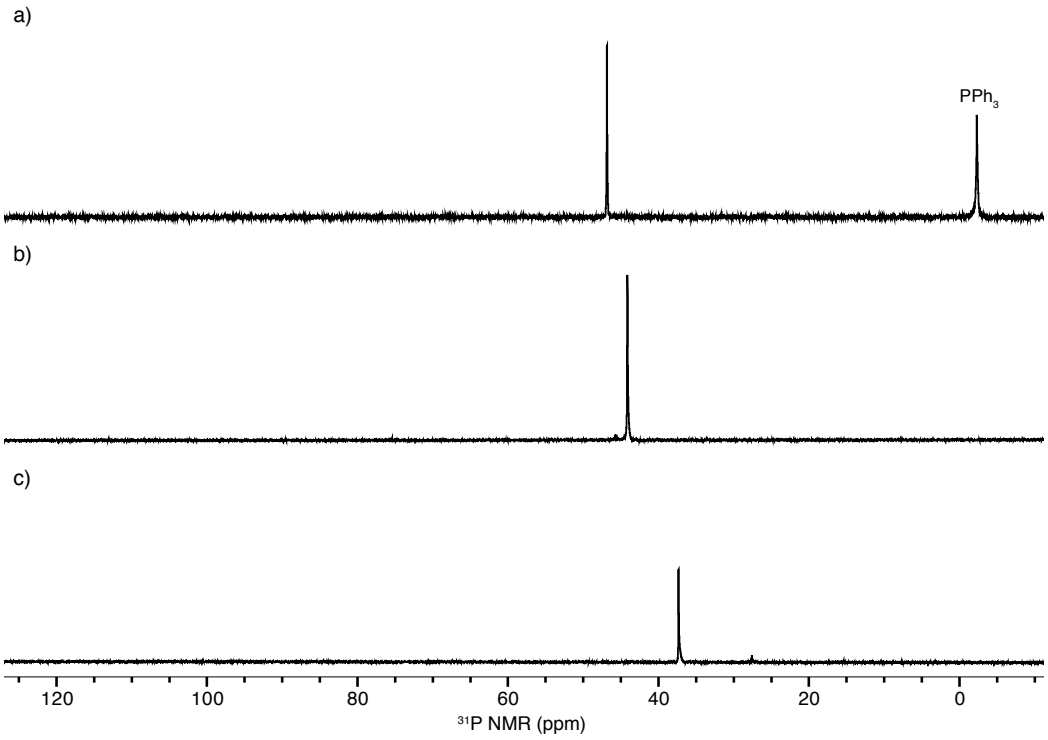

Figure 2.5.38.**1b** pK_a study **a)** fully protonated **1b** using [$HPPh_3$] **b)** pK_a experiment using [$N_2C_3H_5$][BAr_F] **c)** free **1b**

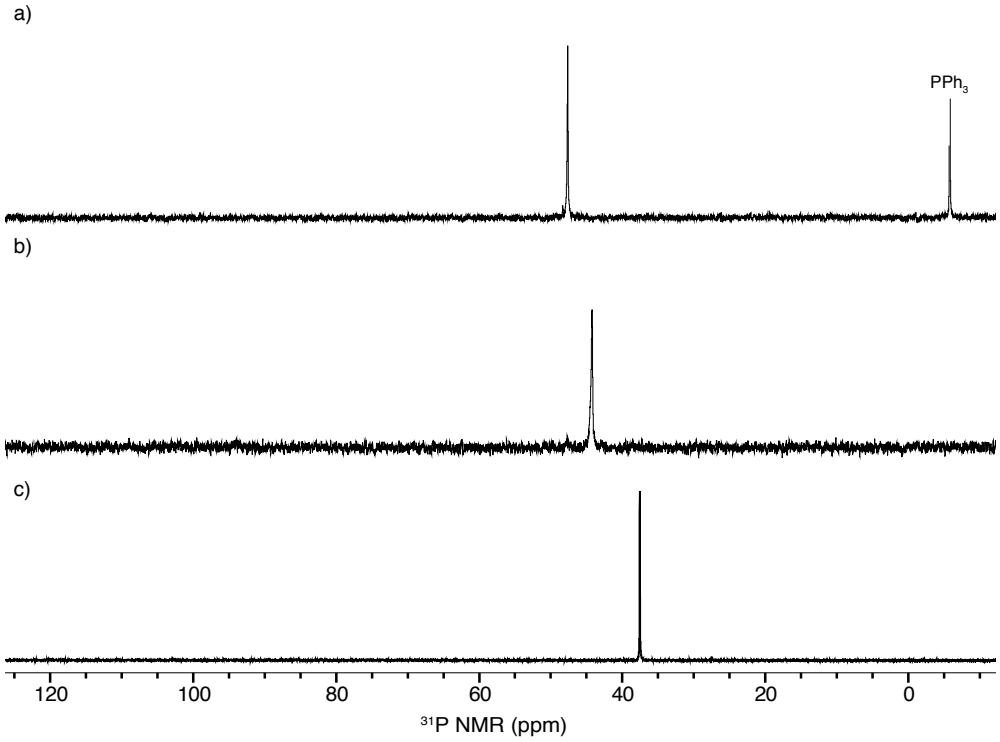

Figure 2.5.39. **1c** pK_a study **a)** fully protonated **1c** using [$HPPh_3$] **b)** pK_a experiment using [$N_2C_3H_5$][BAr_F] **c)** free **1c**

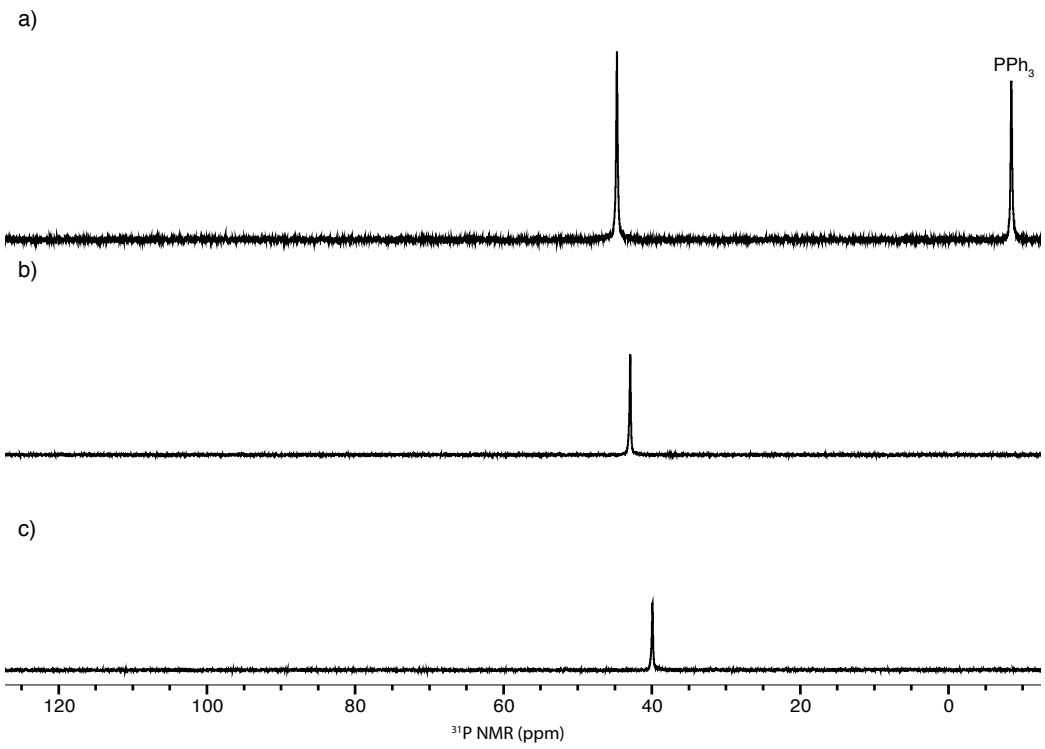

Figure 2.5.40. **1d** pK_a study **a)** fully protonated **1d** using [$HPPh_3$] **b)** pK_a experiment using [$N_2C_3H_5$][BAr_F] **c)** free **1d**

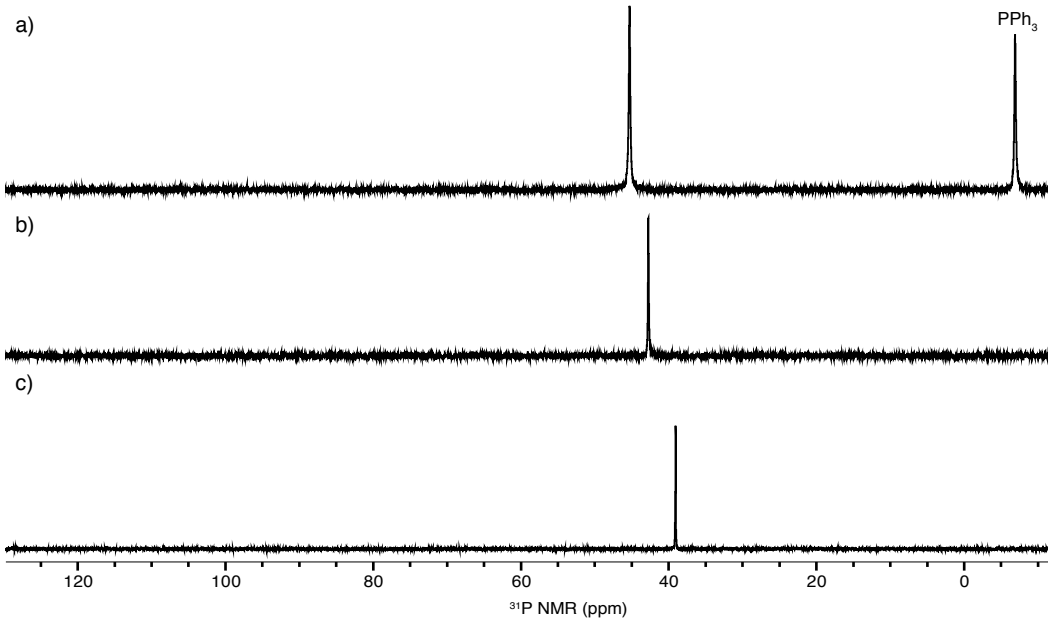

Figure 2.5.41. **1e** pK_a study **a)** fully protonated **1e** using [$HPPh_3$] **b)** pK_a experiment using [$N_2C_3H_5$][BAr_F] **c)** free **1e**

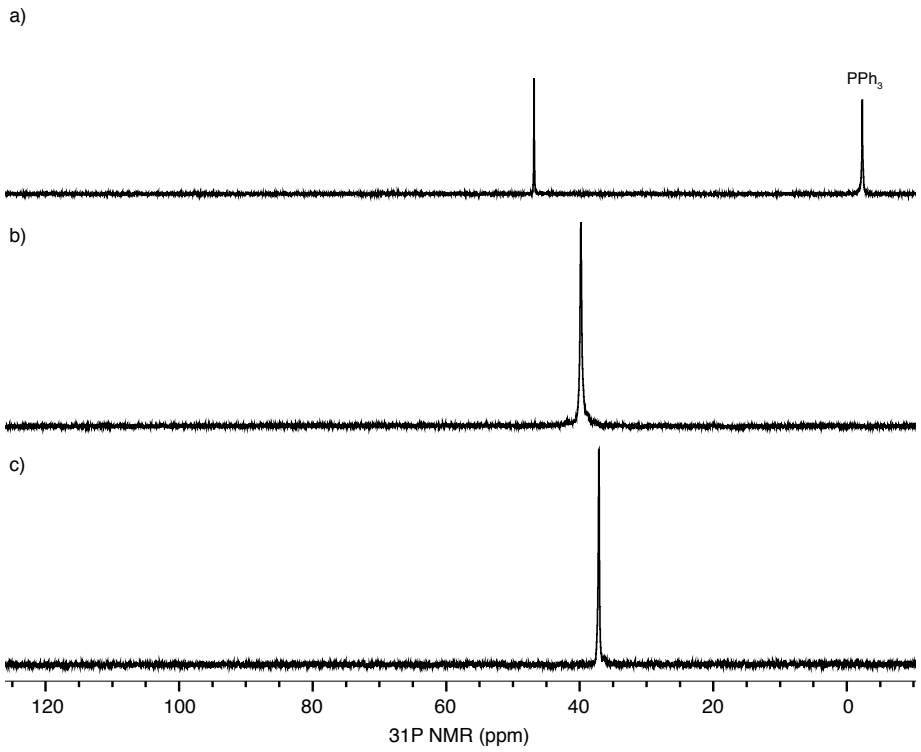

Figure 2. 5. 42. **1f** pK_a study **a)** fully protonated **1f** using [$HPPh_3$] **b)** pK_a experiment using [NHC_5H_5][BAr_F] **c)** free **1f**

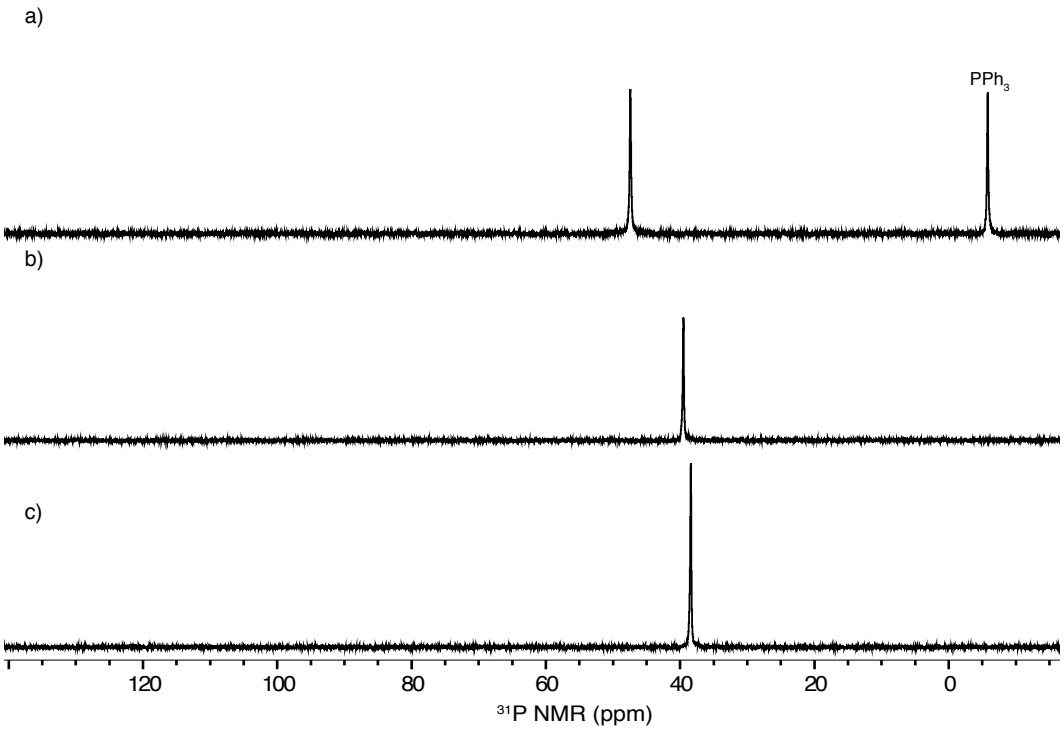

Figure 2.5.43. **1g** pK_a study **a)** fully protonated **1g** using [$HPPh_3$] **b)** pK_a experiment using [NHC_5H_5][BAr_F] **c)** free **1g**

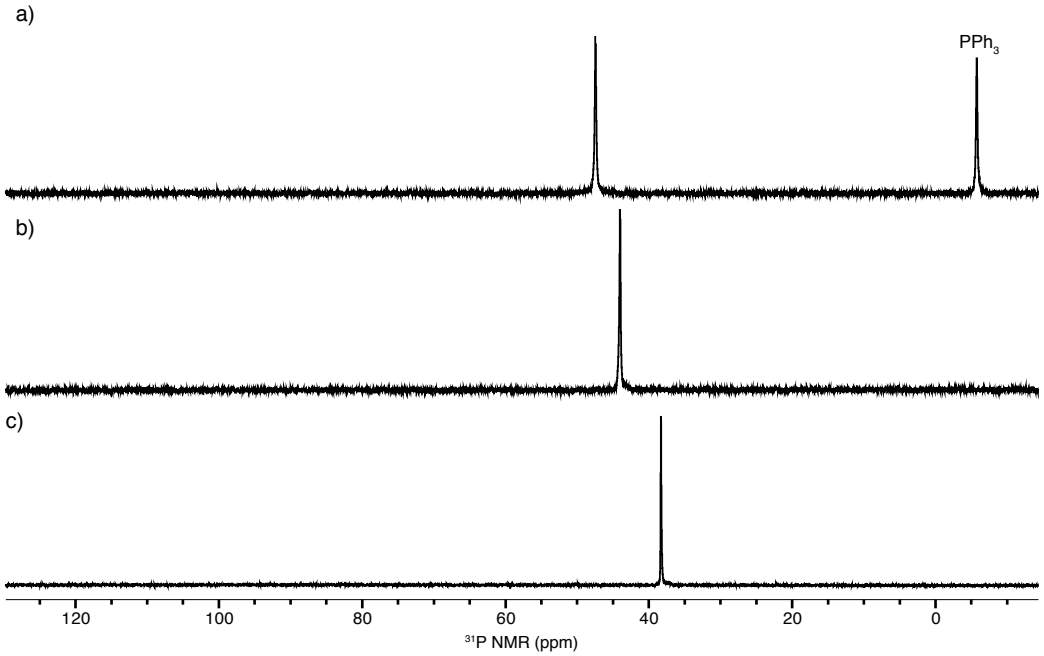

Figure 2.5.44. **1h** pK_a study **a)** fully protonated **1h** using [$HPPh_3$] **b)** pK_a experiment using [NHC_5H_5][BAr_F] **c)** free **1h**

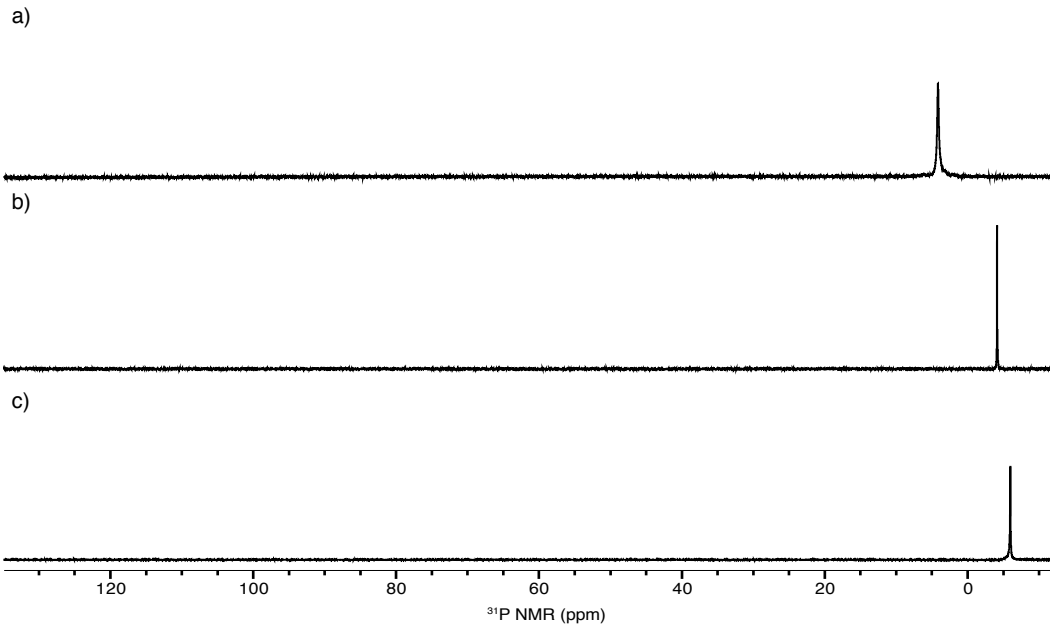

Figure 2.5.45. PPh_3 pK_a study **a)** [$HPPh_3$] **b)** pK_a experiment using [NC_7H_{10}][BAr_F] **c)** free PPh_3

2.6. References

1. Tafazolian, H., Culver, D. B. and Conley, M. P. A Well-Defined Ni(II) α-Diimine Catalyst Supported on Sulfated Zirconia for Polymerization Catalysis. *Organometallics* **36**, 2385–2388 (2017).

2. Culver, D. B., Tafazolian, H. and Conley, M. P. A Bulky Pd(II) α-Diimine Catalyst Supported on Sulfated Zirconia for the Polymerization of Ethylene and Copolymerization of Ethylene and Methyl Acrylate. *Organometallics* **37**, 7 (2018).

3. Stalzer, M. M., Delferro, M. and Marks, T. J. Supported Single-Site Organometallic Catalysts for the Synthesis of High-Performance Polyolefins. *Catal. Letters* **145**, 3–14 (2015).

4. Marie Stalzer, M. *et al.* Single-Face/All-cis Arene Hydrogenation by a Supported Single-Site d0 Organozirconium Catalyst. *Angew. Chemie Int. Ed.* **55**, 5263–5267 (2016).

5. Gu, W. *et al.* Benzene selectivity in competitive arene hydrogenation: Effects of single-site catalyst···acidic oxide surface binding geometry. *J. Am. Chem. Soc.* **137**, 6770–6780 (2015).

6. Williams, L. A. *et al.* Surface structural-chemical characterization of a single-site d0 heterogeneous arene hydrogenation catalyst having 100% active sites. *Proc. Natl. Acad. Sci. U. S. A.* **110**, 413–418 (2013).

7. Kaphan, D. M. *et al.* Surface Organometallic Chemistry of Supported Iridium(III) as a Probe for Organotransition Metal-Support Interactions in C-H Activation. *ACS Catal.* **8**, 5363–5373 (2018).

8. Syed, Z. H. *et al.* Electrophilic Organoiridium(III) Pincer Complexes on Sulfated Zirconia for Hydrocarbon Activation and Functionalization. *J. Am. Chem. Soc.* **141**, 6325–6337 (2019).

9. Hino, M., Kobayashi, S. and Arata, K. Solid catalyst treated with anion. 2. Reactions of butane and isobutane catalyzed by zirconium oxide treated with sulfate ion. Solid superacid catalyst. *J. Am. Chem. Soc.* **101**, 6439–6441 (1979).

10. Hino, M. and Arata, K. Synthesis of solid superacid catalyst with acid strength of H 0 ⩽–16.04. *J. Chem. Soc., Chem. Commun.* **0**, 851–852 (1980).

11. Olah, G. A., Prakash, S., Sommer, J. and Molnar, A. *Superacid chemistry*. (Wiley, 2009).

12. Tabora, J. E. and Davis, R. J. On the Superacidity of Sulfated Zirconia Catalysts for Low-Temperature Isomerization of Butane. *J. Am. Chem. Soc.* **118**, 12240–12241 (1996).

13. Drago, R. S. and Kob, N. Acidity and Reactivity of Sulfated Zirconia and Metal-Doped Sulfated Zirconia. *J . Phys. Chem. B* **101**, 3360–3364 (1997).

14. Haw, J. F. *et al.* NMR and theoretical study of acidity probes on sulfated zirconia catalysts. *J. Am. Chem. Soc.* **122**, 12561–12570 (2000).

15. Klet, R. C. *et al.* Evidence for Redox Mechanisms in Organometallic Chemisorption and Reactivity on Sulfated Metal Oxides. *J. Am. Chem. Soc.* **140**, 6308–6316 (2018).

16. Haase, F. and Sauer, J. The Surface Structure of Sulfated Zirconia: Periodic ab Initio Study of Sulfuric Acid Adsorbed on ZrO2(101) and ZrO2(001). *J. Am. Chem. Soc.* **120**, 13503–13512 (1998).

17. Li, X. *et al.* Oxidative activation of n-butane on sulfated zirconia. *J. Am. Chem. Soc.* **127**, 16159–16166 (2005).

18. Farneth, W. E. and Gorte, R. J. Methods for Characterizing Zeolite Acidity. *Chem. Rev.* **95**, 615–635 (1995).

19. Stoyanov, E. S., Kim, K. C. and Reed, C. A. An infrared vNH scale for weakly basic anions. Implications for single-molecule acidity and superacidity. *J. Am. Chem. Soc.* **128**, 8500–8508 (2006).

20. Osegovic, J. P. and Drago, R. S. Measurement of the Global Acidity of Solid Acids by 31P MAS NMR of Chemisorbed Triethylphosphine Oxide. *J. Phys. Chem. B* **104**, 147–154 (1999).

21. Farcasiu, D. and Ghenciu, A. Acidity functions from carbon-13 NMR. *J. Am. Chem. Soc.* **115**, 10901–10908 (1993).

22. Allman, T. and Goel, R. G. The basicity of phosphines. *https://doi.org/10.1139/v82-106* **60**, 716–722 (2011).

23. Mastryukova, T. A. and Kabachnik, M. I. The Application of the Hammett Equation with the Constants σph in the Chemistry of Organophosphorus Compounds. *Russ. Chem. Rev.* **38**, 795 (1969).

24. Morris, R. H. Brønsted-Lowry Acid Strength of Metal Hydride and Dihydrogen Complexes. *Chem. Rev.* **116**, 8588–8654 (2016).

25. Abdur-Rashid, K. *et al.* An acidity scale for phosphorus-containing compounds including metal hydrides and dihydrogen complexes in THF: Toward the unification of acidity scales. *J. Am. Chem. Soc.* **122**, 9155–9171 (2000).

Chapter 3. Ethylene Polymerization Activity of $(R_3P)Ni(codH)^+$ (cod = 1,5-cylcooctadiene) Sites Supported on Sulfated Zirconium Oxide

3.1. Abstract

PAr_3 containing *o*-OMe, *o*-Me, or *o*-Et substituents react with Brønsted sites on sulfated zirconium oxide (**SZO_{300}**) to form $[HPAr_3][$**SZO_{300}**$]$. The phosphonium sites on this material react with bis(cyclooctadiene)nickel ($[Ni(cod)_2]$) to form $[Ni(PAr_3)(codH)][$**SZO_{300}**$]$ that are active in ethylene polymerization reactions. Selective poisoning studies with pyridine show that ~90% of the $Ni(PAr_3)(codH)+$ sites in this material are active in polymerization reactions.

3.2. Introduction

Organometallic complexes of nickel and palladium containing *o*-phosphinoarenesulfonate ligand ({PO}) catalyzes the polymerization of olefins. In contrast to (α-diimine)Pd–R^+ catalysts,[1,2] {PO}Pd-R complexes polymerize ethylene to form linear polymers, Figure 3.2.1b,[3,4] and show broad functional group tolerance in copolymerization reactions with polar commoners, Figure 3.2.1c.[5,6] Formation of linear polymers with {PO}Pd-R complexes is related to the cis-arrangement of a strong-trans-influence phosphine and a weak-trans-influence sulfonate that leads to electronic asymmetry within the palladium complex.[7] This electronic asymmetry inhibits β-H elimination and reinsertion steps that result in branches in the polymer chain.[8]

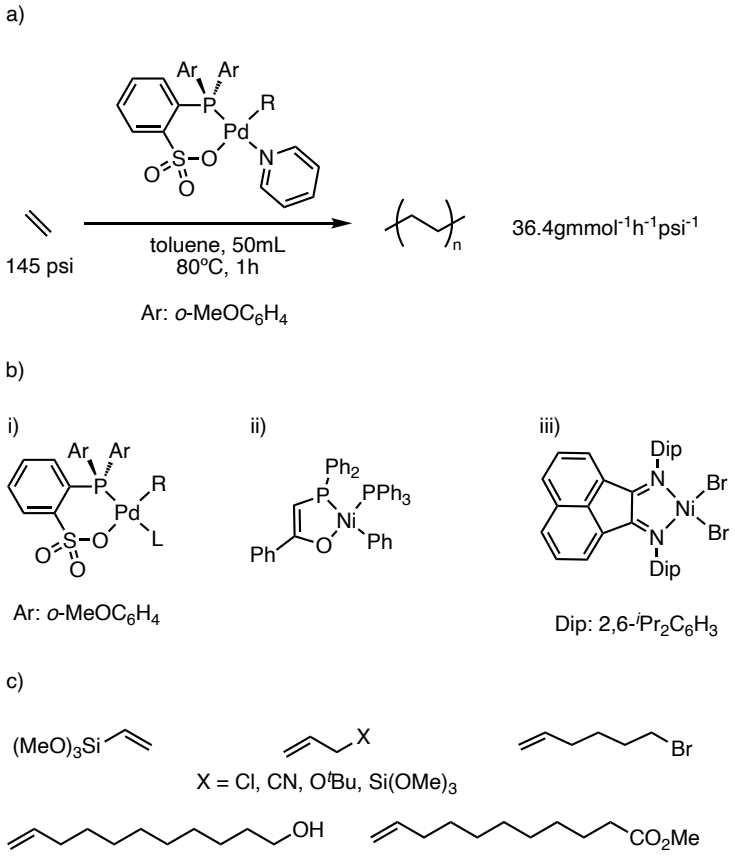

Figure 3.2.1. Ethylene polymerization by Group 10 metals; homopolymerization of ethylene by {PO}Pd system that generates linear polyethylene (a); ethylene polymerization and oligomerization to form linear polyethylene (i), higher olefins (ii), and branched polyethylene (iii) polar comonomers that are suitable for copolymerization (c).

This general design strategy continues to find new applications in novel cationic palladium and nickel catalysts that incorporate electronically dissymmetric ligands that have very high polymerization activities and good functional group tolerance.[9,10] {PO}Ni systems form C4-C20 oligomers that are produced due to repetitive ethylene insertion to alkyl metal species followed by a β-H elimination and release of 1-alkenes, Figure 3.2.1.b.i. Brookhart's catalyst, with either Ni or Pd, give highly branched and high-molecular-weight polyethylene, Figure 3.2.1.b.iii. This is a result of suppression of chain transfer, which

leads to reinsertion of the eliminated olefin into the metal-hydride bond without preference of regioselectivity.

Industrial olefin polymerization catalysts are almost always heterogeneous.[11,12] Silica pretreated with alkylaluminium or methylaluminoxane (MAO) is a very common support for polymerization catalysts but is not generally compatible with late-transition-metal polymerization precatalysts, Figure 3.2.2.a. An example shown in Figure 3.2.2.a shows modified (α-diimine)$NiBr_2$ complexes containing hydroxyl groups react with SiO_2/MAO and polymerize ethylene in the presence of an $Et_3Al_2Cl_3$ activator to give polymers with broad molecular weight distributions, Figure 3.2.2.a.[13,14]

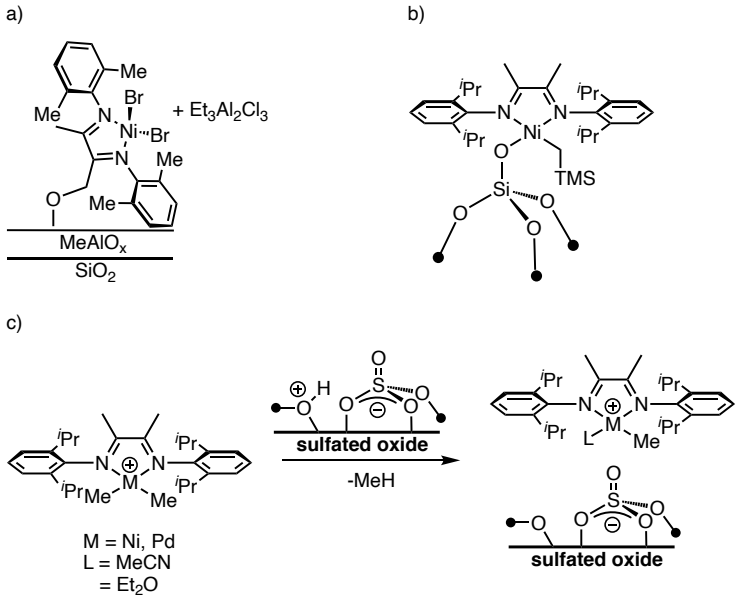

Figure 3.2.2. Examples of heterogeneous (α-diimine)Ni catalysts for olefin polymerization; (α-diimine)Ni catalyst grafted onto MAO/SiO_2 that is active for the polymerization of ethylene in the presence of $Et_3Al_2Cl_3$ (a); [(≡SiO)Ni(α-diimine)(CH_2SiMe_3)] (b); heterogeneous (α-diimine)Ni or -Pd catalysts supported on **SZO_{300}** for the polymerization of olefins.

To overcome this challenge the design and synthesis of well-defined organometallics on oxides is a potentially attractive and synthetic strategy to access these active sites for polymerization reactions.[15–19] This strategy uses a partially dehydroxylated oxide containing –OH groups on the surface to react with an organometallic to form covalent M–O_x (O_x = surface oxygen) or an electrophilic M⋯ O_x ion pair. Supports containing –OH groups with weak Brønsted acidity (e.g. SiO_2) form M–O_x that are inactive for the polymerization reactions in the absence of exogenous activators.[20,21] M⋯ O_x pairs form on supports containing –OH sites that are more Brønsted acidic than silica, such as sulfated oxides,[22] or Lewis-acid activated silica.[23,24] The reaction of (α-diimine)$NiMe_2$ or (α-diimine)$PdMe_2$ with sulfated zirconium oxide partially dehydroxylated at 300°C

(**SZO$_{300}$**) forms the active sites shown in Figure 3.2.2.c that have activities close to their solution analogues and show single-site behavior.[25,26]

The application of this strategy to surface analogues of {PO}M–R (M = Ni, Pd) is not as straightforward.[27,28] {PO}Pd(L) are expected to react with –OH sites on oxides to form [{PO}ML][**SZO$_{300}$**] ion pairs that lack the organometallic unit that is critical to propagate polymer growth, Figure 3.2.3.a. Early reports of polymerization reactions with {PO}Pd complexes were generated from the reactions of Pd_2dba_3 or $Pd(OAc)_2$ and {PO}H, which forms {PO}Pd–H under the reaction conditions, Figure 3.2.3b.[29,30] The Brønsted sites on **SZO$_{300}$** react with sufficiently basic R_3P to form [R_3P][**SZO$_{300}$**], which may serve as a heterogeneous {PO}H-type surface site, Figure 3.2.3.c. This chapter describes the reaction of [R_3PH][**SZO$_{300}$**] with bis(cyclooctadiene)nickel [$Ni(cod)_2$] to produce active sites for the polymerization reaction of ethylene.

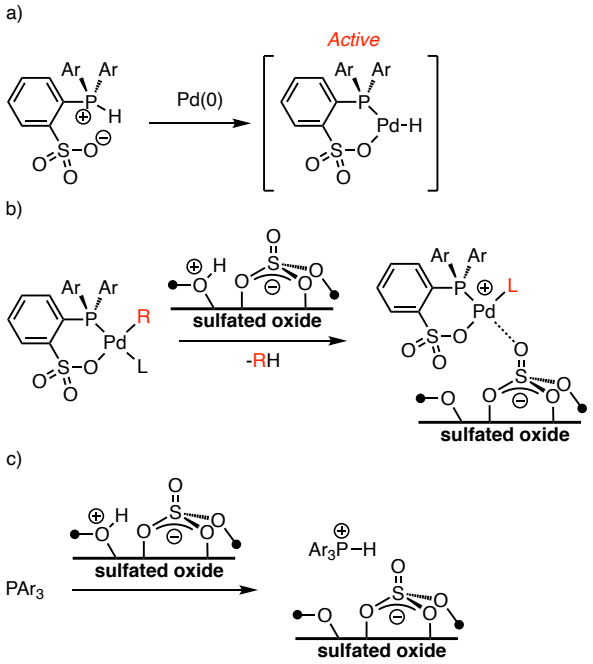

Figure 3.2.3. Reaction of {PO}H with Pd(0) to form Pd-H that is active in olefin polymerization (a); Reaction of a {PO}Pd–R catalyst with **SZO$_{300}$** to form [{PO}Pd][**SZO$_{300}$**], which are unreactive towards olefins (b); design of [Ar$_3$PH][**SZO$_{300}$**] to form heterogeneous {PO}M–R active sites (c).

3.3. Results and Discussion

3.3.1. Synthesis of [Ar$_3$PH][SZO$_{300}$]

The reaction of triarylphosphines with the Brønsted sites on **SZO$_{300}$** is expected to from [Ar$_3$PH][**SZO$_{300}$**], provided that the pK_a value of [Ar$_3$PH] is greater than ~ 6 in acetonitrile.[31] The reaction P(*o*-MeOC$_6$H$_4$)$_2$Ph with **SZO$_{300}$** forms [HP(*o*-OMeC$_6$H$_4$)$_2$Ph][**SZO$_{300}$**], (**1**). The ^{31}P{^{1}H} MAS NMR spectrum contains at a signal at 10 ppm. The FTIR spectrum of 1 shows a characteristic ν_{PH} stretch at 2456 cm^{-1}. Both the ^{31}P{^{1}H} MAS NMR and FTIR confirm the formation of [HP(*o*-OMeC$_6$H$_4$)$_2$Ph][**SZO$_{300}$**].

Similar results were obtained with P(*o*-$EtC_6H_4)_2Ph$ and P(*o*-$MeC_6H_4)_2Ph$ to from [HP(*o*-$EtC_6H_4)_2Ph$][**SZO$_{300}$**], (**2**), and [HP(*o*-$MeC_6H_4)_2Ph$][**SZO$_{300}$**], (**3**), respectively.

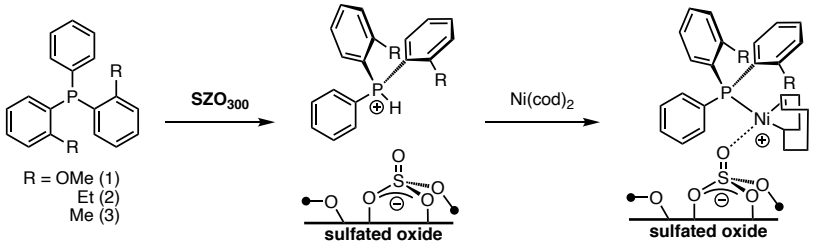

Scheme 3.3.1. The reaction scheme of R_3P and **SZO$_{300}$** to form [R_3PH][**SZO$_{300}$**] which further reacts with $Ni(cod)_2$ to form [$Ni(PAr_3)(codH)$][**SZO$_{300}$**]

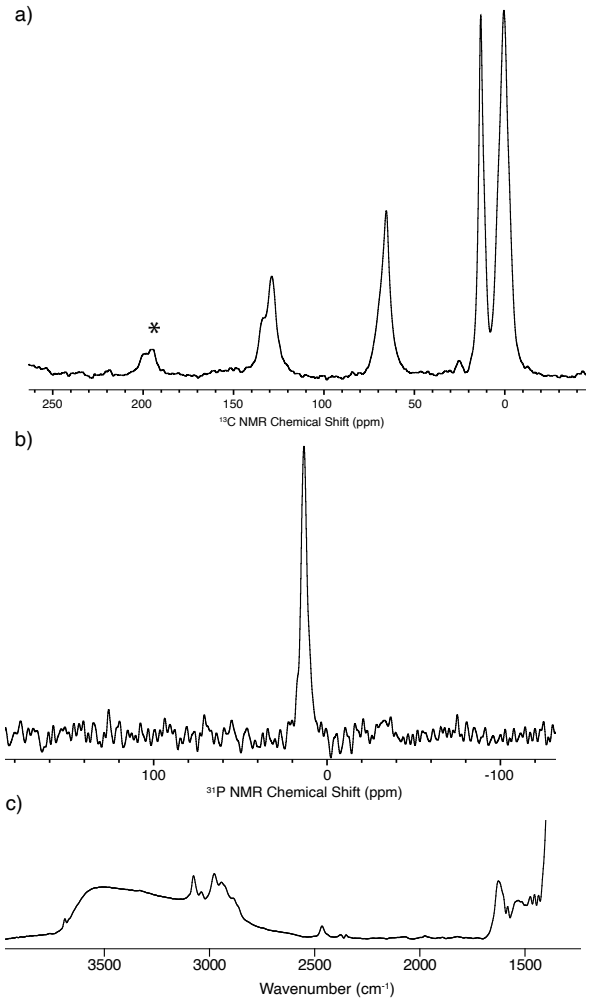

Figure 3.3.1. Characterization data of [HP(o-OMeC$_6$H$_4$)$_2$Ph][**SZO$_{300}$**] (**1**) ^{13}C{^{1}H} CP MAS NMR; grafting reaction performed in Et$_2$O; 10kHz; ns= 40k; d1=1s; * = spinning sidebands(a); ^{31}P{^{1}H} MAS NMR; grafting performed in Et$_2$O; 10kHz; ns = 2k; d1 = 1s (b); FT-IR (c).

*3.3.2. Synthesis and Characterization of **1Ni – 3Ni***

1-3 react with Ni(cod)$_2$ in diethyl ether (Et$_2$O) to form orange [Ni(PAr$_3$)(codH)][**SZO$_{300}$**] (**1Ni-3Ni**). This reaction evolves 0.100 mmol/g cyclooctadiene, which is consistent with the loss of one cod per Ni in **1Ni – 3Ni**. The FTIR spectrum of

1Ni lacks the ν_{PH} stretch at 2456 cm^{-1}. Additionally, the $^{31}P\{^{1}H\}$ NMR of **1Ni** contains a new signal at 47 ppm, 37 ppm downfield from that of **1**. These results indicate that the phosphonium of 1 reacts with $Ni(cod)_2$ to form **1Ni**. The cross-polarization ^{13}C MAS NMR spectrum of **1Ni – 3Ni** contain signals assigned to the $(codH)^+$ fragment in $Ni(PAr_3)(codH)^+$.[32]

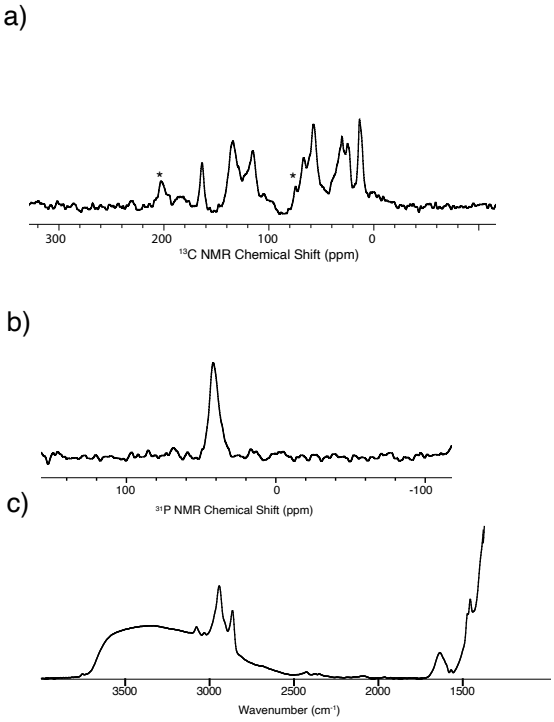

Figure 3.3.2. Analytical data for [1-Ni(codH)][$\mathbf{SZO_{300}}$] (**1Ni**); $^{13}C\{^{1}H\}$ CP MAS NMR; grafting reaction performed in Et_2O; 10kHz; ns = 80k; d1 = 1s; * = spinning sidebands (a); $^{31}P\{^{1}H\}$ MAS NMR; grafting performed in Et_2O; 10kHz; ns = 2k; d1 = 1s (b); FT-IR (c).

Table 3.3.1. Key spectral data for [$HPAr_3$][**SZO_{300}**] and [$Ni(PAr_3)(codH)$[**SZO_{300}**]

PAr_3	$\delta^{31}P$ (ppm)[a]	[$HPAr_3$][SZO_{300}]		[$Ni(PAr_3)(codH)$][SZO_{300}]
		$\delta^{31}P$ (ppm)[b]	ν_{PH} (cm^{-1})	$\delta^{31}P$ (ppm)[b]
1	-26.4	10	2456	47
2	-22.4	13	2447	45
3	-20.8	11	2454	45

[a] C_6D_6 solution, referenced to 85% H_3PO_4. [b] 10kHZ MAS spinning speed, referenced to 85% H_3PO_4.

*3.3.3. Polymerization reactions with **1Ni - 3Ni***

1Ni reacts with 150psi of ethylene on demand at 50 °C, which results in the formation of polyethylene containing 35 branches/1000C. ^{13}C NMR analysis of the polymer shows that methyl, ethyl, and butyl branches are present in this polymer.

The activity of **1Ni – 3Ni** are given in Table 3.3.2. The activity of **1Ni – 3Ni** are modest compared to that of {PO}M–R species, but similar to that of catalysts prepared from {PO}H with similar steric profiles and Pd(0) sources in situ.[33] The formation of branched polymers using **1Ni –3Ni** is in contrast to polymers obtained with homogeneous {PO}Pd–R or {PO}Ni–R catalysts in solution. The origin in difference is unclear, but may related to the formation of a weakly coordinating ion pair between $Ni(PAr_3)(codH)^+$ and the sulfated sites on **SZO_{300}**[22], which may facilitate chain walking.

Table 3.3.2. Ethylene Polymerization Activity of [Ni(PAr_3)(codH)[**SZO_{300}**]^a

Entry	**PAr_3**	***P* (psi)** ^{b}	**T (°C)**	**Yield (mg)**	**Activity**^{c}	**B/1000C**^{d}
1	1	150	50	71	3000(150)	35
2	2	150	50	82	3400(100)	20
3	3	100	50	12	510(10)	n.d.
4	3	150	50	83	3500(100)	24
5	3	200	50	91	3500(500)	n.d.
6	3	250	65	80	3400(300)	n.d.

^{a}Catalyst loading (12 μmol) in toluene. ^{b}Pressure of ethylene on demand. $^c g_{PE}\ mol_{Ni}^{-1} h^{-1}$ calculated from triplicate polymerization runs assuming that all Ni in [Ni(PAr_3)(codH)[**SZO_{300}**] is active in polymerization. The values in parenthesis are associated standard errors based on polymer yield. ^{d}Measured by ^{1}H NMR spectroscopy in CD_2Cl_4 at 120 °C.

*3.3.4. Poisoning studies of **1Ni – 3Ni***

Contacting **1Ni** with a slight excess of pyridine (Ni:pyridine = 1:1.2) results in complete suppression of the polymerization activity, which indicates that pyridine poisons the Ni sites in the polymerization reaction. The addition of substiochiometric pyridine of **1Ni** followed by reaction with 150psi of ethylene on demand results in the formation of polyethylene, although with a lower activity than that of a reaction conducted in the absence of pyridine. Plots of activity versus the molar ratio of pyridine to Ni are linear, and indicate that ~90% of the Ni sites in **1Ni** are capable of initiating ethylene polymerization.

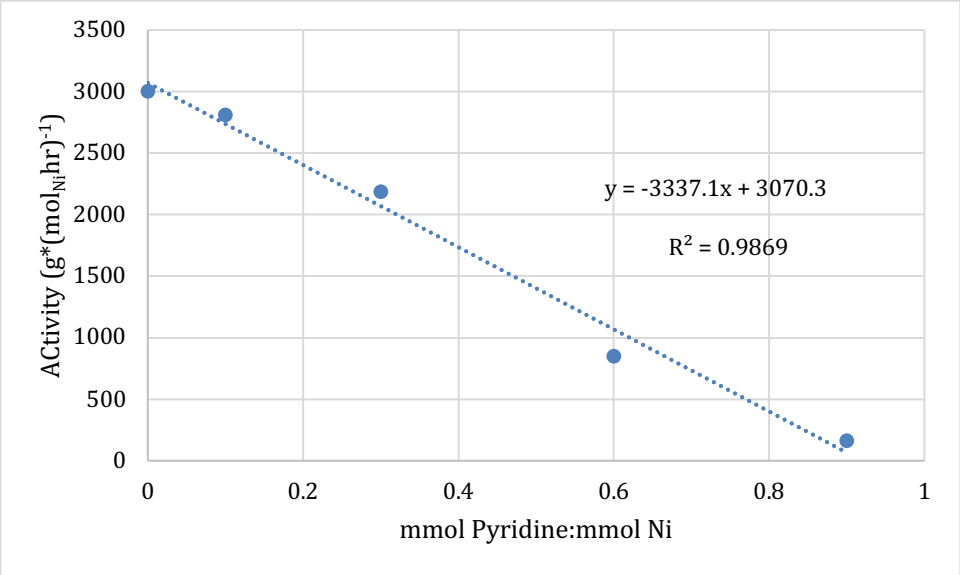

Figure 3.3.3. Plot of mmol pyridine vs activity (g*(mol$_{Ni}$hr)$^{-1}$)

3.4. Conclusions

Triarylphosphines react with SZO_{300} to form $[Ar_3PH][\mathbf{SZO_{300}}]$. These phosphoniums can subsequently react with $Ni(cod)_2$ to form $[Ni(PAr_3)(codH)][\mathbf{SZO_{300}}]$ which are active for the polymerization of ethylene to give polymers with moderate branching in the polymer chain. The activity of $[Ni(PAr_3)(codH)][\mathbf{SZO_{300}}]$ is modest, and similar to that of first-generation {PO}Pd catalysts.

3.5. Materials and Methods

3.5.1. General Considerations

All reactions and manipulations were performed under an inert atmosphere of nitrogen or argon using standard Schlenk techniques. C_6D_6 was purchased from Cambridge Isotope Laboratories, dried over Na/benzophenone, freeze-pump-thawed three times, and distilled under vacuum. Solvents were purchased from Fisher Scientific, dried by passing

through a double-column J. C. Meyer solvent system and degassed before use. Diethyl ether was dried over Na/benzophenone; and distilled under vacuum before use. Other chemicals were purchased from standard suppliers. **SZO$_{300}$** was prepared as previously described.[26] P(*o*-MeC$_6$H$_4$)$_2$Ph,[34] and P(*o*-OMeC$_6$H$_4$)$_2$Ph[35] were previously described. Solution NMR spectra were recorded on a Bruker Avance 300 MHz spectrometer and referenced to C_6D_5H peak at 7.16 ppm. Solid-state NMR experiments were performed on a 600 MHz Bruker NEO spectrometer in 4 mm zirconia rotors packed in an argon filled glovebox. ^{1}H, ^{31}P{^{1}H}, and ^{13}C{^{1}H} CPMAS NMR spectra were recorded in 4 mm zirconia rotors at 10 KHz magic angle spinning speed. FT-IR spectra were recorded as pressed pellets using a Bruker Alpha IR spectrometer in an argon-filled glovebox.

*3.5.2. Synthesis of [R$_3$PH][**SZO$_{300}$**]*

SZO$_{300}$ (500 mg, 0.065 mmol OH) was loaded into a flask containing a Teflon valve and a ground glass joint for connection to a high vacuum line in an argon filled glovebox. A separate flask containing a Teflon valve and a ground glass joint for connection to a high vacuum line was loaded with phosphine (1.2 equiv per OH, 0.078 mmol). The flasks were removed from the glovebox, connected to a high vacuum line, and evacuated. Et_2O (~ 5mL) was transferred under vacuum to each flask cooled to 77 K. The flask containing **SZO$_{300}$** was warmed to 0 °C, and the flask containing the phosphine was warmed to room temperature to form a clear colorless solution. The phosphine solution was transferred by cannula onto the cooled **SZO$_{300}$** slurry. The slurry was stirred for 1 hour at room temperature. After this time phosphine solution was removed by cannula, the flask was evacuated, and Et_2O (~5 mL) was transferred under vacuum at 77 K. The slurry was

warmed to room temperature for 20 min, and the supernatant was removed by a cannula filtration. This procedure was repeated two more times to ensure no physiosorbed phosphine was present in this material. The solid was then dried under high vacuum for 30 minutes and stored in an argon filled glovebox.

[HP(*o*-OMeC$_6$H$_4$)$_2$Ph][SZO$_{300}$] (1). a) $^{13}C\{^1H\}$ CP MAS NMR (125 MHz, 10 kHz): 137(*o-CH*OCH$_3$), 132 (*Aryl*), 70(*Et$_2$O),* 16(*Et$_2$O*), 4*(o*-O*Me*); b) $^{31}P\{^1H\}$ MAS NMR (125 MHz, 10 kHz): δ10 ppm; c) FTIR (solid pellet): ν_{PH} = 2456 cm^{-1}.

[HP(*o*-MeC$_6$H$_4$)$_2$Ph][SZO$_{300}$] (2). a) $^{13}C\{^1H\}$ CP MAS NMR (125 MHz, 10 kHz): 138(*o-CH*CH$_3$), 130(*Aryl*), 24(*pentane*), 15(*o-CH$_3$)*, 7(*pentane*); b) $^{31}P\{^1H\}$ MAS NMR (125 MHz, 10 kHz): δ13 ppm; c) FTIR (solid pellet): ν_{PH} = 2447 cm^{-1}.

[HP(*o*-EtC$_6$H$_4$)$_2$Ph][SZO$_{300}$] (3). a) $^{13}C\{^1H\}$ CP MAS NMR (125 MHz, 10 kHz): 134(*Aryl*), 70(Et$_2$O), 17(*Et$_2$O*), 4(o-CH$_2$*CH$_3$)*; b) $^{31}P\{^1H\}$ MAS NMR (125 MHz, 10 kHz): δ11pm; c) FTIR (solid pellet): ν_{PH} = 2454 cm^{-1}.

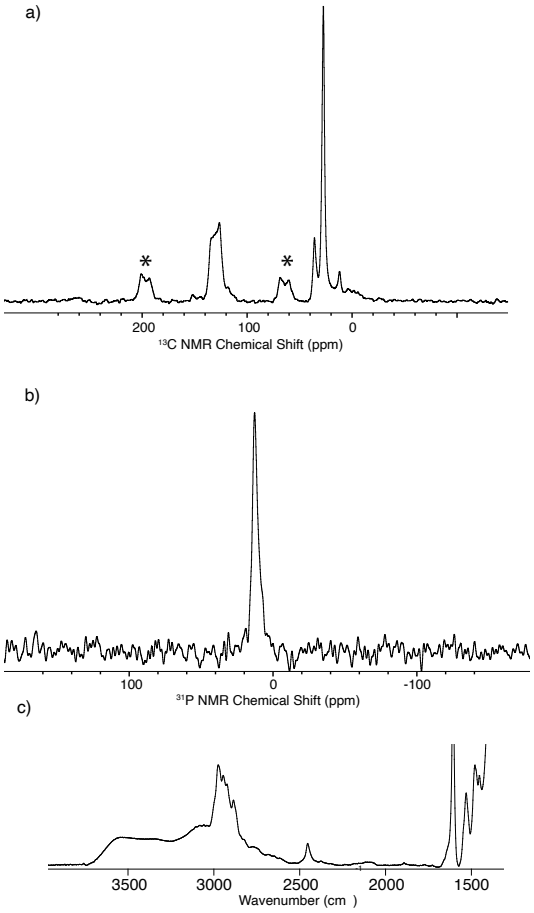

Figure 3.5.1. **[HP(o-MeC$_6$H$_4$)$_2$Ph][SZO$_{300}$] (2).** $^{13}C\{^1H\}$ CP MAS NMR; grafting reaction performed in Et_2O; 10kHz; ns = 40k; d1 = 1s; * = spinning sidebands (a); $^{31}P\{^1H\}$ MAS NMR; grafting performed in Et_2O; 10kHz; ns = 2k; d1 = 1s (b); FT-IR (c).

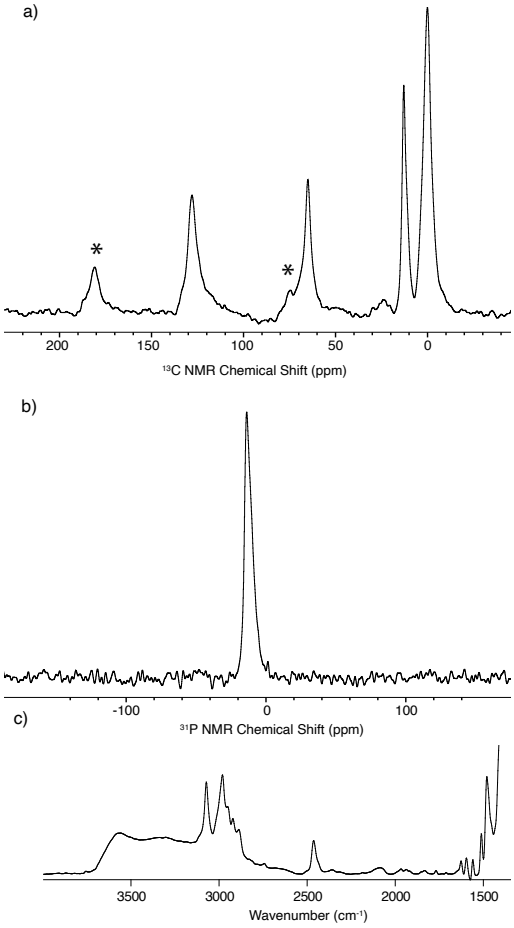

Figure 3.5.2. [HP(o-EtC_6H_4)$_2$Ph][**SZO$_{300}$**] **(3).** $^{13}C\{^1H\}$ CP MAS NMR; grafting reaction performed in Et_2O; 10kHz; ns = 40k; d1 = 1s; * = spinning sidebands (a); $^{31}P\{^1H\}$ MAS NMR; grafting performed in Et_2O; 10kHz; ns = 2k; d1 = 1s (b); FT-IR(c).

*3.5.3. Synthesis of **1Ni – 3Ni***

In an argon filled glovebox, [R_3PH]**[SZO$_{300}$]** (519mg, 0.065mmol OH) and Ni(cod)$_2$ (1.2 equiv, 21.5 mg, 0.078 mmol) were loaded into the same arm of a double-Schlenk flask connected by a frit filter. The double-Schlenk was removed from the glovebox, connected to a high vacuum line, and evacuated. Et_2O (~ 5 mL) was condensed onto the solids at 77 K. The slurry was warmed to 0°C and stirred for 1 hr. During this

period the originally white [R_3PH][**SZO$_{300}$**] evolves to an orange color and the supernatant maintains a clear yellow solution. After the respective time at room temperature the yellow solution was filtered to the other side of the double Schlenk. [Ar_3PNi(codH)][**SZO$_{300}$**] was washed by condensing Et_2O onto the solid at 77 K from the other side of the double-Schlenk. The slurry containing Et_2O and [Ar_3PNi(codH)][**SZO$_{300}$**] was warmed 0°C for 10 min, and the supernatant was filtered to the other side of the double-Schlenk. This process was repeated two more times. The volatiles were removed under vacuum (10^{-6} torr) at room temperature, the salmon colored solid was dried for 30 min under vacuum, and stored inside an argon filled glovebox at -20 °C. Analysis of the volatiles from the reaction mixture by ^{1}H NMR showed that 0.108 mmol/g COD evolved in reactions run in Et_2O.

[1-Ni(codH)][**SZO$_{300}$**] **(1Ni).** a) $^{13}C\{^1H\}$ CP MAS NMR (125 MHz, 10 kHz) δ: 164, 137, 115, 67, 56, 31, 25, 12; b) $^{31}P\{^1H\}$ MAS NMR (125 MHz, 10 kHz) δ :47ppm.

[2-Ni(codH)][**SZO$_{300}$**] (**2Ni**). a) $^{13}C\{^1H\}$ CP MAS NMR (125 MHz, 10 kHz) δ: 133, 31, 15; b) $^{31}P\{^1H\}$ MAS NMR (125 MHz, 10 kHz) δ: 47ppm.

[3-Ni(codH)][**SZO$_{300}$**] **(3Ni).** $^{13}C\{^1H\}$ CP MAS NMR (125 MHz, 10 kHz) δ : 152, 147, 131, 116, 43, 34, 28, 12; b)$^{31}P\{^1H\}$ MAS NMR (125 MHz, 10 kHz) δ: 47ppm.

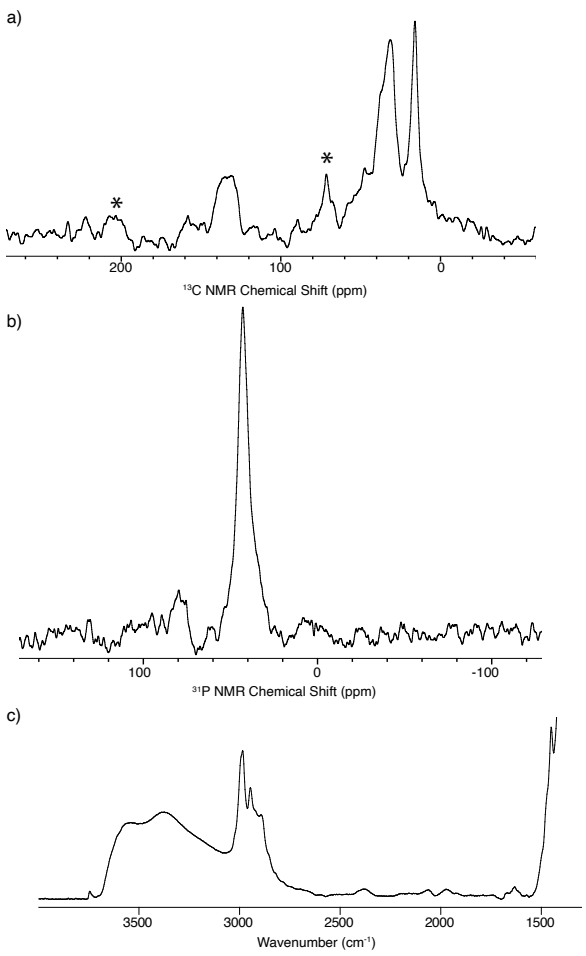

Figure 3.5.3. Analytical Data for [2-Ni(codH)][**SZO$_{300}$**] (**2Ni**). a) $^{13}C\{^{1}H\}$ CP MAS NMR; grafting reaction performed in Et_2O; 10kHz; ns = 40k; d1 = 1s; * = spinning sidebands; b) $^{31}P\{^{1}H\}$ MAS NMR; grafting performed in Et_2O; 10kHz; ns = 2k; d1 = 1s; c) FT-IR.

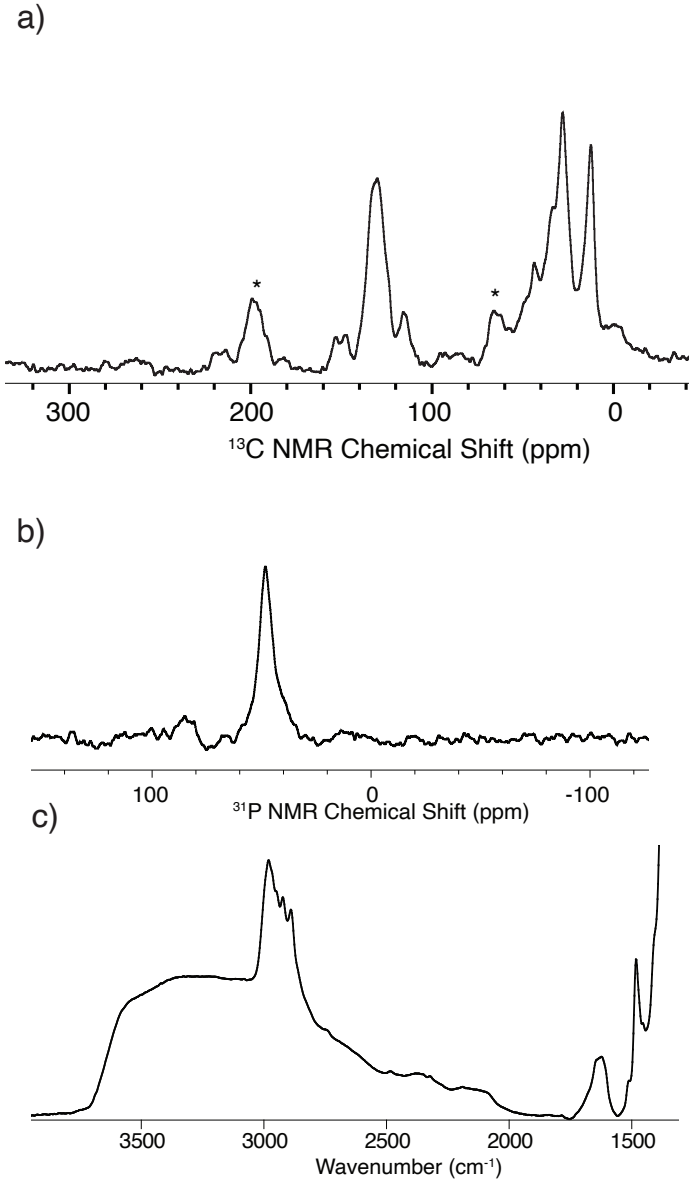

Figure 3.5.4. Analytical data for [3-Ni(codH)][**SZO$_{300}$**] (**3Ni**). a) a) $^{13}C\{^{1}H\}$ CP MAS NMR (125 MHz); grafting reaction performed in Et_2O; 10kHz; ns= 40k; d1=1s; * = spinning sidebands; b) $^{31}P\{^{1}H\}$ MAS NMR; grafting performed in Et_2O; 10kHz; ns = 2k; d1 = 1s; c) FT-IR.

*3.5.4. Quantification of active sites of **1Ni – 3Ni***

In a N_2 filled glovebox, a 12 mL liner was charged with the desired catalyst (**1Ni**) (93.1 mg, 12.1 μmol and toluene (4 mL). A known amount of a 0.1M pyridine stock solution was added to each vial to have 0.1 equiv, 0.3 equiv, 0.6 equiv, 0.9 equiv, and 1.2 equiv of pyridine:Ni. The liner was placed in the well of a Biotage parallel high-pressure reactor, the manifold was connected, and the reactor was pressurized with ethylene to the desired pressure, 150psi, and temperature, 50°C. Polymerizations were conducted with ethylene on demand for 2 hours. The reactor was vented, purged with nitrogen, and the liner containing polymer and spent catalyst was removed from the glovebox. Addition of 5% HCl in methanol (12 mL) resulted in precipitation of the polymer, which was isolated by filtration after maintaining the slurry at room temperature for 3 h. Polymers were washed with MeOH and dried under vacuum for 2 h.

Table 3.5.1. Poisoning of **1Ni** with pyridine

Entry	Equiv of pyridine	Mmol of pyridine	Yield (mg)	Activity ($g_{PE}(mol_{Ni}h)^{-1}$)
1	0.1	0.00121	69	2800
2	0.3	0.00363	50	2200
3	0.6	0.00726	20	850
4	0.9	0.01089	4	180
5	1.2	0.01452	0	0

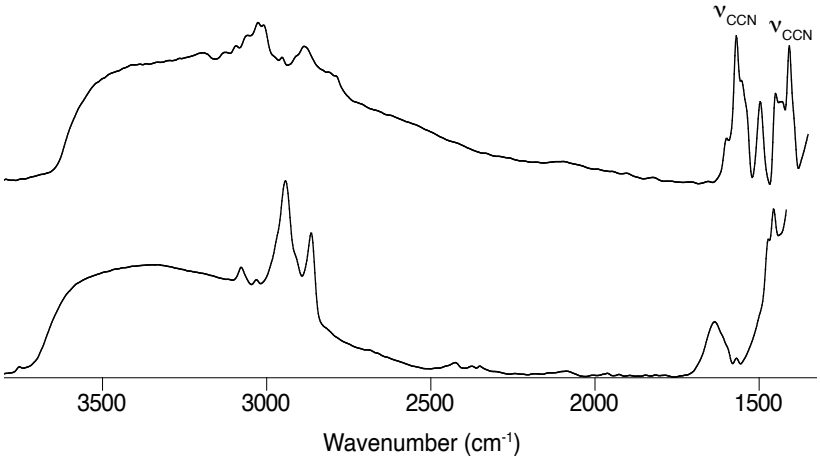

Figure 3. 5. 5. FT-IR of **1Ni** contacted with pyridine (top) and **1Ni** (bottom). The top spectrum shows two strong bands at 1606 cm^{-1} and 1444 cm^{-1} which can be attributed to absorbed pyridine.

3.5.5. Procedure for the polymerization of ethylene

In a N_2 filled glovebox, a 12 mL liner was charged with the desired catalyst (**1Ni – 3Ni**) (91.5(9) mg, 11.9(1) μmol and toluene (4 mL). The liner was placed in the well of a Biotage parallel high-pressure reactor, the manifold was connected, and the reactor was pressurized with ethylene to the desired pressure and temperature. Polymerizations were conducted with ethylene on demand for 2 hours. The reactor was vented, purged with nitrogen, and the liner containing polymer and spent catalyst was removed from the glovebox. Addition of 5% HCl in methanol (12 mL) resulted in precipitation of the polymer, which was isolated by filtered after maintaining the slurry at room temperature for 3 h. Polymers were washed with MeOH and dried under vacuum for 2 h. All polymerizations were run in triplicate and to determine average activity for each temperature and pressure.

Table 3.5.2. Optimization conditions using [3-Ni(codH)][**SZO$_{300}$**]

Entry	**Ni Loading (μmol)**	**$P_{ethylene}$ (psi)**	**T (°C)**	**Yield PE (mg)**	**Activity ($g_{PE}(mol_{Ni}h)^{-1}$)**
1	11.79(1)	100	50	12	508(0.7)
2	11.9(6)	150	50	83	3467(30)
3	12.1(2)	200	50	91	3554(573)
4	12.0(2)	250	65	80	3430(323)

Table 3.5.3. Polymerization of ethylene using Supported [R_3P-Ni(codH)][**SZO$_{300}$**]

Entry	**Phosphine**	**Yield (mg)**	**Activity ($g_{PE}(mol_{Ni}h)^{-1}$)**	**B***
1	P(*o*-$MeOC_6H_4)_2Ph$	71	3000(150)	35
2	P(*o*-$MeC_6H_4)_2Ph$	82	3400(100)	20
3	P(*o*-$EtC_6H_4)_2Ph$	80	3400(30)	24

*Branching is /1000C as calculated by ^{1}H NMR

3.5.6. NMR Spectra of polyethylene

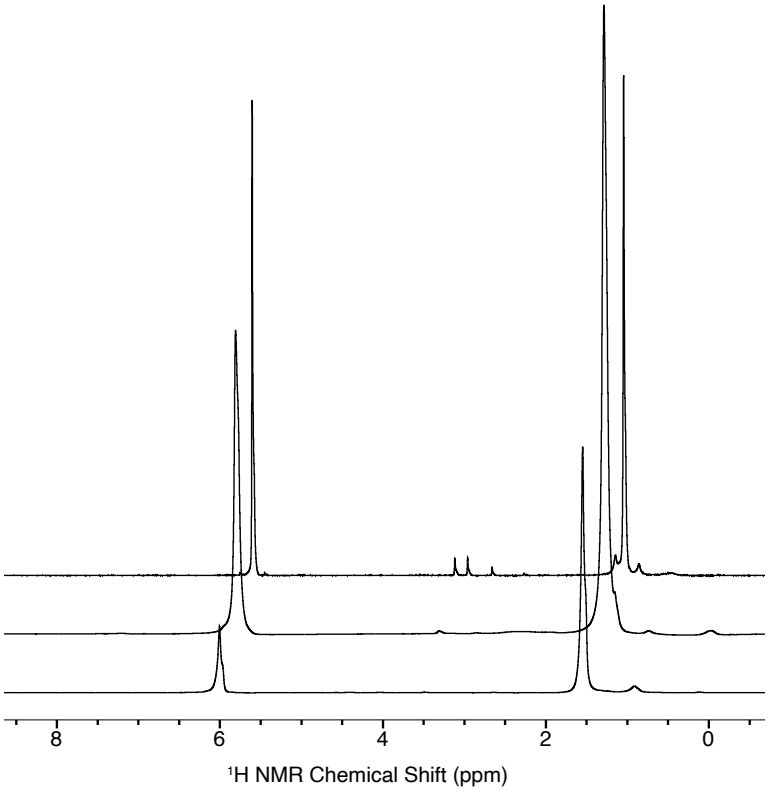

Figure 3.5.6. ^{1}H (600 MHz) NMR spectra (ns=64 in CD_2Cl_4 at 120°C) of polyethylene samples (table 3.5.3 entries 1-3).

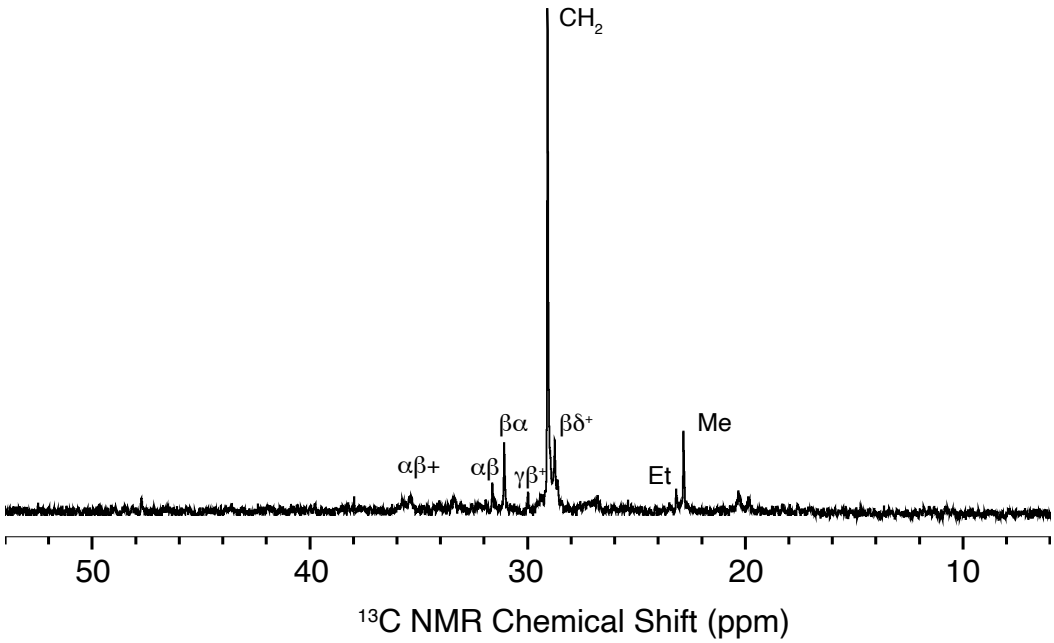

Figure 3.5.7.^{13}C (600 MHz) NMR spectra (ns=10240 in CD_2Cl_4 at 120°C) of polyethylene sample 1 (table 3.5.3 entry 1).

3.6. References

1. Ittel, S. D., Johnson, L. K. and Brookhart, M. Late-Metal Catalysts for Ethylene Homo- and Copolymerization. *Chem. Rev.* **100**, 1169–1203 (2000).

2. Muhammad, Q., Tan, C. and Chen, C. Concerted steric and electronic effects on α-diimine nickel- and palladium-catalyzed ethylene polymerization and copolymerization. *Sci. Bull.* **65**, 300–307 (2020).

3. Nakamura, A. *et al. Ortho* -Phosphinobenzenesulfonate: A Superb Ligand for Palladium-Catalyzed Coordination–Insertion Copolymerization of Polar Vinyl Monomers. *Acc. Chem. Res.* **46**, 1438–1449 (2013).

4. Chen, C. Designing catalysts for olefin polymerization and copolymerization: beyond electronic and steric tuning. *Nat. Rev. Chem. 2018 25* **2**, 6–14 (2018).

5. Nakamura, A., Ito, S. and Nozaki, K. Coordination−Insertion Copolymerization of Fundamental Polar Monomers. *Chem. Rev.* **109**, 5215–5244 (2009).

6. Tan, C. and Chen, C. Emerging Palladium and Nickel Catalysts for Copolymerization of Olefins with Polar Monomers. *Angew. Chemie* **131**, 7268–7276 (2019).

7. Conley, M. P., Jordan, R. F., Conley, M. P. and Jordan, R. F. cis/trans Isomerization of Phosphinesulfonate Palladium(II) Complexes. *Angew. Chemie Int. Ed.* **50**, 3744–3746 (2011).

8. Nakano, R. *et al.* Elucidating the Key Role of Phosphine−Sulfonate Ligands in Palladium-Catalyzed Ethylene Polymerization: Effect of Ligand Structure on the Molecular Weight and Linearity of Polyethylene. *ACS Catal.* **7**, 6101–6113 (2016).

9. Zhang, W. *et al.* Electron-Rich Metal Cations Enable Synthesis of High Molecular Weight, Linear Functional Polyethylenes. *J. Am. Chem. Soc.* **140**, 8841–8850 (2018).

10. Liang, T., Goudari, S. B. and Chen, C. A simple and versatile nickel platform for the generation of branched high molecular weight polyolefins. *Nat. Commun. 2020 111* **11**, 1–8 (2020).

11. Severn, J. R., Chadwick, J. C., Duchateau, R. and Friederichs, N. 'Bound but not gagged' - Immobilizing single-site α-olefin polymerization catalysts. *Chem. Rev.* **105**, 4073–4147 (2005).

12. Hlatky, G. G. Heterogeneous Single-Site Catalysts for Olefin Polymerization. *Chem. Rev.* **100**, 1347–1376 (2000).

13. Preishuber-Pflugl, P. and Brookhart, M. Highly active supported nickel diimine catalysts for polymerization of ethylene. *Macromolecules* **35**, 6074–6076 (2002).

14. Schrekker, H. S., Kotov, V., Preishuber-Pflugl, P., White, P. and Brookhart, M. Efficient slurry-phase homopolymerization of ethylene to branched polyethylenes using α-diimine nickel(II) catalysts covalently linked to silica supports. *Macromolecules* **39**, 6341–6354 (2006).

15. Wegener, S. L., Marks, T. J. and Stair, P. C. Design Strategies for the Molecular Level Synthesis of Supported Catalysts. *Acc. Chem. Res.* **45**, 206–214 (2011).

16. Copéret, C., Chabanas, M., Petroff Saint-Arroman, R. and Basset, J. M. Homogeneous and Heterogeneous Catalysis: Bridging the Gap through Surface Organometallic Chemistry. *Angew. Chemie Int. Ed.* **42**, 156–181 (2003).

17. Stalzer, M. M., Delferro, M. and Marks, T. J. Supported Single-Site Organometallic Catalysts for the Synthesis of High-Performance Polyolefins. *Catal. Letters* **145**, 3–14 (2015).

18. Copéret, C. *et al.* Surface Organometallic and Coordination Chemistry toward Single-Site Heterogeneous Catalysts: Strategies, Methods, Structures, and Activities. *Chem. Rev.* **116**, 323–421 (2016).

19. Marks, T. J. Surface-bound metal hydrocarbyls. Organometallic connections between heterogeneous and homogeneous catalysis. *Acc. Chem. Res.* **25**, 57–65 (1992).

20. Dorcier, A. *et al.* Preparation of a well-defined silica-supported nickel-diimine alkyl complex - application for the gas-phase polymerization of ethylene. *Organometallics* **28**, 2173–2178 (2009).

21. Popoff, N., Gauvin, R. M., De Mallmann, A. and Taoufik, M. On the fate of silica-supported half-metallocene cations: Elucidating a catalyst's deactivation pathways. *Organometallics* **31**, 4763–4768 (2012).

22. Witzke, R. J., Chapovetsky, A., Conley, M. P., Kaphan, D. M. and Delferro, M. Nontraditional Catalyst Supports in Surface Organometallic Chemistry. *ACS Catal.* **10**, 11822–11840 (2020).

23. Culver, D. B., Venkatesh, A., Huynh, W., Rossini, A. J. and Conley, M. P. Al(ORF)3 (RF = C(CF3)3) activated silica: A well-defined weakly coordinating surface anion. *Chem. Sci.* **11**, 1510–1517 (2020).

24. Millot, N., Santini, C. C., Baudouin, A. and Basset, J. M. Supported cationic complexes: selective preparation and characterization of the well-defined electrophilic metallocenium cation [SiO–B(C6F5)3]−[Cp*ZrMe2(Et2NPh)]+ supported on silica. *Chem. Commun.* **3**, 2034–2035 (2003).

25. Culver, D. B., Tafazolian, H. and Conley, M. P. A Bulky Pd(II) α-Diimine Catalyst Supported on Sulfated Zirconia for the Polymerization of Ethylene and Copolymerization of Ethylene and Methyl Acrylate. *Organometallics* **37**, 1001–1006 (2018).

26. Tafazolian, H., Culver, D. B. and Conley, M. P. A Well-Defined Ni(II) α-Diimine Catalyst Supported on Sulfated Zirconia for Polymerization Catalysis. *Organometallics* **36**, 2385–2388 (2017).

27. Dai, S. and Chen, C. A Self-Supporting Strategy for Gas-Phase and Slurry-Phase Ethylene Polymerization using Late-Transition-Metal Catalysts. *Angew. Chemie* **132**, 14994–15000 (2020).

28. Wucher, P., Schwaderer, J. B. and Mecking, S. Solid-supported single-component Pd(II) catalysts for polar monomer insertion copolymerization. *ACS Catal.* **4**, 2672–2679 (2014).

29. Drent, E., van Dijk, R., van Ginkel, R., van Oort, B. and Pugh, R. I. Palladium catalysed copolymerisation of ethene with alkylacrylates: polar comonomer built into the linear polymer chain. *Chem. Commun.* **0**, 744–745 (2002).

30. Drent, E., van Dijk, R., van Ginkel, R., van Oort, B. and Pugh, R. I. The first example of palladium catalysed non-perfectly alternating copolymerisation of ethene and carbon monoxide. *Chem. Commun.* **0**, 964–965 (2002).

31. Rodriguez, J., Culver, D. B. and Conley, M. P. Generation of Phosphonium Sites on Sulfated Zirconium Oxide: Relationship to Brønsted Acid Strength of Surface -OH Sites. *J. Am. Chem. Soc.* **141**, 1484–1488 (2019).

32. Peuckertt, M. and Keim, W. A new nickel complex for the oligomerization of ethylene. *Organometallics* **2**, 594–597 (2002).

33. Vela, J., Lief, G. R., Shen, Z. and Jordan, R. F. Ethylene Polymerization by Palladium Alkyl Complexes Containing Bis(aryl)phosphino-toluenesulfonate Ligands. *Organometallics* **26**, 6624–6635 (2007).

34. Arthur Bennett, M. and A. Longstaff, P. Reaction of rhodium halides with tri-o-tolylphosphine and related ligands. Complexes of divalent rhodium and chelate complexes containing rhodium-carbon .sigma. and .mu. bonds. *J. Am. Chem. Soc.* **91**, 6266–6280 (2002).

35. Zhou, H., Zhang, J., Yang, H., Xia, C. and Jiang, G. Rhodium-Catalyzed Double Alkyl-Oxygen Bond Cleavage: An Alkyl Transfer Reaction from Bis/Tris(o-alkyloxyphenyl)phosphine to Aryl Acids. *Organometallics* **35**, 3406–3412 (2016).

Chapter 4. Hydroboration of Nitrogen containing heterocycles by a supported Ir catalyst on sulfated zirconia

4.1. Abstract

Dihydropyridines (DHP) are an important subset of compounds that are found in naturally occurring molecules as well as pharmacologically active molecules. There have been many stoichiometric methods that have been discovered for the formation of DHPs, but many of these methods can require numerous steps, harsh reaction conditions, or preactivation of the pyridines.[1] Catalytic reduction reactions of pyridines employing mild reducing agents have been reported with many of these reactions consisting of pyridine coordinating to a Lewis acid center under catalytic conditions followed by a hydride addition occurring at the C4 or C2 position of the *in situ* activated pyridine. This chapter will explore metalation of $[R_3PH][\mathbf{SZO_{300}}]$ sites with Ir(III) organometallics resulting in catalysts that are active for the hydroboration of nitrogenous heterocycles

4.2. Introduction

The direct functionalization of pyridines remains a significant challenge due to poor chemoselectivity and pyridine having a lower energy of the π-system with respect to benzene. Despite this, pyridines are one of the most prevalent motifs found in pharmaceutical, agrochemical, and material science targets, Figure 4.2.1. Despite their utility, there are intrinsic challenges when trying to develop a controlled reduction process

especially when trying to access di- or tetrahydropyridines such as: i) the dearomatization process is kinetically and thermodynamically unfavorable due to the resonance stabilization of the N-aromatic core ii) the differential thermodynamic stability between 1,2- and 1,4-dihydropyidines is marginal; and iii) the resulting hydropyridines possessing alkenyl unit(s) can undergo rearomization and/or side reactions.

Due to these challenges, silicon- and boron-based reducing agents (e.g. hydrosilanes and hydroboranes) have become competitive alternatives to H_2 in catalytic reduction chemistry.[4] There are several advantages to applying these reducing agents: i) no special equipment is required; ii) reactions proceed under relatively mild conditions; iii) subtle steric and electronic variations of the reducing agents allows for fine tuning the chemoselective reduction of N-aromatic compounds; and iv) introducing silicon or boron moiety into products could allow for further chemical transformations. This has led to recent efforts focusing on increasing selectivity and functional group tolerance notably with systems using Magnesium[2] or Rhodium.[5]

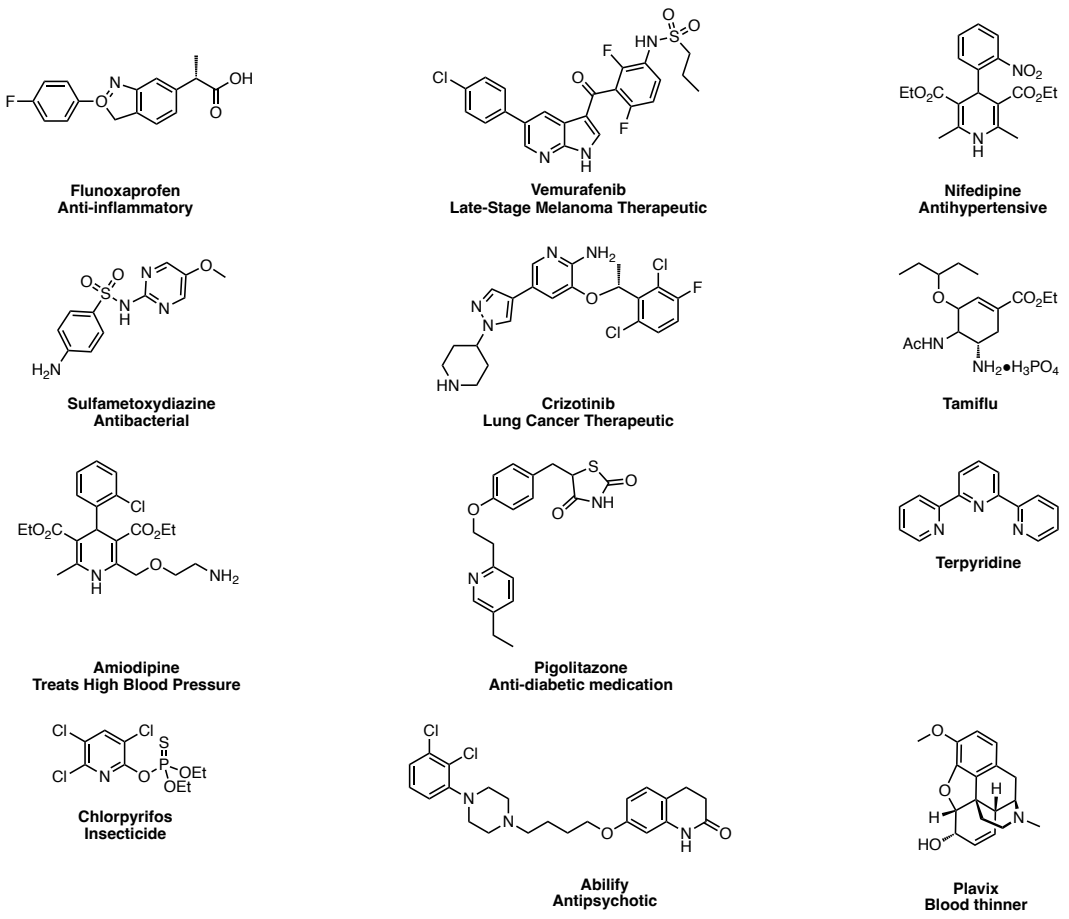

Figure 4.2.1. Selected examples of natural products and pharmaceuticals where dihydropyridines are used as synthetic motifs

Working modes of catalysts for the hydroboration of pyridines can be divided into outer- and inner-sphere pathways, which are closely related to the regio-outcomes of the products. Lewis acids are known to promote 1,4-hydroboration products via an outer-sphere pathway where a borenium species is typically involved, Figure 4.2.2. 1,2-hydroboration occurs within an inner-sphere pathway where insertion of the insertion of C=N of pyridines occurs into the M–H bond, Figure 4.2.2.

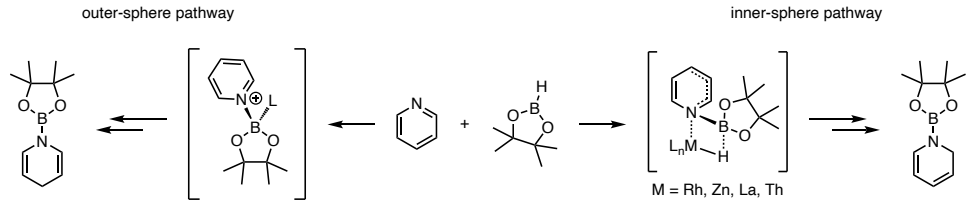

Figure 4.2.2. Outer-sphere pathway (left) shows the formation of a borenium intermediate to give the 1,4-proudct and the inner-sphere pathway (right) shows the formation the insertion of C=N into a M – H bond to give the 1,2-product

Since Harrod and coworkers seminal work,[6] several catalytic reactions for hydrosilylation using metal catalysts or $B(C_6F_5)_3$ have been reported. [7–14] It was not until 2011 when the first catalytic hydroboration of pyridines was reported. Hill and coworkers reported the use of a magnesium catalyst that produced both the 1,2– and 1,4– DHP derivatives, Figure 4.2.3.[2] Since this seminal report, there have been many strides made. Suginome and coworkers used a rhodium catalyst to achieve selective 1,2– hydroboration of pyridines.[3] Delferro and Marks reported pyridine hydroboration with complete selectivity to the 1,2– DHP derivative using an organolanthanide catalyst.[14] Gunanthan and coworkers achieved 1,4–DHP selectivity using a Ruthenium based catalyst. [15] Wang and Li et al. reported the first metal free 1,4–hydroboration reaction using a bulky organoborane.[16]

Recent efforts have focused on unprecedented systems for the hydroboration of N-heteroarenes. Lin and coworkers synthesized a trivalent Zr or Hf hydride centers that are coordinately unsaturated, and electronically unique. These homogeneously inaccessible sites were stabilized by both framework rigidity and site isolation effect.[17,18] Park and Chang reported that KO^{t}Bu catalyzed the hydroboration of N–heteroarenes with a high selectivity for the 1,4–DHP.[19]

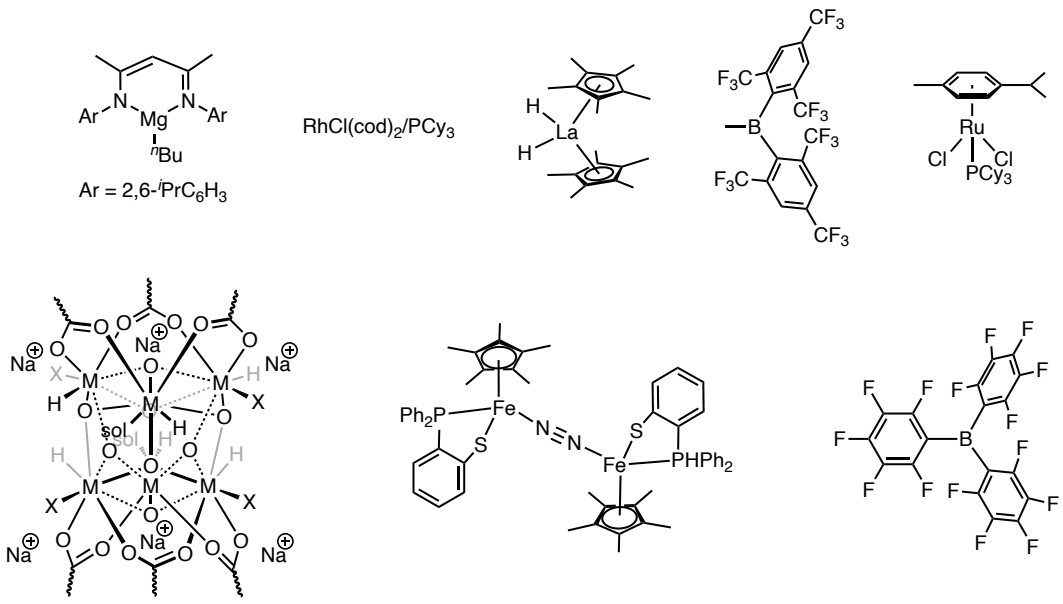

Figure 4.2.3. Selected examples of catalysts for hydroboration reaction

Additionally, Park and Chang reported the double hydroboration of quinolines to yield tetrahydroquinolines with a sp^3 C–B bond β to the nitrogen atom.[20] Wang and coworkers reported a dinitrogen-bridged diiron complex that bears a bidentate ligand based on P and S that is active in hydroboration of N – heteroarenes.[21] The selected examples above illustrate the diversity of previously reported systems that highlight the relationship between the working mode and the relationship to chemo-, regio-, and stereooutcomes.

Although these systems are variable, the metal hydride species that afford the 1,2–regioisomers as a major product undergo a C=N unit insertion into the M–H bond in the inner-sphere of the catalytic species, Scheme 4.2.2. However, if there is limited proximity of the M–H moiety to the C2-position of activated N-heteroarenes then 1,4–regioselectivity can be achieved. There are many systems for the hydroboration of pyridine with the reactions generally proceeding under mild conditions. These low energy barriers can be

attributed to the active catalytic species ability to abstract the hydride from HBpin. Additionally, the Lewis Acidic boron center of hydroborane reducing agents can undergo interactions with the lone pairs of substrates and catalyst ligands causing the B–H bond to be more activated. In the case of metal-free acid catalysts systems, the active catalytic species and pyridine substrate act as a frustrated Lewis pair. Metal-free base catalysts react directly with pyridine or Hbpin to facilitate hydride transfer to the pyridine substrate.

Although there is a wide-variety of systems available for the hydroboration of N-heteroarenes, there are no reported heterogeneous well-defined systems to the best of *our* knowledge. This chapter describes the synthesis and reactivity of [Ircodpy][**SZO$_{300}$**] for the hydroboration of N-heteroarenes via two independent pathways.

4.3. Results and Discussion

*4.3.1. Synthesis of [Ir(cod)(^{t}Bu)$_2$Ph][**SZO$_{300}$**]*

The reaction of di-tert-butylaryl phosphines with the Brønsted sites on **SZO$_{300}$** is expected to form [(^{t}Bu)$_2$ArPH][**SZO$_{300}$**]. Reacting [(^{t}Bu)$_2$PhPH][**SZO$_{300}$**] with [Ir(cod)(OSi(O^{t}Bu)$_3$]$_2$ forms [Ir(cod)P(^{t}Bu)$_2$Ph][**SZO$_{300}$**]. This reaction evolves 0.095 mmol/g of HOSi(O^{t}Bu)$_3$. The FTIR spectrum of **1-Ir** lacks the lacks the ν_{PH} stretch at 2439 cm^{-1} seen in [(^{t}Bu)$_2$ArPH][**SZO$_{300}$**], Figure 4.3.1d. Additionally, the ^{31}P{^{1}H} NMR of **1-Ir** contains a new signal at 37 ppm, which is 12ppm downfield from that of [(^{t}Bu)$_2$PhPH][**SZO$_{300}$**], Figure 4.3.1.c. The ^{13}C{^{1}H} MAS NMR of **1-Ir** contains signals at

139, 128, 32, and 30, for *Ar*, *cod*, and *$^{t}Bu_2$* respectively, Figure 4.3.1.a. This indicates that the phosphonium reacts with [Ir(cod)(OSi(O^{t}Bu)$_3$]$_2$ reacts to form **1-Ir**.

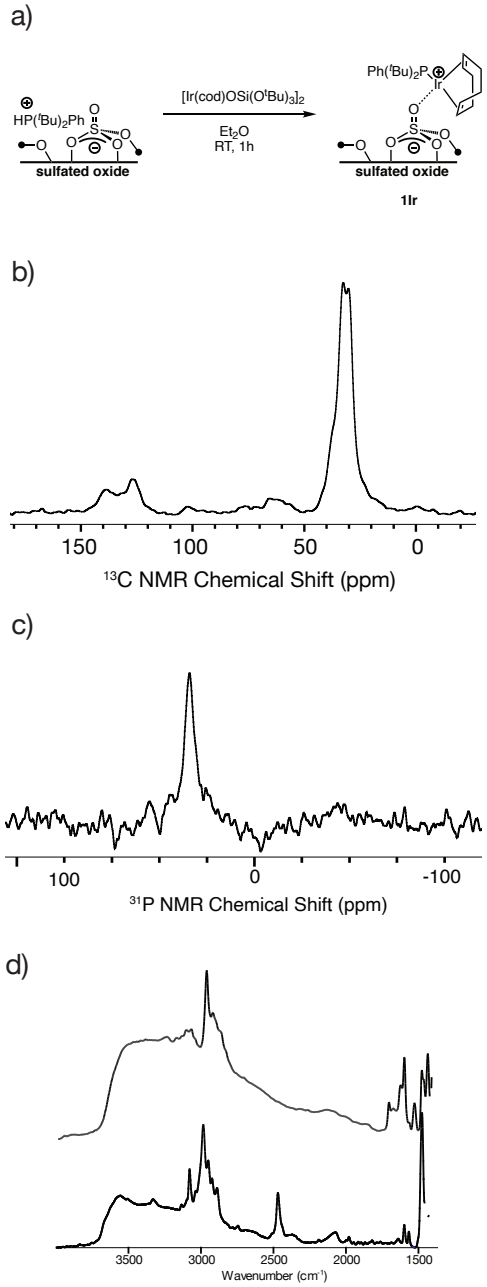

Figure 4.3.1. Reaction scheme of [(^{t}Bu)$_2$PhPH][**SZO$_{300}$**] and [Ir(cod)(OSi(O^{t}Bu)$_3$]$_2$ to form [Ir(cod)(^{t}Bu)$_2$Ph][**SZO$_{300}$**] (a); ^{13}C{^{1}H} CP MAS NMR; grafting reaction performed in Et$_2$O; 10kHz; ns = 80k; d1 = 1s; * = spinning sidebands (b); ^{31}P{^{1}H} MAS NMR; grafting performed in Et$_2$O; 10kHz; ns = 2k; d1 = 1s (c); FT-IR (d).

*4.3.2. Synthesis of [Me_3Si][**SZO_{300}**]*

Reacting **SZO_{300}** with $ClSiMe_3$ generates [Me_3Si][**SZO_{300}**]. The $^{29}Si\{^1H\}$ NMR of [Me_3Si][**SZO_{300}**] is complex, 4.3.2a. Signals at 52 and 41 ppm are characteristic of silylium-like fragment and assigned to [Me_3Si][SZO_{300}].[22] Signals at -83.5, -94, -103 which are characteristic of SiO_x which is known to form in reactions that generate silylium like fragments on **SZO_{300}**.[23] The signal at -1 ppm is assigned to covalent $Me_3Si–O_X$ sites that are commonly observed on oxides that are not weakly coordinating. Signals at 22, 17, and 12 ppm are also likely associated with $Me_3Si–O_X$ sites on the SZO_{300} surface. The $^{13}C\{1H\}$ NMR contains a signal at 0ppm which is for [*Me_3*Si][**SZO_{300}**], Figure 4.3.2.b. The FTIR spectrum shows υ_{CH} stretches at 2958, and 2922 cm^{-1}, Figure 4.3.2.c. This is consistent with the formation of [Me_3Si][**SZO_{300}**].

*4.3.3. Synthesis of **2Ir** (Halide Abstraction pathway)*

$[Ir(cod)Cl]_2$ reacts with pyridine at 0°C to form Ir(cod)pyCl as a bright yellow powder.[24] Reacting [Me_3Si][**SZO_{300}**] with Ir(cod)pyCl forms [Ir(cod)Py][**SZO_{300}**]. This reaction evolves 0.11 mmol/g of $ClSiMe_3$. The FTIR spectrum of **2-Ir** shows the υ_{CH} at 2970 cm^{-1}, 2903 cm^{-1}, and 2869 cm^{-1}, Figure 4.3.3.c. The $^{13}C\{^1H\}$ MAS NMR of **2Ir**, Figure 4.3.3.a, contains signals at 153 ppm, 140 ppm, and 128 ppm, which correspond to *o*-$C_{pyridine}$, *m*-$C_{pyridine}$, and *p*-$C_{pyridine}$, respectively. This indicates that [Me_3Si][**SZO_{300}**] reacts with Ir(cod)pyCl to form [Ir(cod)Py][**SZO_{300}**].

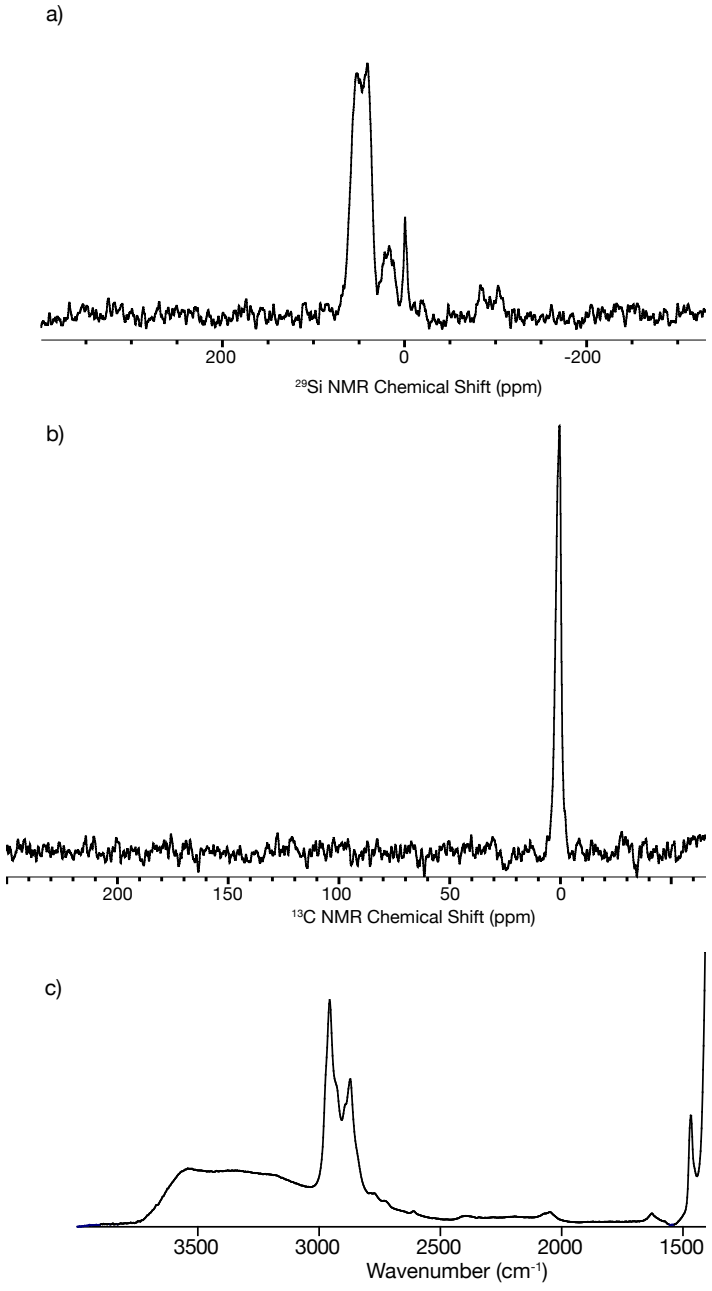

Figure 4.3.2. Characterization data of [Me_3Si][**SZ0$_{300}$**] a) $^{29}Si\{^1H\}$ CP MAS NMR: 8 kHz; ns = 8k, d1 = 2s; b) $^{13}C\{^1H\}$ CP MAS NMR: 10kHz; ns = 40k; d1 = 2s; c) FT-IR (solid pellet)

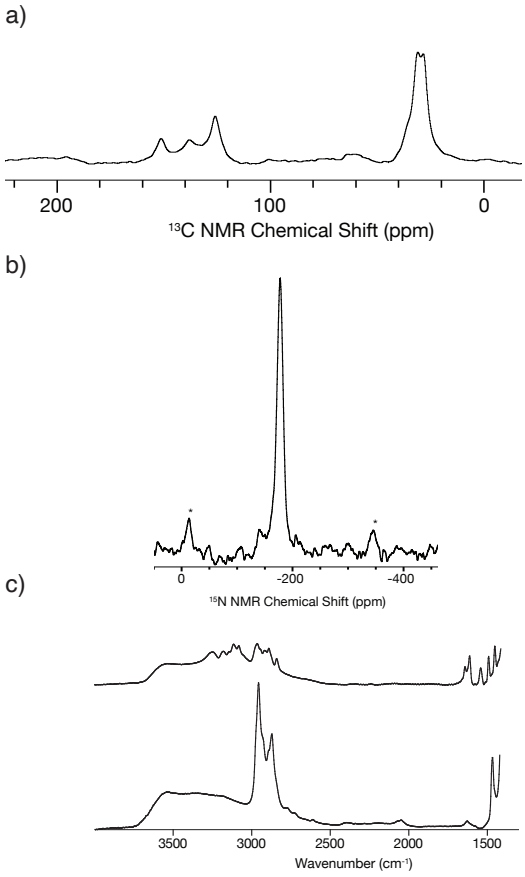

Figure 4.3.3. Characterization data of **2Ir** a) $^{13}C\{^{1}H\}$ CP MAS NMR: 10kHz; ns = 40k; d1 = 2s; b) ^{15}N CP MAS NMR: 10kHz; ns = 5k; d1 = 2s; * = spinning sidebands; c) FT-IR stack of $[Me_3Si][\mathbf{SZO_{300}}]$ (bottom) and **2Ir** (top).

*4.3.4. Synthesis of **2Ir-^{15}N***

$[Ir(cod)Cl]_2$ reacts with ^{15}N-pyridine at 0°C to form Ir(cod)(^{15}N-py)Cl as a bright yellow powder. Reacting $[Me_3Si][\mathbf{SZO_{300}}]$ with Ir(cod)(^{15}N-py)Cl forms [Ir(cod)(^{15}N-Py)][$\mathbf{SZO_{300}}$], **2Ir-^{15}N**. The $^{15}N\{^{1}H\}$ CPMAS NMR contains one signal at -179 ppm corresponding to one species present, Figure 4.3.4b. The FT-IR spectrum of **2Ir** and **2Ir-^{15}N** contain strong ν_{CCN} stretches at 1609 and 1450 cm^{-1} for **2Ir**, which shifts to 1601 and 1442 cm^{-1} for **2-Ir^{15}N**, Figure 4.3.4a.

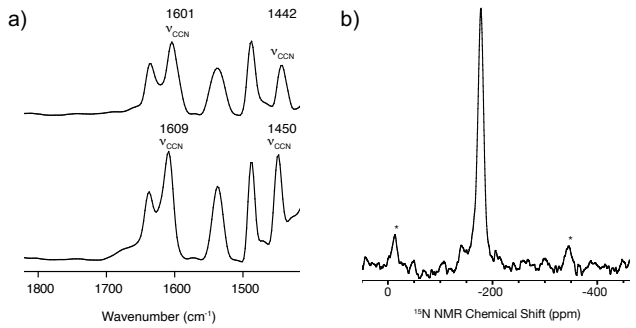

Figure 4.3.4. a) FTIR showing **2Ir** (bottom) and **2Ir-^{15}N** (top); b) ^{15}N{^{1}H} CPMAS NMR of **2Ir-^{15}N**

4.3.5. Dearomatization hydroboration of N-containing heteroatoms

4.3.5.1. Reactivity with pyridine

Figure 4.3.5 shows the conversion of pyridine in the presence of 1mol% of **2Ir**. Monitoring the reaction over time shows that **2a** forms without a noticeable induction period, and is formed in preference to **2b**. However, **2b** is favored over with longer reaction times. After 3 days, **2Ir** gives a 77% yield of borylated products favoring **2b** over **2a** (**2b**:**2a** 1:10). Removal of **2Ir** by filtration in 12h results in 18% conversion to **2a** and **2b**. Heating this mixture at 85 °C for one week does not result in further conversion of pyridine nor a change in the ratio of **2b**:**2a**. This result indicates that there is no desorption of a catalytically active species, and that **2Ir** is responsible for the isomerization of **2a** to **2b**.

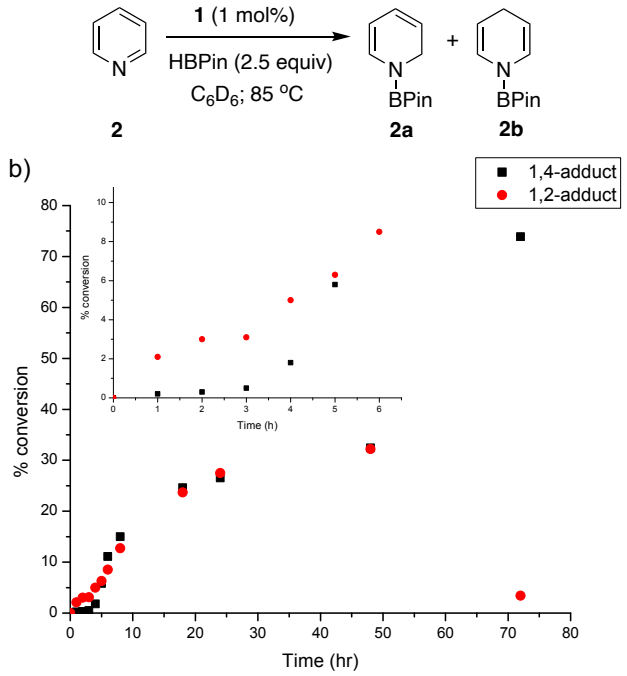

Figure 4.3.5. Reaction of pyridine with **2Ir** to from **2a** and **2b** (a) conversion vs time plot showing the product selectivity over the course of 3 days (b)

4.3.5.2. Reactivity of mono- and di-substituted pyridines

2Ir catalyzes the dearomatization hydroboration of N-containing heteroatoms in the presence of HBpin at 85°C over the course of 2 days. Scheme 4.3.1 shows the wide range of 1,2-dihydropryidines produced under these conditions. 2-phenylpyridine and 2-methoxypyridine failed to undergo hydroboration whereas 2-methylpyridine and 4-methylpyridine resulted to give a 1:10 ratio favoring the 1,4–borylated product. 3-methoxyprydine, 3-methylpyridine, 4-phenylpyridine, and 4 – tBu-pyridine give only 1,2-borylated products. 3-phenylpyidine reacts to give a mixture containing both isomers that are products of 1,2-borylation and the 1,4-borylation product.

The reaction of quinoline proceeded to yield only the 1,2-dihyrdopyrdine exclusively with a yield of 76%. *N*-methylbenzimdiazole was subjected to catalytic conditions to give 90% yield of the 1,2-reduced product in 2 hours. Acridine was dearomatized under these catalytic conditions in good yield as well.

Experiments showed that halogenated pyridines or 2-substitued pyridines were not compatible with this method. CN substituted groups underwent side reactions instead of the hydroboration reaction.

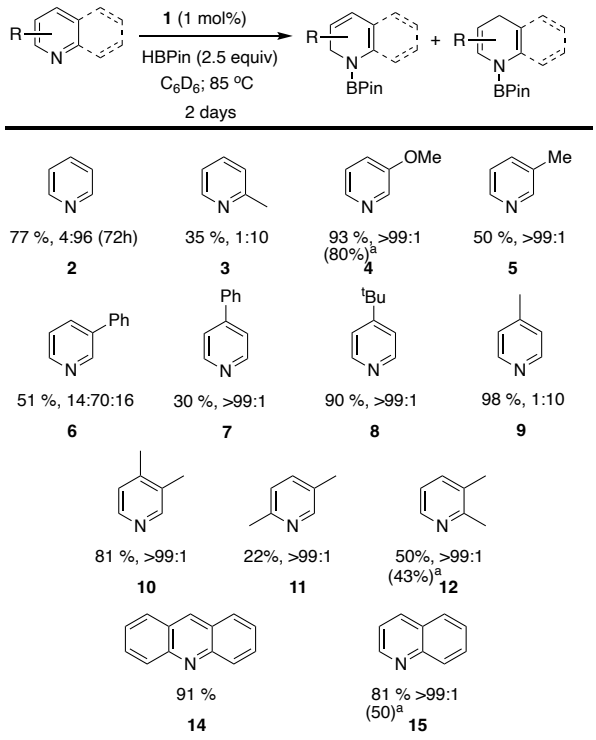

Scheme 4.3.1. Reactivity of pyridines and N-methylimdazole with HBpin and Catalyst **2Ir**

4.3.5.3. Reactivity of pyrazines

The doubly hydroborated products of pyrazines were produced in good yields. The reaction of pyrazine and Hbpin occurs in the absence of a transition metal catalyst.[25] The double hydroboration of pyrazine by **2Ir** is comparable to the double hydroboration in the absence of a transition metal catalyst. 2-methoxypyrazine (**18**) reacts with **2Ir** and HBpin to give the *N,N'*-diboryl-2-methoxy-1,2-dihydropyrazine product. **2Ir** also catalyzes the borylation of of *N*-methylimidazole (**19**) to give the reduced products in good yield in only 2h.

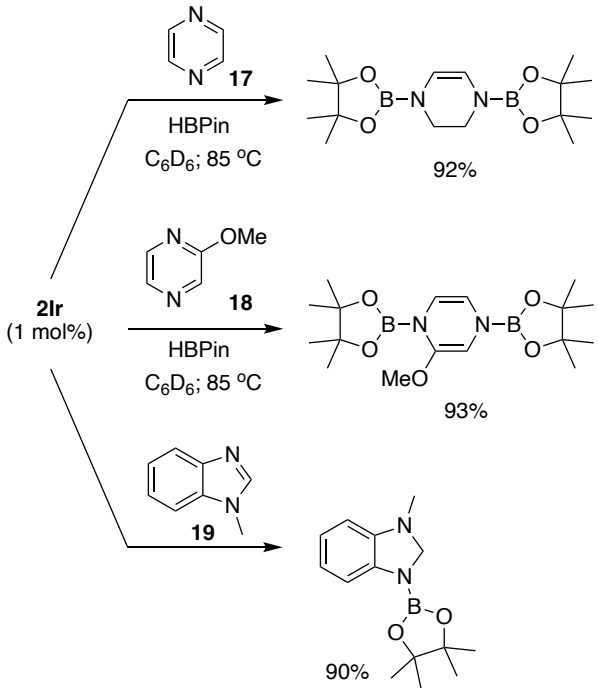

Scheme 4.3. 2. Reactivity of pyrazines and N-methylimidazole with HBpin and catalyst **2Ir**

4.3.6. Control Reactions

Heating pyridine, HBpin, and **SZO$_{300}$** in C_6D_6 over the course at 85°C over the course of 3 days results in low conversion of pyridine and to a 1:2 mixture of 1,2- and 1,4-DHP product. Additionally, this supported catalyst is needed for a clean reaction. Mixtures of $[Ir(cod)Cl]_2$ and AgOTf in the presence of pyridine and HBpin results in 4% yield of 1,4-DHP product over the course of three days.

4.4. Conclusions

Well-defined Iridium sites supported on **SZO$_{300}$** are accessible via two complementary synthetic methods. ^{15}N MAS NMR and FTIR spectroscopy are consistent with the formation of **2Ir** which contains a moderately Lewis Acidic Iridium site. **2Ir** is active for the dearomative borylation of pyridines. Additionally, **2Ir** shows similar reactivity for pyrazines and N-methylimidazole. **2Ir** shows comparable catalytic behavior to homogeneous catalysts, however improvements of **2Ir** would be needed to be applicable under flow conditions. The halide abstraction methodology used to generate **2Ir** provides a general strategy to form well-defined heterogeneous catalysts from readily available organic precursors that could generate active sites for a variety of reactions that are important for small molecule synthesis.

4.5. Materials and Methods

4.5.1. General Considerations

All reactions and manipulations were performed under an inert atmosphere of nitrogen or argon using standard Schlenk techniques. C_6D_6 was purchased from Cambridge Isotope Laboratories, dried over Na/benzophenone, freeze-pump-thawed three times, and distilled under vacuum. Solvents were purchased from Fisher Scientific, dried by passing through a double-column J. C. Meyer solvent system and degassed before use. Et_2O was dried over Na/benzophenone, and distilled under vacuum before use. SZO_{300}[26], ≡Si–OH···Al$(OR^F)_3$[27], [Ir(cod)O(Si$(O^tBu)_3]_2$[28] were previously described. Other chemicals were purchased from standard suppliers. Hexamethylbenzene was sublimed before use. All heteroatoms were distilled prior to use. Solution NMR spectra were recorded on a Bruker Avance 300 MHz spectrometer and referenced to C_6D_5H peak at 7.16 ppm. Solid-state NMR experiments were performed on a 600 MHz Bruker NEO spectrometer in 4 mm zirconia rotors packed in an argon filled glovebox. ^1H, $^{13}C\{^1H\}$ CPMAS NMR, $^{15}N\{^1H\}$ CPMAS, and $^{11}B\{^1H\}$ Hahn Echo MAS spectra were recorded in 4 mm zirconia rotors at 10 KHz magic angle spinning speed. FT-IR spectra were recorded as pressed pellets using a Bruker Alpha IR spectrometer in an argon-filled glovebox.

*4.5.2. Synthesis of [Ir(cod)(^{t}Bu)$_2$Ph][**SZO$_{300}$**]*

[HPR_3][**SZO_{300}**] (1.0g, 0.13mmol OH) and [Ir(cod)OSi$(O^tBu)_3]_2$ (1.2 equiv Ir, 87.9 mg, 0.078mmol) were loaded into the same arm of a double-Schlenk flask connected by a frit filter in an argon filled glovebox. The double-Schlenk was sealed, removed from the

glovebox, connected to a high vacuum line equipped with a single stage diffusion pump, and evacuated. Et_2O (~ 5 mL) was condensed onto the solids at 77 K. The slurry was warmed to room temperature. During this period the originally white [HPR_3][**SZO$_{300}$**] evolves to an orange color and the supernatant maintains a light-yellow solution. After stirring for 1 h at room temperature the yellow solution was filtered to the other side of the double Schlenk flask. [Ir(cod)($P^tBu)_2$Ph][**SZO$_{300}$**] was washed by condensing Et_2O onto the solid at 77 K from the other side of the double-Schlenk flask. The slurry containing Et_2O and [Ir(cod)($P^tBu)_2$Ph][**SZO$_{300}$**] was warmed to room temperature, stirred for 10 min, and the supernatant was filtered to the other side of the double-Schlenk flask. This process was repeated two more times. The volatiles were removed under vacuum (10^{-6} torr) at room temperature, the dark-orange colored solid was dried for 30 min under diffusion pump vacuum, and stored inside an argon filled glovebox at -20 ^oC. Analysis of the volatiles from the reaction mixture by ^1H NMR showed that 0.095 mmol/g $HOSi(O^tBu)_3$ was generated.

*4.5.3. Synthesis of **2Ir***

[Me_3Si][**SZO$_{300}$**] (1.0g, 0.13mmol OH) and Ir(cod)pyCl (1.2 equiv, 64.7 mg, 0.156mmol) were loaded into the same arm of a double-Schlenk flask connected by a frit filter in an argon filled glovebox. The double-Schlenk was sealed, removed from the glovebox, connected to a high vacuum line equipped with a single stage diffusion pump, and evacuated. Et_2O (~ 5 mL) was condensed onto the solids at 77 K. The slurry was warmed to room temperature. During this period the originally white [Me_3Si][**SZO$_{300}$**] evolves to an orange color and the supernatant maintains a light-yellow solution. After

stirring for 1 h at room temperature the yellow solution was filtered to the other side of the double Schlenk flask. **2Ir** was washed by condensing Et_2O onto the solid at 77 K from the other side of the double-Schlenk flask. The slurry containing Et_2O and **2Ir** was warmed to room temperature, stirred for 10 min, and the supernatant was filtered to the other side of the double-Schlenk flask. This process was repeated two more times. The volatiles were removed under vacuum (10^{-6} torr) at room temperature, the orange colored solid was dried for 30 min under diffusion pump vacuum, and stored inside an argon filled glovebox at -20 ^{o}C. Analysis of the volatiles from the reaction mixture by ^{1}H NMR showed that 0.11 mmol/g $ClSiMe_3$ was generated.

4.5.4. Filtration Experiment

0.01mmol of **2Ir** was added to a J. Young NMR tube in a nitrogen filled glovebox. To this flask, 1.0 mmol heteroarene (1.0 equiv) and 2.5mmol HBPin (2.5 equiv.) were added, respectively, ~0.5 mL C_6D_6, and a known amount of hexamethylbenzene was used as an internal standard. The flask was sealed, and allowed to heat at 85°C for 12h. After 12h, the reaction slurry was filtered off over a frit under a N_2 atmosphere. The solution was stored inside a clean J. Young NMR tube and monitored for 1week.

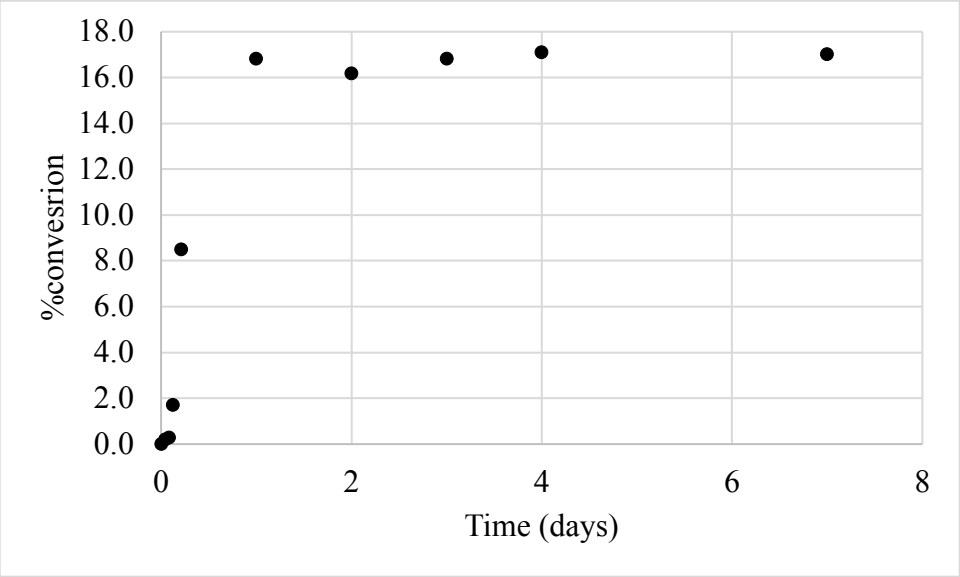

Figure 4.5.1. Plot of time vs % conversion for filtration experiment.

4.5.5. Contacting 1Ir with pyridine

150 mg of [Ir(cod)(P^{t}Bu)$_2$Ph][**SZO$_{300}$**] (1.00 equiv, 0.0165 mmol) was loaded into a J. Young NMR tube in a Nitrogen filled glovebox. 1.2 μL (1.0 equiv, 0.0165 mmol) pyridine and ~0.5mL C_6D_6 was syringed into the NMR tube. The slurry was allowed to sit for 2h at room temperature, and monitored by ^{1}H NMR. Analysis of the reaction by ^{1}H NMR showed that 0.095 mmol/g P^{t}Bu$_2$Ph was present in solution.

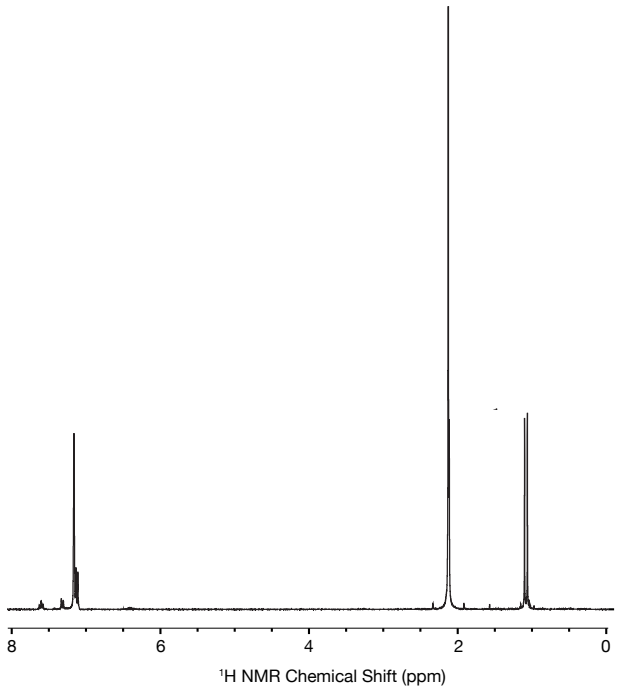

Figure 4.5. 2. ^{1}H NMR of the reaction of **1** with pyridine (1.0 equiv.). Pyridine: 8.53(m, $C_{H2,6}$), 6.98(m, C_{H4}), and 6.66(m, $C_{H3,5}$). Hexamethylbenzene: 2.11(s). P^{t}Bu$_2$Ph: 7.59(m, Ar), 7.31(d, Ar), 1.07(d, C(CH$_3$)$_3$).

4.5.6. General procedure for hydroboration of pyridines

0.01mmol of desired catalyst (**2-Ir**) was added to a J. Young NMR tube in a nitrogen filled glovebox. To this flask, 1.0 mmol heteroarene (1.0 equiv) and 2.5mmol HBPin (2.5 equiv.) were added respectively, ~0.5 mL C_6D_6, and a known amount of hexamethylbenzene were added. The flask was sealed, and allowed to heat at 85°C for the desired time (typically 2d). The reaction was monitored periodically via ^{1}H NMR.

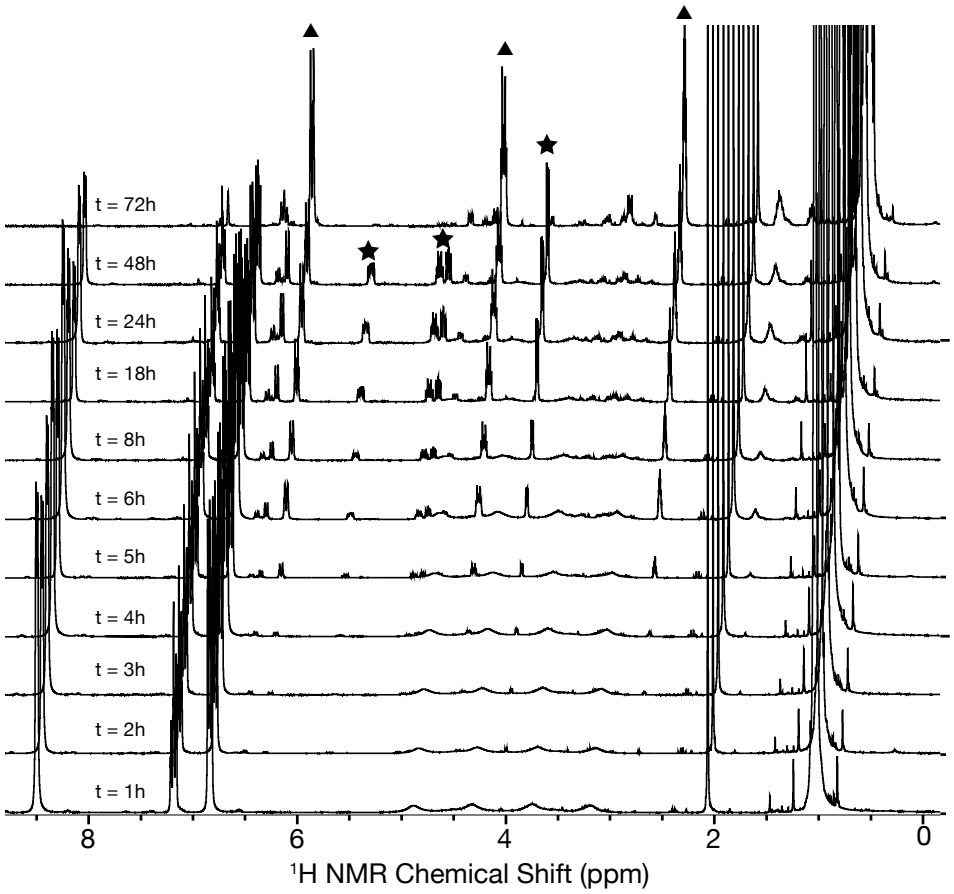

Figure 4.5. 3. ^{1}H NMR of the reaction of pyridine and Hbpin with **2-Ir** (1.0 mol%) over the course of three days under general reaction conditions; ▲ = N-{B(OCMe$_2$)$_2$}-1,4-dihydropyridine and ★ = N-{B(OCMe$_2$)$_2$}-1,2-dihydropyridine product peaks.

4.5.7. Characterization of products

2a: The general procedure was conducted with pyridine. The ^{1}H NMR spectrum matched those in the literature.[2] ^{1}H NMR (300 MHz, C_6D_6) δ: 6.70(dt, 1H, *H*-4, ^{3}J = 7.4Hz, ^{4}J = 1.3 Hz), 5.80(ddq, 1H, *H*-3, ^{3}J = 9.3 Hz, ^{4}J = 1.3Hz) 5.10 (dtt, 1H, *H*-2, ^{3}J =7.4 Hz, ^{3}J = 4.3,^{4}J = 1.3 Hz), 5.05(dd,1H, *H*-5, ^{3}J = 5.4Hz, ^{4}J = 1.3Hz), 4.14 (dd, 2H, *H*-1, ^{3}J = 4.3 Hz, ^{4}J = 1.6Hz), 1.00(s, 12H, C*H*$_3$-pin). ^{11}B NMR (96 Hz, C_6D_6) δ: 27.0(s). **2b:** ^{1}H NMR (300 MHz,

C_6D_6) δ: 6.51(dquint, 2H, *H*-1, ^3J = 7.4 Hz, ^4J = 1.6 Hz), 4.56 (dtt, 2H, , *H*-2, ^3J = 8.4 Hz, ^3J = 3.2Hz, ^4J = 1.6Hz), 2.81(tt, 2H, *H*-3, ^3J = 3.2Hz, ^4J = 1.6 Hz), 0.96 (s, 12H, C*H*$_3$-pin). ^{11}B NMR (96 Hz, C_6D_6) δ: 27.0(s)

3a: The general procedure was conducted with 2-methylpyridine. The ^{1}H NMR spectrum matched those in the literature.[2] ^{1}H NMR (300 MHz, C_6D_6) δ: 5.58 (dd, 1H, ^3J = 9.1 Hz, ^4J = 5.2Hz), 5.28 (dt, 1H, ^3J = 9.0 Hz, ^4J = 4.4Hz), 5.21 (dd, 1H, ^3J = 4.2 Hz, ^4J = 1.1 Hz), 4.10 (dd, 2H, ^3J = 4.4 Hz, ^4J = 1.1 Hz), 2.18 (s, 3H), 1.00 (s, 12H).). ^{11}B NMR (96 Hz, C_6D_6) δ: 27.2 (s). **3b:** ^{1}H NMR (300 MHz, C_6D_6) δ: 6.63(dt, 1H, *H*-5, ^3J = 8.2 Hz, ^4J = 1.7Hz), 4.62 (ddt, 1H, ^3J = 8.2Hz, ^3J = 3.4 Hz, ^4J = 2.1 Hz), 4.40(dt, 1H, ^3J = 5.0 Hz, ^4J = 2.1 Hz), 2.76 (ddd, 2H, ^3J = 5.0Hz, ^3J = 3.4 Hz, ^4J = 1.7Hz), 1.96 (q, 3H, ^4J = 1.4Hz), 1.09(s,12H). ^{11}B NMR (96 Hz, C_6D_6) δ: 27.2 (s)

4a: The general procedure was conducted with 3-methoxypyridine. The ^{1}H NMR spectrum matched those in the literature.[16] ^{1}H NMR (300 MHz, C_6D_6) δ: 6.51(d, 1H, *J* = 7.2Hz), 5.11(dd, 1H, *J* = 7.2 Hz, *J* = 6.0Hz), 4.74(d, 1H, *J* = 6.0Hz), 4.32 (s, 2H, *H*-1), 3.15(s, 3H), 1.01 (s, 12H). ^{11}B NMR (96 Hz, C_6D_6) δ: 27.2 (s).

5a: The general procedure was conducted with 3-methylpyridine.[29] The ^{1}H NMR spectrum matched those in the literature. ^{1}H NMR (300 MHz, C_6D_6) δ: 6.56 (d, 1H, ^3J = 8.1 Hz),

6.36 (s), 4.66 (m, 1H), 2.72 (m, 2H), 1.41 (s, 3H), 1.06 (s, 12H). ^{11}B NMR (96 MHz, C_6D_6) δ: 27.0 (s).

6a: The general procedure was conducted with 3-phenylpyridine. The ^{1}H NMR spectrum matched those in the literature.[30] ^{1}H NMR (300 MHz, C_6D_6) δ: 7.32-7.19(m, 5H), 6.78(d, 1H, *J* = 7.2 Hz), 6.27(d, 1H, *J* = 5.9 Hz), 5.26-5.23(m, 1H), 4.58(s, 2H), 1.02(s, 12H). ^{11}B NMR (96 Hz, C_6D_6) δ: 27.1 (s). **6a':** ^{1}H NMR (300 MHz, C_6D_6) δ: 7.32-7.19(m, 5H), 6.78(d, 1H, *J* = 5.9 Hz), 6.27(d,1H, *J*= 5.9Hz), 5.26-5.23(m, 1H), 4.58(s, 2H), 1.02(s, 12H). ^{11}B NMR (96 Hz, C_6D_6) δ: 27.4 (s). **6b:** ^{1}H NMR (300 MHz, C_6D_6) δ: 7.07 (m, 5H), 7.01-6.98 (m, 1H) 6.59 (dd, 1H, *J* = 8.1 Hz, *J* = 0.8Hz), 4.83-4.71(m, 1H,), 3.15(m, 2H,), 1.00 (s, 12H). ^{11}B NMR (96 Hz, C_6D_6) δ:27.4(s).

7a: The general procedure was conducted with 4-phenylpyridine. The ^{1}H NMR spectrum matched those in the literature.[2] ^{1}H NMR (300 MHz, C_6D_6): 7.14-7.35(m, 2H,), 7.08-7.18 (m, 3H,), 6.84(dd, 1H, ^{3}J = 7.5Hz, ^{4}J 0.9Hz), 5.52 (dd, 1H, ^{3}J = 7.5Hz, ^{4}J 1.9Hz), 5.35 (tdd, 1H, ^{3}J = 7.5Hz, ^{4}J 0.9Hz, ^{5}J = 1.1 Hz), 4.28 (d, 2H, ^{3}J = 4.5Hz), 1.04 (s, 12H). ^{11}B NMR (96 Hz, C_6D_6) δ: 27.2 (s).

8a: The general procedure was conducted with 4-^{t}Bupyridine.[31] ^{1}H NMR (300 MHz, C_6D_6) δ: 6.72 (d, ^{3}J = 7.5 Hz, ^{4}J = 0.8 Hz, 1H), 5.52 (dd, ^{3}J = 9.69 Hz, ^{4}J = 5.76 Hz, 1H), 4.15 (d, *J* = 4.25 Hz, 2H), 1.01(s, 9H), 1.02(s, 12H). ^{11}B NMR (96 Hz, C_6D_6) δ: 27.4(s).

9a: The general procedure was conducted with 4-methylpyridine. The ^{1}H NMR spectrum matched those in the literature.[2] ^{1}H NMR (300 MHz, C_6D_6) δ: 6.67 (d, 1H, ^{3}J = 7.6 Hz), 4.86 – 4.93 (m, 1H, H-2), 4.13 (dq, 2H, ^{3}J = 3.9 Hz, ^{4}J = 1.6 Hz), 1.57 (q, 3H, $^{4/5}J$ = 1.6Hz), 1.03 (s, 12H). ^{11}B NMR (96 Hz, C_6D_6) δ: 27.4 (s). **9b:** ^{1}H NMR (300 MHz, C_6D_6) δ: 6.50 (d, 1H, ^{3}J = 8.4 Hz, ^{4}J = 1.3 Hz), 4.56 (ddm, 2H, ^{3}J = 8.4 Hz, ^{4}J = 3.3 Hz), 3.02 (ttq, 1H, ^{3}J = 4.6 Hz, ^{3}J = 3.3 Hz, ^{4}J = 1.3 Hz), 1.04-1.13 (m, 3H), and 1.0 (s,12H). ^{11}B NMR (96 Hz, C_6D_6) δ: 27.0(s).

10a: The general procedure was conducted with 3,4-dimethylpyridine. The ^{1}H NMR spectrum matched those in the literature.[32] ^{1}H NMR (300 MHz, C_6D_6) δ: 6.44(d, 1H, J = 7.1 Hz,), 4.86(d, 1H, J = 7.2 Hz), 3.94 (2H, s), 1.41 (s, 3H), and 1.05 (s, 12H). ^{11}B NMR (96 Hz, C_6D_6) δ: 23.2 (s).

11a: The general procedure was conducted with 2,5-dimethylpyridine. The ^{1}H NMR spectrum matched those in the literature.[16] ^{1}H NMR (300 MHz, C_6D_6) δ: 6.79 (d, J = 7.2Hz,1H), 5.14 (d, J = 5.45 Hz), 4.31 (d, J = 0.96 Hz), 4.05 (s, 2H) 2.09 (s, 3H), 1.43 (s, 2H) 1.01 (s, 12H). ^{11}B NMR (96 Hz, C_6D_6) δ: 27.0 (s).

12a: The general procedure was conducted with 2,3-dimethylpyridine. The ^{1}H NMR spectrum matched those in the literature.[16] ^{1}H NMR (300 MHz, C_6D_6) δ: 6.83(d, 1H, J = 8.2Hz), 4.73 (m, 1H), 2.72 (m, 2H), 2.07(s, 3H), 1.49 (s, 3H), 1.02 (s, 12H, CH_3-pin). ^{11}B NMR (96 Hz, C_6D_6) δ: 27.4 (s). **12b:** ^{1}H NMR (300 MHz, C_6D_6) δ: 6.53 (d, 1H, J = 7.32

Hz, J = 1.07), 5.57 (d,1H, J = 4.8 Hz) 5.05 (m, 1H, J = 7.26, J = 5.61), 4.27 (q, 1H, J = 6.4 Hz), 1.56 (s, 3H), 1.12 (s, 3H), 1.01 (s, 12H, CH_3-pin). ^{11}B NMR (96 Hz, C_6D_6) δ: 27.4 (s).

14a: The general procedure was conducted with acridine. The ^{1}H NMR spectrum matched those in the literature.[33] ^{1}H NMR (300 MHz, C_6D_6) δ: 7.80(t, 2H, J = 8.3 Hz), 7.14 (s, 2H). 6.99 – 6.91 (m, 4H), 3.54 (s,2H), 1.07 (s,12H). ^{11}B NMR (96 Hz, C_6D_6) δ: 27.6.

15a: The general procedure was conducted with quinoline. The ^{1}H NMR spectrum matched those in the literature.[2] ^{1}H NMR (300 MHz, C_6D_6) δ: 7.71 (d, 1H, H-5, ^3J = 8.1 Hz), 7.07 (ddd, 1H, H-6, ^3J = 8.1 Hz, ^3J = 7.0 Hz, ^4J = 2.1 Hz) 6.81 (dt, 1H, H-7, ^3J = 9.6Hz), 6.79 (dd, 1H, H-8, ^3J = 7.0 Hz, ^4J = 2.1Hz) , 6.24 (d, 1H, H-3, ^3J = 9.6 Hz), 5.57 (dt, 1H, H-2, ^3J = 9.6 Hz, ^4J = 4.0 Hz), 4.11(dd, 2H, H-1, ^3J = 4.0 Hz, ^4J = 1.3 Hz), 1.03 (s, 12H, CH_3-pin). ^{11}B NMR (96 Hz, C_6D_6) δ: 27.0(s)

17a: The general procedure was conducted with pyrazine. The ^{1}H NMR spectrum matched those in the literature.[14] ^{1}H NMR (300 MHz, C_6D_6) δ: 6.15(s, 2H), 3.49 (s, 4H), 1.04(s, 24H). ^{11}B NMR (96 Hz, C_6D_6) δ: 24.5 (s)

18a: The general procedure was conducted with 2-methoxypyrazine. The ^{1}H NMR spectrum matched those in the literature.[14] ^{1}H NMR (300 MHz, C_6D_6) δ: 6.32 (d, 1H, J =

4.8 Hz,), 6.14 (d, 1H, J = 4.98 Hz), 3.95 (s, 2H), 3.55 (s, 3H), 1.01 (d, 24H). ^{11}B NMR (96 Hz, C_6D_6) δ: 24.5 (s)

19a: The general procedure was conducted with 1-methylbenzimidazole. The ^{1}H NMR spectrum matched those in the literature.[30] ^{1}H NMR (300 MHz, C_6D_6) δ: 7.46-7.43(dd, ^{3}J = 8.7 Hz, ^{4}J = 0.75Hz,), 6.83-6.72 (m, 2H), 6.29 (dd, ^{3}J = 8.60, 1H), 4.73(s, 2H), 2.25(s, 3H*),* 1.08(s,12H, C*H*). ^{11}B NMR (96 Hz, C_6D_6) δ: 25.4

4.5.8. ^{1}H NMR of products

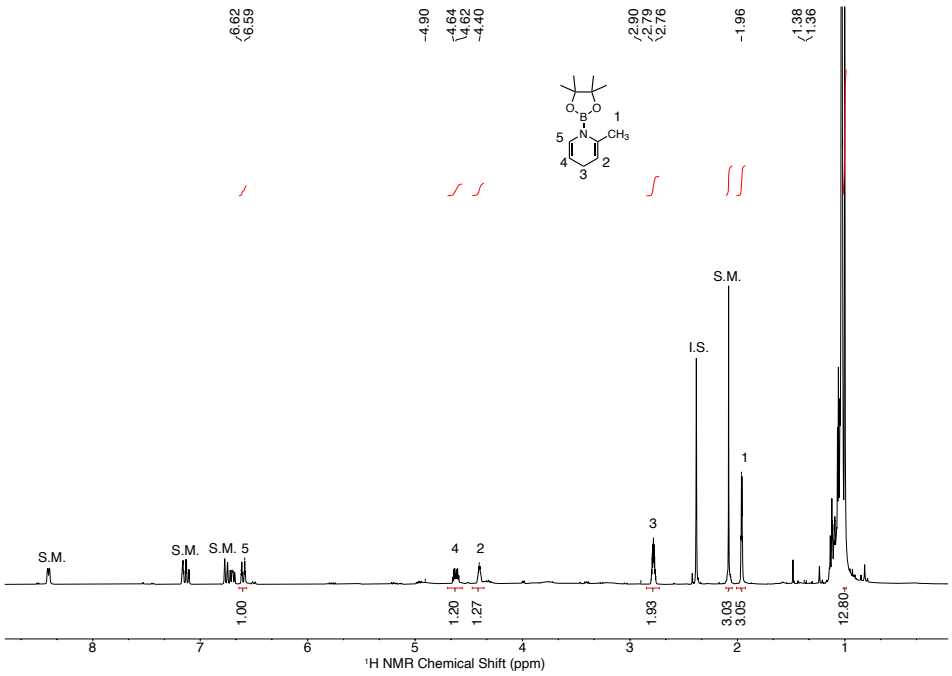

Figure 4.5.4. ^{1}H NMR of **3** and HBpin with 1 mol % **2Ir** in C_6D_6 with hexamethylbenzene used as internal standard (2.11 ppm)

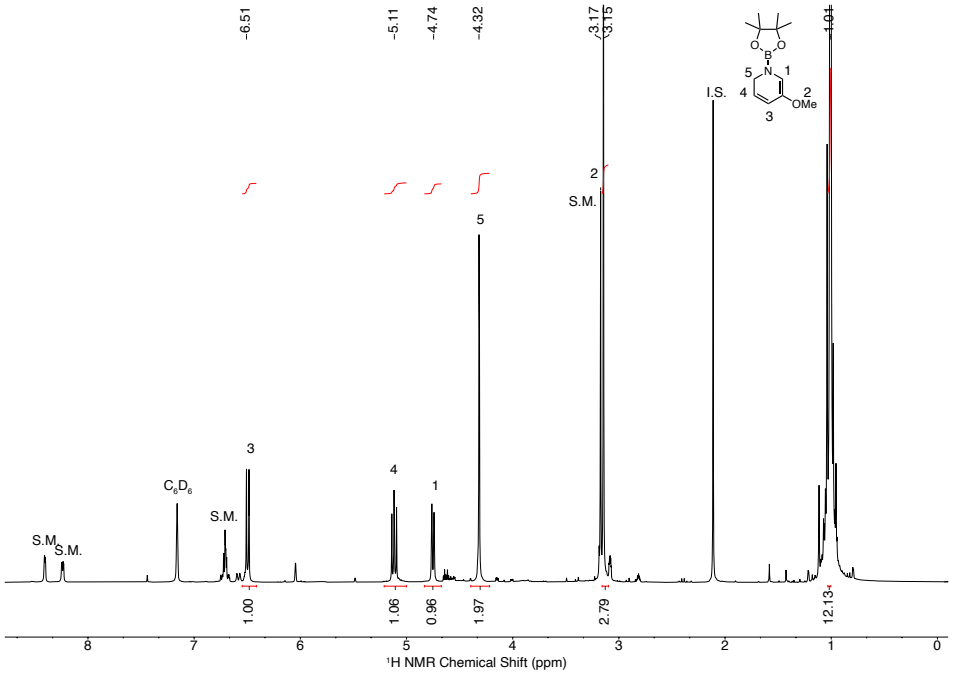

Figure 4.5.5. ^{1}H NMR of **4** and HBpin with 1 mol % **2Ir** in C_6D_6 with hexamethylbenzene used as internal standard (2.11 ppm)

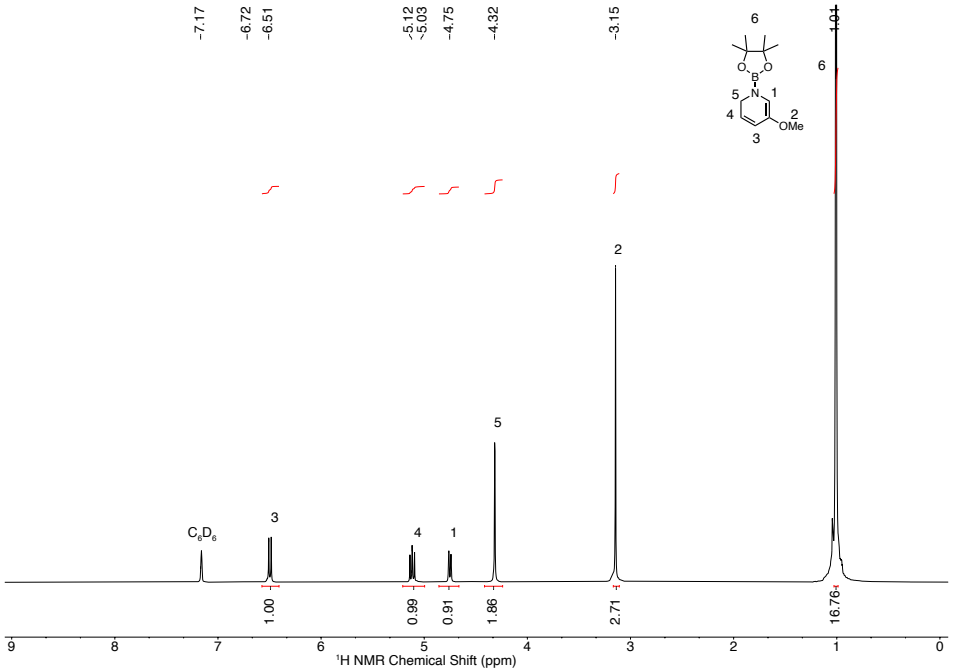

Figure 4.5.6. ^{1}H NMR isolated **4a** in C_6D_6. The isolated yield of **4a** was 80%.

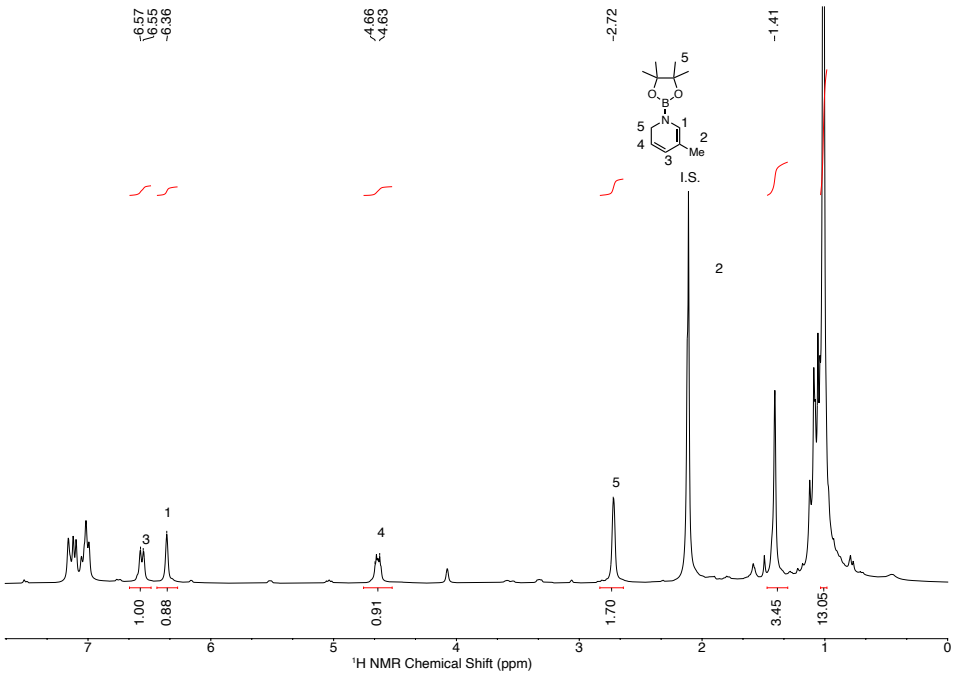

Figure 4.5.7. ^{1}H NMR of 5 and HBpin with 1 mol % **2Ir** in C_6D_6 with hexamethylbenzene used as internal standard (2.11 ppm)

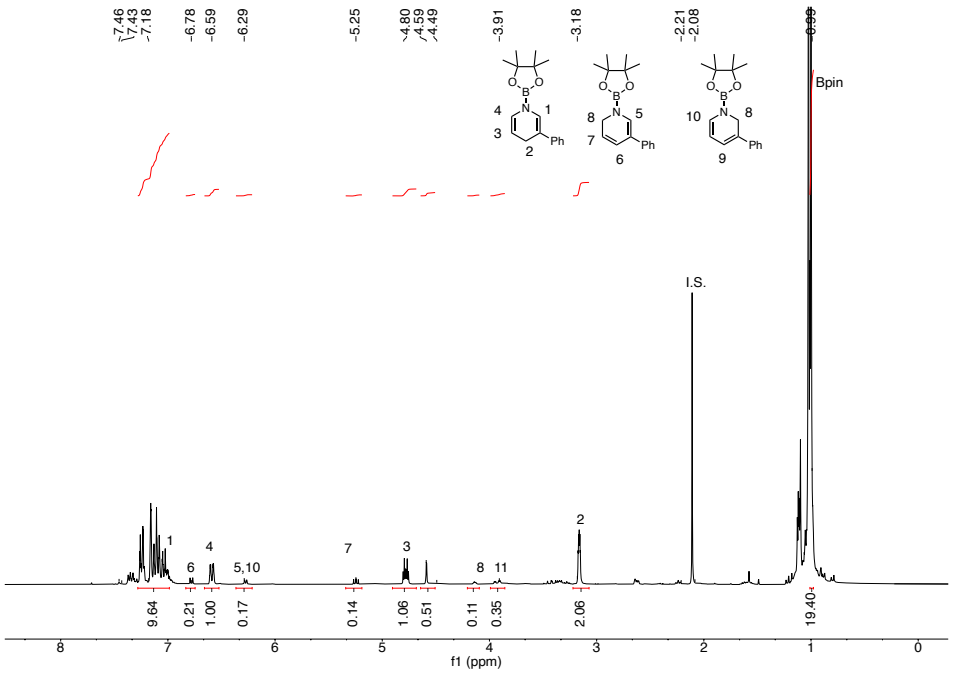

Figure 4.5.8. ^{1}H NMR of **6** and HBpin with 1 mol % **2Ir** in in C_6D_6 with hexamethylbenzene used as internal standard (2.11 ppm).

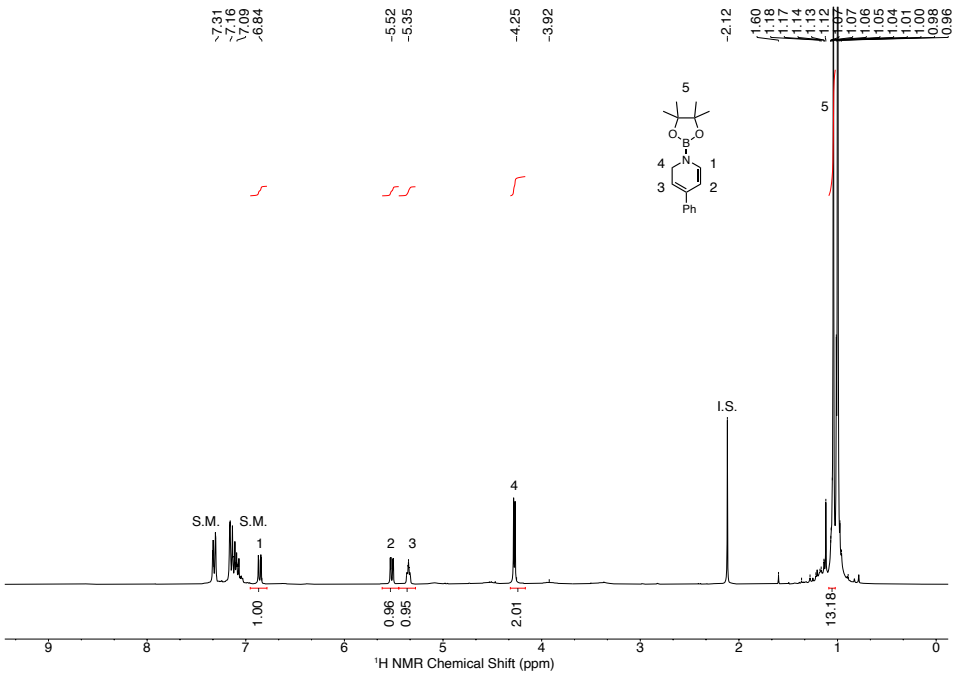

Figure 4.5. 9. ^{1}H NMR of **7** and HBpin with 1 mol % **2Ir** in C_6D_6 with hexamethylbenzene used as internal standard (2.11 ppm)

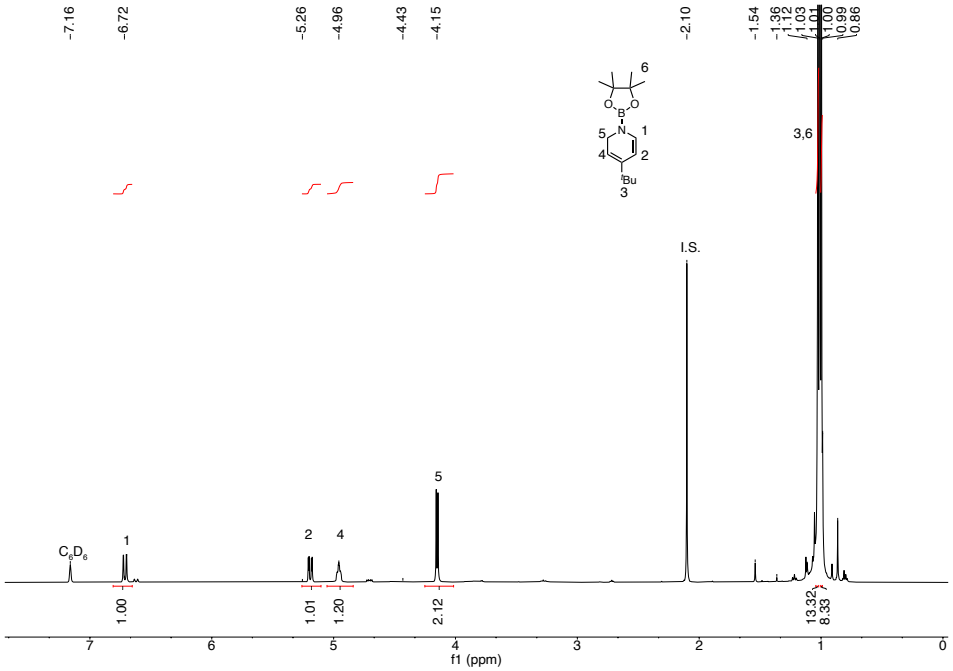

Figure 4.5. 10.^{1}H NMR of **8** and HBpin with 1 mol % **2Ir** in C_6D_6 with hexamethylbenzene used as internal standard (2.11 ppm)

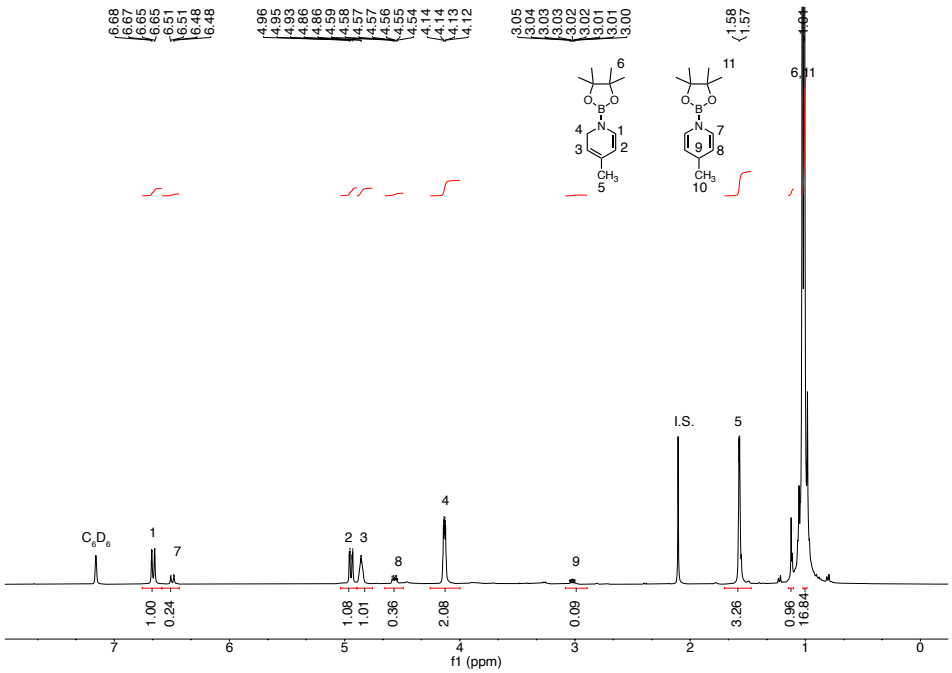

Figure 4.5. 11. ^{1}H NMR of **9** and HBpin with 1 mol % **2Ir** in in C_6D_6 with hexamethylbenzene used as internal standard (2.11 ppm)

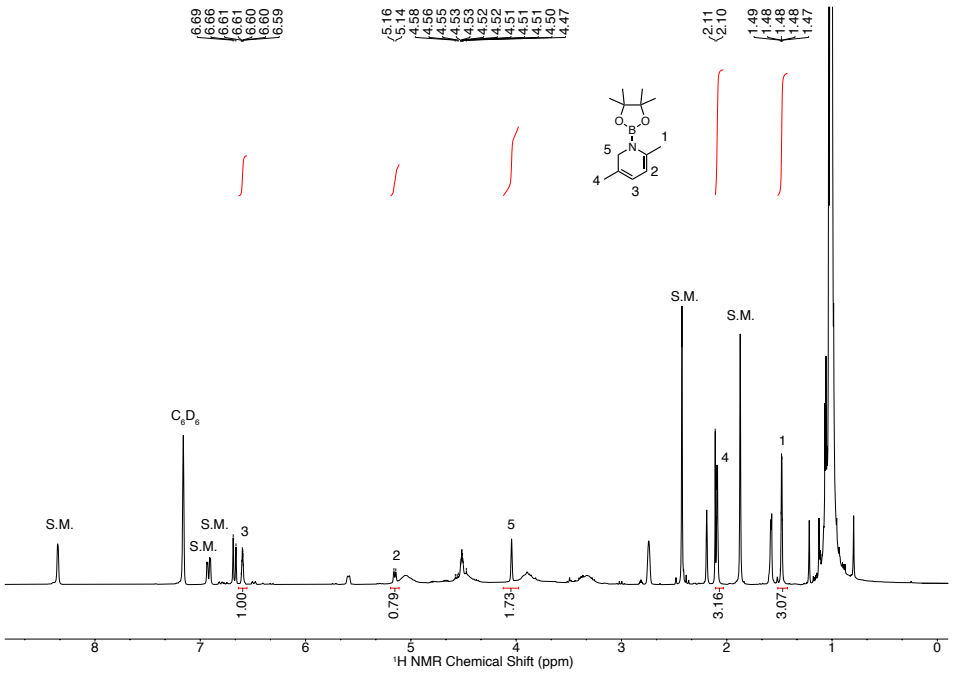

Figure 4.5. 12. ^{1}H NMR of **10** and HBpin with 1 mol % **2Ir** in C_6D_6 with hexamethylbenzene used as internal standard (2.11 ppm)

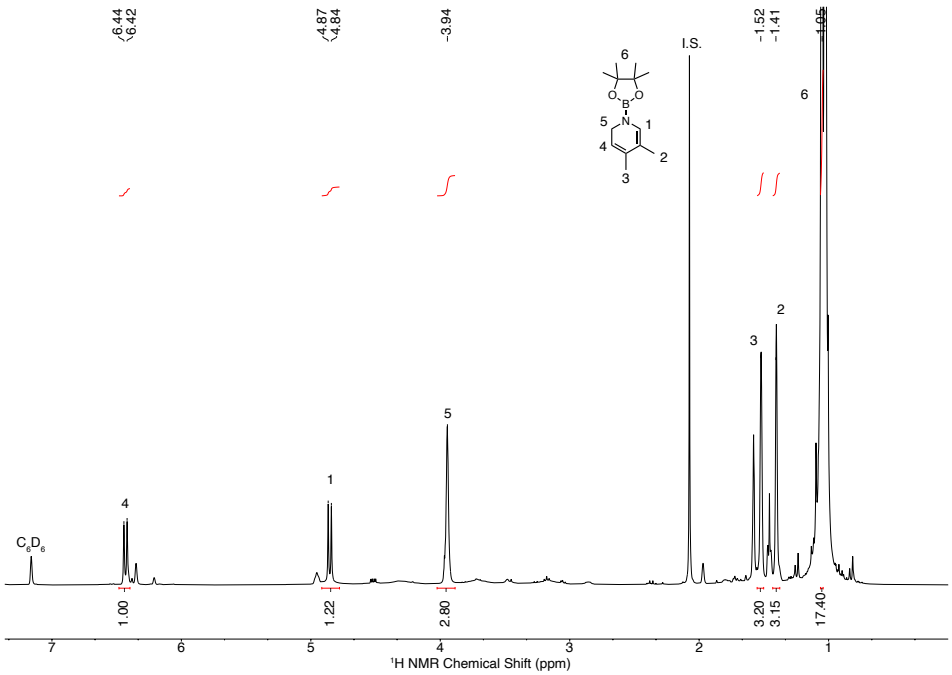

Figure 4.5. 13. ^{1}H NMR of **11** and HBpin with 1 mol % **2Ir** in C_6D_6 with hexamethylbenzene used as internal standard (2.11 ppm)

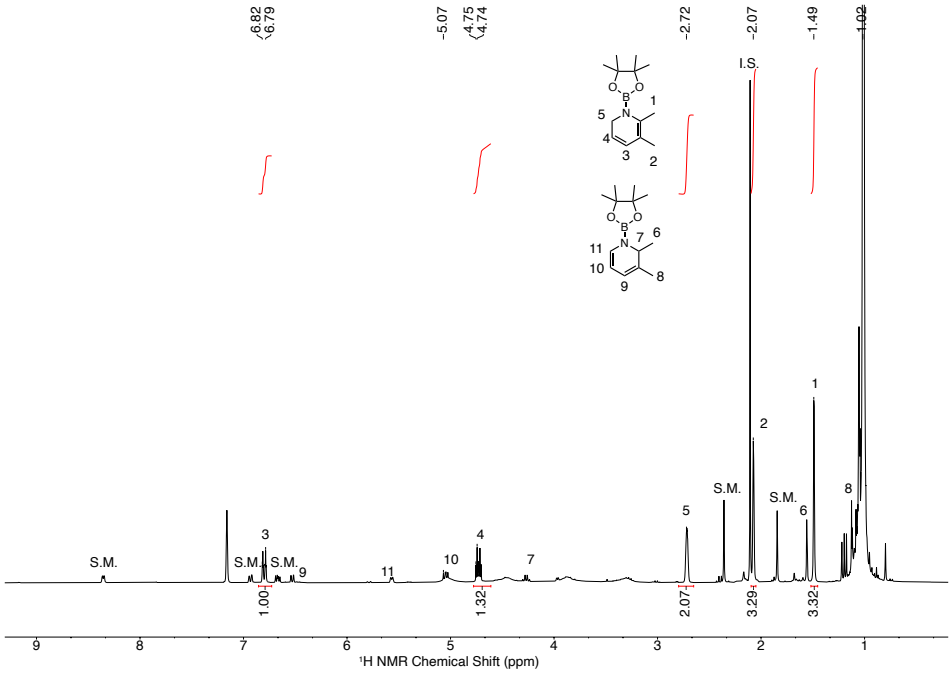

Figure 4.5. 14. ^{1}H NMR of **12** and HBpin with 1 mol % **2Ir** in C_6D_6 with hexamethylbenzene used as internal standard (2.11 ppm)

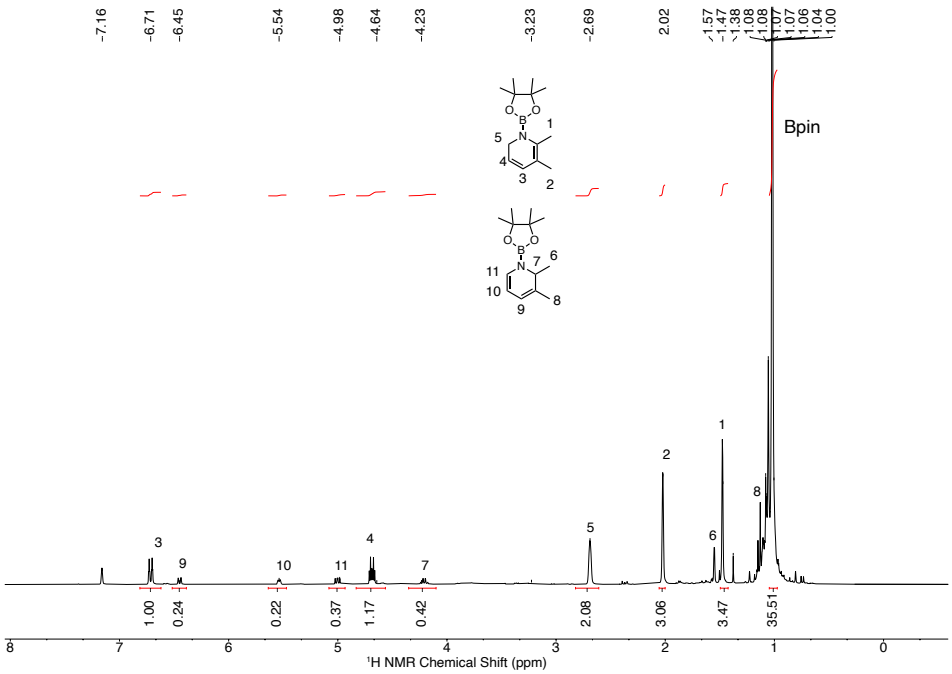

Figure 4.5. 15. 1H NMR of isolated **12a** in C_6D_6 ; Isolated yield for **12a** is 43% and isolated yield for **12a'** is 11%

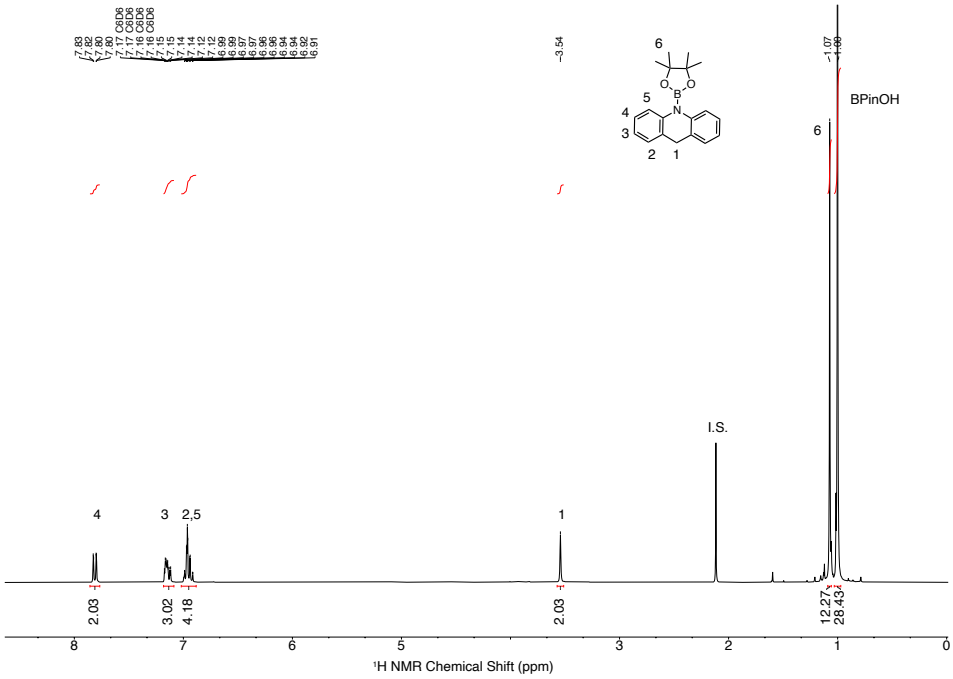

Figure 4.5. 16. ^{1}H NMR of **14** and HBpin with 1 mol % **2Ir** in C_6D_6 with hexamethylbenzene used as internal standard (2.11 ppm)

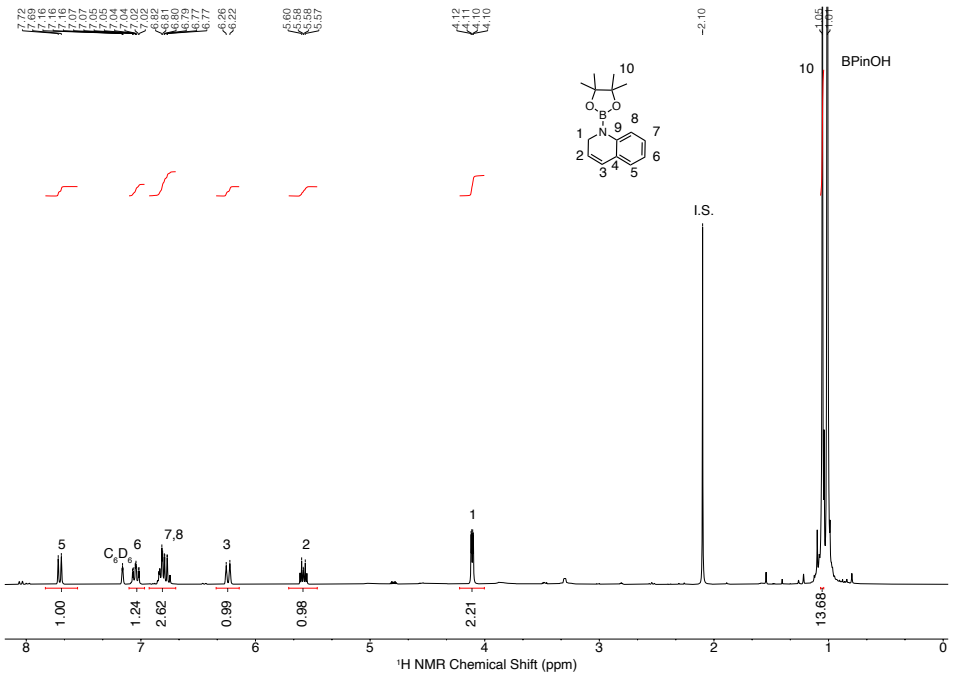

Figure 4.5. 17. ^{1}H NMR of **15** and HBpin with 1 mol % **2Ir** in C_6D_6 with hexamethylbenzene used as internal standard (2.11 ppm)

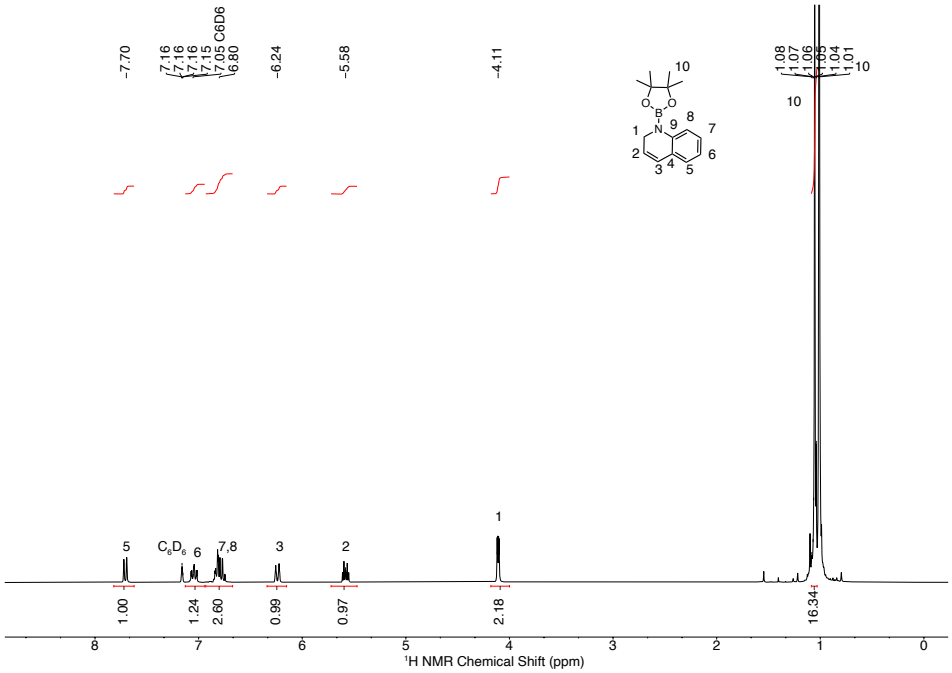

Figure 4.5. 18. ^{1}H NMR of isolated **15a** in C_6D_6.

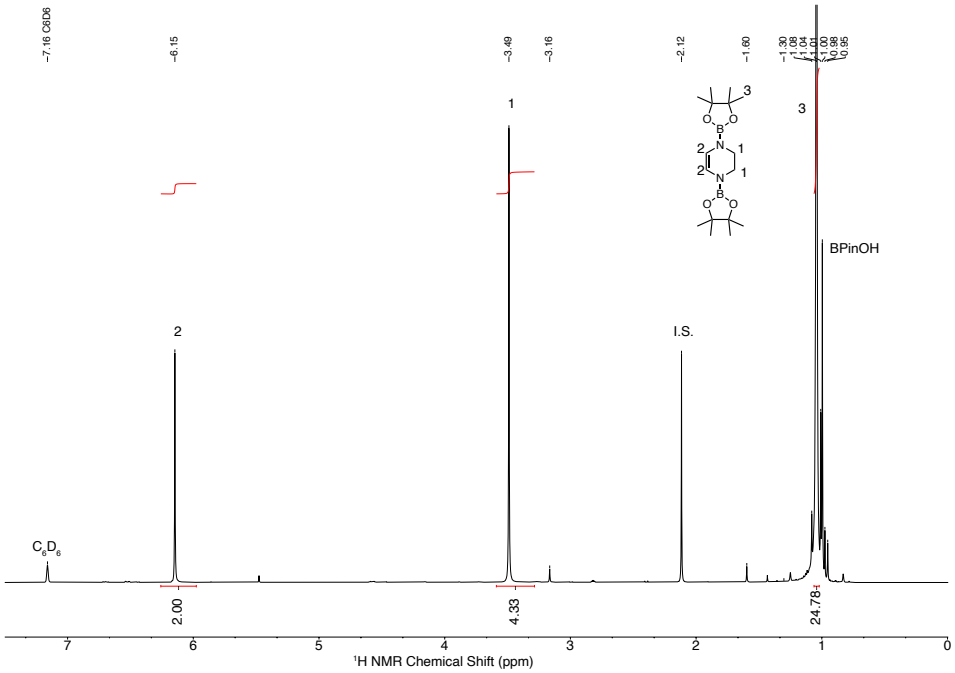

Figure 4.5. 19. ^{1}H NMR of **17** and HBpin with 1 mol % **2Ir** in C_6D_6 with hexamethylbenzene used as internal standard (2.11 ppm).

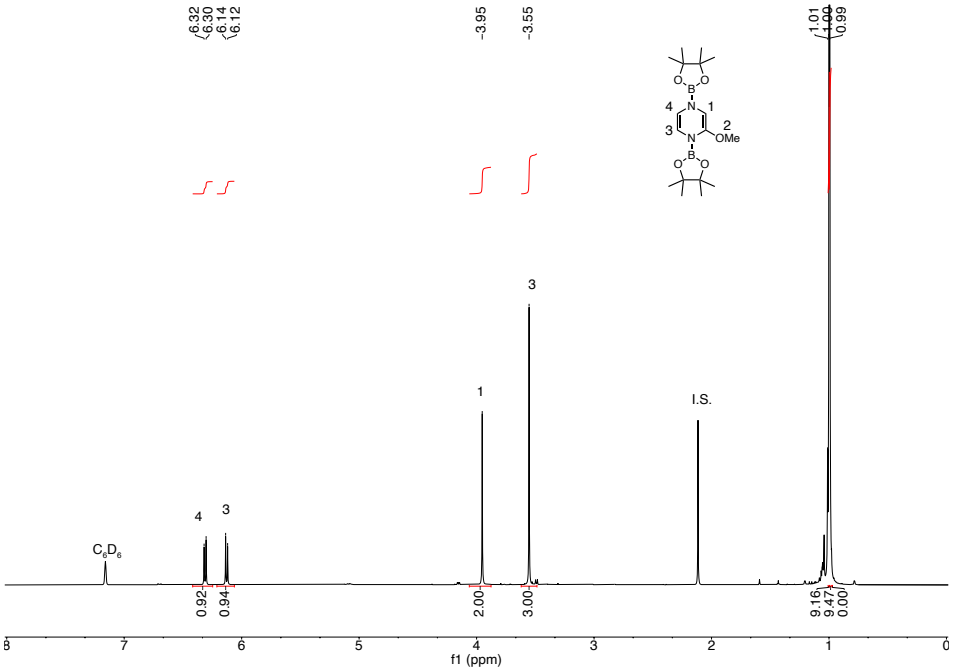

Figure 4.5. 20. ^{1}H NMR of **18** and HBpin with 1 mol % **2Ir** in C_6D_6 with hexamethylbenzene used as internal standard (2.11 ppm).

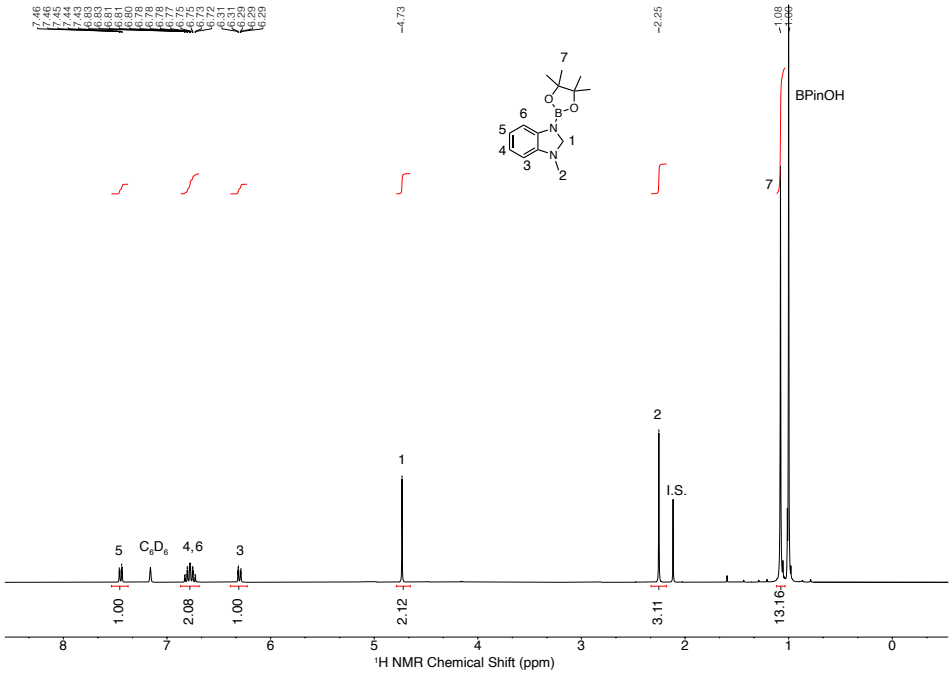

Figure 4.5. 21. ^{1}H NMR of **19** and HBpin with 1 mol % **2Ir** in C_6D_6 with hexamethylbenzene used as internal standard (2.11 ppm).

4.6. References

1. Bull, J. A., Mousseau, J. J., Pelletier, G. and Charette, A. B. Synthesis of pyridine and dihydropyridine derivatives by regio- and stereoselective addition to n -activated pyridines. *Chemical Reviews* vol. 112 2642–2713 (2012).

2. Arrowsmith, M., Hill, M. S., Hadlington, T., Kociok-Köhn, G. and Weetman, C. Magnesium-catalyzed hydroboration of pyridines. *Organometallics* **30**, 5556–5559 (2011).

3. Oshima, K., Ohmura, T. and Suginome, M. Regioselective synthesis of 1,2-dihydropyridines by rhodium-catalyzed hydroboration of pyridines. *J. Am. Chem. Soc.* **134**, 3699–3702 (2012).

4. Lortie, J. L., Dudding, T., Gabidullin, B. M. and Nikonov, G. I. Zinc-Catalyzed Hydrosilylation and Hydroboration of N-Heterocycles. *ACS Catal.* **7**, 8454–8459 (2017).

5. Oshima, K., Ohmura, T. and Suginome, M. Regioselective Synthesis of 1,2-Dihydropyridines by Rhodium-Catalyzed Hydroboration of Pyridines. *J. Am. Chem. Soc.* **134**, 3699–3702 (2012).

6. Harrod, J. F., Shu, R., Woo, H. G. and Samuel, E. Titanocene(III) catalyzed homogeneous hydrosilation-hydrogenation of pyridines. *Can. J. Chem.* **79**, 1075–1085 (2001).

7. Jeong, J., Park, S. and Chang, S. Iridium-catalyzed selective 1,2-hydrosilylation of N-heterocycles †. (2016) doi:10.1039/c6sc01037g.

8. Intemann, J., Bauer, H., Pahl, J., Maron, L. and Harder, S. Calcium Hydride Catalyzed Highly 1,2-Selective Pyridine Hydrosilylation. *Chem. – A Eur. J.* **21**, 11452–11461 (2015).

9. Königs, C. D. F., Klare, H. F. T. and Oestreich, M. Catalytic 1,4-Selective Hydrosilylation of Pyridines and Benzannulated Congeners. *Angew. Chemie Int. Ed.* **52**, 10076–10079 (2013).

10. Gutsulyak, D. V., Van Der Est, A. and Nikonov, G. I. Facile Catalytic Hydrosilylation of Pyridines. *Angew. Chemie Int. Ed.* **50**, 1384–1387 (2011).

11. Lee, S. H., Gutsulyak, D. V. and Nikonov, G. I. Chemo- and regioselective catalytic reduction of N-heterocycles by silane. *Organometallics* **32**, 4457–4464 (2013).

12. Liu, Z.-Y. Y. Z.-Y. *et al.* B(C6F5)3-Catalyzed Cascade Reduction of Pyridines. *Angew. Chemie Int. Ed.* **56**, 5817–5820 (2017).

13. Gandhamsetty, N., Park, S. and Chang, S. Selective Silylative Reduction of Pyridines Leading to Structurally Diverse Azacyclic Compounds with the Formation of sp3 C-Si Bonds. *J. Am. Chem. Soc.* **137**, 15176–15184 (2015).

14. Hao, L. *et al.* Homogeneous Catalytic Hydrosilylation of Pyridines. *Angew. Chemie Int. Ed.* **37**, (1998).

15. Dudnik, A. S., Weidner, V. L., Motta, A., Delferro, M. and Marks, T. J. Atom-efficient regioselective 1,2-dearomatization of functionalized pyridines by an earth-abundant organolanthanide catalyst. *Nat. Chem.* **6**, 1100–1107 (2014).

16. Kaithal, A., Chatterjee, B. and Gunanathan, C. Ruthenium-Catalyzed Regioselective 1,4-Hydroboration of Pyridines. *Org. Lett.* **18**, 3402–3405 (2016).

17. Fan, X., Zheng, J., Li, Z. H. and Wang, H. Organoborane Catalyzed Regioselective 1,4-Hydroboration of Pyridines. *J. Am. Chem. Soc.* **137**, 4916–4919 (2015).

18. Zhang, T., Manna, K. and Lin, W. Metal-Organic Frameworks Stabilize Solution-Inaccessible Cobalt Catalysts for Highly Efficient Broad-Scope Organic Transformations. *J. Am. Chem. Soc.* **138**, 3241–3249 (2016).

19. Li, Z., Rayder, T. M., Luo, L., Byers, J. A. and Tsung, C. K. Aperture-Opening Encapsulation of a Transition Metal Catalyst in a Metal-Organic Framework for CO 2 Hydrogenation. *J. Am. Chem. Soc.* **140**, 8082–8085 (2018).

20. Jeong, E., Heo, J., Park, S. and Chang, S. Alkoxide-Promoted Selective Hydroboration of N-Heteroarenes: Pivotal Roles of in situ Generated BH3 in the Dearomatization Process. *Chem. – A Eur. J.* **25**, 6320–6325 (2019).

21. Kim, E., Jeon, H. J., Park, S. and Chang, S. Double Hydroboration of Quinolines via Borane Catalysis: Diastereoselective One Pot Synthesis of 3-Hydroxytetrahydroquinolines. *Adv. Synth. Catal.* **362**, 308–313 (2020).

22. Rao, B., Chong, C. C. and Kinjo, R. Metal-Free Regio- and Chemoselective Hydroboration of Pyridines Catalyzed by 1,3,2-Diazaphosphenium Triflate. *J. Am. Chem. Soc.* **140**, 652–656 (2018).

23. Huynh, W. and Conley, M. P. Origin of the 29Si NMR chemical shift in R3Si–X and relationship to the formation of silylium (R3Si+) ions. *Dalt. Trans.* **49**, 16453–16463 (2020).

24. Culver, D. B. and Conley, M. P. Activation of C−F Bonds by Electrophilic Organosilicon Sites Supported on Sulfated Zirconia. *Angew. Chemie - Int. Ed.* **57**, 14902–14905 (2018).

25. Zassinovich, G., Mestroni, G. and Camus, A. Diolefinic complexes of rhodium(I) and iridium(I) with nitrogen-containing ligands. *J. Organomet. Chem.* **91**, 379–388 (1975).

26. Oshima, K. *et al.* Dearomatizing conversion of pyrazines to 1,4-dihydropyrazine derivatives via transition-metal-free diboration, silaboration, and hydroboration. *Chem. Commun.* **48**, 8571–8573 (2012).

27. Tafazolian, H., Culver, D. B. and Conley, M. P. A Well-Defined Ni(II) α-Diimine Catalyst Supported on Sulfated Zirconia for Polymerization Catalysis. *Organometallics* **36**, 2385–2388 (2017).

28. Culver, D. B., Venkatesh, A., Huynh, W., Rossini, A. J. and Conley, M. P. Al(OR F) 3 (R F ¼ C(CF 3) 3) activated silica: a well-defined weakly coordinating surface anion †. *Chem. Sci.* **11**, 1510–1517 (2020).

29. Héroguel, F. *et al.* Dense and narrowly distributed silica-supported rhodium and iridium nanoparticles: Preparation via surface organometallic chemistry and chemisorption stoichiometry. *J. Catal.* **316**, 260–269 (2014).

30. Intemann, J., Lutz, M. and Harder, S. Multinuclear magnesium hydride clusters: Selective reduction and catalytic hydroboration of pyridines. *Organometallics* **33**, 5722–5729 (2014).

31. Liu, J. *et al.* Ni–O Cooperation versus Nickel(II) Hydride in Catalytic Hydroboration of N-Heteroarenes. *ACS Catal.* **9**, 3849–3857 (2019).

32. Lemmerz, L. E., Spaniol, T. P. and Okuda, J. 1,4-Dihydropyridyl complexes of magnesium: Synthesis by pyridine insertion into the magnesium-silicon bond of triphenylsilyls and catalytic pyridine hydrofunctionalization. *Dalt. Trans.* **47**, 12553–12561 (2018).

33. Ghosh, P. and Jacobi von Wangelin, A. Manganese-Catalyzed Hydroborations with Broad Scope. *Angew. Chemie - Int. Ed.* **60**, 16035–16043 (2021).

34. Liu, J. *et al.* Ni-O Cooperation versus Nickel(II) Hydride in Catalytic Hydroboration of N-Heteroarenes. *ACS Catal.* **9**, 3849–3857 (2019).

Chapter 5. A W(oxo)adamantylidene supported on SZO_{300}

5.1. Abstract

The reaction of W(=O)(Adene)(2,5-Me_2pyr)$_2$ with **SZO_{300}** results in the formation of [W(=O)(Adene)(2,5-Me_2pyr)][**SZO_{300}**] (**W1**). **W1** is a well-defined W oxo alkylidene species that is active in the homocoupling of terminal olefins and forms the thermolytic E-olefin products. This material is first example of a supported W oxo alkylidene on a sulfated oxide.

5.2. Introduction

Olefin metathesis is a powerful tool to form new carbon–carbon bonds, and is used for the synthesis of fine and bulk chemicals with some of original systems still being used today.[1–3] It has long been presumed that prototypes of the active sites of industrial heterogenous are supported oxo alkylidenes, but clear identification of a W=CH_2 has been elusive. The two key intermediates proposed by Chauvin are a metal alkylidene and a metallacyclobutane intermediate.[4,5] The metathesis active trigonal bipyramidal (TBP) metallacyclobutane intermediate is formed from a [2+2] cycloaddition of an alkene to a d^0 alkylidene. Large research efforts have led to the development of highly active and selective well-defined homogeneous systems, which can be can be divided into two classes: i) d^0 high oxidation state metal alkylidenes that are focused on W and Mo (Schrock type) [6–8] or ii) Ru alkylidenes (Grubb's type), Scheme 5.2.1.[9–11]

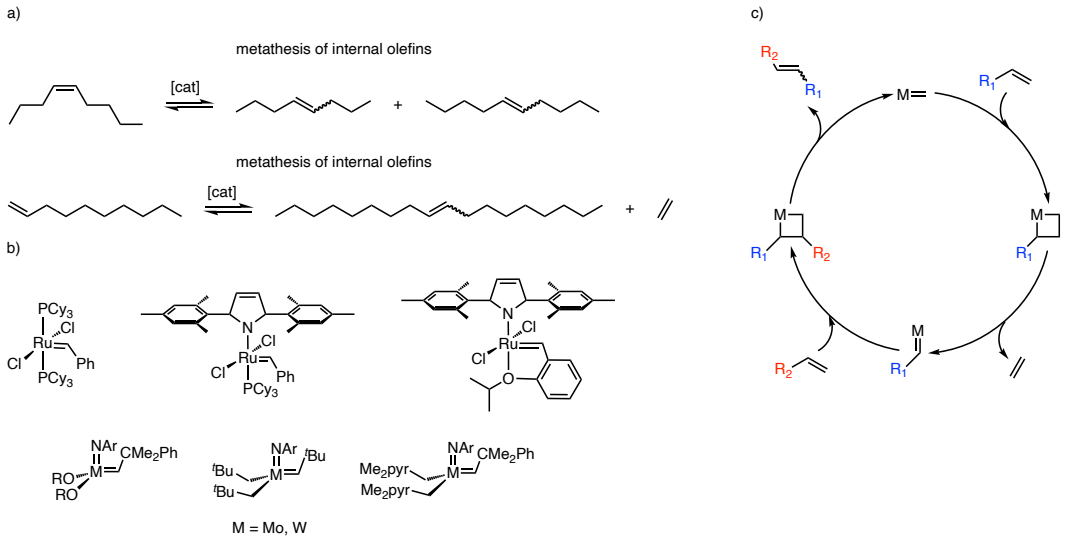

Figure 5. 2. 1. Typical test substrates for metathesis of olefins (a); Design of Grubbs Type catalysts (top) and Schrock type catalysts (bottom) where M is Mo or W (b); Chauvin mechanism for olefin metathesis (c).

Schrock type alkylidenes have the general formula (X)(Y)M(=CHR)E where M is Mo or W, E is either an oxo or imido ligand, both X and Y are anionic ligands. The many studies on olefin metathesis catalysts have found that: i) electronic dissymmetry at the metal center is import for low-energy cycloaddition/cycloreversion,[12,13] ii) strong σ-donor ligands in the coordination sphere destabilizes the metallacyclobutane intermediates,[14–19] and iii) low-lying vacant metal d-orbitals in the same plane of the metallacyclobutane intermediate are needed to allow for efficient cycloaddition/cycloreversion.[20] Additionally, the highest activities are achieved when there is a strongly donating E ligand and weakly donating X and/or Y ligands.[14, 19,21–25]

The intermediates involved in olefin metathesis are prone to various deactivation pathways. Discounting poisoning and the formation of metal hydrides, the loss of alkylidene ligands via bimolecular pathways is a major deactivation pathway.[26,27] This issue can be reduced in homogenous chemistry by using bulky ligands to stabilize these

highly reactive species. SOMC stabilizes the supported species through site isolation on surfaces leading to more active and stable catalysts in comparison to their molecular counterparts, Figure 5.2.2.[28–30] Additionally, these well-defined species can operate at room temperature, and do not require any activation steps.

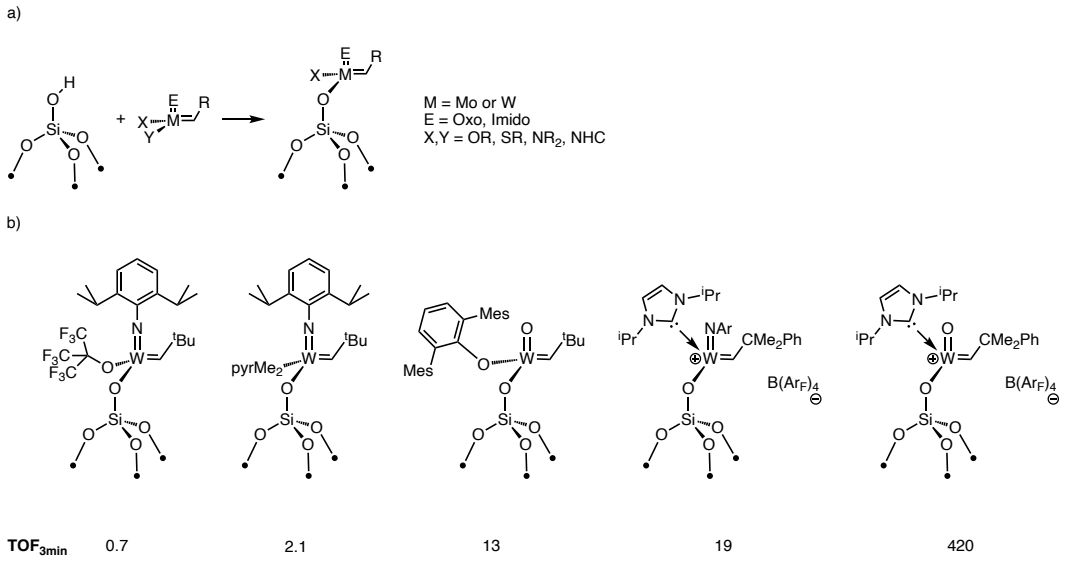

Figure 5. 2. 2. General scheme to generate a supported alkylidene on silica (a); Selected examples of well-defined supported W species that are active for olefin metathesis. The TOF_{3min} is for the terminal olefins (b).

Supported species follow the same trends that were discussed above for well-defined molecular complexes. Supported species are very sensitive to reaction conditions (e.g. purification of substrates, quality of atmosphere, and reaction set ups). In the case of silica support species, it is important to view the surface siloxy group as a rather small ligand with a buried volume (20.6%) less than HMTO (24.3%) and dAdPO (36.8%). Figure 5.2.2 shows a selection of W catalysts that exhibit improved performance for the metathesis of 1-nonene, a typical test substrate.[31–34] To characterize the performance of these catalysts two descriptors are primarily used: initial turnover frequency (TOF_{3min}) and time required

to reach equilibrium (or the highest conversion) known as turnover (TON). Terminal olefins can reach 100% conversion if ethylene is removed from the reaction solution, but metathesis of internal olefins (e.g. *cis*-4-nonene) can only reach ~50% conversion.

Imido complexes[22,35] have been investigated more in comparison to their oxo counterparts due to isolable oxo complexes being more difficult to prepare.[36–38] However, Schrock and coworkers recently reported the synthesis of a novel W oxo adamantylidene, W(=O)(Adene)(2,5-Me_2pyr)$_2$.[39] W(=O)(Adene)(2,5-Me_2pyr)$_2$ contains two strongly donating 2,5-Me_2pyr ligands as well as a sterically demanding adamantylidene. This chapter discusses the reaction of W(=O)(Adene)(2,5-Me_2pyr)$_2$ with **SZO$_{300}$** to form the first supported W oxo adamantylidene on a sulfated oxide, Scheme 5.2.3.

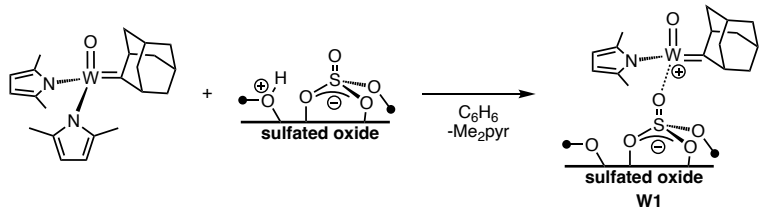

Figure 5. 2. 3. Reaction of W(=O)(Adene)(2,5-Me_2pyr)$_2$ with **SZO$_{300}$** to form **W1**

5.3. Results and Discussion

5.3.1. Synthesis of [W(=O)(Adene)(2,5-Me2pyr)][SZO$_{300}$]

W(=O)(Adene)(2,5-Me_2pyr)$_2$ reacts with **SZO$_{300}$** in a slurry of benzene to form [W(=O)(Adene)(2,5-Me_2pyr)][**SZO$_{300}$**] (**W1**). Analysis of the volatiles show that 0.078 mmol/g Me_2pyr is released during the reaction. The FT-IR of **W1** contains sp^2 ν_{CH} and sp^3 ν_{CH} stretches at 2905, 2849, and the $\nu_{C=N}$ stretch 1647 cm^{-1}. The solid-state ^{13}C CPMAS NMR spectrum of **W1** contains signals at 134 (C-CH_{3pyr}), 106(CH_{pyr}), 47(Ad), 42(Ad),

38(Ad), 32(Ad), 22(Ad), and 15(CH_3pyr) ppm. The alkylidene signal is not observed in the solid-state NMR which is unfortunately common when studying supported-materials due to the low coverage of active sites.

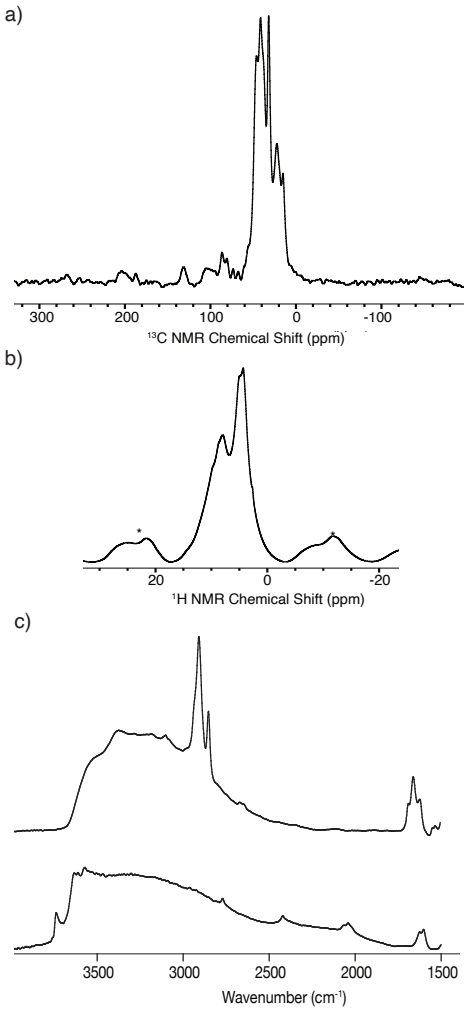

Figure 5. 3. 1. Analytical data for **W1** a) $^{13}C\{^{1}H\}$ CP MAS NMR; grafting reaction performed in C_6H_6; 10kHz; ns= 40k; d1=1s; * = spinning sidebands; b) ^{1}H MAS NMR; grafting performed in C_6H_6; 10kHz; ns = 2k; d1 = 1s; c) FT-IR; top: **W1** and bottom: **SZO$_{300}$**.

5.3.2. Reaction of W1 with ^{13}C-ethylene

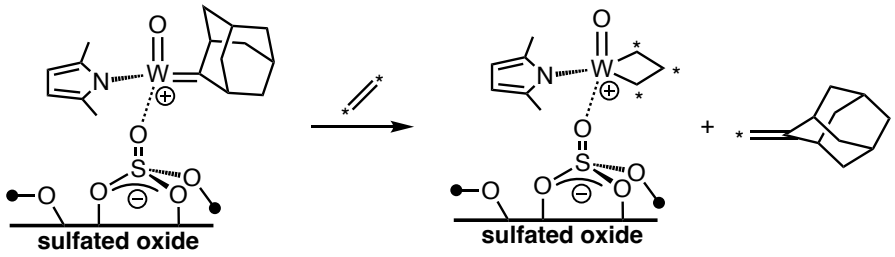

Figure 5. 3. 2. Reaction of **W1** with ^{13}C-ethylene to form ^{13}C-adamantylethylene and a W-metallacyclobutane (**W2**); * = ^{13}C-label

W1 reacts with ^{13}C-ethylene to form 0.065 mmolg^{-1}1-^{13}C-adamantylethylene and 0.012 mmolg^{-1} ^{13}C labelled propylene. The ^{13}C CPMAS NMR contains signals at 137 and 107 which are assigned to (C-CH_{3pyr}) and CH_{pyr}, respectively. The signals at 58, 40, 31, and 19 ppm belong to the formation of a tungstacyclobutane [W(O)(C_3H_6)(2,5-Me_2pyr)][**SZO$_{300}$**] (**W2**). A product rearrangement of **W2** occurs to form [W(O)(propylene)][**SZO$_{300}$**] which releases propylene from a reaction with free ethylene. The ^{1}H–^{13}C two-dimensional (2D) heteronuclear correlation (HETCOR) spectrum is shown in Figure 5.3.4. This spectrum contains correlations between ^{1}H signals ~4 ppm and ^{13}C signals at

~20–40 ppm from the ^{13}C-labeled metallacyclobutane in **W2**. In addition, the broad ^{13}C signal at ~50ppm correlates with ^{1}H signals at ~ppm, which is assigned the W-propylene species.

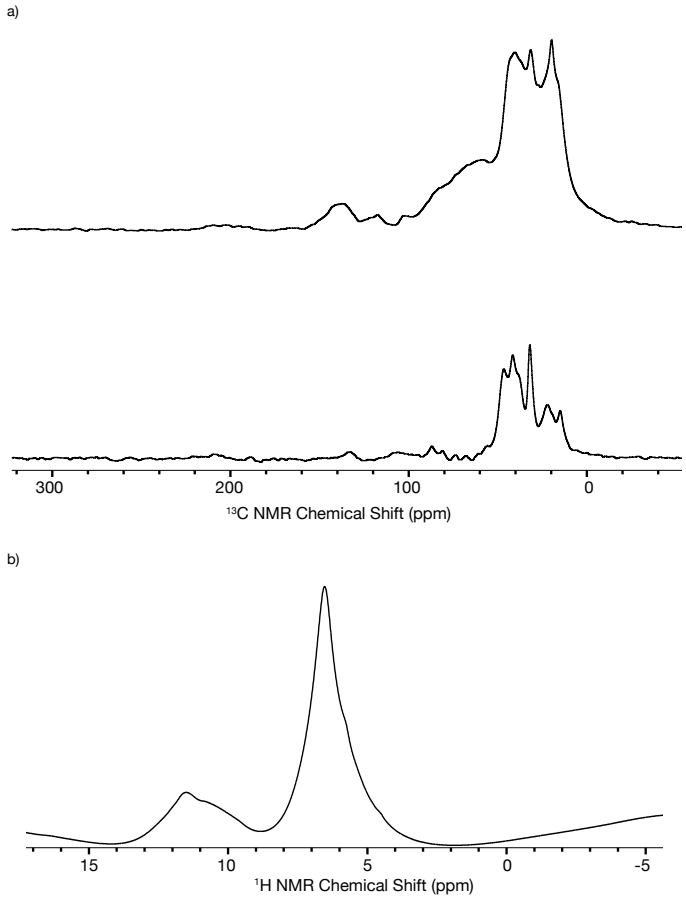

Figure 5. 3. 3. Analytical data for **W2** a) top: $^{13}C\{^{1}H\}$ CP MAS NMR of **W2**; bottom: $^{13}C\{^{1}H\}$ CP MAS NMR of **W1**; 10kHz; ns= 40k; d1=1s; b) ^{1}H MAS NMR of **W2**; reaction performed in C_6H_6; 10kHz; ns = 128; d1 = 1s; * = spinning sidebands.

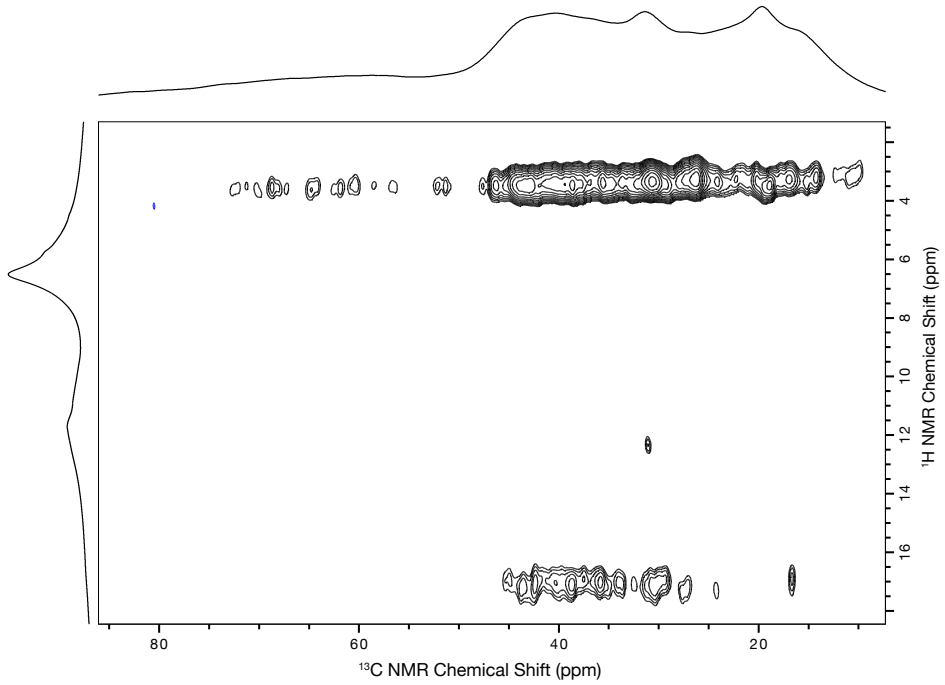

Figure 5.3.4. Two-dimensional ^{1}H-^{13}C HETCOR spectrum of **W2** zoomed to highlight the region from 20 ppm to 80 ppm. Full spectra can be found in Figure 5.5.5.

*5.3.3. Metathesis reactions with **W1***

*5.3.3.1. Metathesis with **W1***

The catalytic activities of **W1** in the metathesis of 1-decene, *cis*-4-nonene, methyl 10-undecenoate, and 1-octene-8-triisopropylsilane are shown in Table 5.3.1. **W1** displays high activity for the metathesis of 1-decene at room temperature. At low loadings of 0.05 mol%, 1-decene reaches 91% conversion to 9-octadecene with a of TOF_{3min} = 24. At 0.05mol% **W1**, *cis*-4-nonene reaches equilibrium (42% conversion) to cis/trans mixtures of 4-octene and 4-decene in 5 hours with a TOF_{3min} of 23. Methyl 10-undecenoate reaches 12% conversion with a TOF_{3min} of 18. Additionally, 1-octene-8-triisopropylsilane reaches 17% conversion with a TOF_{3min} of 39. In all cases, the E-olefin is preferred in high

selectivity. **W1** exhibits competitive activity for terminal unfunctionalized olefins with respect to neutral supported W oxo alkylidenes, Figure 5.3.6.[40,41] Reacting **W1** with partially dehydroxylated silica forms (=SiO)W(=O)(Adene)(Me_2pyr) which exhibits superior activity in the metathesis of terminal and internal olefins with respect to **W1**.[42] **W1** is less active than the [(=SiO)W(=O)(=CH_2Ph(IMes)$^+$][B(Ar^F)$_4^-$] where IMes = 1,3-bis(2,4,6-trimethylphenyl)-imidazol-2-ylidene and B(Ar^F)$_4$ = B(3,5-(CF_3)$_2$$C_6H_3$)$_4$, Figure 5.2.2.

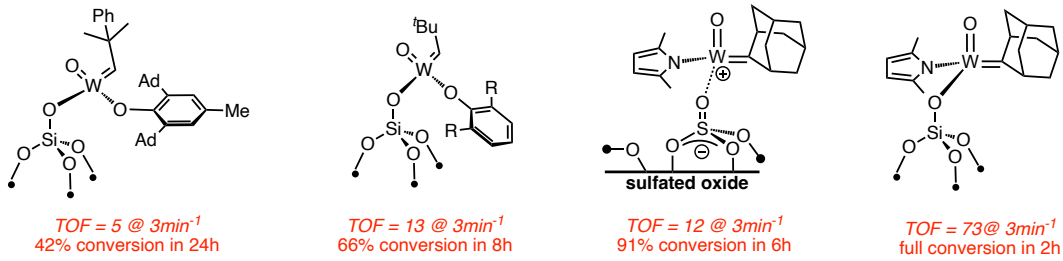

Figure 5. 3. 5. Activity of reported neutral and cationic W oxo alkylidenes at 0.1 mol% loading

Table 5.3. 1. Summary of % conversion, TON, and TOF values for the metathesis of alkenes by W1

Entry	Substrate	mol%	% conv	Time to equilibrium (hrs)	TON	TOF[a]
1	1-decene	1	98	2	98	4
2	1-decene	0.1	98	6	980	12
3	1-decene	0.05	91	12	1800	24
4	Cis-4-nonene	0.05	42	5	850	23
5	Methyl 10-undecenoate	0.05	12	8	240	18
6	1-octene-8-triisopropylsilane	0.05	17	16	340	39

[a]Turnover frequency (TOF) at 3 min, given in min^{-1}

5.4. Conclusions

The reaction of W(=O)(Adene)(2,5-Me_2pyr)$_2$ with **SZO$_{300}$** results in the formation of **W1**, which was fully characterized by FT-IR, solid-state NMR, and reactivity studies. Reacting **W1** with ^{13}C-ethylene results in the formation of **W2**, which rearranges to form a W-propylene complex. The W-propylene complex can react with free ethylene to generate propylene. **W1** is active in the metathesis for 1-decene, *cis*-4-nonene, and functionalized olefins with a high preference for the E-olefin products. **W1** exhibits comparable activity to supported neutral W oxo alkylidenes.

5.5. Materials and Methods

5.5.1. General Considerations

All reactions and manipulations were performed under an inert atmosphere of nitrogen or argon using standard Schlenk techniques. C_6D_6 was purchased from Cambridge Isotope Laboratories, dried over Na/benzophenone, freeze-pump-thawed three times, and distilled under vacuum. Solvents were purchased from Fisher Scientific, dried by passing through a double-column J. C. Meyer solvent system and degassed before use. Toluene and benzene were dried over Na/benzophenone, and distilled under vacuum before use. Toluene was stored over Selexsorb for five hours and passed through Selexsorb immediately before use. Cyclohexane was dried over CaH_2 and distilled under vacuum before use. Other chemicals were purchased from standard suppliers. **SZO_{300}** was prepared as previously described.[42] W(O)(Adene)(Me_2Pyr)$_2$ was previously described.[39] 1-decene and methyl 10-undecenoate were dried over CaH_2 and cis-4-nonene was dried over Na and all were distilled under reduced pressure. After distillation, the alkenes were stored over Selexsorb for five hours in a N_2 filled glovebox, filtered in the glovebox, and stored over 4A molecular sieves in the glovebox. Prior to metathesis reactions all alkenes were passed through a short (~1 cm) column of Selexsorb immediately before use. Hexamethylbenzene and 1,3,5-trimethylbenzene were sublimed before use. Solution NMR spectra were recorded on a Bruker Avance 300 MHz spectrometer and referenced to C_6D_5H peak at 7.16 ppm. Solid-state NMR experiments were performed on a 600 MHz Bruker NEO spectrometer in 4 mm zirconia rotors packed in an argon filled glovebox. ^{1}H and $^{13}C\{^{1}H\}$ CPMAS NMR (5.50 μs contact time) spectra were recorded in 4 mm zirconia rotors at 10

KHz magic angle spinning speed. FT-IR spectra were recorded as pressed pellets using a Bruker Alpha IR spectrometer in an argon-filled glovebox. Gas chromatography was carried out using Agilent 7820A GC system equipped with an HP-88 Column.

*5.5.2. Synthesis of **W1***

*5.5.2.1. Synthesis of **W1***

SZO_{300} (519mg, 0.065mmol OH) and W(=O)(Adene)(Me_2Pyr)$_2$ (1.2 equiv, 21.5 mg, 0.078 mmol) were loaded into the same arm of a double-Schlenk flask connected by a frit filter in an argon filled glovebox. The double-Schlenk was sealed, removed from the glovebox, connected to a high vacuum line equipped with a single stage diffusion pump, and evacuated. C_6H_6 (~ 5 mL) was condensed onto the solids at 77 K. The slurry was warmed to room temperature. During this period the originally white **SZO_{300}** evolves to a dark brown color and the supernatant maintains a clear red solution. After stirring for 1 h at room temperature the red solution was filtered to the other side of the double Schlenk flask. **W1** was washed by condensing C_6H_6 onto the solid at 77 K from the other side of the double-Schlenk flask. The slurry containing C_6H_6 and **W1** was warmed to room temperature, stirred for 10 min, and the supernatant was filtered to the other side of the double-Schlenk flask. This process was repeated two more times. The volatiles were removed under vacuum (10^{-6} torr) at room temperature, the brown colored solid was dried for 30 min under diffusion pump vacuum, and stored inside an argon filled glovebox at -20 ^{o}C. Analysis of the residuals left in the flask after removing the volatiles by ^{1}H NMR showed that 0.078 mmol/g Me_2Pyr was generated.

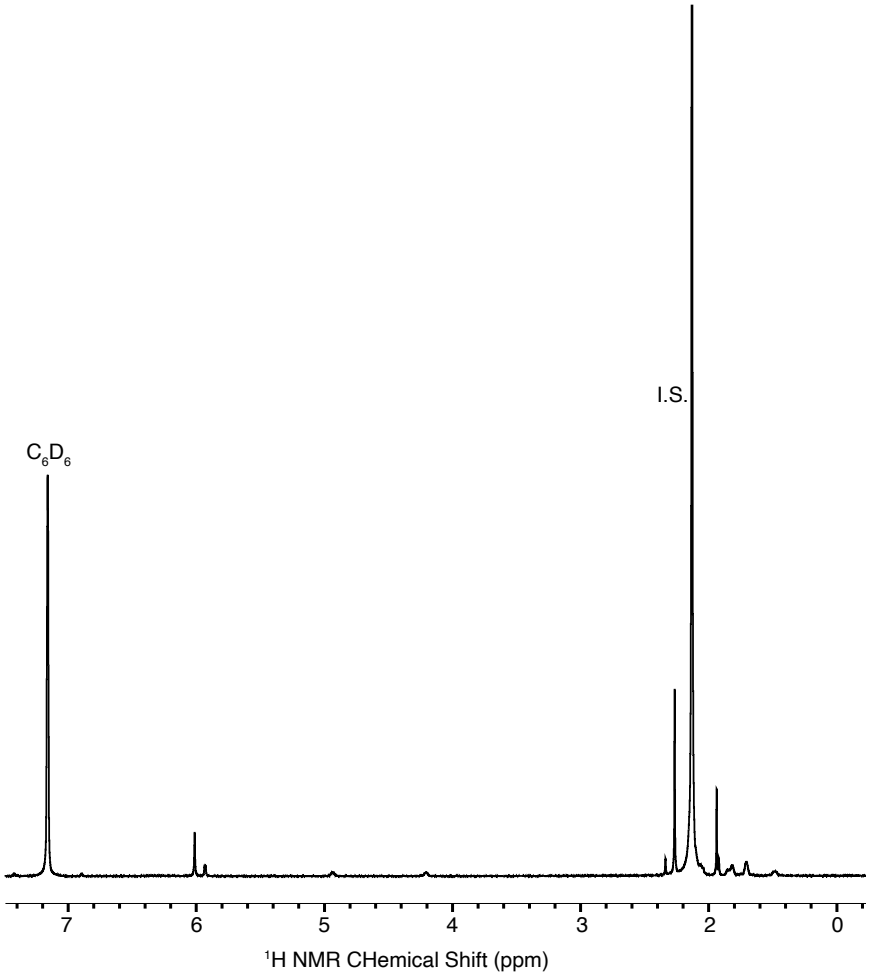

Figure 5. 5. 1. ^{1}H NMR of the volatiles of the reaction

*5.5.2.2. Reaction of W1 with ^{13}C-ethylene (**W2**)*

W1 (100 mg, 7.8 μmol of W) was loaded into a high pressure valved NMR tube in a glovebox. The tube was sealed, connected to a vacuum line, and freeze pumped thawed three times. 30 psi of $^{13}C_2H_4$ (~10 equiv.) was passed through a O_2/H_2O purifying trap and added to the flask at room temperature. The flask was sealed and allowed to react for 2 hours at room temperature. The slurry was decanted off and the material was washed

five times with C_6H_6 resulting in a brown solid. The solid was dried for 1h under high vacuum and the solid was stored at -20 °C in an Ar filled glovebox. The reaction solution was analyzed by ^1H NMR in C_6D_6 with C_6Me_6 as internal standard. This mixture contains 1-^{13}C-adamantylethylene (0.065 mmol g^{-1}). ^{13}C labelled propylene (0.012 mmol g^{-1}) is also formed in this reaction, and is likely a byproduct of intramolecular metallacyclobutane decomposition.

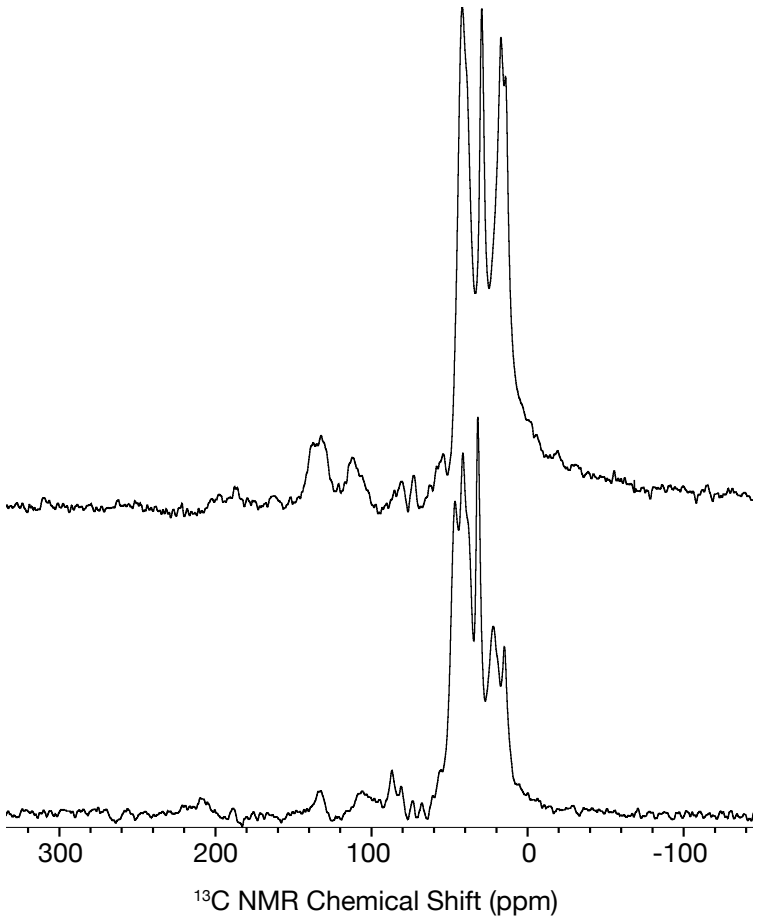

Figure 5. 5. 2. Analytical data for **W2** a) top: $^{13}C\{^{1}H\}$ CP MAS NMR of **W2**; 11kHz, ns = 62k, d1 = 1s; bottom: $^{13}C\{^{1}H\}$ CP MAS NMR of **W2**; 10kHz; ns= 40k; d1=1s.

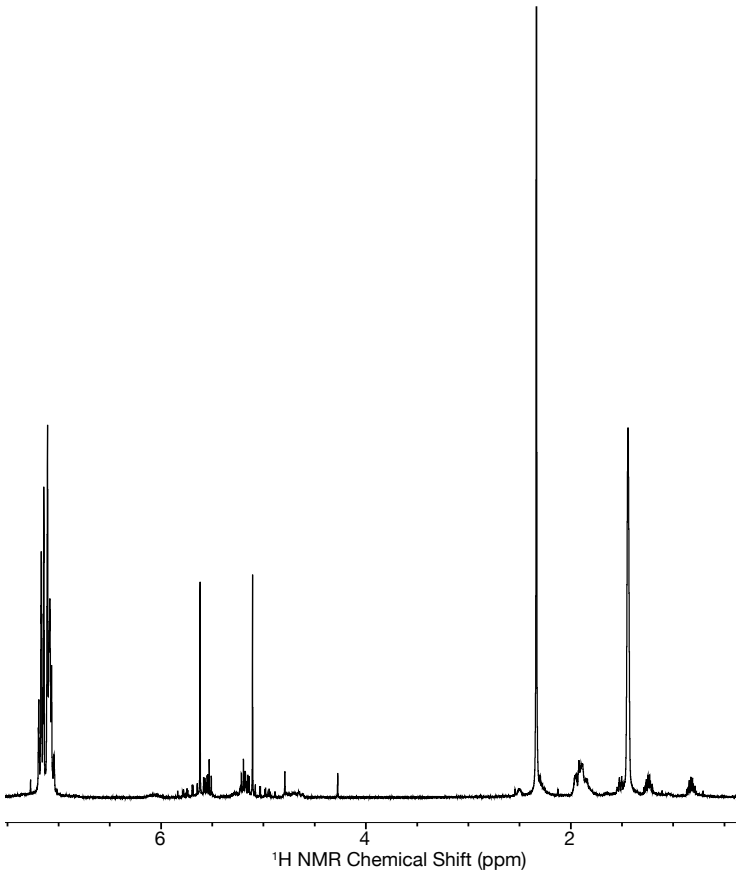

Figure 5. 5. 3. ^{1}H NMR of in-situ reaction between $^{13}C_2H_4$ and **W1**. 0.068mmol/g ethyladamantane evolves during the reaction. 0.012 mmol/g propylene is also formed during this reaction. ^{13}C-ethylene :5.14(d); $2^{13}CH_2Ad$: 4.27(d), 2.67(br s), 1.71-1.94 (m); propylene: 5.84 (m-CH_2), 4.93 (dm-CH_2), 1.28(dt), 1.67(m-CH_3); toluene: (6.96-7.01m), (7.09m), and 2.11(s), cyclohexane: 1.43(s).

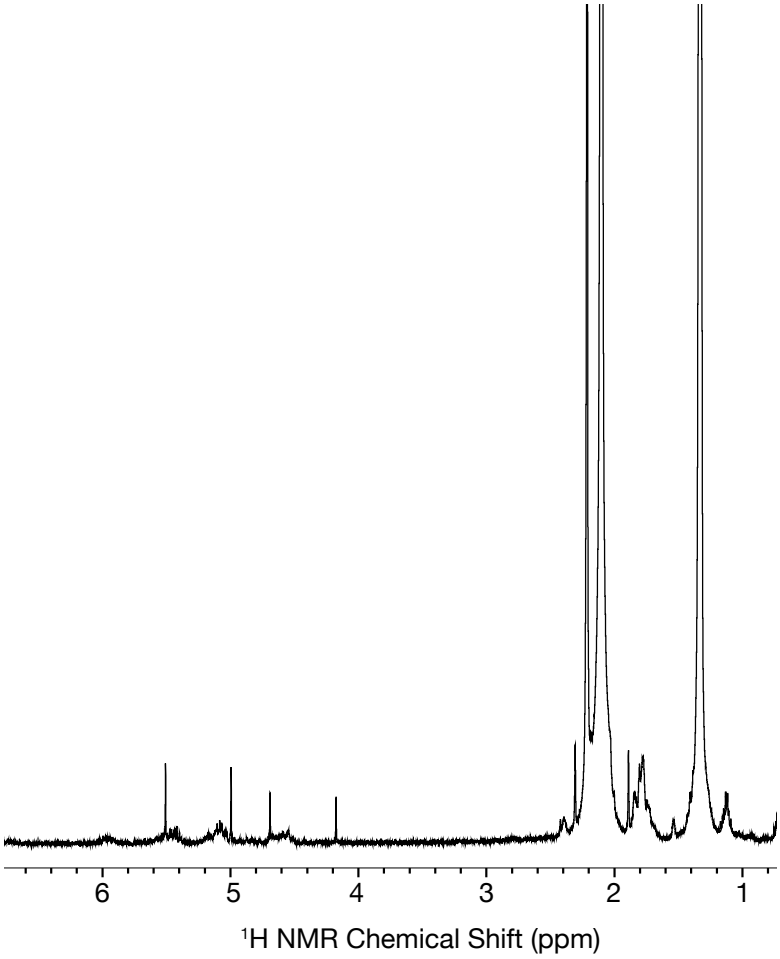

Figure 5. 5. 4. ^{1}H NMR of washings of the reaction of $^{13}C_2H_4$ and **W1**. 0.068mmol/g ethyladamantane evolves during the reaction. 5.41(^{13}C-ethylene), 4.88(^{13}C-ethylene); $^{13}C_2H_4$ $2CH_2Ad$: 4.27(d), 2.67(br s), 1.71-1.94 (m); hexamethylbenzene: 2.11(s); cyclohexane (1.43s), toluene: 2.11(s).

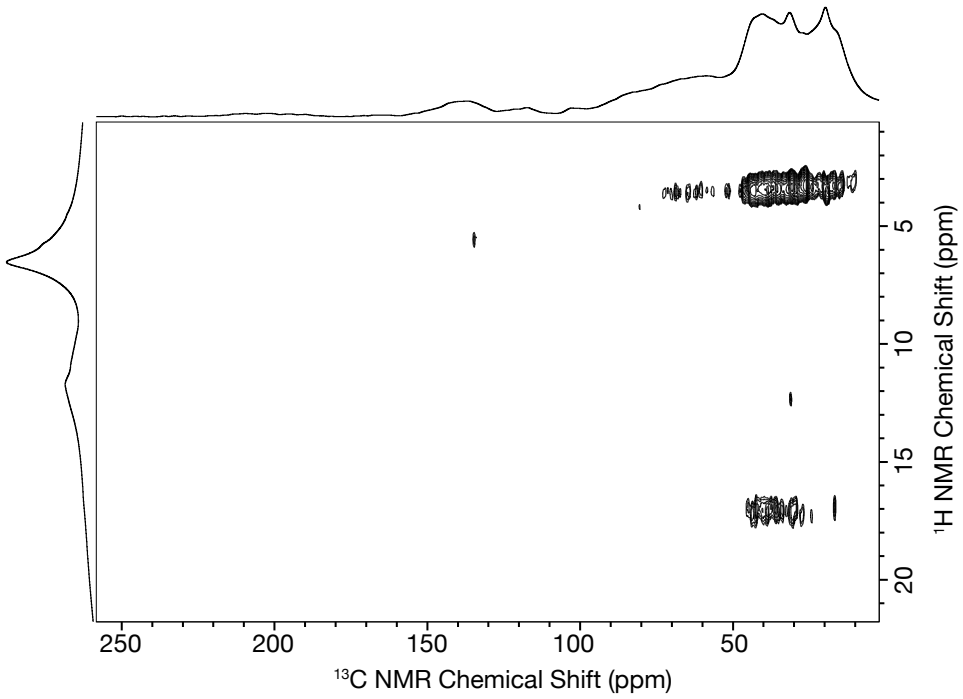

Figure 5. 5. 5. Two-dimensional ^{1}H-^{13}C HETCOR spectrum of **W2**.

5.5.3. Catalytic Metathesis reactions with W1

5.5.3.1. Catalytic metathesis

W1 was loaded into a vial equipped with a stir bar and capped with a septum and a needle in a N_2 filled glovebox. Neat alkene was added to the solid and the mixture was stirred at room temperature. An aliquot (~10 μL) was periodically removed from the mixture and analyzed by ^{1}H NMR spectroscopy against hexamethylbenzene as the internal standard. All reactions were carried out in a vial plugged with a septum and pierced with a needle to allow ethylene to escape from the mixture. For cis-4-nonene, the aliquots were subjected to gas chromatography to determine % conversion. Product formation was determined without taking cis/trans isomerization of the substrate into account.

5.5.4. ^{1}H NMR spectra of reactions

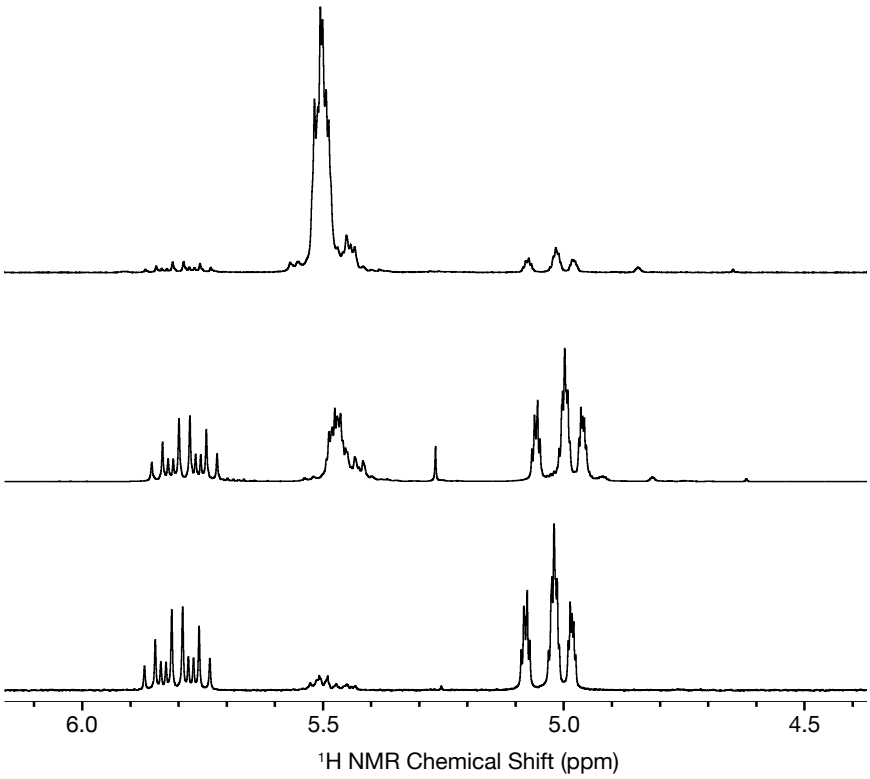

Figure 5. 5. 6. ^{1}H NMR of raw data for metathesis of 1-decene (1mol% W) on the olefinic region

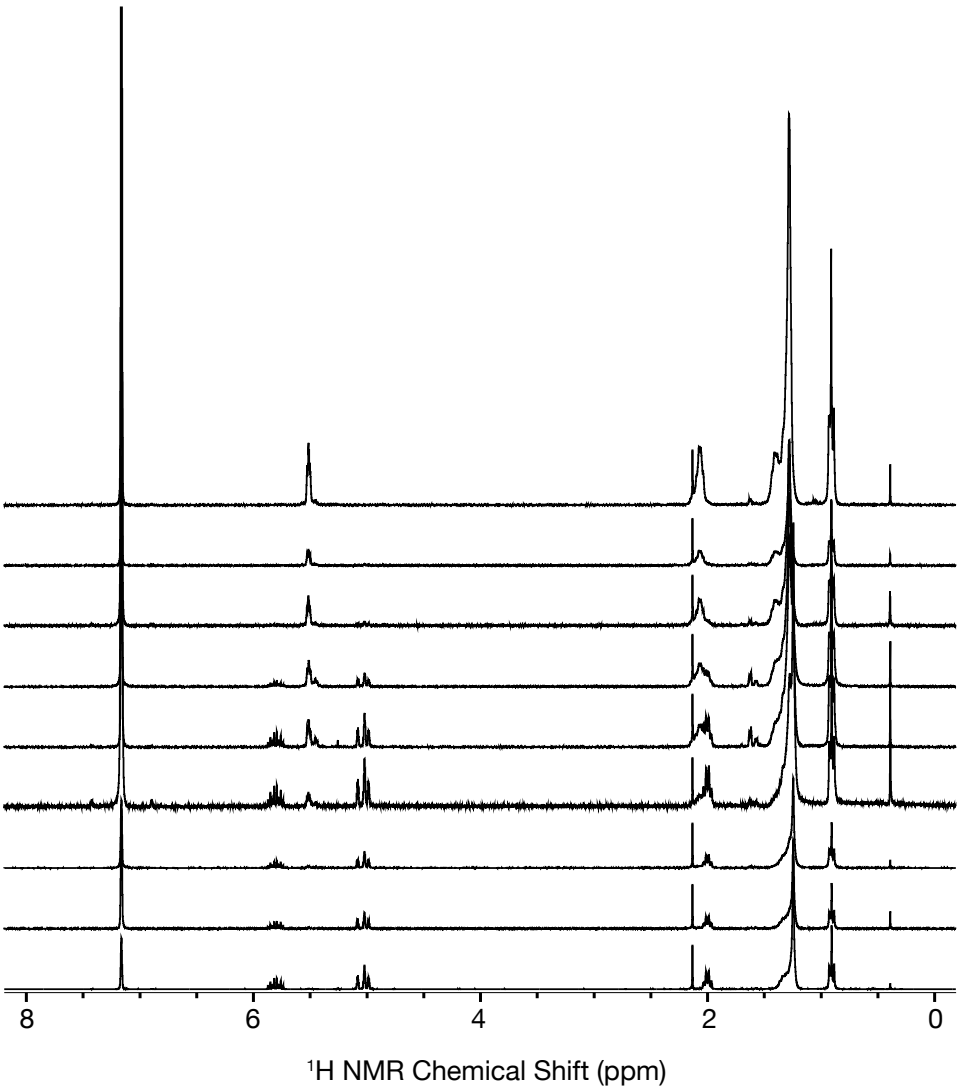

Figure 5. 5. 7. Raw data of the metathesis of 1-decene (0.05mol% W)

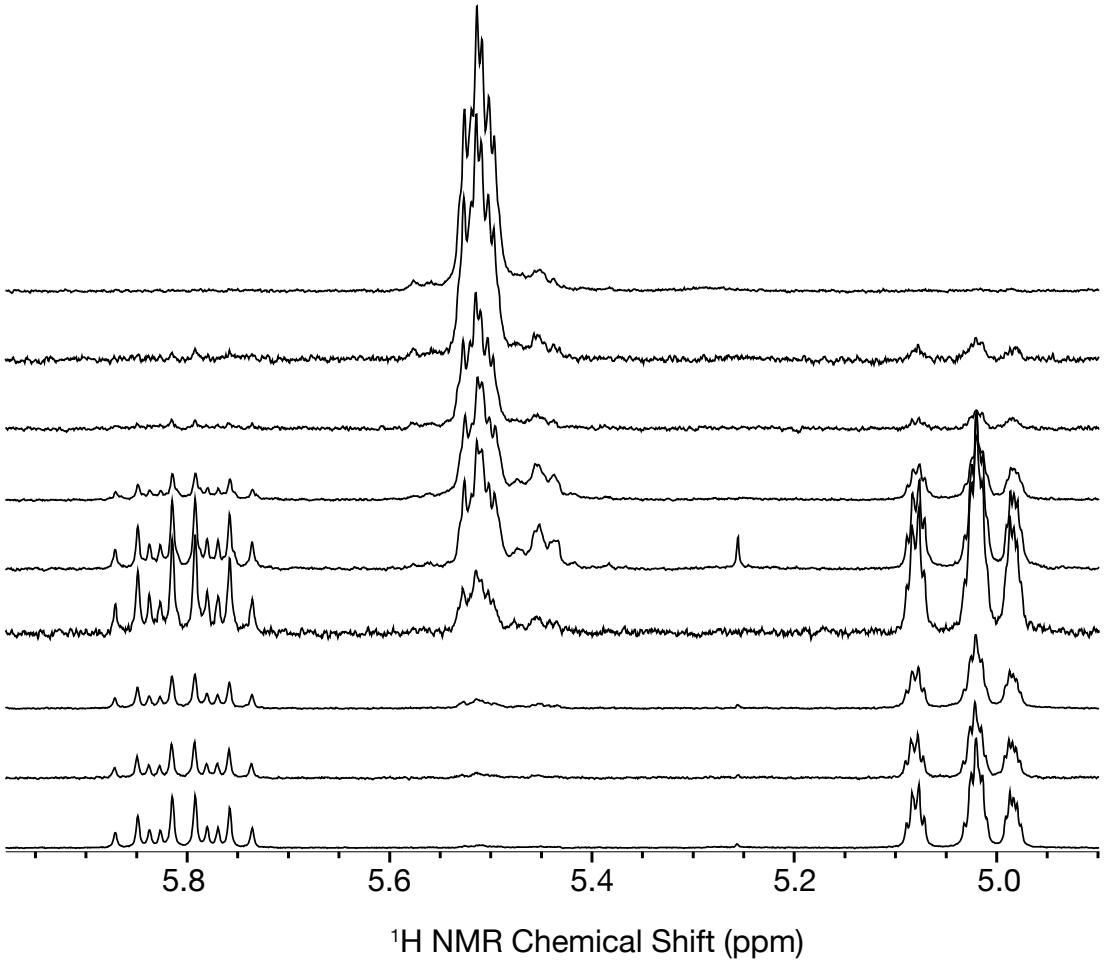

Figure 5. 5. 8. Zoom in of the region of 6.0ppm to 5.0 ppm of the raw data metathesis of 1-decene (0.05mol% W)

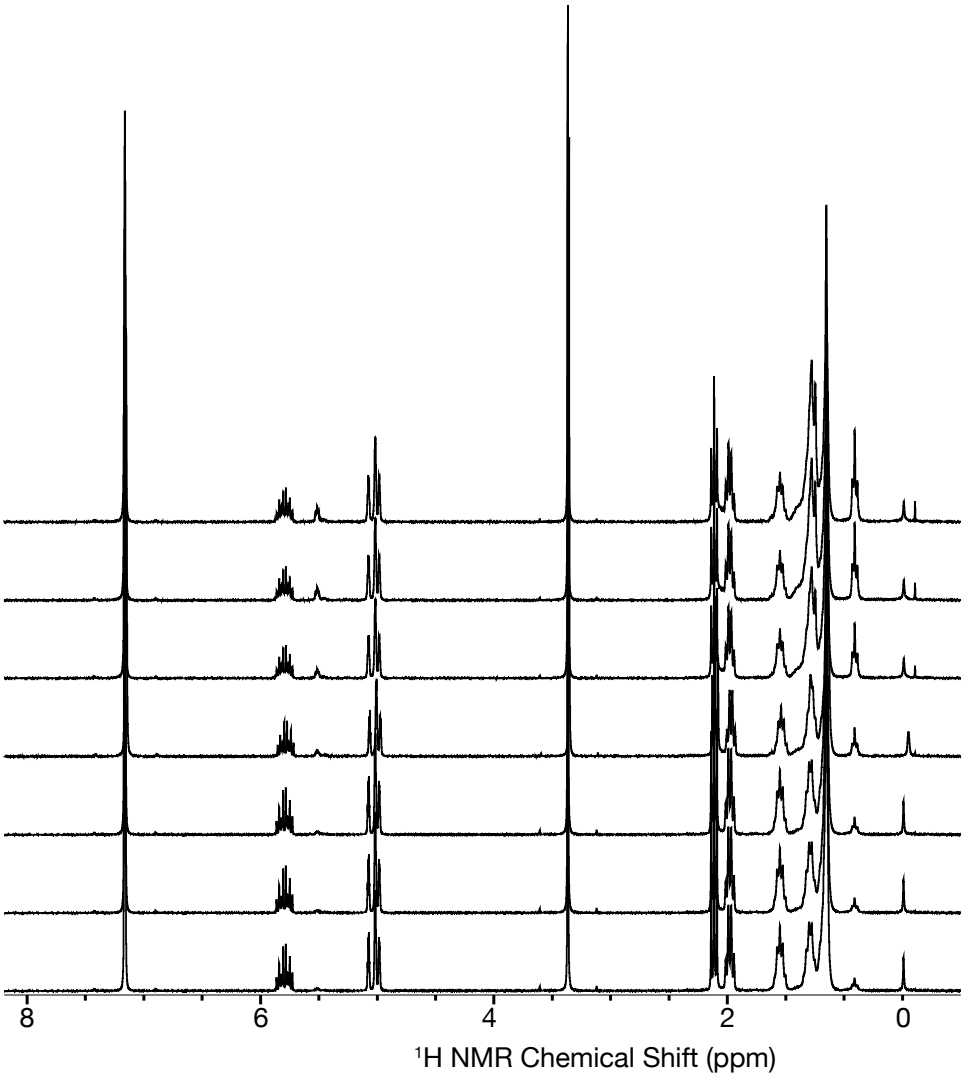

Figure 5. 5. 9. Raw data for the metathesis of methyl 10-undeconate

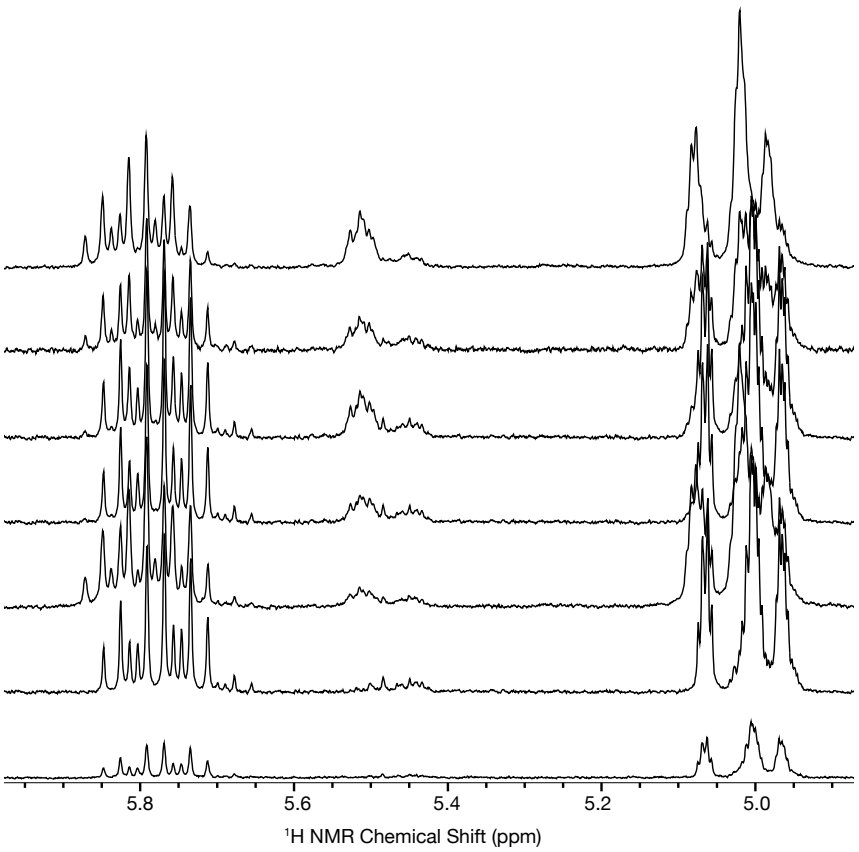

Figure 5. 5. 10. Raw data for the metathesis of 1-octene-8-triemthylsilane

5.5.5. E vs Z Plots

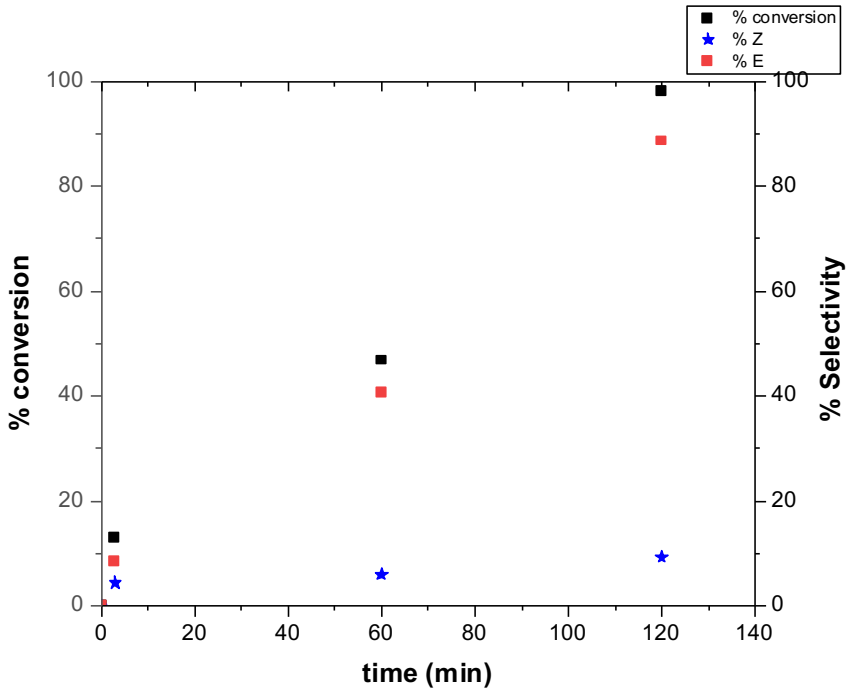

Figure 5. 5. 11. Product conversion vs time plot for the metathesis of 1-decene (1mol% W); black square trace = total % conversion; blue star trace = %Z conversion; red square trace = % E conversion

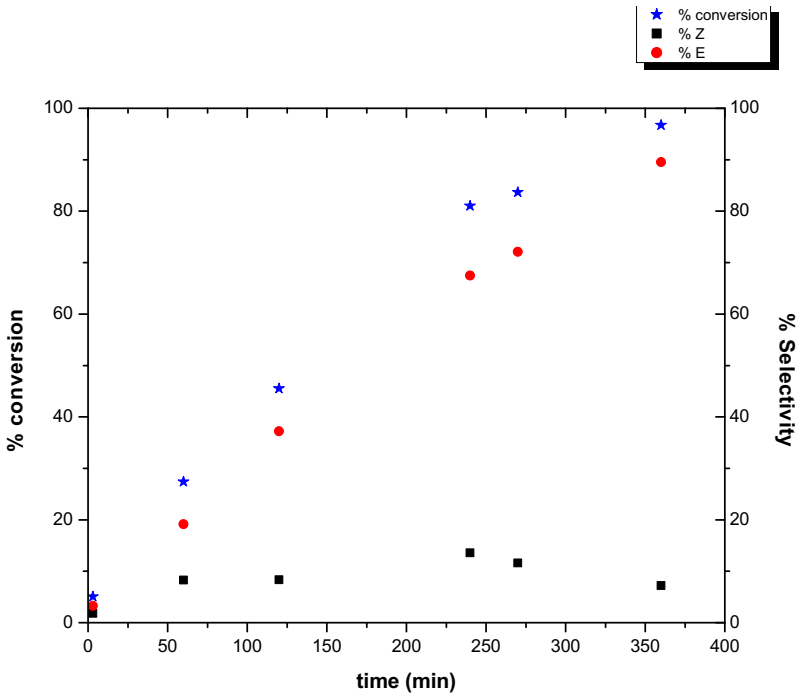

Figure 5. 5. 12. Product conversion vs time plot for the metathesis of 1-decene (0.1mol% W); blue star trace = % conversion; red circle trace = % E selectivity; black squares = % Z selectivity.

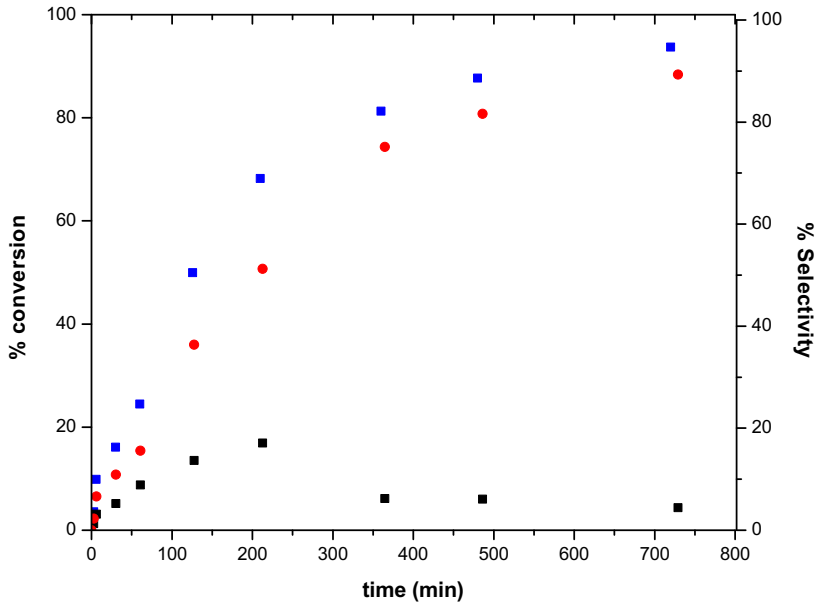

Figure 5. 5. 13. Product conversion vs time plot for the metathesis of 1-decene (0.05mol% W); blue square trace = total conversion; black square trace = % Z selectivity; red circle trace = % E selectivity

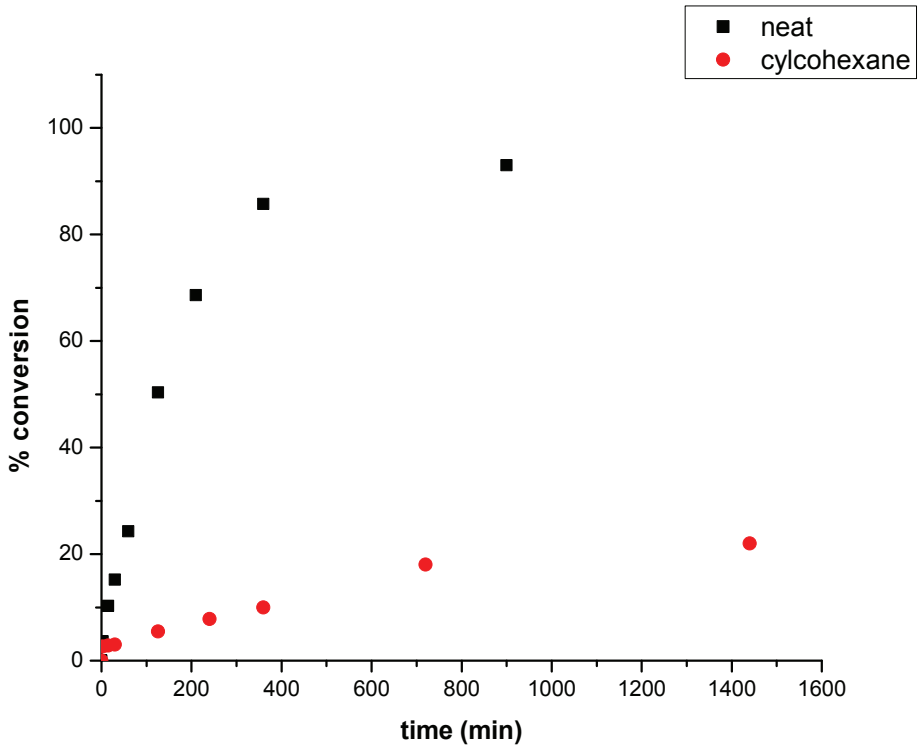

Figure 5. 5. 14. Product conversion vs time plot for the metathesis of 1-decene (0.05mol% W); black trace is neat; red trace is 0.1M cyclohexane solution of 1-decene. Note 0.1M DCM solution of 1-decene did not result in any product formation.

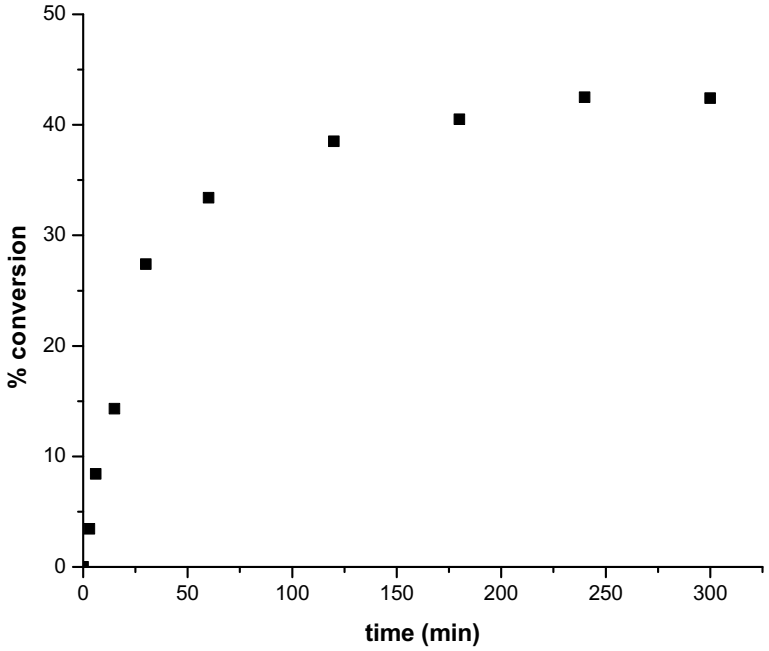

Figure 5. 5. 15. Product conversion vs time plot for the metathesis of cis-4-nonene (0.05mol% W)

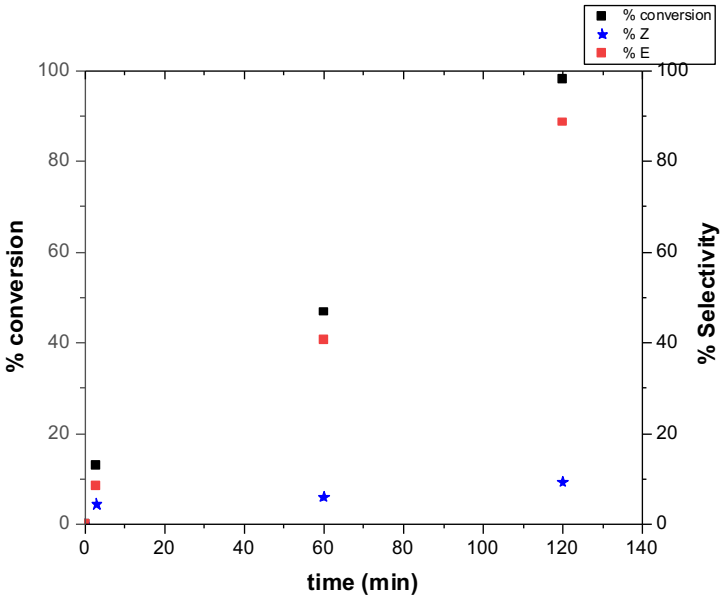

Figure 5. 5. 16. Product conversion vs time plot for the metathesis of methyl 10-undecenoate (0.05mol% W); black square trace = overall % conversion; blue start trace = % Z conversion; red square conversion = % E conv

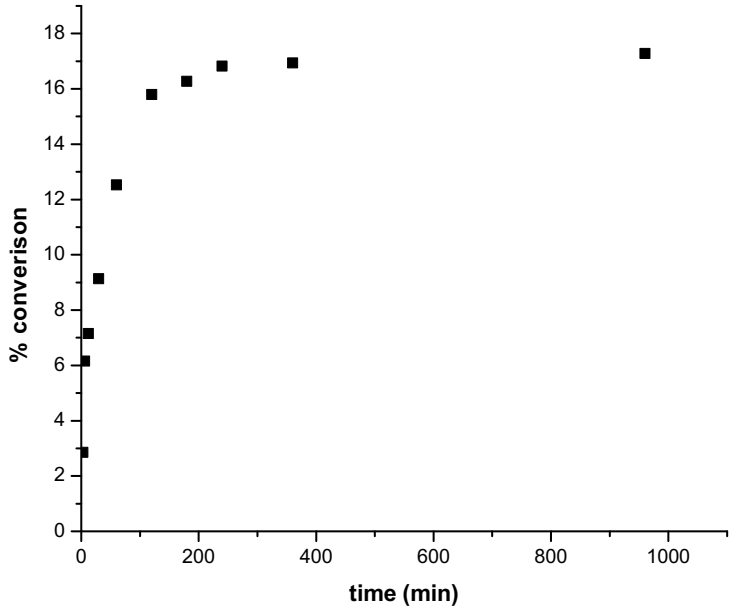

Figure 5. 5. 17. Product conversion of 1-octene-8-trimethylsilane vs time plot (0.05mol% W)

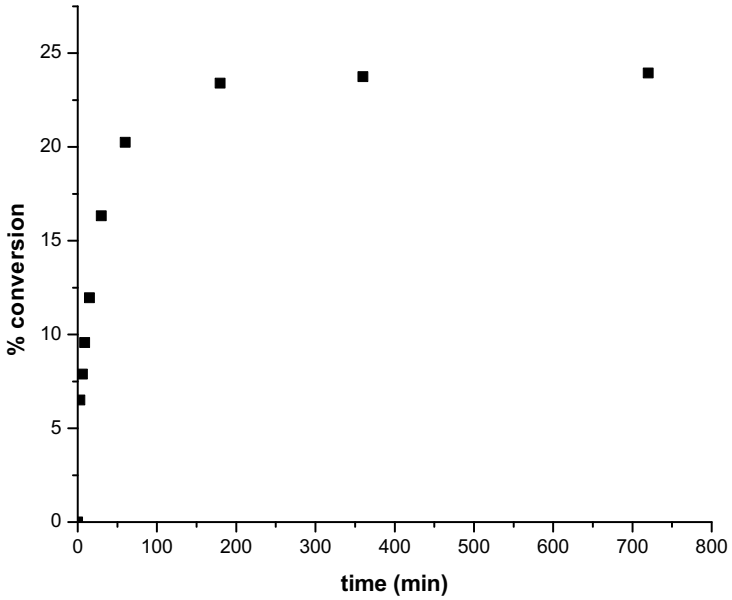

Figure 5. 5. 18. Product conversion of cis-3-hexene to trans-3-hexene (0.05mol% W)

5.6. References

1. Ivin, K. J. (Kenneth J., Mol, J. C. and Ivin, K. J. (Kenneth J. Olefin metathesis and metathesis polymerization. 472 (1997).

2. Streck, R. Olefin metathesis in industry - a status report. *J. Mol. Catal.* **46**, 305–316 (1988).

3. Lwin, S. and Wachs, I. E. Olefin metathesis by supported metal oxide catalysts. *ACS Catal.* **4**, 2505–2520 (2014).

4. Hérisson, P. J.-L. and Chauvin, Y. Catalyse de transformation des oléfines par les complexes du tungstène. II. Télomérisation des oléfines cycliques en présence d'oléfines acycliques. *Die Makromol. Chemie* **141**, 161–176 (1971).

5. Chauvin, Y. Olefin metathesis: The early days (nobel lecture). *Angew. Chemie - Int. Ed.* **45**, 3740–3747 (2006).

6. Schrock, R. R. Multiple metal-carbon bonds for catalytic metathesis reactions (nobel lecture). *Angew. Chemie - Int. Ed.* **45**, 3748–3759 (2006).

7. Schrock, R. R. Recent advances in olefin metathesis by molybdenum and tungsten imido alkylidene complexes. *J. Mol. Catal. A Chem.* **213**, 21–30 (2004).

8. Schrock, R. R. Olefin Metathesis by Well-Defined Complexes of Molybdenum and Tungsten. in *Alkene Metathesis in Organic Synthesis* 1–36 (Springer, Berlin, Heidelberg, 1998). doi:10.1007/3-540-69708-X_1.

9. Grubbs, R. H. Olefin-Metathesis Catalysts for the Preparation of Molecules and Materials (Nobel Lecture). *Angew. Chemie Int. Ed.* **45**, 3760–3765 (2006).

10. Grubbs, R. H. and Chang, S. Recent advances in olefin metathesis and its application in organic synthesis. *Tetrahedron* **54**, 4413–4450 (1998).

11. Trnka, T. M. and Grubbs, R. H. The Development of L2X2RuCHR Olefin Metathesis Catalysts: An Organometallic Success Story. *Acc. Chem. Res.* **34**, 18–29 (2000).

12. Poater, A., Solans-Monfort, X., Clot, E., Copéret, C. and Eisenstein, O. Understanding d0-olefin metathesis catalysts: Which metal, which ligands? *J. Am. Chem. Soc.* **129**, 8207–8216 (2007).

13. Solans-Monfort, X., Clot, E., Copéret, C. and Eisenstein, O. d0 Re-based olefin metathesis catalysts, Re(≡CR)(=CHR)(X) (Y): The key role of X and Y ligands for

efficient active sites. *J. Am. Chem. Soc.* **127**, 14015–14025 (2005).

14. Schowner, R. *et al.* Mono- and Bisionic Mo- and W-Based Schrock Catalysts for Biphasic Olefin Metathesis Reactions in Ionic Liquids. *Chem. – A Eur. J.* **24**, 13336–13347 (2018).

15. Greene, R. M. E., Ivin, K. J., Rooney, J. J., Kress, J. and Osborn, J. A. Preparation of block copolymers by ring-opening polymerization of cycloalkenes initiated by a tungstencyclopentylidene complex. *Die Makromol. Chemie* **189**, 2797–2805 (1988).

16. Kress, J. and Osborn, J. A. Stereochemically Nonrigid Tungsten Alkylidene Complexes. Barriers to Rotation about the Tungsten to Carbon Double Bond. *J. Am. Chem. Soc.* **109**, 3953–3960 (1987).

17. Schrock, R. R., Hoveyda, A. H., Schrock, R. R. and Hoveyda, A. H. Molybdenum and Tungsten Imido Alkylidene Complexes as Efficient Olefin-Metathesis Catalysts. *Angew. Chemie Int. Ed.* **42**, 4592–4633 (2003).

18. Schrock, R. R. Recent advances in high oxidation state Mo and W imido alkylidene chemistry. *Chem. Rev.* **109**, 3211–3226 (2009).

19. Zhizhko, P. A., Mougel, V., De Jesus Silva, J. and Copéret, C. Benchmarked Intrinsic Olefin Metathesis Activity: Mo vs. W. *Helv. Chim. Acta* **101**, e1700302 (2018).

20. Gordon, C. P. *et al.* Metathesis Activity Encoded in the Metallacyclobutane Carbon-13 NMR Chemical Shift Tensors. *ACS Cent. Sci.* **3**, 759–768 (2017).

21. De Jesus Silva, J. *et al.* Boosting the Metathesis Activity of Molybdenum Oxo Alkylidenes by Tuning the Anionic Ligand σ Donation. *Inorg. Chem.* **60**, 6875–6880 (2021).

22. Mougel, V. and Copéret, C. Magnitude and consequences of or ligand σ-donation on alkene metathesis activity in d0 silica supported (≡SiO)W(NAr)(=CHtBu) (OR) catalysts. *Chem. Sci.* **5**, 2475–2481 (2014).

23. Pucino, M. *et al.* Promoting Terminal Olefin Metathesis with a Supported Cationic Molybdenum Imido Alkylidene N-Heterocyclic Carbene Catalyst. *Angew. Chemie Int. Ed.* **57**, 14566–14569 (2018).

24. De Jesus Silva, J. *et al.* Silica-Supported Cationic Tungsten Imido Alkylidene Stabilized by an N-Heterocyclic Carbene Ligand Boosts Activity and Selectivity in the Metathesis of α-Olefins. *Helv. Chim. Acta* **103**, e2000161 (2020).

25. Nater, D. F., Paul, B., Lätsch, L., Schrock, R. R. and Copéret, C. Increasing Olefin Metathesis Activity of Silica-Supported Molybdenum Imido Adamantylidene Complexes through E Ligand σ-Donation. *Helv. Chim. Acta* **104**, e2100151 (2021).

26. Schrock, R. R., Hoveyda, A. H., Schrock, R. R. and Hoveyda, A. H. Molybdenum and Tungsten Imido Alkylidene Complexes as Efficient Olefin-Metathesis Catalysts. *Angew. Chemie Int. Ed.* **42**, 4592–4633 (2003).

27. Schrock, R. R. Recent advances in high oxidation state Mo and W imido alkylidene chemistry. *Chem. Rev.* **109**, 3211–3226 (2009).

28. Stalzer, M. M., Delferro, M. and Marks, T. J. Supported Single-Site Organometallic Catalysts for the Synthesis of High-Performance Polyolefins. *Catal. Lett. 2014 1451* **145**, 3–14 (2014).

29. Wegener, S. L., Marks, T. J. and Stair, P. C. Design strategies for the molecular level synthesis of supported catalysts. *Acc. Chem. Res.* **45**, 206–214 (2012).

30. Copéret, C. *et al.* Olefin metathesis: what have we learned about homogeneous and heterogeneous catalysts from surface organometallic chemistry? *Chem. Sci.* **12**, 3092–3115 (2021).

31. De Jesus Silva, J. *et al.* Boosting the Metathesis Activity of Molybdenum Oxo Alkylidenes by Tuning the Anionic Ligand σ Donation. *Inorg. Chem.* **60**, 6875–6880 (2021).

32. Pucino, M. *et al.* Cationic Silica-Supported N-Heterocyclic Carbene Tungsten Oxo Alkylidene Sites: Highly Active and Stable Catalysts for Olefin Metathesis. *Angew. Chemie Int. Ed.* **55**, 4300–4302 (2016).

33. De Jesus Silva, J. *et al.* Silica-Supported Cationic Tungsten Imido Alkylidene Stabilized by an N-Heterocyclic Carbene Ligand Boosts Activity and Selectivity in the Metathesis of α-Olefins. *Helv. Chim. Acta* **103**, e2000161 (2020).

34. Blanc, F. *et al.* Direct observation of reaction intermediates for a well defined heterogeneous alkene metathesis catalyst. *Proc. Natl. Acad. Sci. U. S. A.* **105**, 12123–12127 (2008).

35. Mougel, V. *et al.* Quantitatively Analyzing Metathesis Catalyst Activity and Structural Features in Silica-Supported Tungsten Imido-Alkylidene Complexes. *J. Am. Chem. Soc.* **137**, 6699–6704 (2015).

36. Conley, M. P. *et al.* A well-defined silica-supported tungsten oxo alkylidene is a highly active alkene metathesis catalyst. *J. Am. Chem. Soc.* **135**, 19068–19070

(2013).

37. Conley, M. P., Forrest, W. P., Mougel, V., Copéret, C. and Schrock, R. R. Bulky Aryloxide Ligand Stabilizes a Heterogeneous Metathesis Catalyst. *Angew. Chemie Int. Ed.* **53**, 14221–14224 (2014).

38. Mougel, V., Pucino, M. and Copéret, C. Strongly σ donating thiophenoxide in silica-supported tungsten oxo catalysts for improved 1-alkene metathesis efficiency. *Organometallics* **34**, 551–554 (2015).

39. Boudjelel, M., Zhai, F., Schrock, R. R., Hoveyda, A. H. and Tsay, C. Oxo 2-Adamantylidene Complexes of Mo(VI) and W(VI). *Organometallics* **40**, 838–842 (2021).

40. Conley, M. P. *et al.* A well-defined silica-supported tungsten oxo alkylidene is a highly active alkene metathesis catalyst. *J. Am. Chem. Soc.* **135**, 19068–19070 (2013).

41. Conley, M. P. *et al.* Bulky Aryloxide Ligand Stabilizes a Heterogeneous Metathesis Catalyst. *Angew. Chemie* **126**, 14445–14448 (2014).

42. Nater, D. F., Boudjelel, M., Lätsch, L., Schrock, R. R. and Copéret, C. W-oxo Adamantylidenes: Stable Molecular Precursors for Efficient Silica-Supported Metathesis Catalysts. *Helv. Chim. Acta* **105**, e202200013 (2022).

43. Tafazolian, H., Culver, D. B. and Conley, M. P. A Well-Defined Ni(II) α-Diimine Catalyst Supported on Sulfated Zirconia for Polymerization Catalysis. *Organometallics* **36**, 2385–2388 (2017).

Chapter 6. Direct Synthesis of Propylene from Ethylene

6.1. Abstract

Propylene is a vital small molecule feedstock, and current methods to produce propylene are unsustainable. This chapter shows high oxidation state W(VI) metallacyclopentanes supported on $SiO_{2\text{-}700}$ ring contracts to Me-substituted metallacyclobutanes that release propene under mild conditions. ^{13}C MAS NMR experiments show these intermediates are formed, and are likely responsible for the mild ethylene to propylene reactivity. This first-generation catalyst gives 29 ± 1 mol propylene per mol W at 85°C in the presence of blue LEDs.

6.2. Introduction

The most common catalytic methods to produce propylene are steam cracking (> 850°C), propane dehydrogenation, and ethenolysis of 2-butenes. All of these methods are energy intensive. Propane dehydrogenation is thermodynamically unfavorable at 25°C with a ΔG(298) of ~ 20.9 $kcalmol^{-1}$, Figure 6.1.1. Ethenolysis of 2-butenes is thermodynamically favorable, ΔG(298) of ~-5.7 $kcalmol^{-1}$, but operates at 400°C due to complicates with forming active sites in common industrial catalysts. This shows the need for more energy- and atom-efficient manufacturing processes of propylene.

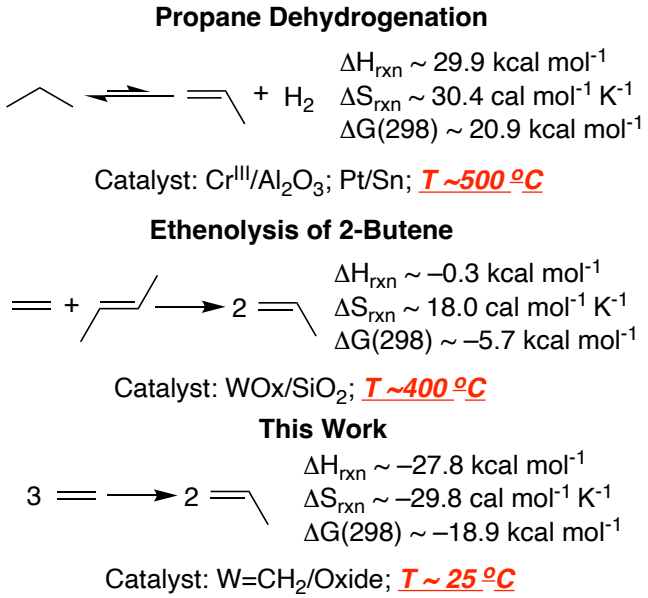

Figure 6.1.1. Catalytic methods to produce propylene

This chapter describes a new reaction to synthesize propylene directly from ethylene. This reaction is thermodynamically more favorable than propane dehydrogenation or ethenolysis of 2-butenes. The proposed mechanism is shown in Scheme 6.1.1. This mechanism involves a ring contraction of a metallacyclopentane (WC_4) to form a substituted Me–metallacyclobutane (WC_3), which releases propylene to form a W–methylidene that reacts with ethylene to form an unsubstituted WC_3. The unsubstituted WC_3 rearranges to a W–propylene complex,[1] and reacts with excess ethylene to form a WC_4 closing the catalytic cycle.

The first report on ring contraction showed that propylene could be dimerized to a 2,3-1,1-dimethyl-butene and 2-methyl-1,1-pentene in the prescene of Cp^*Cl_2Ta(propylene) complex.[2] It was proposed that the head-to-tail dimer is formed from an unobservable α,β'–dimethyl tantallacyclopentane complex and the

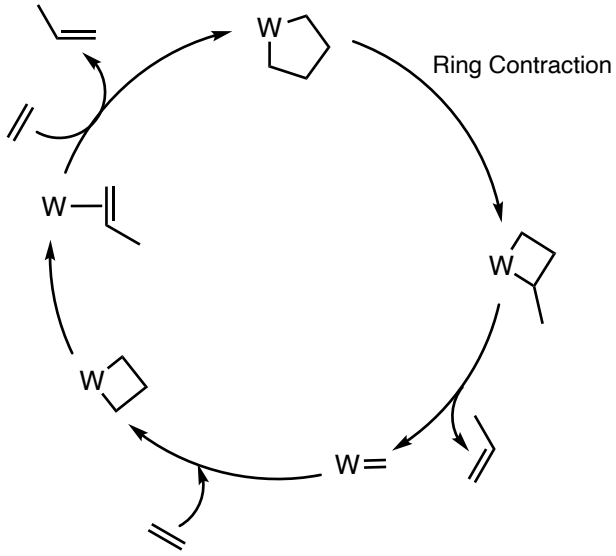

Scheme 6.1.1. Proposed catalytic cycle for ethylene to propylene

tail-to-tail dimer is formed from an observable trans-β,β'-dimethyl tantallacycle, Scheme 6.1.32. Deuterium labelling studies showed that a ring contraction mechanism was plausible for the formation of each dimer. The second report shows that the contraction of MC_4 to MC_3 was a reasonable mechanistic pathway to form alkylidenes considering that MC_3 complexes may rearrange to give metathesis-type products.[3] These are the only two documented ring-contractions of MC_4.

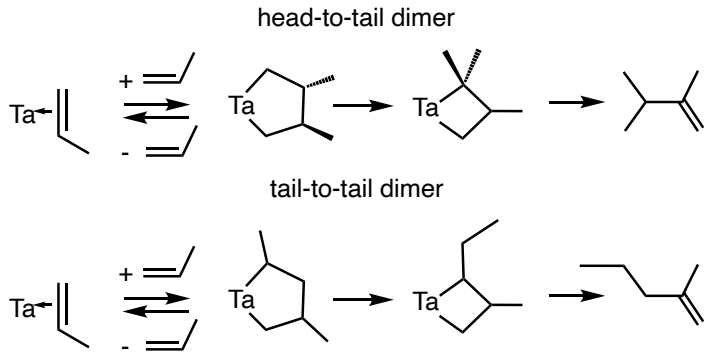

Scheme 6.1.2. Formation of 2,3-1,1-dimethyl-butene and 2-methyl-1,1-pentene via proposed tantallacycles

Schrock and coworkers reported the first experimental evidence of a ring-contraction in high oxidation state W chemistry, Scheme 6.1.3. $W(NAr)(OSiPh_3)_2(C_4H_8)$ reacts with ethylene at room temperature in the presence of blue LEDs to give a propylene complex and the square pyramidal tungstacyclobutane complex. The intermediates in this reaction are proposed to be α and β–methyl tungstacyclobutane complexes. The α–methyl tungstacyclobutane complex is the key to enter an olefin metathesis active system, since it can cyclorevert to form the W–methylidene. The reformation of a W–methylidene in the presence of ethylene leads to an important step in ethenolysis reactions. This chapter will discuss the reaction of $W(NAr)(C_4H_8)(OSiPh_3)_2$ with $SiO_{2\text{-}700}$ to generate a species that is active for catalytic cross-metathesis of ethylene to propylene.

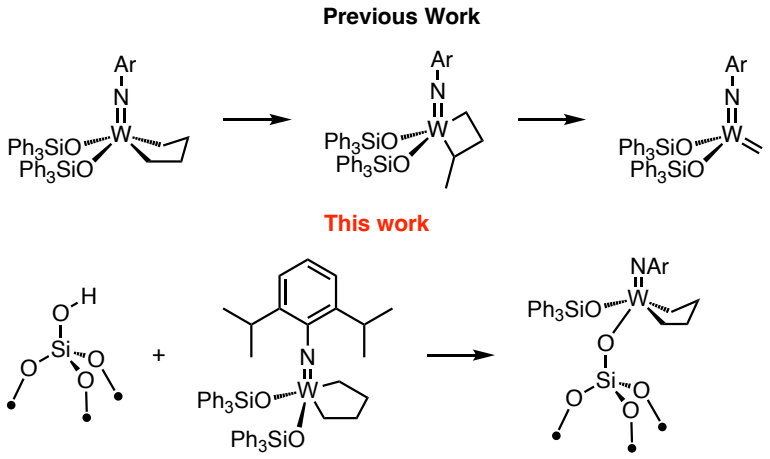

Scheme 6.1.3. Ring contraction of $W(NAr)(C_4H_8)(OSiPh_3)_2$ to form the α methyl tungstacyclobutane that cycloreverts to form a metathesis active W-methylidene (top). Reaction of $W(NAr)(C_4H_8)(OSiPh_3)_2$ with $SiO_{2\text{-}700}$ to form a supported metallacyclopentane species (bottom).

6.3. Results and Discussion

6.3.1. Synthesis of (≡SiO)(W(NAr)($^{13}C_4H_8$)(OSiPh$_3$)

Under rigorous exclusions of light, $W(^{13}C_4H_8)NAr(OSiPh_3)_2$ reacts with silica partially dehydroxylated at 700°C ($SiO_{2\text{-}700}$) to form (≡SiO)(W(NAr)($^{13}C_4H_8$)(OSiPh$_3$), and isomers of (≡SiO)(W(NAr)($^{13}C_3H_5$Me)(OSiPh$_3$), Scheme 6.3.1. This mixture of species can be readily identified using solid-state ^{13}C NMR methods. The 2D Dipolar Assisted Rotational Resonance (DARR) spectra shows the correlations between C_α and C_β as well as the characteristic coupling pattern connecting the W($^{13}C_3H_5$Me) fragment, Figure 6.1.2.

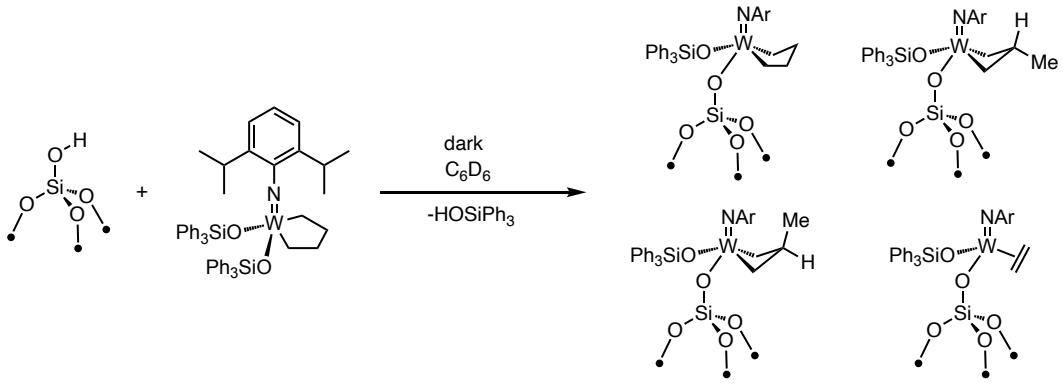

Scheme 6.3.1. Reaction of W($^{13}C_4H_8$)NAr(OSiPh$_3$)$_2$ with $SiO_{2\text{-}700}$

The ^{13}C Dipolar Assisted Rotational Resonance (DARR) contains crosspeaks between ^{13}C signals at 71.5 and 34.1ppm that correspond to the C_α and C_β of (≡SiO)(W(NAr)($^{13}C_4H_8$)(OSiPh$_3$). The signals at 63.3 (C_α), 27.2(C_β), and 12.1(Me) ppm correspond to the W(NAr)($^{13}C_3H_5Me$)(OSiPh$_3$)$_2$. In rigorous exclusion of light there is no evidence that the ethylene complex is formed, Figure 6.3.1, but in less rigorous light exclusion, formation of the ethylene complex can be readily identified by 2D DARR experiments, Figure 6.3.2. The signals at 60.0 and 51.7 ppm correspond to (≡SiO)(W(NAr)($^{13}C_2H_4$)(OSiPh$_3$).

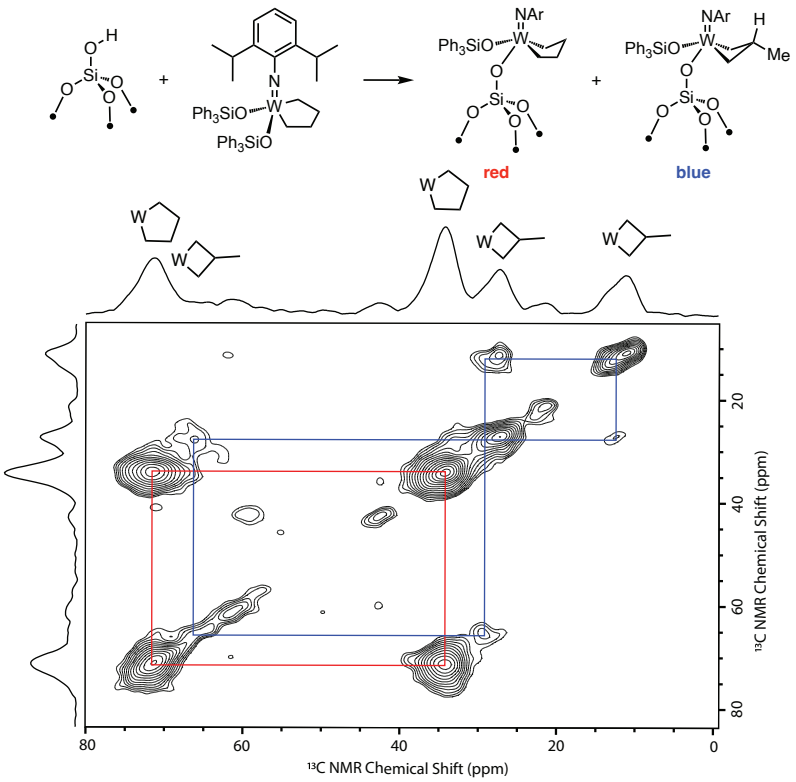

Figure 6.3.1. Expansion of the ^{13}C-^{13}C Dipolar Assisted Rotational Resonance spectrum of the grafting reaction. The grafting reaction was performed with rigorous exclusion of light.

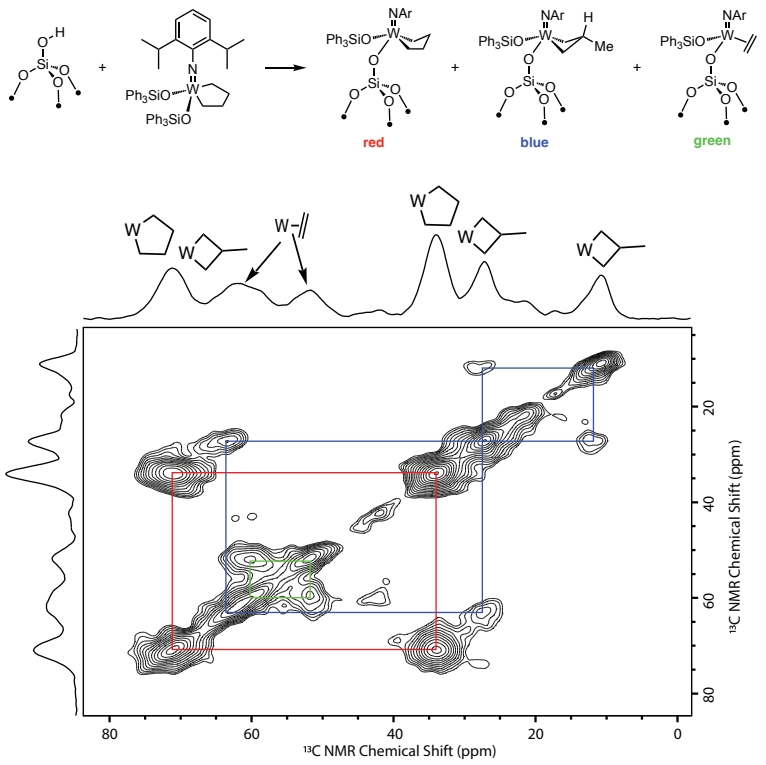

Figure 6.3.2. Expansion of the ^{13}C–^{13}C Dipolar Assisted Rotational Resonance Spectrum of the grafting reaction under less rigorous light exclusion.

6.3.2. Photolysis with Blue LEDs at 85°C

Treatment of (≡SiO)(W(NAr)($^{13}C_4H_8$)(OSiPh$_3$) with LEDs at 85°*C* temperature resulted in the formation of (≡SiO)W(NAr)(OSiPh$_3$)($^{13}C_3H_5$Me) and (≡SiO)W(NAr)(OSiPh$_3$)($^{13}C_2H_4$). The isomers were readily distinguished by ^{13}C–^{13}C DARR NMR experiments. Figure 6.3.3. does not contain any signals for the W(C_4H_8). The signals in the spectra are consistent with the formation of W(C_2H_4), β-(WC_3H_5Me), and one isomer of the α–WC_3H_5Me.

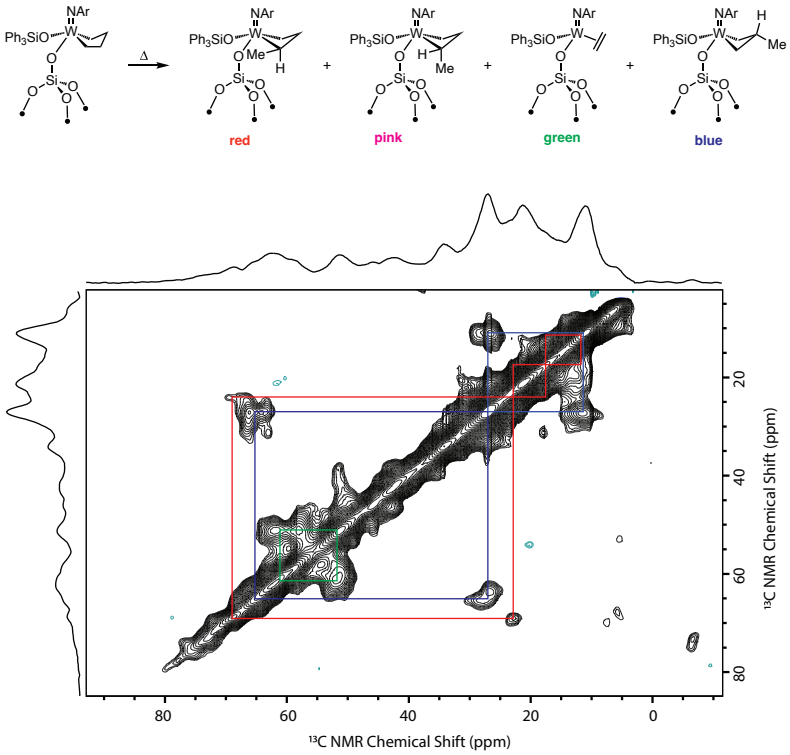

Figure 6.3.3. Expansion of the ^{13}C–^{13}C Dipolar Assisted Rotational Resonance Spectrum of the material exposed to LEDs for 6h.

6.3.3. Thermal Treatment of (≡SiO)(W(NAr)($^{13}C_4H_8$)(OSiPh$_3$)

(≡SiO)(W(NAr)($^{13}C_4H_8$)(OSiPh$_3$) was heated at 85°C for 6 hours under rigorous exclusion of light. Figure 6.3.4 is significantly more complex, and does not contain any signals for (≡SiO)(W(NAr)($^{13}C_4H_8$)(OSiPh$_3$). The spectra shows that (≡SiO)(W(NAr)($^{13}C_2H_4$)(OSiPh$_3$), one isomer of the β–W($^{13}C_3H_5$Me), and two isomers of the α–W($^{13}C_3H_5$Me) are formed. This NMR experiment cannot distinguish between the two α–W($^{13}C_3H_5$Me) isomers.

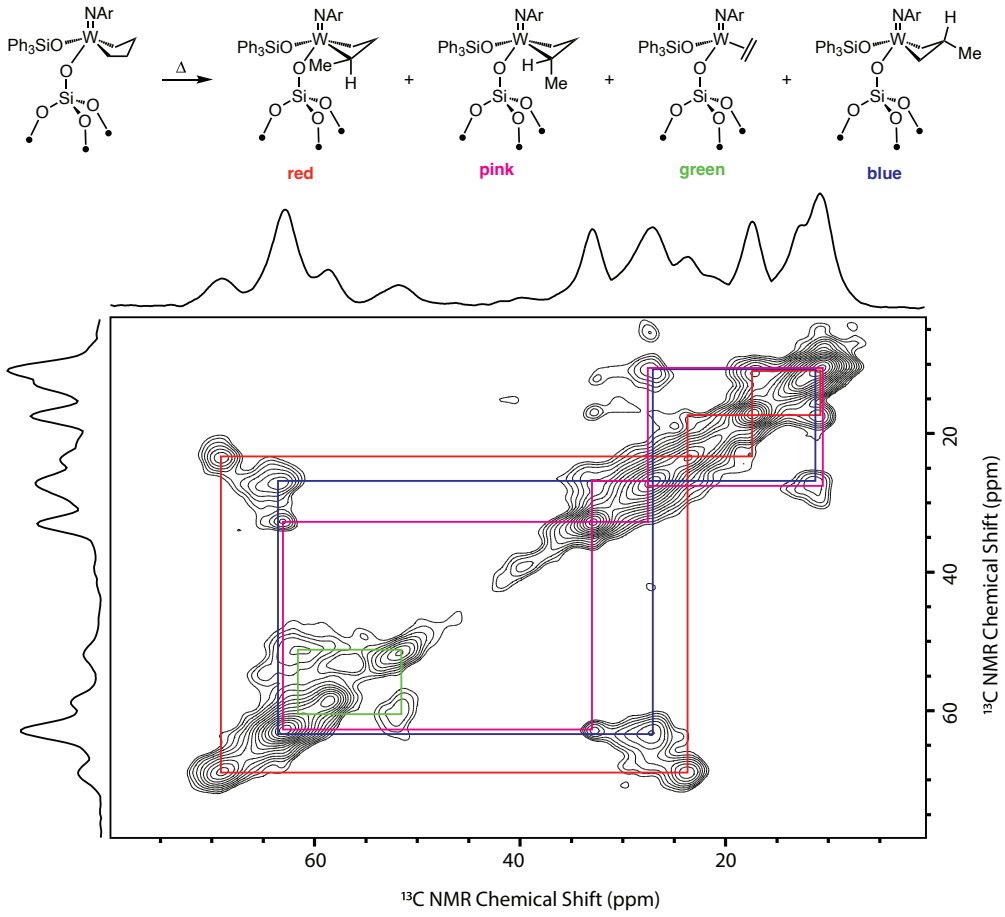

Figure 6.3.4. Expansion of the ^{13}C–^{13}C Dipolar Assisted Rotational Resonance Spectrum of the material heated in the dark at 85°C for 6 hours.

6.3.4. Proposed Mechanism

Scheme 6.1.7. is the proposed mechanism for the conversion of ethylene to propylene. In the first step, a high oxidation W(VI) metallacyclopentane undergoes a ring contraction to form a substituted W(VI) metallacyclobutane, which occurs during the grafting reaction. A cycloreversion of the substituted W(VI) metallacyclobutane gives a W-methylidene. In the presence of excess ethylene, the W-methylidene forms the unsubstituted W(IV) metallacyclobutane. Rearrangement of the unsubstituted W(IV)

metallacyclobutane forms the W(IV) propylene adduct that reacts with two equivalents of ethylene to form propylene.

6.3.5. Catalytic Reaction of Ethylene to Propylene

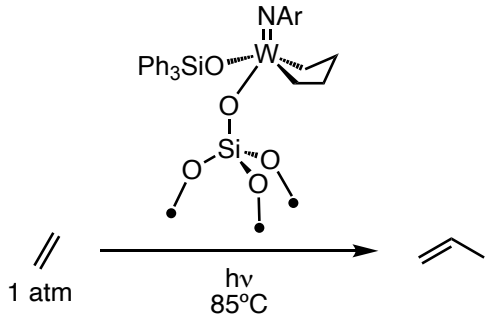

Scheme 6.3.2. Photocatalytic reaction of ethylene by (≡SiO)W(NAr)($OSiPh_3$)(C_4H_8)

(≡SiO)W(NAr)($OSiPh_3$)(C_3H_5Me) converts excess ethylene to 28 propylene per W in the presence of blue LEDS over the course of 2 days, Figure 6.1.6. This reaction is exceptionally selective, and butenes are not detected at any point during catalysis, Figure 6.1.7. A temperature dependence study was performed, and it was shown that maximum TON occurs at 85°C, Figure 6.1.8.

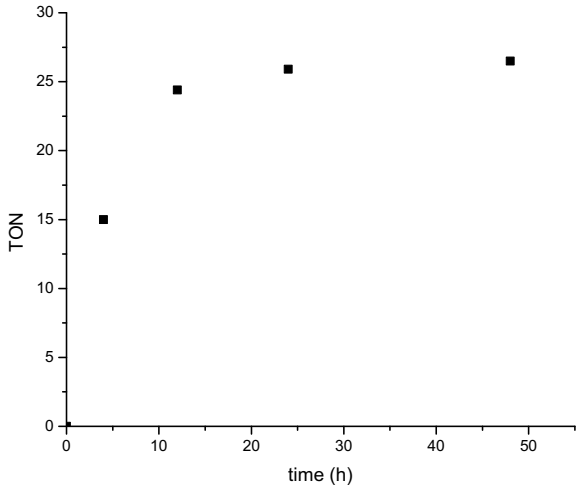

Figure 6.3.5. Plot of TON over time (h) for the reaction of ethylene to propylene at 85°C with irradiation using (≡SiO)W(NAr)(OSiPh$_3$)(C$_4$H$_8$)

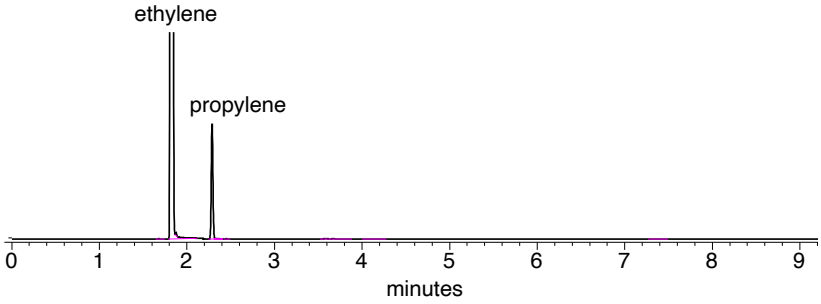

Figure 6.3.6. Chromatogram of the reaction of ethylene to propylene with (≡SiO)W(NAr)(OSiPh$_3$)(C$_4$H$_8$) at 85°C

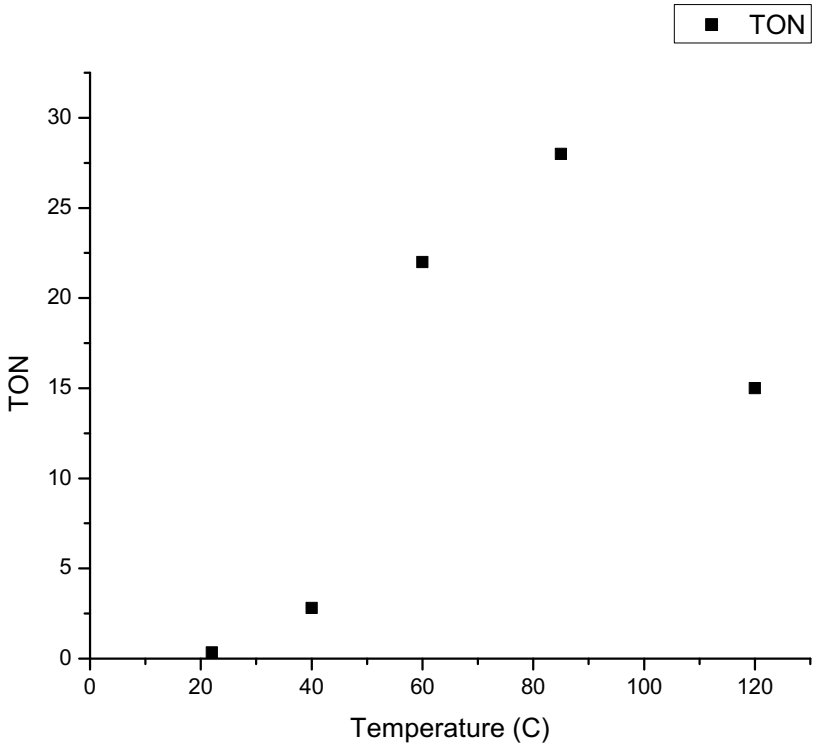

Figure 6.1.2. Temperature vs TON plot for the conversion of ethylene to propylene (TONs are determined at 48h)

6.4. Conclusions

The reaction of $W(NAr)(OSiPh_3)_2(^{13}C_4H_8)$ (Ar = 2,6-$^{i}Pr_2C_6H_3$) with $SiO_{2\text{-}700}$ results in the formation of $(\equiv SiO)(W(NAr)(^{13}C_4H_8)(OSiPh_3)$, isomers of $(\equiv SiO)(W(NAr)(^{13}C_3H_5Me)(OSiPh_3)$, $(\equiv SiO)(W(NAr)(^{13}C_2H_4)(OSiPh_3)$, and ethylene which can be readily distinguished by DARR NMR. A cycloreversion of the substituted W(VI) metallacyclobutane gives a W–methylidene that generates an active unsubstituted metallacyclobutane in the presence of ethylene. The unsubstituted metallacyclobutane

rearranges to form a W(IV)–propylene adduct that can react with two equivalents of ethylene to form propylene. This is the first example this new mechanism.

6.5. Materials and Methods

6.5.1. General Considerations

All reactions and manipulations were performed under an inert atmosphere of nitrogen or argon using standard Schlenk techniques. C_6D_6 was purchased from Cambridge Isotope Laboratories, dried over Na/benzophenone, freeze-pump-thawed three times, and distilled under vacuum. Solvents were purchased from Fisher Scientific, dried by passing through a double-column J. C. Meyer solvent system and degassed before use. C_6H_6 was dried over Na/benzophenone, and distilled under vacuum before use. SZO_{300},[4] ≡Si–OH···$Al(OR^F)_3$,[5] and $SiO_{2\text{-}700}$,[6] were previously described. $W(NAr)(OSiPh_3)_2(C_4H_8)$ was previously described. Ethylene Ultra High Purity was used as received from Airgas. Irradiations with Blue LEDs were realized with 30 Blue 5050 SMD (nominal power 3.1 mW, on a strip), powered by a 12V DC power supply and with an inline DC dimmer. Solution NMR spectra were recorded on a Bruker Avance 300 MHz spectrometer and referenced to C_6D_5H peak at 7.16 ppm. Solid-state NMR experiments were performed on a 600 MHz Bruker NEO spectrometer in 4 mm zirconia rotors packed in an argon filled glovebox. ^1H and $^{13}C\{^1H\}$ CPMAS NMR were recorded in 4 mm zirconia rotors at 10 KHz magic angle spinning speed. FT-IR spectra were recorded as pressed pellets using a Bruker Alpha IR spectrometer in an argon-filled glovebox.

6.5.2. Synthesis of (≡SiO)WNAr(OSiPh$_3$)(C$_4$H$_8$)

200 mg (0.04 mmol OH, 1.0 equiv) and 46.2 mg (0.048 mmol, 1.2 equiv.) W(NAr)(OSiPh$_3$)$_2$(C$_4$H$_8$) were loaded into a teflon valved side arm flask. ~1 mL C_6H_6 was added to the flask, and the flask was wrapped in aluminum foil. The slurry was allowed to stir at room temperature in the dark for 1 hour. During this period the originally white $SiO_{2\text{-}700}$ evolves to a yellow color, and the supernatant maintained a yellow solution. C_6H_6 was decanted off, and the material was washed with ~1mL of C_6H_6 until the supernatant was clear. The material was dried under vacuum (10^{-6} torr) for 30 minutes under diffusion pump vacuum, and stored inside an argon glovebox at -20 °C. Analysis of the supernatant showed a 30% grafting efficiency on $SiO_{2\text{-}700}$.

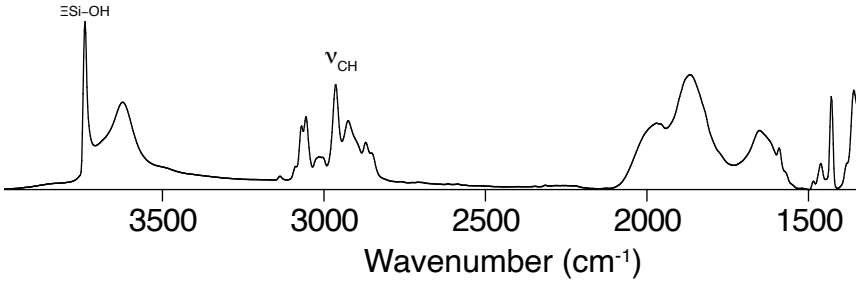

Figure 6.5.1. FT-IR of (≡SiO)WNAr(OSiPh$_3$)(C$_4$H$_8$)

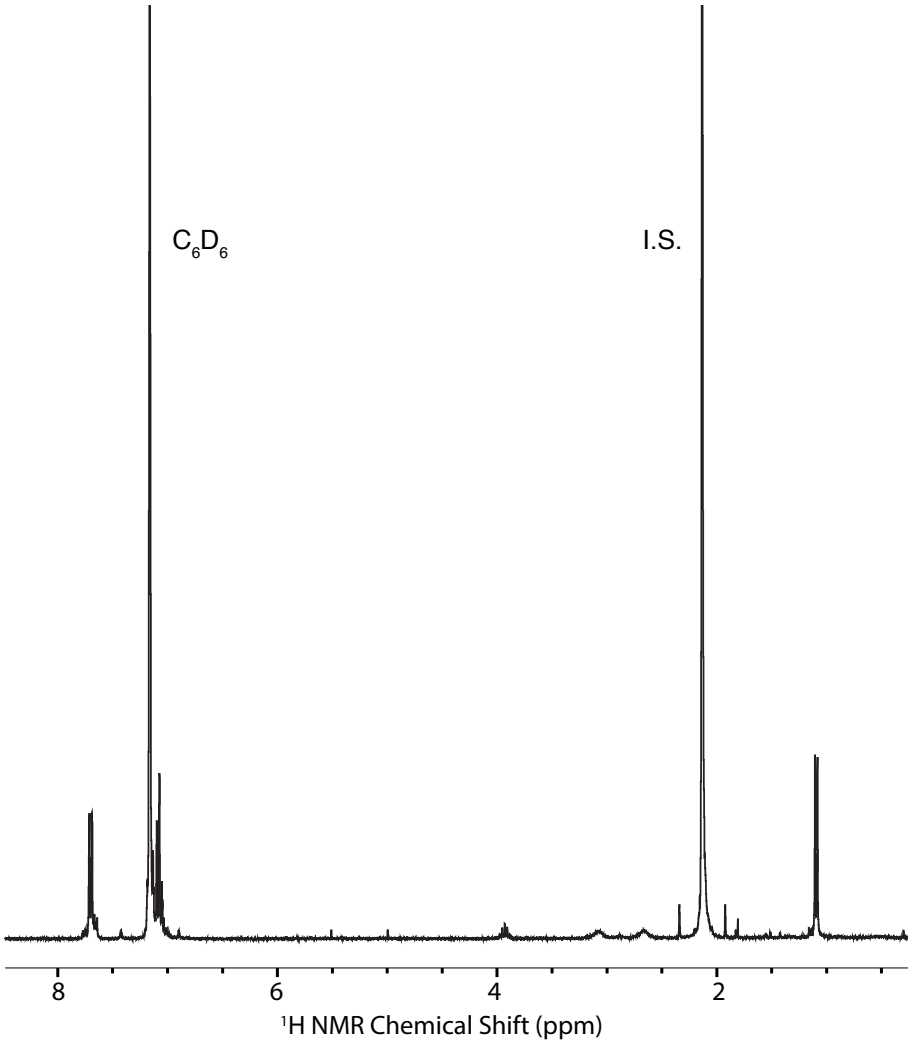

Figure 6.5.2. ^{1}H NMR of the grafting reaction of (≡SiO)WNAr($OSiPh_3$)(C_4H_8) with $SiO_{2\text{-}700}$. No free $HOSiOPh_3$ is seen in the spectra. I.S. = internal standard (hexamethylbenzene)

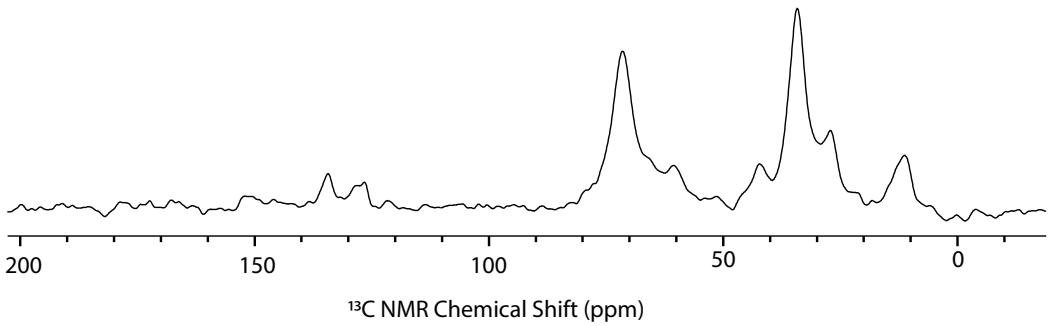

Figure 6.5.3. $^{13}C\{^{1}H\}$ CPMAS NMR spectrum of the grafting reaction. The grafting reaction was performed with rigorous exclusion of light.

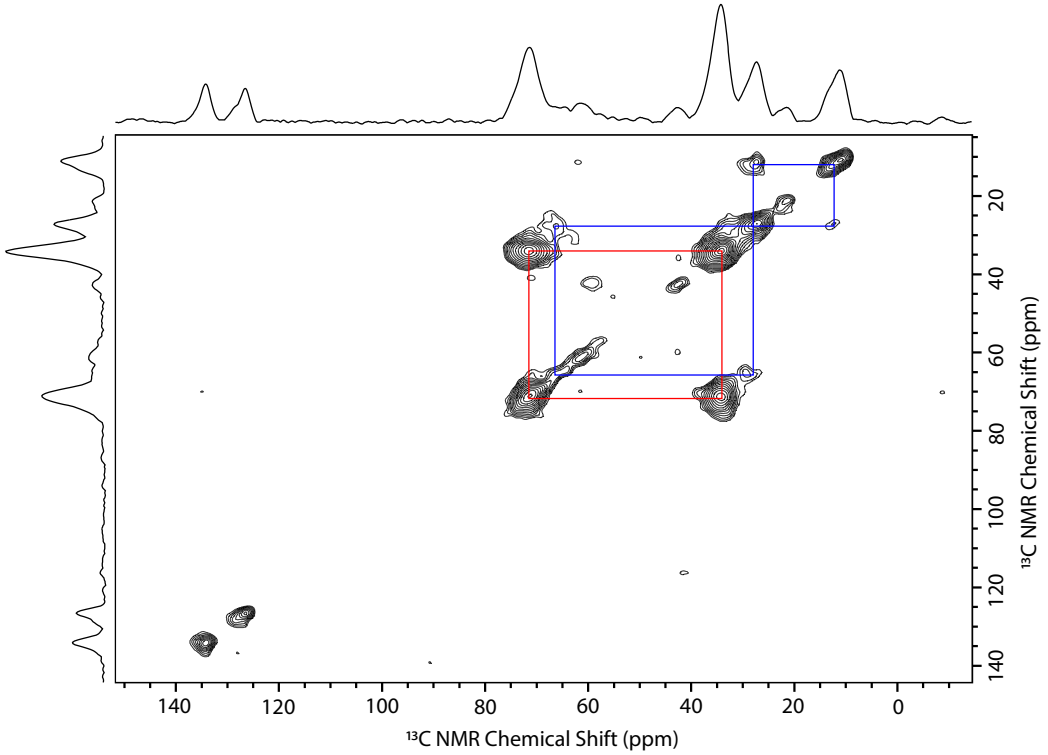

Figure 6.5.4. Full ^{13}C-^{13}C Dipolar Assisted Rotational Resonance spectrum of the grafting reaction. The grafting reaction was performed with rigorous exclusion of light.

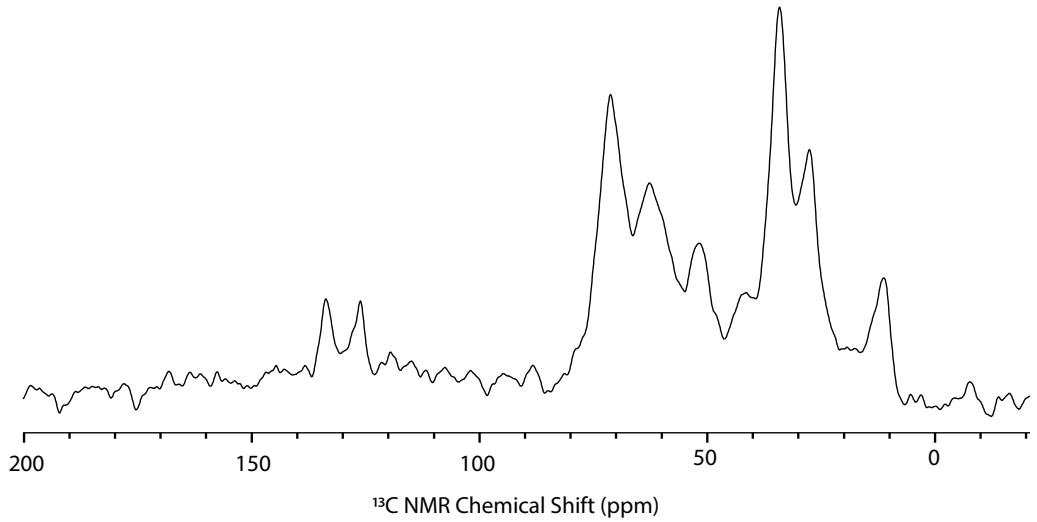

Figure 6.5.5. $^{13}C\{^{1}H\}$ CPMAS NMR spectrum of the grafting reaction under less rigorous light exclusion.

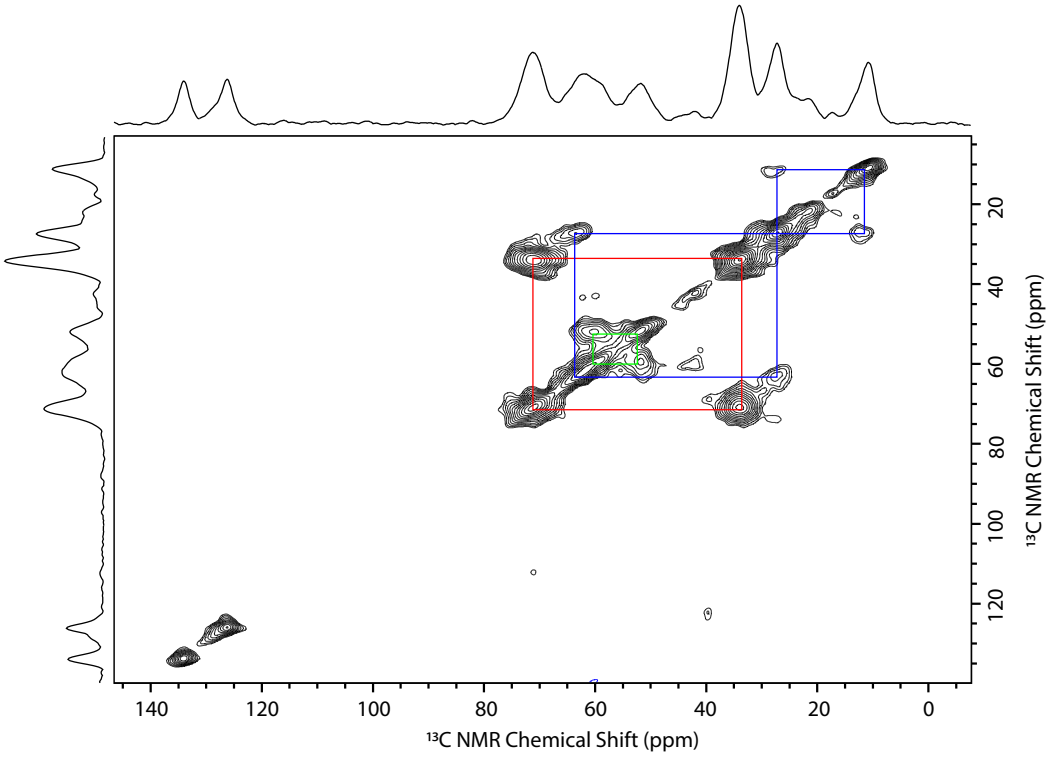

Figure 6.5.6. Expansion of the ^{13}C-^{13}C Dipolar Assisted Rotational Resonance spectrum of the grafting reaction under less rigorous light exclusion.

6.5.3. Thermal Treatment

A valved NMR tube was loaded with 100 mg of material, and immediately wrapped in aluminum foil. The NMR tube was heated at 85°C for 6 hours. During this time, the light-yellow solid evolved into a dark orange material. The material was stored in inside an argon glovebox at -20 °C.

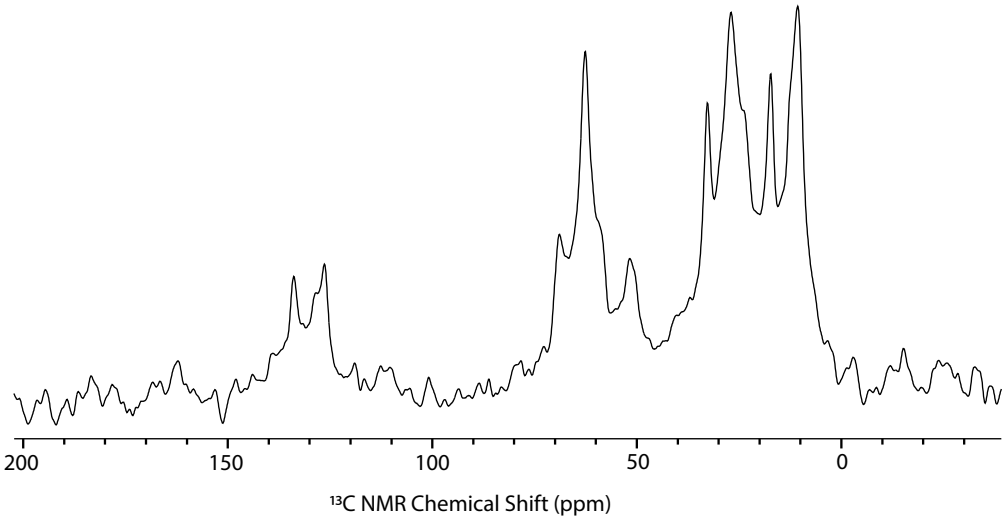

Figure 6.5.7. $^{13}C\{^{1}H\}$ CPMAS NMR spectrum of the material heated in the dark at 85 °C for 6 hours.

6.5.4. Photolytic Treatment

A valved NMR tube was loaded with 100 mg of material, and immediately wrapped in aluminum foil. The NMR tube was then photolyzed with blue LEDs ($\lambda_{max} = 450$ nm) at ambient temperature for 6 hours. Note: ambient temperature of reactor is 37.5 °C. During this time, the light-yellow solid evolved into a dark orange material. After 6 hours, the NMR tube was removed, and allowed to cool to room temperature. The material was stored in inside an argon glovebox at -20 °C.

6.5.5. Photocatalytic reaction of Ethylene to Propylene

A teflon-valved side arm flask (100mL) was charged with 2.3 μmol (~30 mg) of catalyst and a stir bar in the dark. The flask was immediately wrapped in aluminum foil. The flask was placed under vacuum (10^{-6} torr) under diffusion pump vacuum for 15 minutes, and 1 atm of ethylene was added at room temperature. The flask was sealed, and heated to the desired temperature while being photolyzed with blue LEDs ($\lambda_{\max} = 450$ nm) until the reaction no longer turned over. The reaction was aliquoted (200 μL) and volatiles were analyzed via GC.

6.5.5.1. GC Parameters

The GC column oven was held at 150 °C for 15 min. 200 µL of gas was injected using a split ratio of 76.926:1. He was used as the carrier gas at a flow rate of 23.5 mL/min. The temperature of the flame ionization detector (FID) was set at 350 °C at a flow rate of air and hydrogen at 400 mL/min and 30 mL/min, respectively. In order to quantify the amount of gas, the response factor of the FID was calibrated to known pressures of methane. FID response for hydrocarbons is proportional to the number of carbon atoms in the analyte. The amount of propylene was calculated based on this equation 6.5.1:

Equation 6.5.1.

$$\frac{\left(\frac{\text{Area of peak}}{\text{Number of Carbons}}\right)}{\text{Response Factor}}\ x\ \text{V(L)} = \text{n(mol)RT(K)}$$

6.5.5.2. ***Conversion Plots***

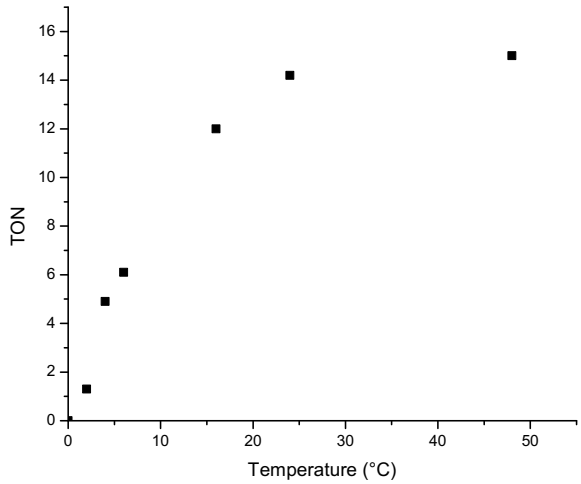

Figure 6.5.8. Plot of TON over time (h) for the reaction of ethylene to propylene at 120°C with irradiation

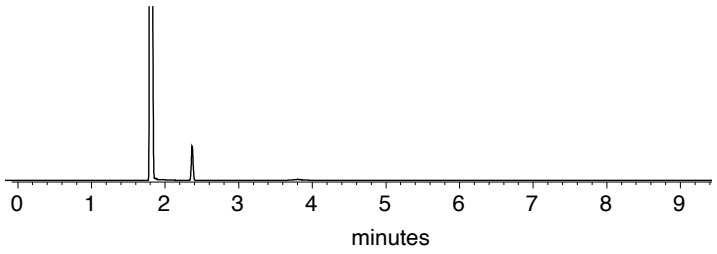

Figure 6.5.9. Chromatogram of the reaction of ethylene to propylene at 120°C with irradiation

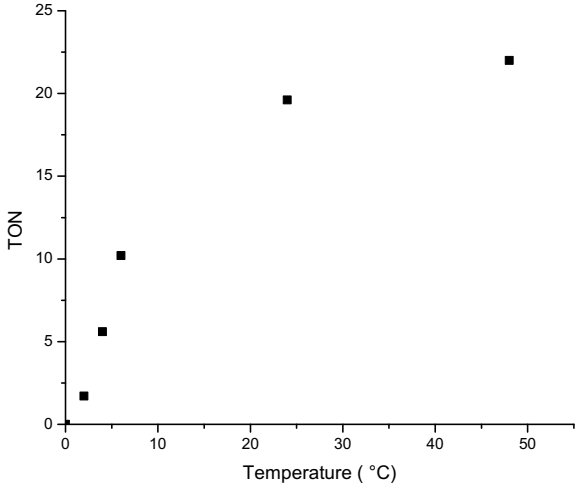

Figure 6.5.10. Plot of TON over time (h) for the reaction of ethylene to propylene at 60°C with irradiation

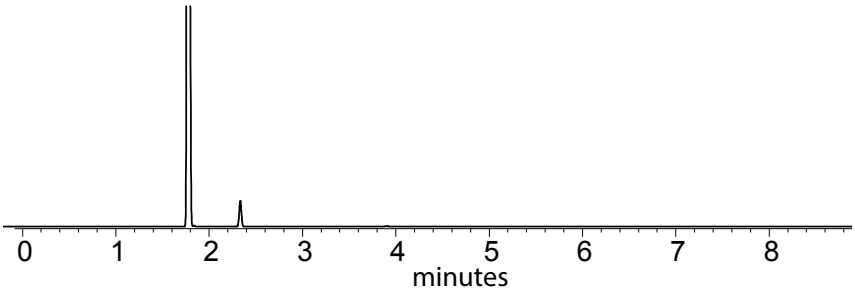

Figure 6.5.11. Chromatogram of the reaction of ethylene to propylene at 60°C with irradiation

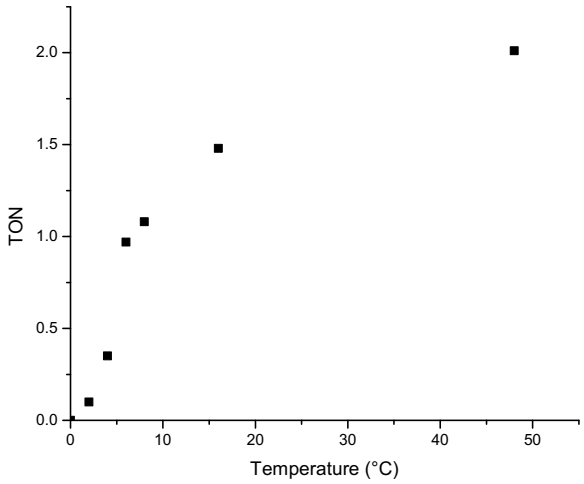

Figure 6.5.12. Plot of TON over time (h) for the reaction of ethylene to propylene at 40°C

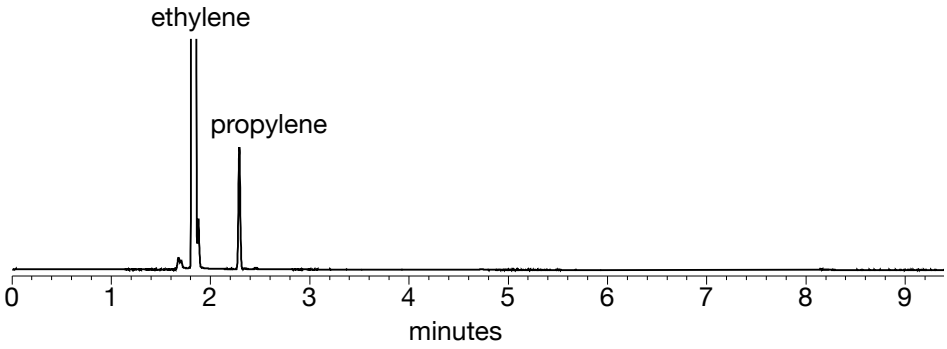

Figure 6.5.13. Chromatogram of the reaction of ethylene to propylene with irradiation at 40°C

6.6. References

1. Peryshkov, D. V., Forrest, W. P., Schrock, R. R., Smith, S. J. and Müller, P. B(C6F5)3 activation of oxo tungsten complexes that are relevant to olefin metathesis. *Organometallics* **32**, 5256–5259 (2013).

2. McLain, S. J., Wood, C. D. and Schrock, R. R. Preparation and Characterization of Tantalum(III) Olefin Complexes and Tantalum(V) Metallacyclopentane Complexes Made from Acyclic α Olefins. *J. Am. Chem. Soc.* **101**, 4558–4570 (1979).

3. McLain, S. J., Sancho, J. and Schrock, R. R. Metallacyclopentane to Metallacyclobutane Ring Contraction. *J. Am. Chem. Soc.* **101**, 5451–5453 (1979).

4. Tafazolian, H., Culver, D. B. and Conley, M. P. A Well-Defined Ni(II) α-Diimine Catalyst Supported on Sulfated Zirconia for Polymerization Catalysis. *Organometallics* **36**, 2385–2388 (2017).

5. Culver, D. B., Venkatesh, A., Huynh, W., Rossini, A. J. and Conley, M. P. Al(OR F) 3 (R F ¼ C(CF 3) 3) activated silica: a well-defined weakly coordinating surface anion †. *Chem. Sci.* **11**, 1510–1517 (2020).

6. Le Roux, E. *et al.* Detailed structural investigation of the grafting of [Ta(=CHtBu)(CH 2tBu)3] and [Cp*TaMe4] on silica partially dehydroxylated at 700 °C and the activity of the grafted complexes toward alkane metathesis. *J. Am. Chem. Soc.* **126**, 13391–13399 (2004).